

**A Thesis Submitted for the Degree of PhD at the University of Warwick**

**Permanent WRAP URL:**

<http://wrap.warwick.ac.uk/131581>

**Copyright and reuse:**

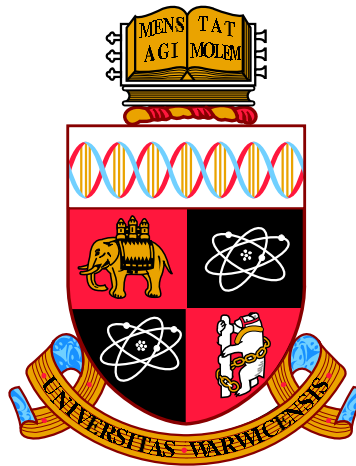
This thesis is made available online and is protected by original copyright.

Please scroll down to view the document itself.

Please refer to the repository record for this item for information to help you to cite it.

Our policy information is available from the repository home page.

For more information, please contact the WRAP Team at: [wrap@warwick.ac.uk](mailto:wrap@warwick.ac.uk)



**A Physics-Driven Model for the Closed-Loop  
Quality Control of Remote Laser Welding**

by

**ERKAN CANER OZKAT**

**Thesis**

Submitted to the University of Warwick

for the degree of

**Doctor of Philosophy**

**Warwick Manufacturing Group**

May 2018

# Contents

<b>Contents</b>	<b>i</b>
<b>List of Tables</b>	<b>v</b>
<b>List of Figures</b>	<b>vii</b>
<b>Declarations</b>	<b>xiv</b>
<b>List of Publications</b>	<b>xv</b>
<b>Acknowledgments</b>	<b>xvi</b>
<b>Abstract</b>	<b>xvii</b>
<b>Abbreviations</b>	<b>xix</b>
<b>Chapter 1 Introduction</b>	<b>1</b>
1.1 The Motivation for the RLW in the Automotive Industry . . . . .	2
1.2 The Research Scope . . . . .	10
1.3 Research Objectives & Contributions . . . . .	14
1.4 Thesis Organization . . . . .	18
<b>Chapter 2 Background</b>	<b>20</b>
2.1 The Characteristic Properties of Laser Beam . . . . .	20
2.1.1 Coherence . . . . .	22
2.1.2 Monochromatic . . . . .	23
2.1.3 Transverse Electromagnetic Mode . . . . .	23
2.1.4 Polarisation . . . . .	24
2.1.5 Wavelength . . . . .	25
2.2 The Geometrical Parameters of Laser Beam . . . . .	26
2.2.1 Beam Waist Radius . . . . .	27

2.2.2	Beam Divergence Angle . . . . .	27
2.2.3	Rayleigh Length . . . . .	28
2.3	The Quality of Laser Beam . . . . .	28
2.4	The Laser Welding Process Parameters . . . . .	29
2.4.1	Laser Power . . . . .	30
2.4.2	Welding Speed . . . . .	31
2.4.3	Focal Offset . . . . .	31
2.4.4	Incidence Angle . . . . .	32
2.4.5	Laser Intensity . . . . .	33
2.4.6	Interaction Time . . . . .	34
2.5	Modes of Laser Welding . . . . .	35
2.5.1	Conduction Mode . . . . .	35
2.5.2	Keyhole Mode . . . . .	35
2.6	The Weld Quality . . . . .	36
2.6.1	Metallurgical Weld Quality . . . . .	37
2.6.2	Mechanical Weld Quality . . . . .	44
2.6.3	Aesthetic Weld Quality . . . . .	47
2.7	Summary . . . . .	49
<b>Chapter 3 Literature Review</b>		<b>51</b>
3.1	Related Work on the Mitigation Methods of Zinc Vapour in Laser Welding of Galvanized Steels . . . . .	52
3.1.1	Removal of Zinc Coating . . . . .	53
3.1.2	Reduction in Zinc Vapour Pressure . . . . .	54
3.1.3	Ventilation of Zinc Vapour . . . . .	55
3.2	Related Work on the Process Monitoring . . . . .	58
3.3	Related Work on Numerical Simulation Modelling of Laser Welding	62
3.3.1	Heat Transfer . . . . .	63
3.3.2	Fluid Flow . . . . .	66
3.3.3	Keyhole Surface Generation . . . . .	67
3.4	Summary . . . . .	73
<b>Chapter 4 Laser Dimpling Process Parameters Optimization Using Surrogate-Driven Process Capability Space</b>		<b>75</b>
4.1	Definition of Key Control Characteristics & Key Performance Indicators	81
4.2	Problem Formulation for the Proposed Research Approach . . . . .	83
4.2.1	Formulation of Surrogate Modelling for the Process Charac- terization . . . . .	87

4.2.2	Formulation of Deterministic & Stochastic Process Capability Spaces . . . . .	89
4.2.3	Formulation of Process Parameter Optimization Using Calculated Surrogate Models . . . . .	90
4.3	Research Methodology to Develop Surrogate-Driven Process Capability Space . . . . .	91
4.3.1	Materials & Experimental Setup . . . . .	91
4.3.2	Design of Experiments . . . . .	94
4.3.3	Development of Surrogate Models . . . . .	94
4.3.4	Development of Deterministic & Stochastic Process Capability Spaces . . . . .	95
4.4	The Laser Dimpling Process Parameter Optimization Using Surrogate-Driven Process Capability Space . . . . .	97
4.5	Results of Surrogate-driven Process Capability Space . . . . .	99
4.5.1	Statistical Data Analysis . . . . .	99
4.5.2	Deterministic Surrogate Models . . . . .	100
4.5.3	Deterministic Process Capability Space ( <b>DC<sub>p</sub>-space</b> ) . . . . .	104
4.5.4	Stochastic Process Capability Space ( <b>SC<sub>p</sub>-space</b> ) . . . . .	104
4.5.5	Process Parameters Optimization . . . . .	105
4.6	Sensitivity Analysis . . . . .	108
4.7	Summary of the Chapter . . . . .	112

**Chapter 5 Decoupled Multi-physics Multi-Fidelity Modelling of Laser Welding for In-process Monitoring** **114**

5.1	Definition of Key Control Characteristics & Key Performance Indicators	116
5.2	Problem Formulation for the Proposed Research Approach . . . . .	119
5.2.1	Formulation of the Laser Intensity . . . . .	123
5.2.2	Formulation of the Keyhole Profile . . . . .	126
5.2.3	Formulation of the Temperature Profile . . . . .	128
5.2.4	Formulation of FZDs Extraction . . . . .	131
5.3	Research Methodology to Develop Multi-Fidelity Model . . . . .	132
5.3.1	Materials & Experimental Setup . . . . .	132
5.3.2	Design of Experiments . . . . .	135
5.3.3	Off-line Generation of Scaling Functions . . . . .	136
5.3.4	Development & Validation of Multi-Fidelity Model . . . . .	139
5.4	Results & Discussion . . . . .	141

5.4.1	The Results of the High-Fidelity, Multi-Fidelity, & Low-Fidelity Models . . . . .	141
5.4.2	Scaling Functions . . . . .	151
5.4.3	Validation Results . . . . .	153
5.5	Summary of the Chapter . . . . .	159
<b>Chapter 6 Conclusions and Future Works</b>		<b>161</b>
6.1	Conclusions . . . . .	161
6.2	Engineering Contribution . . . . .	165
6.3	Limitations & Future Works . . . . .	166
<b>Bibliography</b>		<b>167</b>
<b>Appendix A</b>		<b>181</b>
<b>Appendix B</b>		<b>192</b>
<b>Appendix C</b>		<b>194</b>
<b>Appendix D</b>		<b>197</b>
<b>Appendix E</b>		<b>206</b>
<b>Appendix F</b>		<b>223</b>

# List of Tables

1.1	The specific strength of different materials [Adapted from Cunat (2000)]	5
1.2	Macro-section images and the grain morphology of different zones in the joints [Adapted from Zhang et al. (2016)] . . . . .	9
2.1	The spatial and the temporal coherence of different beams. The laser beam is both spatial and temporal coherent . . . . .	23
2.2	Comparison between conduction and keyhole welding modes . . . . .	36
2.3	The chemical composition of DX54D+Z steel (wt %) . . . . .	37
2.4	The mechanical properties of DX54D+Z steel . . . . .	38
2.5	The thermal properties of DX54D+Z steel . . . . .	38
2.6	Welding quality in terms of Fusion Zone Dimensions (FZDs) and their allowance limits. $t_{upper}$ indicates the thickness of the upper sheet; $t_{lower}$ indicates the thickness of the lower sheet . . . . .	47
3.1	Related work on the selection of optimum laser dimpling process parameters . . . . .	58
3.2	Process signals and detectors used in process monitoring for the laser welding . . . . .	59
3.3	In-process monitoring of KPIs highlighting the proposed monitoring approach . . . . .	62
3.4	Interactions of occurring physical phenomenon in laser welding . . . . .	69
3.5	Computational time for different modelling approaches and their main properties . . . . .	72
3.6	The multi-physics and decoupled multi-physics modelling approaches	73
4.1	KCCs and their corresponding allowance limits . . . . .	83
4.2	KPIs and their corresponding allowance limits . . . . .	83
4.3	Laser focusing and repositioning module (SmartLaser) . . . . .	92
4.4	Key control characteristics and corresponding levels . . . . .	94

4.5	The proposed design option to find out optimum process parameters	98
4.6	$R^2$ & RMSE values for different surrogate models . . . . .	100
4.7	The optimization results showing the proposed design . . . . .	106
4.8	The validation of the optimization results for all design options . . .	107
4.9	The effect of % change in mean and standard deviation into the results	111
5.1	The temperature values at the sampling points and the computational time for each mesh size. The temperature value at each sampling point converges to a certain temperature value as the mesh size is increased. The computational time also increases with the increase in the mesh size . . . . .	131
5.2	The constant parameters used in the LF model . . . . .	132
5.3	The procedure to be followed for the metallographic analysis of the weld . . . . .	134
5.4	The methodological steps for computing FZDs using the multi-fidelity (MF) model in the overlap welding . . . . .	140
5.5	The comparison of the keyhole opening radius ( $r_{KH_0}$ ) for different models at various welding speeds . . . . .	154
5.6	The results of the validation experiments to determine the accuracy of the MF model. The accuracy is computed based on the MAE values.	157
6.1	Characteristics of the remote laser welding process . . . . .	162
A.1	DoE Table and Experimental Results for Laser Dimpling . . . . .	181
C.1	DoE Table and Experimental Results for Penetration ( $PT$ ) in Bead-on-plate Welding . . . . .	194
C.2	DoE Table and Experimental Results for Top Width ( $TW$ ) in Bead-on-plate Welding . . . . .	195
D.1	DoE Table and Experimental Results for Penetration ( $PT$ ) in Overlap Welding . . . . .	197
D.2	DoE Table and Experimental Results for Top Width ( $TW$ ) in Overlap Welding . . . . .	199
D.3	DoE Table and Experimental Results for Interface Width ( $IW$ ) in Overlap Welding . . . . .	201



# List of Figures

1.1	A schematic diagram of the required flange size in RSW and RLW processes [Adapted from Bea et al. (2011)] . . . . .	4
1.2	An industrial laser welding robot showing robot arm, laser optics and scanning head . . . . .	6
1.3	The longitudinal cross-section illustration of the laser welded joint . . . . .	7
1.4	The variation of heat input to the workpiece with power intensity of the heat source [Adapted from Kou (2003)] . . . . .	8
1.5	The outline of the dissertation: (a) controlling minimum joining gap requirement in the RLW process by utilizing the laser dimpling process ( <i>Chapter 4</i> ), (b) the physics-driven process model for quality assurance for the RLW process ( <i>Chapter 5</i> ) . . . . .	12
2.1	Components of a typical laser system: Pump Source, Gain Medium, Optical Resonator . . . . .	21
2.2	Transverse Electromagnetic Modes: a) Rectangular coordinate, b) Polar coordinate . . . . .	24
2.3	Polarization types: a) Linear polarization, b) Circular polarization, c) Elliptical polarization . . . . .	25
2.4	Absorption of various metals at relevant wavelengths [Adapted from Saucedo et al. (2016)] . . . . .	26
2.5	A schematic diagram of a typical optical system showing the geometrical parameters of a laser beam [Adapted from Abt et al. (2007)] . . . . .	27
2.6	The comparison between (a) high BPP, (b) low BPP that highlights focal length, Rayleigh length, and laser optics . . . . .	29
2.7	The fundamental process parameters for laser welding . . . . .	30
2.8	The grain morphology (a) low welding speed, (b) high welding speed [Adopted from Lienert et al. (2011)] . . . . .	31

2.9	Transverse cross sections of weld using $P_L$ : 550 W, $W_S$ : 35 mm/s, $Gap$ : 0.15 mm and $F_O$ of: (a) -0.3 mm, (b) -0.2 mm, (c) -0.1 mm, (d) 0 mm, (e) +0.1 mm, and (f) +0.2 mm (D:Penetration, W:Top Width, C:Top Concavity) [Adopted from Zhao et al. (2012)] . . . . .	32
2.10	Experiment results showing the influence of incidence angle on the weld shape (a) Top view of welded spot and (b) Transverse cross sections of the weld (c) Characteristic lengths of the welded spot as functions of incident angle [Adopted from Liao and Yu (2007)] . . . . .	33
2.11	The experimental result that shows the penetration as a function of: (a) laser intensity for different interaction times, and (b) interaction time for different laser intensities [Adopted from Suder and Williams (2012)] . . . . .	34
2.12	The modes of laser welding. a) Conduction mode, b) Keyhole mode	36
2.13	(a) The distribution of the different zones in a welded joint as a function of temperature in relation to (b) the iron-carbon phase equilibrium	39
2.14	Top view of the fusion zone structure at different welding speeds (a) elliptical molten pool, (b) teardrop shape molten pool [Adopted from Lienert et al. (2011)] . . . . .	40
2.15	Effect of temperature gradient G and growth rate R on the morphology and size of solidification microstructure [Adopted from Kou (2003)]	41
2.16	Variation in solidification mode across the fusion zone [Adopted from Kou (2003)] . . . . .	42
2.17	A schematic representation of a) the partially melted zone, and b) temperature history for given points in the welded material . . . . .	42
2.18	The solidification modes of grain boundary liquid in the PMZ [Adopted from Huang et al. (2001)] . . . . .	43
2.19	The different microstructural regions in a steel weld highlighting the grain growth and the grain refinement regions inside the HAZ [Adopted from Layus et al. (2018)] . . . . .	44
2.20	a) Instron 100kN tensile testing machine used for the lap shear tensile tests, b) Dimensions of the welded samples to be tested via lap shear tensile test [Prepared based on the industrial standard EN ISO 5817 (2014)] . . . . .	45
2.21	Deformation of the different laser lap welded structures under tensile shear load and configuration of breaking point after fracture a) at the base metal, b) at adjacent to the weld, c) at the weld [Adopted from Miyazaki and Furusako (2007)] . . . . .	46

2.22	A schematic description of spatter formation based on the localized evaporation of metal in the keyhole front, and the flow conditions in the molten around the keyhole . . . . .	49
4.1	A schematic diagram of the joining gap between two sheet metals a) ideal case b) real case . . . . .	76
4.2	The effect of joining gap variation on the weld quality (a) the strength at the failure (b) macro-section image showing weld shape and contour	77
4.3	A macro-section image of a laser welded joint highlighting the fusion zone of the weld, the generated gap, and two dimples . . . . .	78
4.4	(a) Illustration of humping effect during a dimpling process, (b) dimple upper surface, (c) dimple lower surface . . . . .	79
4.5	The conceptual representation of (a) Experimental results, (b) Success rate models for the deterministic and the stochastic scenarios. The tolerance limits that determine the process capability space in each scenario are also presented. . . . .	86
4.6	An overview of the experimental setup (a) Beam quality measurement (b) Laser Dimpling setup (first series of experiments) (c) Remote Laser Welding setup (second series of experiments) . . . . .	92
4.7	(a) Experimental setup for profilometer, (b) An example of 3D reconstruction. Process parameters: $S_S$ : 2 m/min, $\alpha$ : 20°, $L_T$ : 4 mm, $F_O$ : 35 mm . . . . .	93
4.8	Measurement of the dimple lower surface area (a) Grabbed image with scale bar. (b) Dimple lower surface area for the first right experiment configuration. Process parameters: $S_S$ : 2 m/min, $\alpha$ : 10°, $L_T$ : 4 mm, $F_O$ : 25 mm . . . . .	93
4.9	The procedure flow for computing process capability spaces . . . . .	96
4.10	The estimated dimple height value ( $D_H$ ) over <b>KCC-space</b> in the deterministic scenario for varying Scanning Speed ( $S_S$ ) and Incidence Angle ( $\alpha$ ) for constant Laser Track ( $L_T$ ) and Focal Offset ( $F_O$ ) values	101
4.11	The estimated dimple upper surface area value ( $D_U$ )over <b>KCC-space</b> in the deterministic scenario for varying Scanning Speed ( $S_S$ ) and Incidence Angle ( $\alpha$ ) for constant Laser Track ( $L_T$ ) and Focal Offset ( $F_O$ ) values . . . . .	102

4.12	The estimated dimple lower surface area value ( $D_L$ ) over <b>KCC-space</b> in the deterministic scenario for varying Scanning Speed ( $S_S$ ) and Incidence Angle ( $\alpha$ ) for constant Laser Track ( $L_T$ ) and Focal Offset ( $F_O$ ) values . . . . .	103
4.13	Effect of focal offset on three KPIs when process parameters are constant at: $S_S$ : 3 m/min, $\alpha$ : 10°, $L_T$ : 3 mm. (Upper Surface) Surface profilometer results – (Lower Surface) Image processing results . . .	103
4.14	Deterministic Process Capability Space ( <b>DC<sub>p</sub>-space</b> ) over <b>KCC-space</b> for varying Scanning Speed ( $S_S$ ) and Incidence Angle ( $\alpha$ ) for constant Laser Track ( $L_T$ ) and Focal Offset ( $F_O$ ) values	104
4.15	Stochastic Process Capability Space ( <b>SC<sub>p</sub>-space</b> ) over <b>KCC-space</b> for varying Scanning Speed ( $S_S$ ) and Incidence Angle ( $\alpha$ ) for constant Laser Track ( $L_T$ ) and Focal Offset ( $F_O$ ) values . . . . .	105
4.16	Remote laser welded joint looking from the backside. (a) Trial-and-error method before optimization. (b) Optimized configuration based on the proposed methodology . . . . .	108
4.17	The schematic illustration of shifting mean and standard deviation on the PDF (a) The original mean and standard deviation, (b) The new mean $\mu_1$ is bigger than the original mean $\mu_0$ , (c) The new standard deviation $\sigma_1$ is bigger than the original standard deviation $\sigma_0$ . . . .	109
4.18	The two-dimensional design space showing the effect of % change in the mean and the standard to the change in success rate. The change in the mean value is much more significant than the change in the standard deviation. . . . .	111
5.1	A schematic diagram showing laser welding process parameters and laser beam parameters . . . . .	118
5.2	The distinct regions and the fusion zone dimensions to assess the weld quality . . . . .	119
5.3	The overall representation of the proposed methodology in multi-fidelity modelling. It highlights the high-fidelity model (Point A), the low-fidelity model (Point B), the low-fidelity model with scaling, called the multi-fidelity model (Point C), and physical experimentation with high-fidelity . . . . .	120
5.4	The framework of the proposed sequential decoupled model (Low-Fidelity (LF) model – Moving from Point A to Point B in Fig. 5.3) .	121

5.5	The methodology of computing the scaling function over the design space . . . . .	122
5.6	The flow chart of the sequential decoupled model with scaling function (Multi-Fidelity (MF) Model – Moving from Point B to Point C in Fig. 5.3) . . . . .	123
5.7	A schematic description of the absorption mechanism in the laser welding process (a) outside the keyhole: the plasma absorption ( $I_0 \cdot (1 - \alpha_{plasma})$ ) and the surface absorption ( $I_1 = I_0 \cdot \alpha_{surf} \cdot (1 - \alpha_{plasma})$ ) (b) inside the keyhole: the inverse-Bremsstrahlung absorption ( $I_2 = I_1 \cdot \exp(-\alpha_{inBre} \cdot \Delta z)$ ) and the Fresnel absorption ( $I_{2_{abs}} = I_2 \cdot \alpha_{Fre}$ ) . . . . .	126
5.8	The computational domains generated employing different mesh sizes (a) Coarse Mesh, (b) Normal Mesh, (c) Fine Mesh, and three sampling points within these domains . . . . .	130
5.9	Experimental setup. (a) The welding robot, (b) The welding table and clamp locations, (c) Top view and cross-section of welding fixture showing laser welding location and direction . . . . .	133
5.10	The process flow of the validation experiments to verify the MF model and scaling functions utilized in the MF model . . . . .	141
5.11	The results of the HF, the LF and the MF models are presented to the characterization of Top Width (TW) over the KCC-space. TW reduces with increasing welding speed and joining gap, but it increases with increasing incidence angle. The results of the MF model follow the same pattern as the results of the HF model, and they are within the tolerance limits. . . . .	143
5.12	The results of the HF, the LF and the MF models are presented to the characterization of Interface Width (IW) over the KCC-space. IW reduces with increasing welding speed, but it increases with joining gap and increasing incidence angle. At the larger joining gap, the HF model results (i.e. physical experiments) violate the allowance limits. At these points, the results of the LF model will become lower than the results of the HF model because the mass transfer is not considered in the LF model. The results of the MF model follow the same pattern as the results of the HF model, and they are within the tolerance limits. . . . .	145

5.13	The results of the HF, the LF and the MF models are presented to the characterization of Penetration (PT) over the KCC-space. PT reduces with increasing welding speed. Two modes are seen, the open keyhole mode, and the blind keyhole mode. The results of the HF model in the blind keyhole mode are out of the allowance limits. The results of both LF and MF models are constant values (1 mm) due to fluid flow is not considered in these models. The results of the MF model are within the tolerance limits. . . . .	147
5.14	The comparison of (i) the macro-section images obtained by the HF model (i.e. experiment) against the computed by the MF model, and (ii) the measured FZDs against the computed FZDs using the MF model. The process parameters not specified in the graph are welding speed ( $W_S$ ): 2.0 m/min, focal offset ( $F_O$ ): 0 mm, and laser power ( $P_L$ ): 3 kW . . . . .	150
5.15	The comparison of (i) the macro-section images obtained by the HF model (i.e. experiment) against the computed by the MF model, and (ii) the measured FZDs against the computed FZDs using the MF model. The process parameters not specified in the graph are welding speed ( $W_S$ ): 3.2 m/min, focal offset ( $F_O$ ): 0 mm, and laser power ( $P_L$ ): 3 kW . . . . .	151
5.16	The estimated first scaling factor ( $\hat{\beta}_{1/3\mu}$ ) over the KCC-space using the first scaling function ( $f_{\beta_{1/3\mu}}$ ) developed based on the mean-only analysis (See Eq. (5.24)) . . . . .	152
5.17	The estimated second scaling factor ( $\hat{\beta}_{2\mu}$ ) over the KCC-space using the second scaling function ( $f_{\beta_{2\mu}}$ ) developed based on the mean-only analysis (See Eq. (5.24)) . . . . .	153
5.18	The comparison of (i) the macro-section images obtained by the validation experiments against the computed by the MF model, and (ii) the measured FZDs against the computed FZDs using the MF model. The process parameters not specified in the graph are welding speed ( $W_S$ ): 2.45 m/min, focal offset ( $F_O$ ): 0 mm, and laser power ( $P_L$ ): 3 kW . . . . .	155

5.19	The comparison of (i) the macro-section images obtained by the validation experiments against the computed by the MF model, and (ii) the measured FZDs against the computed FZDs using the MF model. The process parameters not specified in the graph are welding speed ( $W_S$ ): 3.0 <i>m/min</i> , focal offset ( $F_O$ ): 0 <i>mm</i> , and laser power ( $P_L$ ): 3 <i>kW</i> . . . . .	156
C.1	DoE table and experimental results showing cross-section images in bead-on-plate welding . . . . .	196
D.1	DoE table and experimental results showing cross-section images in overlap welding . . . . .	203

# Declarations

This thesis is the original work of the author and submitted to the University of Warwick in support of my application for the degree of Doctor of Philosophy. I hereby declare that this thesis has not been submitted in any previous application for any degree. The work presented was carried out by the author, except where explicitly stated. Over the course of PhD research, parts of this thesis have been published by the author and these publication are given in the list of publication at page xv.



Erkan Caner OZKAT



# List of Publications

## Journal Papers

E. C. Ozkat, P. Franciosa, and D. Ceglarek. Laser dimpling process parameters selection and optimization using surrogate-driven process capability space. *Optics and Laser Technology*, 93:149–164, 2017. ISSN 00303992. doi: 10.1016/j.optlastec.2017.02.012. URL <http://www.sciencedirect.com/science/article/pii/S0030399216309513>.

E. C. Ozkat, P. Franciosa, and D. Ceglarek. Development of decoupled multi-physics simulation for laser lap welding considering part-to-part gap. *Journal of Laser Applications*, 29(2):022423, 2017. ISSN 1042-346X. doi: 10.2351/1.4983234. URL <http://lia.scitation.org/doi/10.2351/1.4983234>.

E. C. Ozkat, P. Franciosa, and D. Ceglarek. Decoupled multi-physics multi-fidelity model of RLW for in-process monitoring. *To be submitted to Lasers in Manufacturing and Materials Processing*.

## Conference Papers

E. C. Ozkat, P. Franciosa, and D. Ceglarek. Monitoring remote laser welding process of overlap joints based on energy balance model. In *ICALEO 2016 - International Congress on Applications of Laser and Electro-Optics*, page 602–610, 2016.

E. C. Ozkat, P. Franciosa, and D. Ceglarek. A Framework for physics-driven in-process Monitoring of penetration and interface width in laser overlap welding. *Procedia CIRP*, 60:44–49, 2017. ISSN 22128271. doi: 10.1016/j.procir.2017.01.043. URL <http://dx.doi.org/10.1016/j.procir.2017.01.043>.

## Poster Presentation

E. C. Ozkat, P. Franciosa, and D. Ceglarek. In-Process Monitoring of Remote Laser Welding Process Based on Decoupled Multiple-physics Simulation. In *WMG Doctoral Research & Innovation Conference*, 2016. doi: 10.13140/RG.2.2.23679.30880. Poster Presentation awarded with runner’s up prize.

# Acknowledgments

In the name of Allah (c.c.), the most gracious and the most merciful.

I would like to express my gratitude to my supervisors Prof. Darek Ceglarek and Dr Pasquale Franciosa for their invaluable advice, guidance, and to my examiners for their constructive suggestions in order to improve the overall quality of the thesis.

I would also like to extend my thanks to the Digital Lifecycle Management Group (DLM) members, in particular Dr Manoj Kumar Babu, Dr Ken Asare, Dr Arnab Palit, Dr Aniruddha Gupta, Sandra Holtom, Armando Serino.

I am deeply grateful to the Ministry of National Education of Turkey for providing the government scholarship that provided me the opportunity to study in the UK.

I dedicate this thesis to my family. I am also grateful to my parents Ayse and Ziya Ozkat, as well as my sister Saadet Ozkat for their endless support not only during my study but also throughout my life.

A special thanks goes to my friends that I have meet during my study, in particular Dr Karim El Haloui, Dr Mustafa Demirbilek, Mustafa Emre Dogukaya, Captain Pilot Deniz Hazir, Sinan Kahveci, Dr Pinar Satilmis, Selin Erden, Dr Nilgun Ince, Dr Elvan Gokalp, Dr Mumim Ozplot and my old friend Dr Bugra Alkan for their kind suggestions.

# Abstract

Remote Laser Welding (RLW) has grown in importance over conventional joining methods such as Gas Metal Arc Welding (GMAW), Resistance Spot Welding (RSW), Self-Pierce Riveting (SPR) since it offers advantages, such as weight reduction, high processing speed, ability to weld a wide range of metals, and better weld quality. Despite such advantages, it also poses several challenges that have prevented its widespread implementation in the industry.

The presented thesis deals with the RLW of galvanized steel (i.e. zinc-coated steel) since it is widely used in the automotive industry due to better resistance to corrosion and better adhesion of the paint to the surface. However, RLW of such steel is challenging because the zinc vapour disturbs the molten pool resulting in weld defects. Therefore, RLW of galvanized steel is performed in overlap configuration with a joining gap to ventilate the zinc vapour from the welding area.

An important challenge faced during the laser welding of galvanized steels is to achieve a consistent joining gap between two metals. If the gap is too wide, two metals do not join together. If the gap is too narrow, welding takes place with defects such as explosions, spatters and porosities. The maximum joining gap is controlled by the welding fixture; whereas, the minimum joining gap is controlled by the laser dimpling process (i.e. an upstream process). In the literature, the following research gaps have been identified regarding the laser dimpling process. These gaps are as follows: *(i)* lack key performance indicators to determine the dimple quality, *(ii)* lack a comprehensive characterization of dimpling process considering multi-inputs (i.e. key control characteristics) and multi-outputs (i.e. key performance indicators), and *(iii)* an effective implementation in a real manufacturing system taking into consideration process variation. Overcoming the aforementioned limitations in the literature, the presented thesis introduces proposes methodologies to develop: *(i)* surrogate models for dimpling process characterization considering multi-inputs and multi-outputs system by conducting physical experimentation, *(ii)* process capability spaces based on the developed surrogate models that allows the estimation of a desired process fallout rate in the case of violation of process requirements, and *(iii)* the optimization of the process parameters based on the developed process capability spaces.

The weld quality is measured by key performance indicators defined in industrial standards (EN ISO 13919-1, 1997; EN ISO 13919-2, 2001). The weld must

be produced such that each key performance indicator meets its defined allowable limits and any deviation from these limits is considered as a weld defect. The weld profile is important because the weld should have a desired profile for achieving the maximum strength. In this thesis, the weld profile is determined by penetration, top width, interface width (i.e. fusion zone dimensions).

It must be pointed out that the presented fusion zone dimensions are difficult to measure directly during the welding process unless production is stopped which is nearly unfeasible as it is economically unjustified; whereas, it can be monitored by process signals (e.g. acoustic, optical, thermal). Today, in-process monitoring is often provided by photodiodes or cameras. Owing to the lack of understanding of the process, it is limited to empirical correlations between the appearance of a weld defect and signal changes. The lack of methods linking (i) in-process monitoring data (e.g. visual sensing, acoustic and optical emissions); with, (ii) multi fusion zone dimensions (e.g. penetration, interface width, *etc.*), and (iii) welding process parameters (e.g. laser power, welding speed, focal point position) underscores the limitations of current data-driven in-process monitoring methods. Furthermore, the current in-process monitoring methods is an indirect measurement of fusion zone dimensions. Therefore, an accurate model to perform non-destructive measurement of fusion zone dimension is essential for on-line monitoring of laser welding as a part of quality assurance.

Based on this requirement, the occurring physics in the laser welding process are decoupled by sequential modelling. It consists of three steps as follows: (i) calculating the laser intensity acting on the material, (ii) calculating the key-hole profile in using an analytic method, and (iii) solving the heat equation using the FEM to calculate the temperature distribution. After obtaining the temperature distribution, the fusion zone profile is defined by selecting an isotherm. Then, the aforementioned fusion zone dimensions (i.e. Penetration, Top Width, Interface Width) are measured from the calculated the fusion zone profile according to the industrial standard.

**Keywords:** *Laser Dimpling Process • Process Capability Space • Process Robustness • Remote Laser Welding • Numerical Multi-Fidelity Modelling • In-process Monitoring*

# Abbreviations

<i>RLW</i>	Remote Laser Welding
<i>RSW</i>	Resistance Spot Welding
<i>SPR</i>	Self Piercing Rivet
<i>BIW</i>	Body-In-White
<i>TW</i>	Top Width
<i>IW</i>	Interface Width
<i>PT</i>	Penetration
<i>FZ</i>	Fusion Zone
<i>FZD</i>	Fusion Zone Dimension
<i>FZDs</i>	Fusion Zone Dimensions
<i>HAZ</i>	Heat Affected Zone
<i>BM</i>	Base Material
<i>D<sub>H</sub></i>	Dimple Height
<i>D<sub>U</sub></i>	Dimple Upper Surface Area
<i>D<sub>L</sub></i>	Dimple Lower Surface Area
<i>KCC</i>	Key Control Characteristic
<i>KCCs</i>	Key Control Characteristics
<i>KPI</i>	Key Performance Indicator
<i>KPIs</i>	Key Performance Indicators
<i>PDF</i>	Probability Density Function
<i>SR</i>	Success Rate
<i>LL</i>	Lower Limit
<i>UL</i>	Upper Limit

# Chapter 1

## Introduction

Remote Laser Welding (RLW) is a single-sided, non-contact laser welding technique which consists of a laser source to generate the laser beam, a welding robot to position the laser beam on the surface of the workpiece and a scanner head to focus and move the laser beam rapidly along the surface of the workpiece. Currently, RLW is mainly utilized in high volume production, such as Body-in-White (BIW) assembly (e.g. pillars, door panels, side walls *etc.*) in the automotive industry. However, a leading challenge preventing its systematic uptake in the industry is the lack of efficient in-process monitoring and assuring the weld quality in the presence of process variability (Ceglarek et al., 2015; Mirapeix et al., 2016; Song et al., 2017; Chen et al., 2018). Furthermore, this problem is even more challenging since welding takes place in a fraction of a second and there is not any contact between the scanner head and the workpiece.

The purpose of any welding process is to join two or more components into a single structure. The physical integrity of the structure thus formed depends on the weld quality. It is often evaluated by “*Key Performance Indicators*” (KPIs) defined in the industrial standards (EN ISO 13919-1, 1997; EN ISO 13919-2, 2001). The weld should be produced such that each KPI must meet its defined allowable upper and lower limits and any deviation from these specified limits is considered as a weld defect. The predominately used KPIs to assess the weld quality are characteristic dimensions of the weld, called “*Fusion Zone Dimensions*” (FZDs) (Rong et al., 2015; Ai et al., 2016; Jiang et al., 2016). Therefore, a significant amount of research has been conducted to understand the relationship between process parameters and FZDs so that a constant weld geometry throughout the weld seam can be obtained by adequately controlling process parameters (Anawa and Olabi, 2008; Olabi et al., 2013; Jiang et al., 2016; Liu et al., 2017). FZDs are usually categorized into two groups: (*i*) external FZDs which are located outside of the weld seam and can be

directly visible, and *(ii)* internal FZDs which are inside the weld seam and cannot be directly visible.

Statistical process control (SPC) is a method of quality control which employs statistical methods to monitor and control a manufacturing process. It involves steps of monitoring the quality or product design specifications (i.e. FZDs in the welding process), decision and control actions. The control action (i.e. process adjustment) is only taken place when there is statistical evidence that the process is out of control. The weld quality is usually unknown until the results of the inspection tests and statistical analysis become available. SPC will fail in high productivity manufacturing due to the increasing lag time between detection of the weld quality and process adjustment. To address this problem, it is possible to equip the welding robot with sensors to guarantee consistent weld quality by monitoring process emissions obtained through the molten pool, the keyhole and the metallic vapour. Signals/Data gathered from these sensors are then correlated to FZDs using statistic methods and machine learning algorithms. However, the limitations of data-driven monitoring methods are that *(i)* the process emissions are indirect measurements of the actual FZDs, and *(ii)* currently only penetration (i.e. one of the internal FZDs) is directly measured. Thus, the main aim of this thesis is to develop a computer simulation for quality assurance of the RLW process which integrates “*Finite Element Modelling*” (FEM), process parameters that affect the weld quality, and process emissions. As a result, the proposed simulation can be used to directly monitor multi-FZDs (i.e. penetration, top and interface widths) and such information will provide a greater insight of the RLW process which is necessary for process control, and thereby, towards zero defects in manufacturing.

The rest of the chapter is organised as follows: *(i)* the importance of the RLW in the automotive industry, *(ii)* a brief explanation of the research scope, *(iii)* the research objectives and contributions, and *(iv)* the thesis organization.

## 1.1 The Motivation for the RLW in the Automotive Industry

Rapid changes in the market needs, technological breakthroughs and new regulations force the automotive industry to utilize new emerging technologies that can help to manufacture faster, cheaper and better quality automotive components (Sturgeon et al., 2009; De Wit and Poulis, 2012). Furthermore, there has been a strong focus on light-weighting in the industry to improve fuel economy without losing performance. It has been reported that for every 10% of weight reduction the

fuel economy would improve by 7% (Ghassemieh, 2011). The major contributors to the total weight of a modern-day family size vehicle are the BIW and the ICE (Davies, 2012). Therefore, the BIW is an important factor in lightweight vehicle designs which cannot be disregarded.

According to Jou (2003), the highly utilized welding method in the BIW is resistance spot welding due to the simplicity of the welding equipment (e.g. welding without using consumable electrodes, filler materials and shield gas), the ease of implementation in robotic systems, and the low operation cost in mass production. This process uses a combination of heat and pressure to accomplish the weld. Two opposing spots guns apply pressure on both sides to clamp materials that are going to be welded together, creating intimate contact. Electrodes are located inside spot guns, and when the current is passed through the electrodes to the materials, heat is generated due to the higher electrical resistance where the surfaces contact each other. The heat energy supplied to the welding process depends on the current flow, the resistance of the circuit, and the duration of time that the current is applied. The resistance in the welding circuit is the sum of (i) resistance of the electrodes, (ii) resistances of the materials, and (iii) contact resistances between electrodes and materials. Furthermore, electrodes generally are made of a low resistance alloy, usually copper, and they are often water cooled to dissipate the heat that is generated (Williams and Parker, 2004; Marya and Gayden, 2005).

Thanks to the advancement of laser technology (i.e. development of high power and quality lasers with efficient delivery systems such as fiber optics), the RLW has been gradually replacing traditional welding methods (e.g. Resistance Spot Welding (RSW), Gas Metal Arc Welding (GMAW), Friction Stir Welding (FSW), *etc.*) since the RLW offers the following advantages:

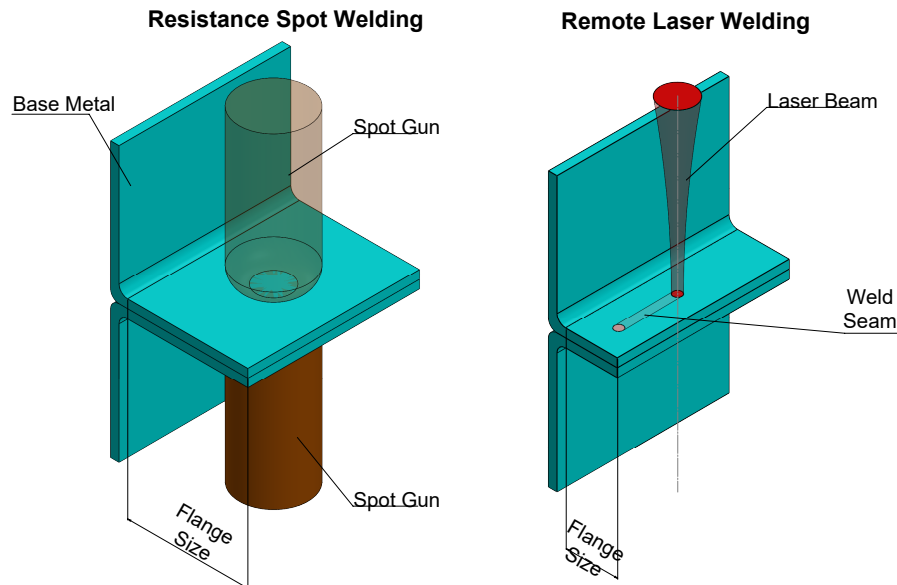
(i) weight reduction in the BIW:

The weight reduction can be achieved through the application of either topology optimization (i.e. to optimize the shape of a component to reduce excess material weights that do not contribute to the stiffness and strength of the BIW) or utilizing light metals (i.e. to use the low-density materials in the BIW such as aluminium, magnesium, composites *etc.* However, it is more difficult to laser weld these metals due to the lower absorptance of the laser beam at the surface of these metals). The material used in this thesis is galvanized steel (i.e. zinc coated steel), which is highly utilized in the automotive industry (Hosking et al., 2007). Thus, laser welding of any other metals is not investigated in this thesis.

The RSW usually requires a large flange size (around 16 *mm*) in order to the



spot guns (diameter around 8 *mm*) access the welding area to perform the weld. This non-structural feature adds weight and increases material cost. However, it can be considerably reduced and even eliminated by employing the RLW since it is a non-contact welding process and requires one-sided access to the welding area, which means that there is not any physical contact between the scanner head and the workpiece. Furthermore, the spot diameter of a modern laser beam (e.g. Nd:YAG, Ytb:YAG, *etc.*) are less than 1 *mm*. Consequently, significant weight reduction in the BIW can be achieved. Figure 1.1 shows the flange size for the RSW and the RLW processes and highlights the distinctive features of the RLW process which are being non-contact and one-sided access.



**Fig. 1.1.** A schematic diagram of the required flange size in RSW and RLW processes [Adapted from Bea et al. (2011)]

A review conducted by Hong and Shin (2017) pointed out that total weight reduction can reach up to 12.2 *kg* in the BIW by converting a spot-welded structure into a laser welded structure. Furthermore, it has been reported that for door panels a weight reduction up to 0.5 *kg* can be achieved by employing the RLW (Ceglarek et al., 2015).

As there is a high emphasis on light-weighting in the automotive industry, auto-makers have been investigating the replacement of steel with low-density materials, such as aluminium, magnesium, composites, *etc.* The emerging material must meet various criteria before it is fully utilized. One of these cri-

teria is the safety requirement which can be examined by “*crashworthiness*” and “*penetration resistance*”. The ability to absorb impact energy and be survivable for the passengers is called crashworthiness. The penetration resistance is concerned with the total absorption without allowing projectile or fragment penetration (Jacob et al., 2002).

Components in the BIW should be able to absorb or transmit impact energy in a crash situation. The materials deformation and progressive failure behaviour in terms of the stiffness, the yield strength, and the total elongation at the break point are very important in the energy absorption. The prime reason for still using steel in the BIW is its inherent capability to absorb impact energy in a crash (Marsh, 2000). Furthermore, the good formability, joining capability and low cost make steel the first-choice material for the light-weighting (Magnusson and Anderson, 2001).

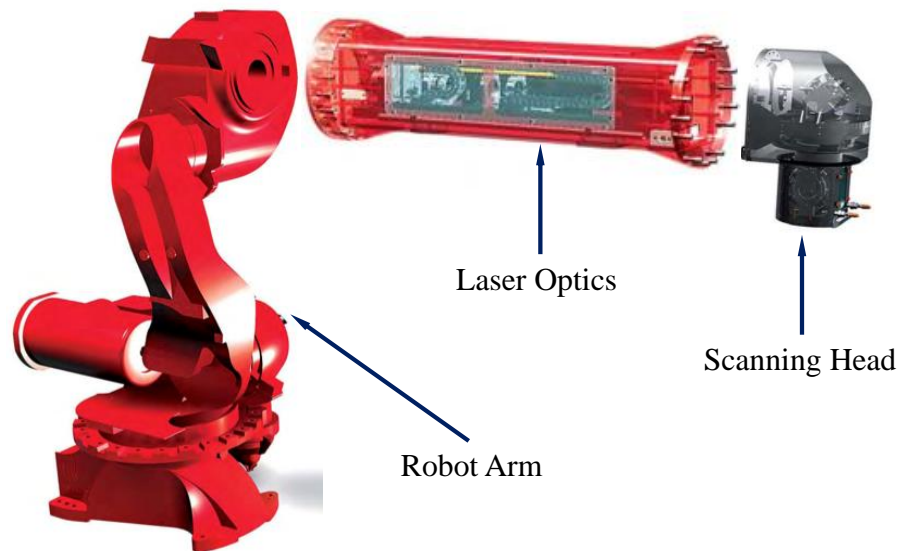
Specific strength or strength-to-weight ratio basically is the ratio of the yield strength of a material to its density. It is a helpful measure when the mass of a component is important because it characterizes the weight advantage of material considering its strength. For example, the strength-to-weight ratio of low carbon steel is very similar to that of aluminium alloy and high-strength low-alloy (HSLA) steel, which means that the three materials can all be considered as “*light materials*”. The materials with the highest specific strengths are typically fibres, such as carbon fibre, glass fibre and various polymers. The specific strengths of different materials are tabulated in Table 1.1.

**Table 1.1:** The specific strength of different materials [Adapted from Cuna (2000)]

Property	Low Carbon Steel (AISI 1010)	Aluminium Alloy (6010-T4)	High Strength Low Alloy Steel	Carbon Fiber (T1100G)
Density ( $g/cm^3$ )	7.89	2.70	7.80	1.79
Tensile Strength ( $N/mm^2$ )	370	130	410	7000
Specific Strength ( $kNm/kg$ )	46.8	48.1	52.4	3911

(ii) better processing speed:

The term “*remote*” in the RLW is used to describe the stand-off distance (e.g. around 1 m - 2 m in laser welding of steel) between the scanning head and the base metal, and it emphasises that there is not any physical contact. In RLW, the laser beam is delivered from the laser source via optical fibre. Then, pass through the laser optics which is embedded within the robot, finally reaching the scanning head. Mirrors are located inside the scanning head, and the weld is accomplished by the rapid movement of the laser beam across the base metal. Moreover, the robot repositioning time between two welds is much shorter in RLW compare to RSW since the weld is performed while the robot is moving from one location to another location. This is achieved by synchronization of robot and mirror movements. As a result, the welding speed is increased, and the robot repositioning time is reduced. The laser welding robot, laser optics and the scanning head are shown in Fig. 1.2.



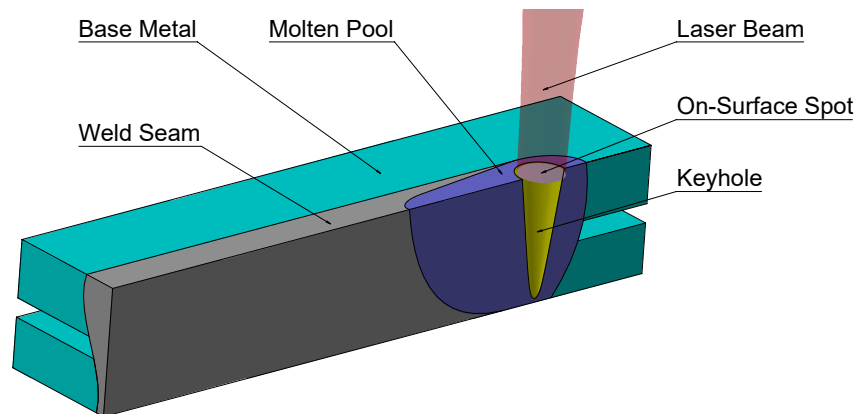
**Fig. 1.2.** An industrial laser welding robot showing robot arm, laser optics and scanning head

For example, in order to achieve an economically justified productivity in laser welding of steels, the welding speed should be around 3 m/min - 6 m/min. The welding time based on the given range is between 0.2 s - 0.4 s provided that the weld seam is 20 mm long (Ceglarek et al., 2015). On the other hand, Papkala (1992) reported that the welding speed in the RSW process was around 30 spots/min - 40 spots/min for the metal sheet thickness of 1.0 mm to 1.2 mm. Furthermore, it was pointed out that the welding time

increased when joining thicker sheet metals. For instance, the welding speed was around 15 *spot/min* - 25 *spot/min* for the metal sheet thickness of 1.8 mm to 2.0 mm.

(iii) better weld quality:

In RLW, the laser beam is focused to a very small on-surface spot resulting high laser intensity. When the laser intensity ( $I$ ) exceeds the critical value (i.e.  $I \geq 10^6 W/cm^2$ ) for steels), instantaneous vaporization occurs and generates a cavity named as “*keyhole*”. It allows the laser beam to penetrate deeper inside the material so that less energy is spent to heat up the surrounding area which creates narrow heat affected zone (HAZ) leading to low thermal distortion. Furthermore, continuous weld seams can be achieved with the movement of the laser beam. On the contrary, the weld seam and its position are limited to the spot gun location in the RSW. As a consequence of narrow HAZ, deep penetration and continuous weld seam, the weld obtained by RLW has better the weld quality (e.g. tensile, shear strength) than the weld obtained by other welding methods. The keyhole, the molten pool and the weld seam are illustrated in Fig. 1.3.

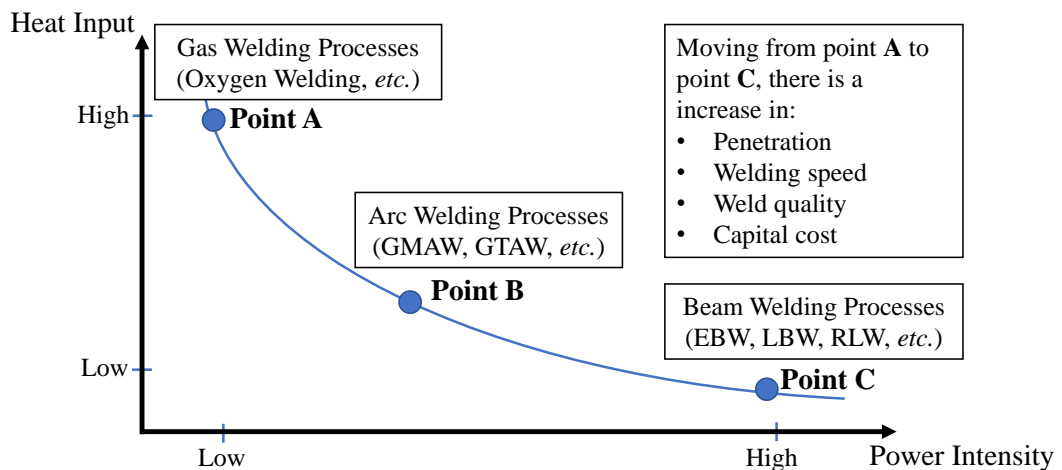


**Fig. 1.3.** The longitudinal cross-section illustration of the laser welded joint

Yang and Lee (1999) concluded in their experimental research to compare the fatigue strength of RSW and laser spot welding (LSW) in which the laser beam is stationary. The diameter of the spot gun and the diameter of the laser on-surface spot size were selected as equal in order to compare these two processes. It was reported that the fatigue strength of joints obtained by LSW was 3 times higher as well as the tensile strength was 5 times greater than that of resistance spot welds in overlap configuration (Ribolla et al., 2005).

Heat input and power intensity are introduced to compare different welding

processes. Heat input is the ratio of the heat delivered to the base metal to the velocity at which the heat source travels. This means that a welding process which has a high-speed capability has a low heat input value. Power intensity is defined as the ratio of the delivered power from the heat source to the area over which the heat source is applied. Power intensity associated with a welding process directly affects the amount of heat required to be supplied for welding. An increase in power intensity decreases the heat input because it decreases the time required for melting the base metal. The decrease in time lowers the amount of heat dissipated away so most of the applied heat on the faying surfaces is used only for melting (Kou, 2003). The advantages of increasing the power intensity are deeper penetration, higher welding speed, better weld quality, and high capital cost as indicated in Fig. 1.4.

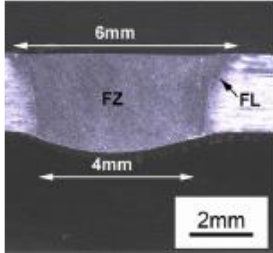
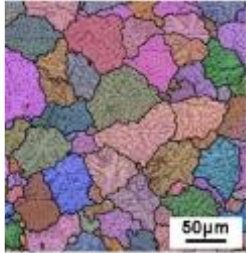
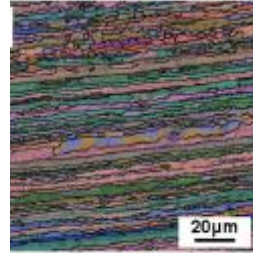
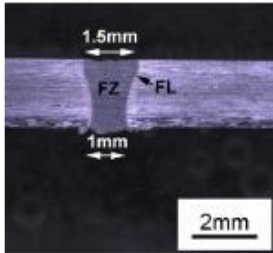
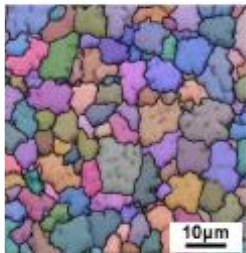
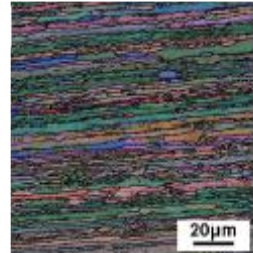


**Fig. 1.4.** The variation of heat input to the workpiece with power intensity of the heat source [Adapted from Kou (2003)]

Most welding processes use heat to transform the base metal from solid to liquid phase. The molten pool solidifies when the applied heat is removed. During the solidification stage, grains are formed. The grain size is important because it affects the mechanical properties of the weld. The grain size is determined by the number of nucleation sites in the molten pool and the cooling rate (Zhao et al., 2013). Another factor influencing mechanical properties is the presence of grain boundaries. They represent imperfections in the crystalline structure that interrupt the continued movement of dislocations. Therefore, smaller grain size and more grain boundaries are generally preferable from a design point because they increase the strength and hardness of the material (Midawi et al., 2014).

During the welding, the base metal is influenced by a thermal cycle, the rapid heating and cooling. Such thermal cycle alters the microstructure of the base metal. The grain size is inversely proportional to the cooling rate, and the main parameters influencing the cooling rate are welding speed, heat input and power intensity (Sokolov et al., 2011). RLW can produce deep and narrow welds at high welding speed with a smaller grain size because of its higher power intensity and lower heat input. Zhang et al. (2016) investigated grain structure, tensile strength and hardness of TIG and laser welding. The heat input of TIG and laser welding is about  $250 J/mm$  and  $50 J/mm$ , respectively. Results showed that the mean grain size in the FZ for both processes are  $33.9 \mu m$  and  $6.1 \mu m$  respectively. It was noted that decrease in the heat input results in an increase in the average hardness and decrease in the HAZ width. Macro-section image, the grain morphology in the FZ and the HAZ for both welding processes are given in Table 1.2.

**Table 1.2:** Macro-section images and the grain morphology of different zones in the joints [Adapted from Zhang et al. (2016)]

Welding Process	Macro-section Image	The Grain Morphology in Fusion Zone	The Grain Morphology in Heat Affected Zone
Tungsten Inert Gas Welding (TIG)			
Laser Beam Welding (LBW)			

To sum up, RLW makes the welding process much faster with better weld quality as well as helps to weight reduction. Furthermore, it provides flexible design due to the single-side access and large stand-off distance. However, RLW still faces many challenges in welding of zinc coated sheet metals, and in ensuring acceptable as well as reliable weld quality, especially the required FZDs.

## 1.2 The Research Scope

As for any other welding process, an unsuitable selection of process parameters leads to unacceptable weld defects. Without effective monitoring and control strategy, many engineering solutions have to be considered in order to overcome quality related problems which will increase time and cost of production (You et al., 2014; Stavridis et al., 2017).

Traditionally, weld quality is assessed manually which consists of four steps: (i) establishing satisfactory welding parameters by procedure trials and testing, (ii) selecting and maintaining the same parameters/procedure in production, (iii) monitoring process by final inspection (i.e. non-destructive/destructive testing to ensure that the required results are being achieved), and (iv) correcting for deviation from stated quality requirement by adjusting welding parameters. Furthermore, final inspection may involve selecting random samples from a batch of finished welds and corrective action is normally based on statistical quality control techniques. The described approach, known as *off-line inspection*, is costly, reduces productivity, and requires dedicated test equipment and people.

To ensure the acceptable weld quality, to increase productivity and to eliminate the need for post weld examination, the welding process can be monitored during the process with sensors, known as *in-process monitoring*. The information gathered from sensors is then transmitted to the process controller that fine adjusts the welding process parameters to produce consistently acceptable quality welds. It must be pointed out that the weld quality, in terms of FZDs, is difficult to measure directly during the welding process unless production is stopped which is nearly infeasible as it is economically unjustified; whereas, it is measured by signals and relating these signals to relevant KPIs such as FZDs.

Therefore, development of in-process monitoring methodologies is essential to assure the weld quality. The quality assurance consists of two stages: (i) process monitoring, and (ii) process control. The process monitoring is the manipulation of measurements in determining the current state of the welding processes; whereas, the process control is the manipulation of process parameters based on the information gathered from the monitoring stage in order to regulate the processes.

Figure 1.5 shows the outline of the dissertation consists of two major components as follows:

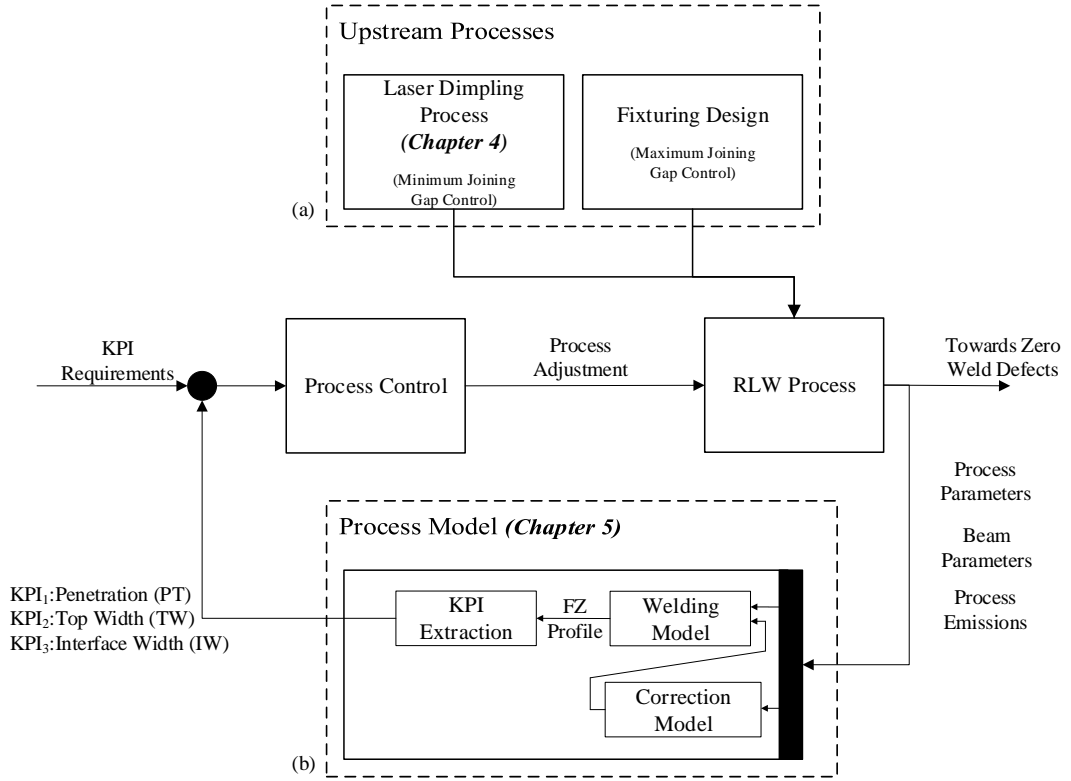
- (a) The process parameters are defined as the parameters required to setup a welding process and they can be divided into two categories: (i) controllable parameters are those that can be varied during welding (e.g. laser power, weld-

ing speed, focal offset, *etc.*), and *(ii)* uncontrollable parameters are those that cannot be modified during welding, such as joining gap. In this dissertation, the laser dimpling process (upstream process) is utilized to develop a joining gap between two sheet metals. A methodology is developed in **Chapter 4** to select robust the laser dimpling process parameters in the presence of process variation.

- (b) The primary aims of the proposed framework are to consistently produce adequate quality welds by monitoring FZDs and to control the process parameters that affect FZDs. The effectiveness of the proposed framework is dependent on the prediction of the process model. It is the mathematical representation of the actual process (i.e. remote laser welding process) which could be theoretical, empirical or simulation based.

Theoretical models are based on analytical solutions of governing physical equations, empirical models are developed from experimental design methods for example response surface methodology, and simulation models are numeric solutions of the governing physical equations with the help of computers. It should be noted that the computational time and accuracy of the developed model should be as close as possible to the process time and the output (e.g. macro-section image of the weld) to utilize the developed model in the proposed framework. A physics-driven model based on the occurring physical phenomena is developed in **Chapter 5** by considering the computational time and the accuracy of the prediction.





**Fig. 1.5.** The outline of the dissertation: (a) controlling minimum joining gap requirement in the RLW process by utilizing the laser dimpling process (*Chapter 4*), (b) the physics-driven process model for quality assurance for the RLW process (*Chapter 5*)

Based on the aforementioned research scopes, the definition of the research questions (RQ) are outlined as:

RQ 1 *How to select robust dimple process parameters to achieve given quality requirements in the presence of process variation?*

The scope of this thesis is the laser welding of galvanized sheet metal which is highly utilized in the BIW due to its corrosion resistance, strength, cost and hardness (Ma et al., 2012; Zhao et al., 2012; Chen et al., 2013). However, the laser welding of this metal is unstable and difficult to control because of the vaporization temperature of the zinc ( $\sim 907\text{ }^{\circ}\text{C}$ ) is lower than the melting temperature of the steel ( $\sim 1500\text{ }^{\circ}\text{C}$ ) resulting in highly pressurized zinc vapour on the faying surfaces during the welding process. Left unaddressed, such zinc vapour can easily be trapped inside the molten pool which can lead to welding defects such as porosity, spatter, burn-through, and severe undercuts (Norman et al., 2009; Chen et al., 2013).

Over the past few years, various methodologies have been developed to mitigate zinc vapour from the welding medium without causing any disturbance in the molten pool and the keyhole. The state-of-the-art method in the automotive industry is the ventilation of zinc vapour through a joining gap. The required gap can be developed by, for example, “laser dimpling process”. It is a very promising manufacturing process as it does not require any additional equipment and suppliers. Additionally, the same laser source and the fixture adopted for welding can be utilized. In this process, dimples with a height of  $0.05\text{ mm} - 0.2\text{ mm}$  are produced on the surfaces by the rapid movement of the laser beam at a short distance. The number of dimples and the position depends on the weld seam (i.e. linear or circular weld). After the realization of dimples, two sheet metals are placed in overlap configuration and welding is performed.

Dimples work as a spacer between two sheet metals which control the minimum joining gap. On the other hand, the maximum joining gap is controlled by the welding fixture (Das et al., 2015). Since the joining gap is an uncontrollable process parameter and achieved by an upstream process, a novel methodology is introduced to control dimples so that minimum joining gap is always achieved in the presence of process variation to prevent weld defects, such as blow-hole, spatters, *etc.*

According to the reviewed literature in Section 3.1, the research gap is identified as: (i) lack of KPIs to determine the dimple quality, (ii) complete characterisation of the dimpling process since the existing literature have focussed mainly on single-input (i.e. welding speed), single-output (i.e. dimple height) scenario (SISO scenario), and (iii) selection of process parameters for given quality requirement in the presence of the process variation.

RQ 2 *How to directly monitor multi Fusion Zone Dimensions (Penetration, Top Width, Interface Width) in the overlap laser welding of galvanized steels to assess the weld quality?*

Currently, data-driven process models are widely utilized for in-process monitoring. These models work according to the principle of the acquisition of data (i.e. acoustic, optical and visual emissions) using sensors then correlated them using multivariate statistical methods and machine learning algorithms to the formation of weld defects. The most common sensors in use today for in-process monitoring are photodiode (Eriksson et al., 2010), high-speed and thermal cameras (Kawahito et al., 2009; Tenner et al., 2015).

According to the reviewed literature about process monitoring, which is given in Section 3.2, the limitations of current data-driven in-process monitoring methods are that sensor signals are multi-dimensional and multi-modal, it is often not realistic to use them directly as an input for control algorithms. They do not monitor directly weld defects, but instead they monitor signals arising from the process and develop predictive models. As a result, changes in process parameters or material properties can be handled only by rebuilding these predictive models. Moreover, they are capable of detecting external KPIs but insufficient to directly monitoring internal KPIs, especially FZDs such as interface width.

An alternative to the data-driven process model is a physics-driven model which numerically solves the governing physics in the laser welding process. The developed model emulates the transverse cross-section of the weld. However, the problem is to obtain simulation results at a given accuracy within the welding process time. Therefore, a simplified model is developed that allows a fast estimation of FZDs namely; penetration, top width; and interface width. The key idea is to integrate the physics-driven model with gathered data to reduce computational time without losing accuracy. Furthermore, the physics-driven model consists of four steps as: *(i)* calculating laser intensity acting on the material, *(ii)* calculating keyhole profile in using an analytic method, *(iii)* solving the heat equation using FEM to calculate fusion zone (FZ) profile, and *(iv)* aforementioned FZDs are obtained from the calculated FZ profile.

### 1.3 Research Objectives & Contributions

According to *Research Question 1*, the following key objectives that will help to satisfy the aforementioned research gap to select the robust laser dimpling process parameters to achieve given quality requirements in the presence of process variation.

- **Objective 1:** To understand the quality requirements of a dimple:  
In essence, the dimple works as a spacer between two sheet metals to create a joining gap in which the zinc vapour is ventilated through. According to the revised literature given in Section 3.1, the only studied key performance indicator (KPI) is the dimple height which directly affects the joining gap size. However, there is a continuous clamping force acting upon the dimple during

welding. Thus, the dimple upper spot area can be another KPI to assess the strength of a dimple to prevent excessive deformation of the dimple height under compression of clamping force. Furthermore, the excessive amount of laser power creates a dark black spot on the lower surface of the sheet metal which degrades the surface finish. The dimple lower spot area can be considered as another KPI to assess the aesthetic quality of a dimple.

- **Objective 2:** To obtain process capability space considering a multi-input, multi-output (MIMO) based scenario:

Laser welding is a complicated multi-phases and multi-physics process which involves interaction between the laser beam and material. This interaction is governed by a number of factors including laser power, laser intensity distribution; and process parameters such as scanning speed, incidence angle and focal offset. The proposed modelling approach addresses two key limitations as discussed in the literature by taking into consideration *(i)* approximation of comprehensive multi-variate relations between multi-input (i.e. process parameters) and multi-output (i.e. key performance indicators), and *(ii)* process variation over the design space by introducing deterministic and stochastic process capability spaces. The deterministic process capability space is a measure of the dimpling process capability to satisfy simultaneously all the allowance limits of KPIs; whereas, the stochastic process capability space is the estimation of success rate (SR) which is the probability of making a dimple that satisfies simultaneously all the allowance limits.

- **Objective 3:** To find robust process parameters that are less sensitive to the process variation:

The laser dimpling process is a pre-process for laser welding of galvanized sheet metals. It is important to note that the requirements of the laser dimpling process are determined by an upstream process, such as assembly fixture design and clamp layout optimization. For example, assembly fixture design for laser welding might require a specific value of KPIs with a given variability. In this case, deterministic and stochastic process capability spaces are utilized to find the robust process parameters that are less sensitive to process variation.

Based on the aforementioned objectives and the defined framework, the methodology for calculating surrogate driven deterministic and stochastic process capability space have been proposed in **Chapter 4**. The research contributions of the proposed work are listed as:

- **Contribution 1:** The new KPIs and their intervals are defined to assess the dimple quality:

The product quality can be analysed by three features: *(i)* functionality, *(ii)* durability, and *(iii)* aesthetic. According to the revised literature, one KPI, which is the dimple height, is studied to address only the functionality of the dimple. Two new KPIs (i.e. the dimple upper spot area and the dimple lower spot area) are introduced to address the remaining features. The dimple upper and lower spot areas are utilized to assess durability and aesthetic quality of the dimple quality, respectively.

- **Contribution 2:** A comprehensive characterization of the laser dimpling process:

The industrial needs are addressed in this study by *(i)* introducing two new KPIs, and *(ii)* studying the effect of incidence angle and focal offset, which are required for accessibility issue of the laser beam as well as scanning speed and laser track, which are required for the cycle time. Furthermore, the deterministic process capability space is introduced to find feasible the process parameters which simultaneously satisfy all quality requirements. Due to the stochastic nature of the process, the feasible process parameters might produce dimples that violate the allowance limits of KPIs. Therefore, the stochastic process capability space is introduced to measure the success rate using a probabilistic approach. Based on the desired success rate, the natural specification limits are determined to satisfy all quality allowance limits.

- **Contribution 3:** Process parameters selection and optimization using surrogate-driven process capability space:

The proposed methodology offers a unique simulation tool which is generic and can be applied not only to the laser dimpling process but also it can be exploited in the context of selection and optimization of process parameters in the presence of process variation. The current best practice for process parameters selection is based on costly and time-consuming trial and error approach. The proposed methodology offers identification of risky areas and low reliable parameters settings which help to the selection of optimum process parameters and shorten the time for design and commissioning.

According to the **Research Question 2**, the following key objectives that will help to satisfy the aforementioned research gap to directly monitor multi Fusion Zone Dimensions (Penetration, Top Width, Interface Width) in overlap laser welding of galvanized steels to assess the weld quality

- **Objective 1:** To develop a fast model by decoupling occurring multi-physics in laser welding:

Laser welding is a complicated multi-phases and multi-physics process. As discussed, there is a requirement for monitoring multi FZDs to assess the weld quality. The lack of comprehensive models linking (i) in-process monitoring data (e.g. visual sensing, acoustic and optical emissions); with, (ii) multiple quality indicators (e.g. penetration depth, interface width), and (iii) welding process parameters (e.g. laser power, welding speed, focal point position) underscores the limitations of current data-driven in-process monitoring methods. Therefore, a model that gives results in a short time is required to predict the transverse cross-section of weld in which FZDs are obtained. To meet this objective, the sequential decoupled multi-physics model has been developed. The model calculates the keyhole profile in overlap joint using an analytic method; and then, solves the heat equation using FEM to obtain FZDs.

- **Objective 2:** To integrate experiment and numeric simulation results to improve the accuracy of the model:

The term fidelity refers to the level of accuracy or complexity of the developed model. A simplified numeric simulation model (i.e. Low Fidelity (LF) model) of laser welding is developed by sequential solving the occurring physics. The key idea is to integrate the LF model with experiment-based model (i.e. High Fidelity (HF) model) to reduce computational time without losing accuracy. For this purpose, two correction models are developed to increase the accuracy of the keyhole profile calculation in overlap joint. Then, heat equation is numerically solved based on the corrected keyhole profile.

Based on the aforementioned objectives and the defined framework, the methodology for calculating the decoupled multi-physics multi-fidelity (DMPMF) model is given proposed in **Chapter 5**. The research contributions of the proposed work are listed as:

- **Contribution 1:** Development of sequential decoupled multi-physics model considering incidence angle and joining gap:

Complex welding simulation models have a realistic estimation of the FZ profile as well as FZDs, but they are often computationally expensive. Inexpensive and less accurate the LF model can be achieved by dimension reduction, linearisation and considering simple physics. However, the LF model cannot be directly utilized for in-process monitoring because the output of the LF model (e.g. the FZ profile, FZDs, *etc.*) has a significant error. In the literature,

the influence of the incidence angle on the keyhole shape has not been fully addressed. In this work, the laser beam was assumed as a hyperboloid and the interaction of hyperboloid with any plane in the space was analytically calculated so that the laser beam on-surface shape and the laser intensity were obtained considering the incidence angle. According to the obtained intensity, the keyhole profile was calculated using a well-established analytical method.

- **Contribution 2:** Integration of correction model in to the LF model:

The multi-fidelity (MF) modelling method combines the information gain from both LF and HF models by using correction model. The correction model can be based on either *(i)* scaling factor ( $\beta$ ) which is the ratio of the HF model results to the LF model results, *(ii)* discrepancy factor ( $\delta$ ) which is the difference between HF and LF model results, or *(iii)* combination of both. After obtaining scaling and discrepancy factor, the correction model is generally developed by employing surrogate modelling approach (i.e. regression, Kriging, *etc.*). The MF model in this research is based on scaling factor to corrected calculated the keyhole profile based on the decoupled multi-physics modelling approach.

## 1.4 Thesis Organization

**Chapter 2** provides background information and basics concepts relevant to this thesis such as the operational characteristic of the laser welding process, the weld quality assessment criteria.

**Chapter 3** reviews the related literature in the field of zinc vapour mitigation methods during the laser welding of galvanized steels by addressing limitations in terms of manufacturing perspective; and highlighting the research gap in the laser dimpling process which is the best practice in the automotive industry. Further, it reviews the reported work in the field of thermal modelling and prediction of fusion zone dimension in laser welding of steels.

**Chapter 4** presents the methodology used for process parameters selection and optimization using surrogate-driven process capability space. Deterministic and stochastic process capability spaces are developed by the proposed success rate. It is calculated as the probability value of satisfying the allowance limits of given KPIs namely; dimple height, dimple upper spot area, and dimple lower spot area. The developed process capability spaces are used to optimize process parameters under competing quality requirements such as maximizing the dimple height while minimizing the dimple lower surface area.

**Chapter 5** introduces a novel decoupled multi-physics multi-fidelity (DMPMF) model for predicting multi FZDs (penetration, top and interface widths) in overlap laser welding of galvanized steel. The key idea is to calculate keyhole profile in overlap joint using an analytic method; and then, to solve the heat equation to obtain the transverse cross-section of weld in which FZDs are obtained by looking melting isotherm. The key idea is to incorporate results derived from the welding experiments (high fidelity model) into the low fidelity model to reduce computational time without losing accuracy.

**Chapter 6** presents the overall thesis conclusions and indicated a direction for future work resulting from it.



# Chapter 2

## Background

This chapter focuses on the background information related to the laser material processing. A special focus has drawn on the fundamental information associated with the laser beam in Sections 2.1 to 2.3. Section 2.1 highlights components of the laser source and the classification of lasers; and further, it introduces the characteristic properties of the laser beam by explaining coherence, monochromatic, transverse electromagnetic mode (TEM), polarization and wavelength. The definition of geometrical parameters of the laser beam (i.e. beam waist radius, divergence angle and Rayleigh length) is described in Section 2.2. Furthermore, the quality of laser beam is presented in terms of  $M^2$  value and beam parameter product (BPP) in Section 2.3.

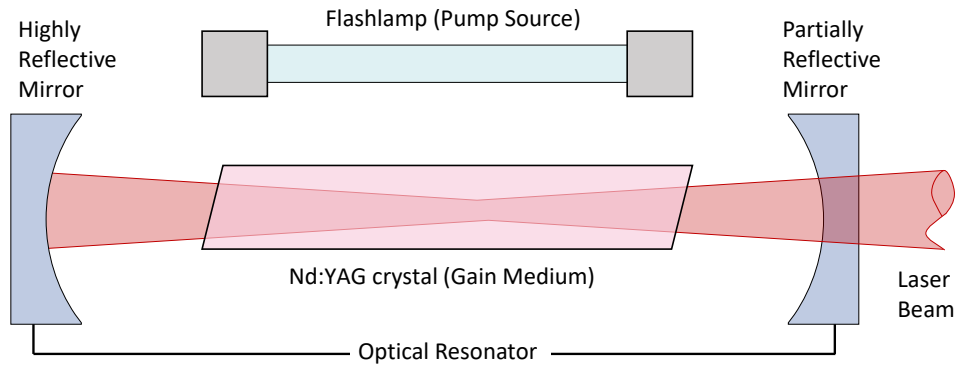
The operational characteristics of laser welding are pointed out in Sections 2.4 to 2.6. Initially, the fundamental laser welding process parameters (i.e. laser power, welding speed, focal offset, incidence angle, laser intensity and interaction time) are given in Section 2.4. Secondly, modes of laser welding (i.e. conduction and keyhole modes) are defined in Section 2.5. Finally, the assessment of weld quality is explained in Section 2.6 by defining three major criteria namely; (i) mechanical quality considers the functionality of weld, (ii) metallurgical quality refers to the microstructure of the weld, and (iii) aesthetic quality related to the surface finish.

### 2.1 The Characteristic Properties of Laser Beam

The word “*LASER*” is an acronym for “*Light Amplification Stimulated Emission of Radiation*”. The stimulated emission was first hypothesised by Albert Einstein in 1917. Maiman (1960) invented the first operational laser in the world which produced a laser beam in the visible range of the spectrum around 694 *nm* wavelength. In 1962, Robert N. Hall introduced the first diode pumped laser device which

was made from gallium arsenide which emitted the laser beam at 850 nm wavelength. Since then, various types of lasers have been developed for different applications such as medical, industrial, scientific research, *etc.* Although their development purposes are different, they are constructed from mainly three components namely; (i) pump source, (ii) gain medium, and (iii) optical resonator.

The pump source supplies the required energy for stimulated emission to the gain medium in terms of electrical current or light at the different wavelength. The gain medium is a material with properties that allow the light to amplify by stimulated emission. Optical resonator consists of two or more mirrors which are replaced on either end of the gain medium. The basic working principle of stimulated emission is that if a light bundle with proper energy is sent to an excited atom from the pump, the atom falls into its lower energy and duplicates the light bundle. While the light reflects back and forth between mirrors, it is being amplified each time and finally the optical resonator focuses the amplified light in order to generate the laser beam. Figure 2.1 shows three main components of laser.



**Fig. 2.1.** Components of a typical laser system: Pump Source, Gain Medium, Optical Resonator

Lasers can be categorized according to either (i) the operation mode (i.e. continuous wave or pulsed mode) or (ii) the type of gain medium (i.e. solid, liquid and gas states lasers). In continuous wave (CW) mode, the laser beam is formed by constant amplitude and frequency which is represented mathematically by a sine wave which means that the laser emits a steady laser beam continuously over a period of time. On the other hand, a series of light at a certain pulse width and frequency is emitted until the laser is stopped in pulsed mode (PM). In general, there are on and off periods to the pulsed laser beam which is the same concept with resistance spot welding. Thus, the laser penetrates deeper in CW mode than pulsed welding because it is emitting light continuously. Furthermore, the parameters normally

used for characterising continuous wave lasers are laser power, beam diameter, and welding speed; whereas, pulsed lasers are pulse energy, pulse duration and beam diameter (Assuncao and Williams, 2013).

The gas-state lasers utilize a tube filled of low density gaseous in the gain medium, which are made from neutral atoms, ions or molecules such as Helium, Neon, Argon, Carbon dioxide, *etc.* The most commonly employed gas is carbon dioxide ( $CO_2$ ) which generates a laser has a wavelength of  $10.6 \mu m$ . The higher the value, the less energy is spent on unnecessary heating which leads to thermal distortion (Suder et al., 2011). In general, the  $CO_2$  laser is easily absorbed by organic materials (e.g. plastics, glass, fabrics), but it is not easily absorbed by metal due to its high wavelength value.

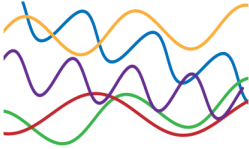
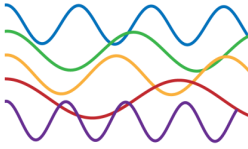
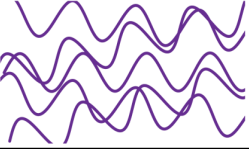
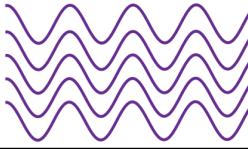
The solid-state lasers employ high-density solid material substances in gain medium which is crystalline or glass. Glasses can be easier to fabricate, but crystals have better thermal properties. Neodymium is extensively used in solid-state laser and the most crystals such as Nd: YVO<sub>4</sub>, (Neodymium Yttrium Ortovanadate), Nd: YLF (Neodymium Yttrium Fluoride) and Nd: YAG (Neodymium Yttrium Aluminium Garnet). Among those, Nd: YAG is the most common solid-state laser which has an operating wavelength around  $1.064 \mu m$  which makes it ideally suited for absorption in most metals. Therefore, CW solid-state lasers have been widely used in cutting, brazing, forming and welding due to its reasonable joining efficiency, low-cost operation and small laser spot size compare to the gas-state lasers.

The laser has unique properties (i.e. coherent, monochromatic, collimated and uniform polarization) setting it apart from conventional radiation source. The power intensity of a laser cannot easily be diminished on the way from the laser source. The most important characteristic properties are now examined in more details in the following sections.

### 2.1.1 Coherence

The laser consists of streams of beams which can be spatial and temporal coherent. If the beams propagate in the same direction, parallel to each other, the laser is called spatially coherent. Likewise, the laser is temporally coherent if wavelengths of beams are the same and constant over time. It is easy to understand that the two properties are independent, the laser beam can be spatial coherence without temporal coherence and vice versa. These different situations are illustrated in Table 2.1. Temporal coherence expresses how the laser emits lights in a narrow spectrum, whereas, spatial coherence defines the ability of collimation over great distances.

**Table 2.1:** The spatial and the temporal coherence of different beams. The laser beam is both spatial and temporal coherent

		Spatial	
		Not Coherent	Coherent
Temporal	Not Coherent		
	Coherent		

### 2.1.2 Monochromatic

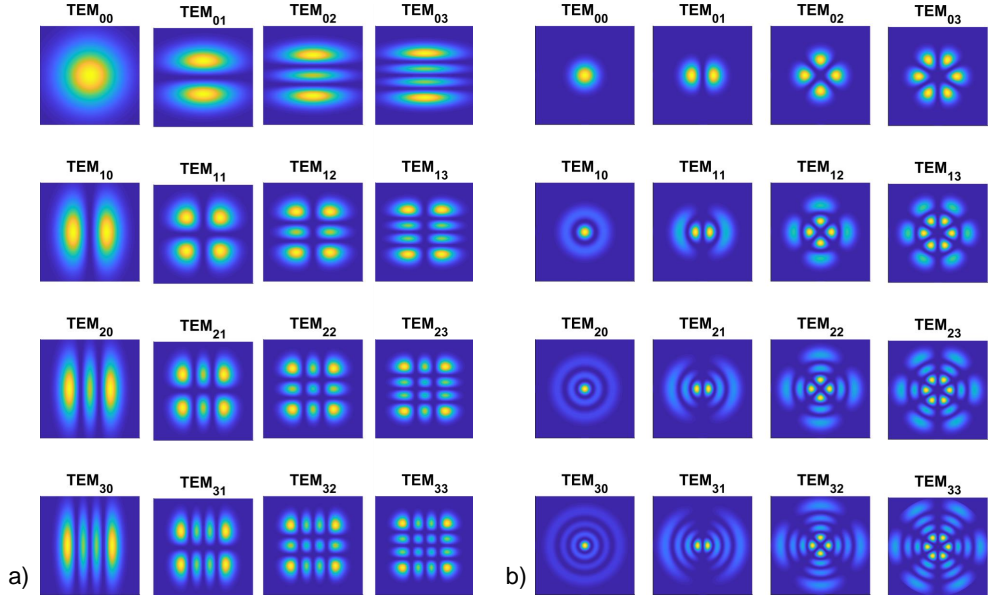
Monochromatic light consists only a single wavelength which leads to a single colour. All the photons obtained in stimulated emission have the same energy level and the photons are gathered in a narrow range of wavelength so that laser appears in a single colour. For instance; in the visible spectra, the red laser has a wavelength in the range of 635 *nm* to 660 *nm*, the green laser has the range of 520 *nm* to 532 *nm* and the violet laser has the range of 400 *nm* to 450 *nm*. The colour of the laser is important because the delivered energy to the material is dependent on the wavelength indirectly colour of the laser. In the visible range, lasers have shorter wavelengths tend to look much brighter than longer wavelength lasers.

### 2.1.3 Transverse Electromagnetic Mode

Transverse Electromagnetic Mode (TEM) defines the spatial distribution of the laser in a plane which is perpendicular to the propagating direction of the laser. The distribution is determined by the geometry of the optical resonator which is determined by the alignment of the mirrors, their radius of curvature, the spacing and the bore of the discharge tube (Breck, 1986).

The mode is universally denoted as  $TEM_{pq}$  where  $p$  and  $q$  are numbers of nodes contained within two specified directions. In the rectangular coordinates,  $p$  and  $q$  are the nodes in two orthogonal directions; whereas, in polar coordinates, they describe the radial and angular directions, respectively.  $TEM_{00}$  beams have the best focusing and highest symmetry characteristic among other modes. In most laser welding application,  $TEM_{00}$  and  $TEM_{01}$  mode structures are employed as they provide smaller focused spot size. A few examples of mode patterns and intensity

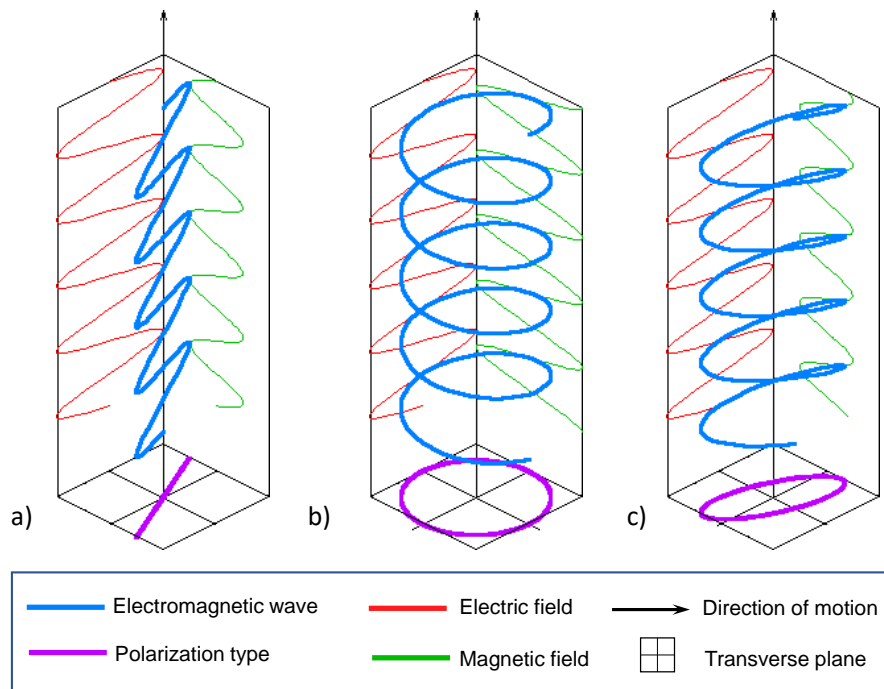
distribution are shown in Fig. 2.2 for rectangular and polar coordinates, respectively.



**Fig. 2.2.** Transverse Electromagnetic Modes: a) Rectangular coordinate, b) Polar coordinate

### 2.1.4 Polarisation

The electric and magnetic waves are orthogonal in space. Polarization is the property that defines the direction of oscillations in the plane which is perpendicular to the direction of the electromagnetic wave. Linear, circular and elliptical polarization are three basic forms of polarisation. In linear polarization, the electromagnetic wave oscillates in a single direction. However, it has a constant magnitude, but its direction rotates with time at a steady rate in circular polarization. The direction rotates and the magnitude changes in the elliptical polarization. These three types of polarization are illustrated in Fig. 2.3.



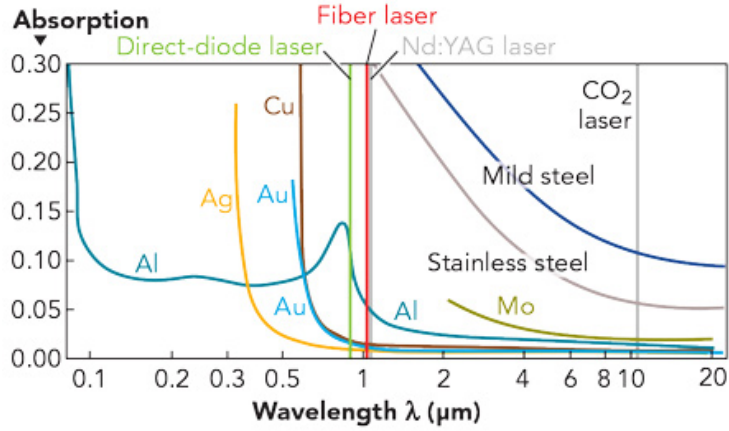
**Fig. 2.3.** Polarization types: a) Linear polarization, b) Circular polarization, c) Elliptical polarization

The importance of polarisation on laser welding is related to the absorption mechanism because reflections are minimised since free electrons are vibrating parallel to the plane of incidence. Such effect has more influence on laser cutting since the beam has direct interaction with surface whereas in welding operation the effect is not significant since the beam is absorbed inside the molten pool regardless of the plane of polarisation.

### 2.1.5 Wavelength

Depending on the wavelength of a laser ( $\lambda$ ), each material has a different absorption level. Therefore, the selection of a laser with the right wavelength is very significant to the laser-material process since the wavelength is constant during the welding process. The absorptivity level is higher in shorter wavelength (i.e. Nd:YAG laser where  $\lambda = 1.064 \mu m$ ) especially for the reflective metals such as copper, aluminium. The absorptivity level significantly drops with the increasing wavelength (i.e.  $CO_2$  laser where  $\lambda = 10.6 \mu m$ ). By comparing high and low wavelength lasers, less power is required for low wavelength lasers to achieve the same amount of weld penetration for the same material. Thus, the joining efficiency is low for high wavelength lasers. The absorption levels of various metals against

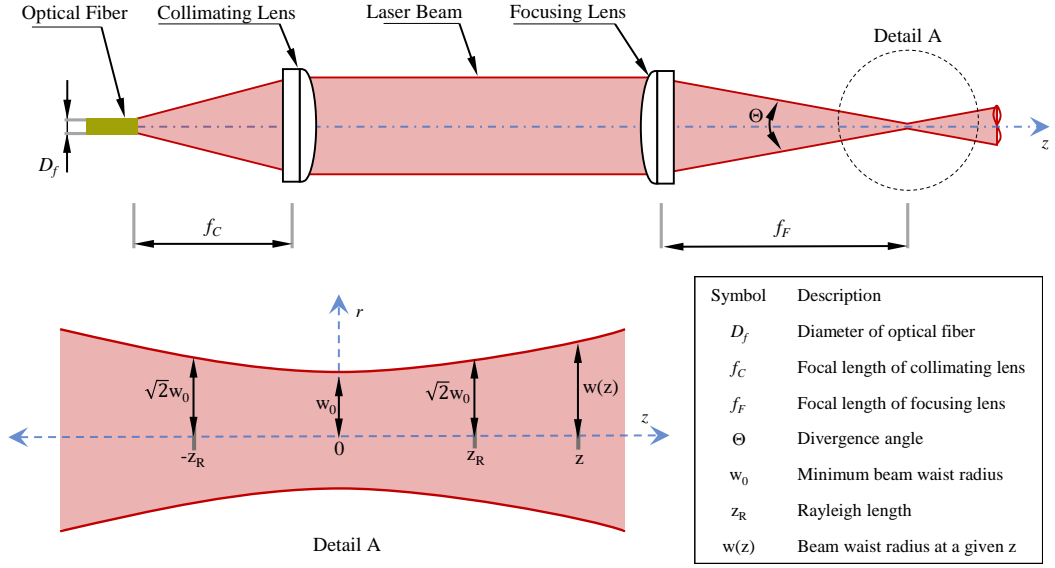
wavelengths for different types of laser are given in Fig. 2.4.



**Fig. 2.4.** Absorption of various metals at relevant wavelengths [Adapted from Saucedo et al. (2016)]

## 2.2 The Geometrical Parameters of Laser Beam

In laser optics, an ideal Gaussian laser beam is both spatial and temporal coherent, monochromatic, and it has a  $\text{TEM}_{00}$  mode which enables the beam to be focussed into the most concentrated spot. This makes them very useful for laser machining applications, particularly in laser cutting of materials. Furthermore, it has a circular shape in the transverse plane in which intensity distribution is expressed in a Gaussian profile. The beam parameters determine the geometry of the laser beam at a given wavelength ( $\lambda$ ). These parameters are *(i)* beam waist radius ( $w(z)$ ), *(ii)* beam divergence angle ( $\Theta$ ), and *(iii)* Rayleigh length ( $z_R$ ) which are illustrated in Fig. 2.5 and described below.



**Fig. 2.5.** A schematic diagram of a typical optical system showing the geometrical parameters of a laser beam [Adapted from Abt et al. (2007)]

### 2.2.1 Beam Waist Radius

The beam waist radius ( $w(z)$ ) is the distance to the propagation direction of the laser beam ( $z$ ). It is defined expressed as:

$$w(z) = w_0 \sqrt{1 + \left(\frac{z}{z_R}\right)^2} \quad (2.1)$$

where  $w_0$  is the minimum beam waist radius and  $z_R$  is the Rayleigh length which is discussed in Section 2.2.3. A practical calculation of the minimum beam waist radius ( $w_0$ ) is the product of optical magnification factor and the core diameter of fibre ( $D_f$ ). The optical magnification factor is the ratio between the focal lengths of the focusing lens ( $f_f$ ) and the collimating lens ( $f_c$ ). It is expressed in Eq. (2.2) and the geometry of the laser beam is illustrated in Fig. 2.5.

$$w_0 = \frac{D_f f_f}{2 f_c} \quad (2.2)$$

### 2.2.2 Beam Divergence Angle

The beam divergence angle ( $\Theta$ ) of a laser beam is an angular measure of beam waist ( $w(z)$ ) from the optical aperture along the propagation direction ( $z$ ) of the laser beam. In other words, it measures how fast the laser beam diverging from minimum beam waist ( $w_0$ ). For instance, the laser beams with a small divergence



angle has a minimum beam waist that is almost constant over a long propagation distance. This is important for applications such as communication, laser pointing, laser cutting, laser cladding, *etc.* The beam divergence angle for an ideal Gaussian beam is given as:

$$\Theta = \frac{2\lambda}{\pi w_0 n} \quad (2.3)$$

where  $n$  is the refractive index of the medium the beam propagates through.

### 2.2.3 Rayleigh Length

In laser optics, Rayleigh length ( $z_R$ ) is mathematically defined such that it is the distance along the propagation direction where the variation of the beam waist is not larger than  $\sqrt{2}$ . It is the measurement of how sharply the beam is focused, and it is written as:

$$z_R = \frac{\pi w_0^2}{\lambda} \quad (2.4)$$

## 2.3 The Quality of Laser Beam

The characteristic properties and main three geometrical parameters of the laser beam are defined in Section 2.1 and Section 2.2, respectively. In this section, two new parameters are defined in order to measure the quality of the laser beam.

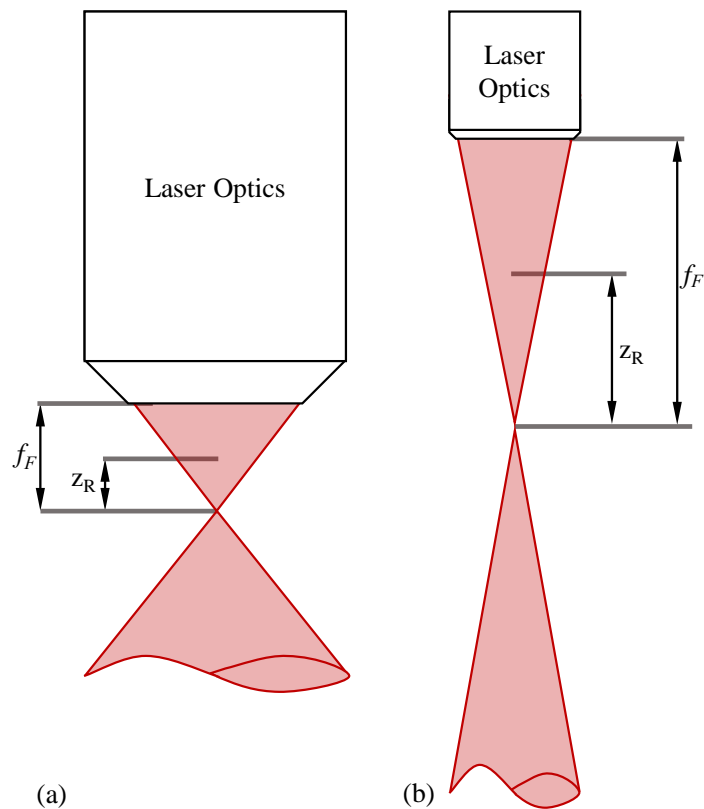
An ideal laser beam has got  $TEM_{00}$  mode which has a circular shape in the transverse plane. However, it is difficult to generate  $TEM_{00}$  mode laser beam. Therefore,  $M^2$  is introduced to define the ratio of the beam waist radius of the actual laser beam to that of an ideal Gaussian beam at the same wavelength. By definition  $M^2$  value is more than 1 and it is the measure of how close a laser beam to the ideal Gaussian laser. For example, a laser beam characterised by an  $M^2$  value of 1.2 will provide a beam diameter larger by 20%, as compared to the ideal Gaussian laser. The  $M^2$  is formulated as:

$$M^2 = \frac{\pi 2w_0 \Theta}{4\lambda} \quad (2.5)$$

On the other hand, the beam parameter product (BPP) is the product of the minimum beam waist diameter and beam divergence angle which is given in Eq. (2.6).

$$BPP = \frac{2w_0 \Theta}{4} \quad (2.6)$$

A practical meaning of the BPP is the focus-ability of a laser beam into a small spot. The lower the BPP the smaller beam waist diameter is achieved with a given magnification factor. This can be beneficial in some applications where a long working distance is required, such as remote welding. Furthermore, low BPP enables a reduction of the dimensions of the laser optics allowing a faster movement. In order to achieve the same minimum beam waist radius, the focal length of the focusing lens ( $f_L$ ) and Rayleigh length ( $z_R$ ) are short in the high BPP compare to the low BPP. This comparison is illustrated in Fig. 2.6.

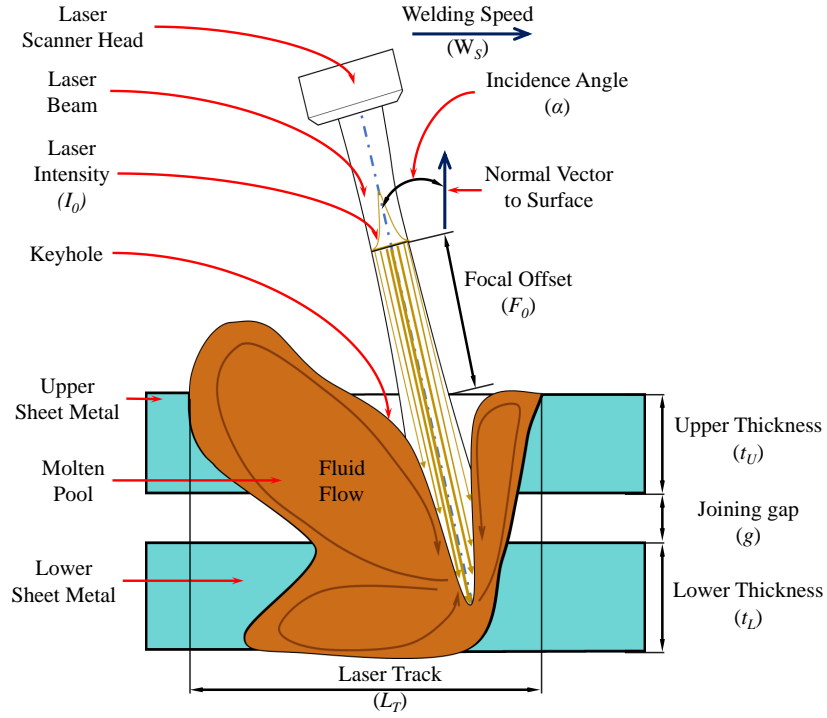


**Fig. 2.6.** The comparison between (a) high BPP, (b) low BPP that highlights focal length, Rayleigh length, and laser optics

## 2.4 The Laser Welding Process Parameters

In the laser welding process, the parts to be joined are locally melted by a high laser intensity, followed by a solidification process. The selection of process parameters regulates the occurring physical phenomenon which determine the weld shape and its quality. In order to achieve a high-quality weld, it is required to have a knowledge of the key process parameters and their effects on the weld quality. This

section represents the main process parameters namely; laser power ( $P_L$ ), welding speed ( $W_S$ ), focal offset ( $F_O$ ), incidence angle ( $\alpha$ ), laser intensity ( $I_0$ ) and interaction time ( $t_i$ ), which are shown in Fig. 2.7.



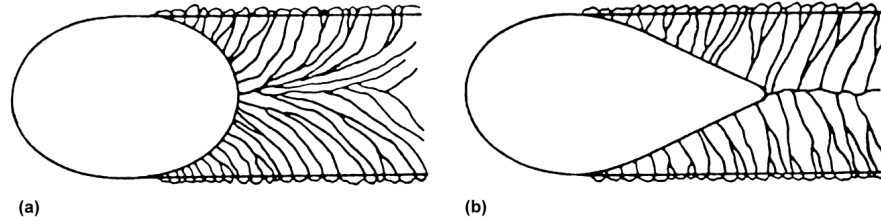
**Fig. 2.7.** The fundamental process parameters for laser welding

### 2.4.1 Laser Power

The laser power ( $P_L$ ) is directly linked to the weld quality. It is the rate of the energy flow from the laser source to the workpiece. Thus, it needs to be adjusted within certain limits in order to produce a high-quality weld. If the power is too low, the weld can be weak resulting in low levels of strength. On the other hand, high power will lead to welding defects such as spatter, undercut that violate given quality requirements. The laser power should be adjusted according to material composition and its thickness. For a given material, penetration is controlled by the combination of laser power, welding speed and on-surface spot area of the laser beam. Increasing the laser power normally increases the penetration considering the other parameters are kept constant (Khan et al., 2011). An experimental study by Li et al. (2015) investigated the influence of laser power and welding speed on penetration-to-width ratio, the maximum welding speed to achieve the full penetration was increased with increasing laser power.

### 2.4.2 Welding Speed

The welding speed ( $W_S$ ) is the linear speed of the laser beam along the welding direction. It affects the weld shape, the fluid flow in the molten pool, and the cooling rate which determines the final microstructure of the weld. The grain growth during solidification is perpendicular to the boundary of the molten pool. Grains are large, wide and the molten pool is elliptical at low speeds, whereas, they are small, narrow and the molten pool is teardrop shape at high speeds (Lienert et al., 2011). Figure 2.8 represents the effect of welding speed towards grain formation.



**Fig. 2.8.** The grain morphology (a) low welding speed, (b) high welding speed [Adopted from Lienert et al. (2011)]

Rizzi et al. (2011) investigated the influence of laser power and welding speed on penetration. During the experiments 2.5 kW CW  $CO_2$  laser was employed to weld AISI304 stainless steel in overlap joint. It was found that penetration was inversely proportional to the welding speed considering other process parameters were kept constant. Furthermore, increasing welding speed caused undercut since a strong fluid flow from the edge of the molten pool to the centre was observed; and hence, the molten pool was solidified as an undercut at the sides of the weld. In addition, the plasma plume electron temperature was increased as the keyhole got deeper. This was because more material was vaporized resulting in more hotter plasma plume.

### 2.4.3 Focal Offset

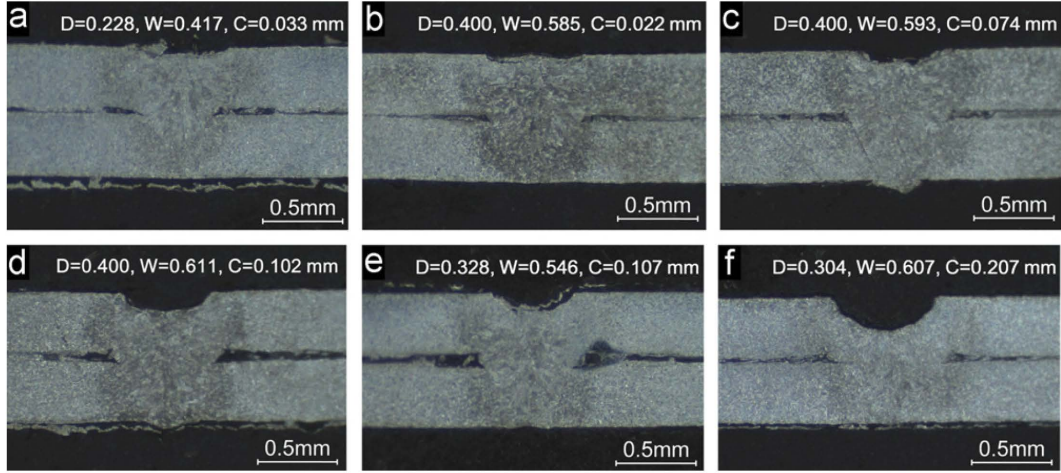
The focal offset ( $F_O$ ) means the distance along the laser beam axis between the focal plane and workpiece. Eq. (5.1) is modified considering the focal offset as:

$$w(z) = w_0 \sqrt{1 + \left( \frac{z \mp F_O}{Z_R} \right)^2} \quad (2.7)$$

The focal offset is generally controlled in such way that minimum beam waist radius ( $w_0$ ) is located on the surface of workpiece so that the maximum laser

intensity is achieved on the surface. Generally, the positive direction is inwards the workpiece; whereas, the negative direction is outwards the workpiece.

Zhao et al. (2012) carried out experimental study on thin-gauge galvanized steel with thickness of 0.4 mm in lap joint configuration. 1.5 kW CW mode IPG YLR-1500 ytterbium laser source utilized which delivered an on-surface spot diameter of 202.14  $\mu\text{m}$ . The focal length of the laser beam was 200 mm. The focal offset was varied in positive and negative directions. It was observed that penetration obtained with negative defocusing was shallower than the positive defocusing. Since the maximum laser intensity was obtained inside the workpiece while positive defocusing. Thus, powerful melting and evaporation occurred resulting deeper penetration. Also, it was found that top concavity was larger in positive defocusing. The experimental results are shown in Fig. 2.9.

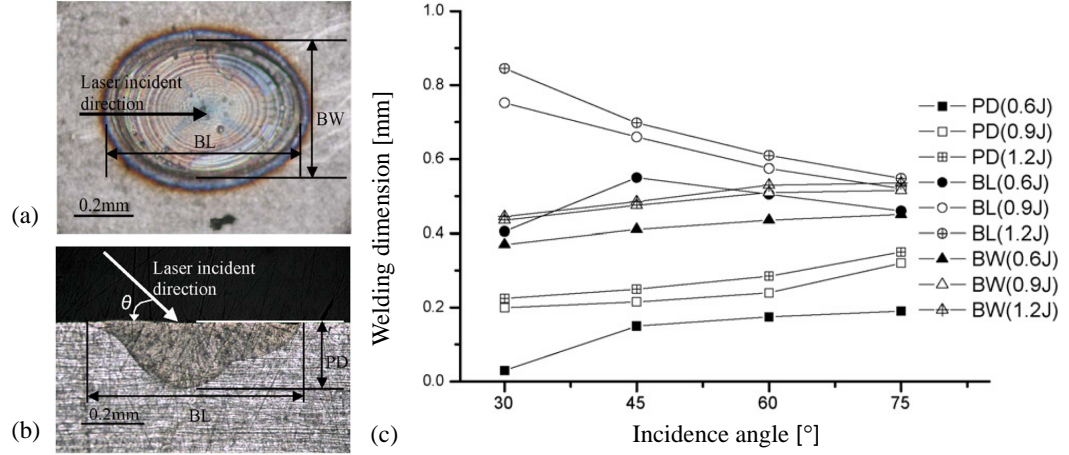


**Fig. 2.9.** Transverse cross sections of weld using  $P_L$ : 550 W,  $W_S$  : 35 mm/s, Gap : 0.15 mm and  $F_O$  of: (a) -0.3 mm, (b) -0.2 mm, (c) -0.1 mm, (d) 0 mm, (e) +0.1 mm, and (f) +0.2 mm (D:Penetration, W:Top Width, C:Top Concavity) [Adopted from Zhao et al. (2012)]

#### 2.4.4 Incidence Angle

The incidence angle ( $\alpha$ ) is the angle between the beam axis and the normal vector to the surface of the workpiece. The laser beam is not always perpendicular to the workpiece because there might be an obstacle between the laser beam and workpiece. Furthermore, the welding robot may not reach the certain position of the workpiece without having an incidence angle. Therefore, the incidence angle is crucial for practical applications. If the laser beam is perpendicular to the surface of the workpiece, the on-surface spot is a circular shape, but if the laser beam hits the surface, the spot becomes elliptical shape which decreases laser intensity.

Liao and Yu (2007) investigated the influence of laser power and incidence angle on the weld shape. The results illustrated that as the delivered energy increased, deeper penetration was achieved while top width decreased at the same incidence angle. On the other hand, both penetration and top width increased as the incidence angle increased for constant laser power. The author's experimental results are shown in Fig. 2.10.



**Fig. 2.10.** Experiment results showing the influence of incidence angle on the weld shape (a) Top view of welded spot and (b) Transverse cross sections of the weld (c) Characteristic lengths of the welded spot as functions of incident angle [Adopted from Liao and Yu (2007)]

### 2.4.5 Laser Intensity

The four laser process parameters (i.e. laser power ( $P_L$ ), welding speed ( $W_S$ ), focal offset ( $F_O$ ), and incidence angle ( $\alpha$ )) play an important role to define the weld quality. However, the same penetration can be achieved with many combinations of these parameters. Apart from the similar depths of penetration, these welds may exhibit different properties. Therefore, Suder and Williams (2012) conducted a comprehensive experimental study to gather these parameters together and represented in terms of (i) laser intensity and (ii) interaction time.

The laser power per unit area at the on-surface spot is commonly known as the laser intensity or irradiance ( $I$ ). The peak laser intensity and its distribution in Cartesian coordinates at a given focal plane is defined in Eqs. (2.8) and (2.9), respectively.

$$I(x, y, z) = \frac{2P_L}{\pi w(z)} \quad (2.8)$$

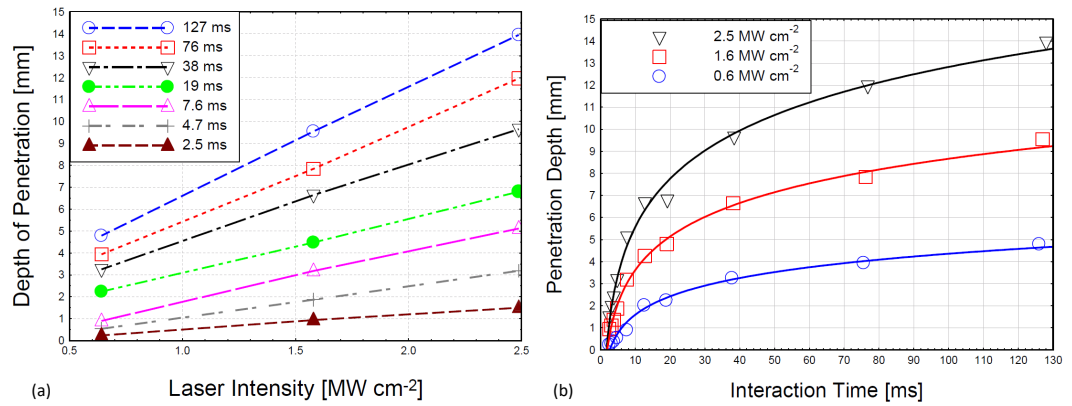
$$I(x, y, z) = \frac{2P_L}{\pi w(z)} \exp\left(-\frac{x^2}{w(z)^2} - \frac{y^2}{w(z)^2}\right) \quad (2.9)$$

### 2.4.6 Interaction Time

According to Suder and Williams (2012) defines interaction time ( $t_i$ ) as time in which a particular point on the surface of the workpiece is exposed to the laser beam, whilst the beam is moving with a constant speed. This is similar to the pulse duration from pulsed laser welding. Based on this definition the interaction time ( $t_i$ ) is given as:

$$t_i(z) = \frac{2w(z)}{W_S} \quad (2.10)$$

Suder and Williams (2012) conducted a comprehensive experimental study to investigate the amount of energy delivered to the workpiece. The work showed that the following three parameters: (i) laser intensity, (ii) interaction time, and (iii) specific energy point would define the weld. The results indicated that the penetration was linearly correlated with laser intensity, but it was logarithmically dependent on the interaction time. It is because a certain part of the laser intensity develops the keyhole and the remaining is utilized to increase the penetration. However, a certain keyhole depth can be obtained at a given laser intensity and a further increase in the interaction time has only a small effect. It was also concluded that constant laser intensity and interaction time did not provide a constant penetration when the beam diameter was increased. Since the energy delivered to the workpiece is increased when the beam diameter gets larger at a given laser intensity and interaction time. The author's experimental results are depicted in Fig. 2.11.



**Fig. 2.11.** The experimental result that shows the penetration as a function of: (a) laser intensity for different interaction times, and (b) interaction time for different laser intensities [Adopted from Suder and Williams (2012)]

## 2.5 Modes of Laser Welding

An important aspect in laser beam welding is the interaction of the laser beam with the material. The interaction mechanism between the laser beam and the workpiece is mostly influenced by the laser intensity at the surface, interaction time and material properties such as absorption, reflectivity, conductivity, *etc.* This mechanism defines the shape and mode of the welding. Two fundamental modes of laser welding are namely; *(i)* conduction welding, and *(ii)* keyhole welding. The main difference between these two modes is how the laser energy transfers to the workpiece.

### 2.5.1 Conduction Mode

The dividing line between conduction mode and keyhole mode is the level of the laser intensity. In conduction mode the intensity level is relatively lower ( $I < 10^6 \text{ W/cm}^2$  for steel) and on-surface spot size is rather large. A small amount of the laser energy is absorbed in the surface of the workpiece and substantial amount of the energy is reflected. The absorbed energy is transferred by heat conduction within the workpiece. The main advantage of this mode is that material melts but cannot vaporize. As a consequence, the welds show neither porosity nor undercut or spatter formations. The cross section of the weld is in a bowl shape and the molten pool is shallow and wide. However, it is a stable process that weld seam does not need any further post-processing. Conduction welding is usually used for welding the compact size of parts in medical and electrical industries.

### 2.5.2 Keyhole Mode

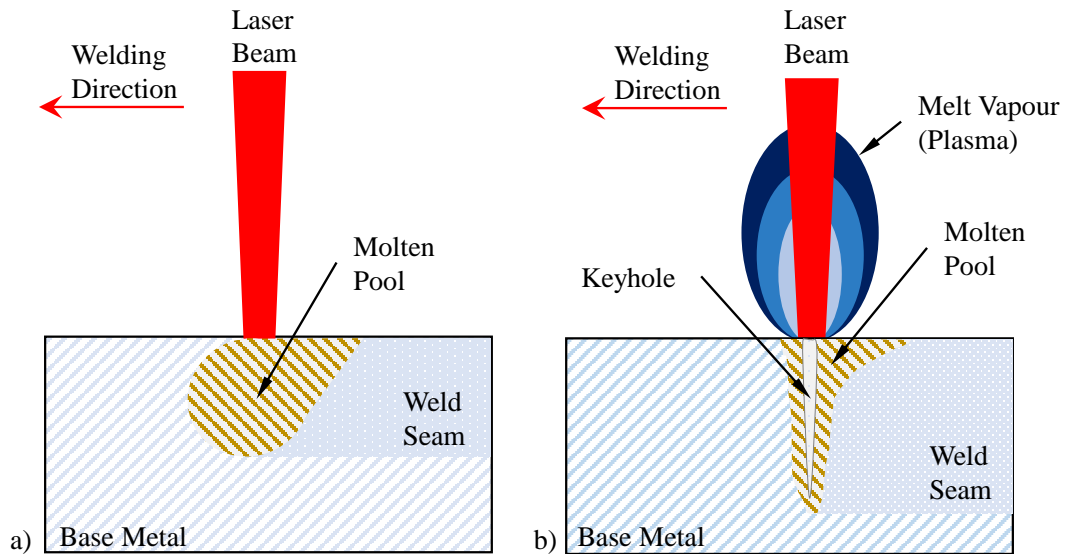
When the laser intensity exceeds a critical value ( $I > 10^6 \text{ W/cm}^2$  for steels), instantaneous vaporization occurs along with melting on the surface of the workpiece. Such vaporization generates a pressure which pushes liquid material downwards, creating a vapour cavity named as the “*keyhole*”. Due to the vaporization, a plasma forms above the surface of the workpiece which absorbs or inhibits laser power. The keyhole allows the laser beam to go deeper in the material developing “wine glass” shape. The molten pool is deep and narrow resulting in a small heat affected zone (HAZ). Moreover, during the welding, the keyhole walls are not stable, they are vibrating since the vapour pressure and recoil pressure try to keep open the keyhole walls whilst the hydrostatic pressure and surface tension try to close it. Therefore, metal vapour can be easily trapped inside the keyhole and trapped vapour causes weld defects such as porosity, spatter, cracks, *etc.* (Tzeng and Yih-



Fong, 2006; Zhou and Tsai, 2007). A brief summary and schematic presentation of modes of laser welding are given in Table 2.1 and Fig. 2.12, respectively.

**Table 2.2:** Comparison between conduction and keyhole welding modes

Welding Mode	Advantages	Disadvantages
Conduction Mode	Stable process without controlling heat input	Slow process
	No spatter, no porosity, no crack	Low productivity
	No vaporisation	High thermal distortion
	No requirement for high quality beam	Low penetration
Keyhole Mode	High productivity	Unstable process
	Low thermal distortion	High levels of porosity and spatter
	Low Heat Affected Zone	Requires high quality beam
	High penetration	High joining efficiency



**Fig. 2.12.** The modes of laser welding. a) Conduction mode, b) Keyhole mode

## 2.6 The Weld Quality

Welding is a joining process in which two or more parts are coalesced together at their faying surfaces by a suitable application of heat and/or pressure. The faying surfaces are the part surfaces that are going to be joined. These surfaces are either

in contact or close proximity. The welding process is divided into two major classes: (i) fusion welding, in which the weld is accomplished by melting the base metal, in some cases using filler metal, and (ii) solid-state welding, in which heat and/or pressure are used to achieve the weld, but no melting of the base metals occurs, and no filler metal is used.

The purpose of any welding process is to join parts into a single structure. The physical integrity of the structure depends on the weld quality. The typical requirements for the weld quality can be listed as follows: (i) the weld satisfies the design dimensions and has almost no distortion, (ii) the weld bead has uniform waves, and no cracks or holes found in the weld bead, (iii) the weld offers the required functionality and strength, and (iv) the appearance of the weld satisfies the required level. Based on these requirements, the weld quality can be assessed into the following three categories: (i) metallurgical, (ii) mechanical, and (iii) aesthetic. The discussion of the weld quality in this dissertation primarily deals with fusion welding.

### 2.6.1 Metallurgical Weld Quality

Metallurgical based weld quality refers to the weld microstructure. During the welding process, the base metal to be welded experiences a thermal cycle, which is the rapid heating and cooling. Such a thermal cycle results in microstructural changes in the base metal. It is important to understand these microstructural changes since they affect the mechanical properties of the weld (Mishra and Debroy, 1995).

According to the American Iron and Steel Institute (AISI), steels that include carbon content up to 0.20% carbon is called “*low-carbon steels*”, and between 0.20%-0.40% carbon is called “*mild steels*”. In this dissertation, a hot-dip galvanized low carbon steel (DX54D+Z) with a nominal carbon content of 0.12% is used and its chemical composition % by mass, mechanical and thermal properties are given in Tables 2.3 to 2.5. These values are taken from the industrial standard (EN ISO 10327, 2004).

**Table 2.3:** The chemical composition of DX54D+Z steel (wt %)

Material	Elements (wt %)						
	C	Si	Mn	P	S	Ti	Fe
DX54D+Z	0.12	0.5	0.6	0.1	0.045	0.3	98.335

**Table 2.4:** The mechanical properties of DX54D+Z steel

Material	Yield Strength ( <i>MPa</i> )	Tensile Strength ( <i>MPa</i> )	Total Elongation (%)
DX54D+Z	120 - 220	260 - 350	38

**Table 2.5:** The thermal properties of DX54D+Z steel

Material	Density ( <i>kg/m<sup>3</sup></i> )	Thermal Conductivity ( <i>W/(m × K)</i> )	Specific Heat Capacity ( <i>J/(kg × K)</i> )
DX54D+Z	7800	49.8	435

The generalized heat transfer equation is solved using the Finite Element Method (FEM) in Chapter 5. The required material properties for the FEM are density, thermal conductivity, specific heat capacity, latent heat, and liquidus, solidus and vaporization temperatures. The aforementioned temperatures and the latent heat of DX54D+Z steel are not given in the standard (EN ISO 10327, 2004). The liquidus and the solidus temperature of DX54D+Z are calculated from the iron-iron carbide phase diagram based on the equivalent carbon content. The vaporization temperature and the latent heat of fusion of pure iron (Fe) are used for the vaporization temperature and the latent heat of the DX54D+Z steel.

A phase diagram in metallurgy represents the equilibrium phases present in a pure metal or an alloy. The most common type phase diagram used in the metallurgy of steels is the iron-iron carbide phase diagram, which is used to understand the solidification process and the subsequent microstructure (Blondeau, 2013). It contains liquidus, solidus, and solvus temperatures as a function of carbon content. The liquidus line separates all liquid material from a mixture of liquid and solid. Similarly, the solidus line separates completely solid material from a mixture of liquid and solid. The solvus line defines the limit of solid solubility.

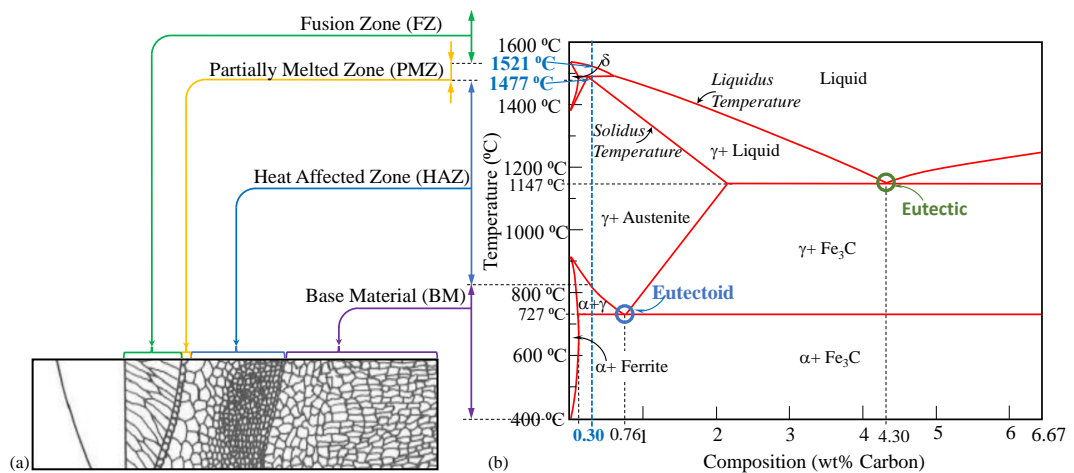
Carbon Equivalent (CE) is an empirical value in weight percent, relating the combined effects of different alloying elements used in the making of carbon steels to an equivalent amount of carbon. This value is calculated in Eq. (2.11) (ANSI/AWS D1.1, 2000).

$$\%CE = \%C + \frac{(\%Mn + \%Si)}{6} + \frac{(\%Cr + \%Mo + \%V)}{5} + \frac{(\%Ni + \%Cu)}{15} \quad (2.11)$$

The solidus and liquidus temperatures of the material used in this thesis

are determined according to the carbon equivalent value from the iron-iron carbide phase diagram as  $1477\text{ }^{\circ}\text{C}$  and  $1521\text{ }^{\circ}\text{C}$ , respectively.

During the welding process (in the case of fusion welding), the region just right under the heat source has experienced a temperature which is greater than or equal to liquids temperature. This region undergoes melting followed by solidification, similar to the casting process. On the other hand, the region which is slightly away from the heat source undergoes heat treatment. In general, a weld can be divided into four different zones depending upon experienced temperature. These zones are (i) the fusion zone (FZ) is the region which has experienced a temperature which is greater than or equal to liquids temperature, (ii) the partially melted zone (PMZ) is defined as the region that experiences temperatures in the freezing range (between liquidus and solidus temperature), (iii) the heat affected zone (HAZ) is the region that experiences a peak temperature that is well below the solidus temperature while high enough that can change the microstructure, and (iv) the base metal (BM) is the region where there is not any heat treatment. The schematic illustration of different zone in the weld and iron-iron carbide phase diagram is given in Fig. 2.13.

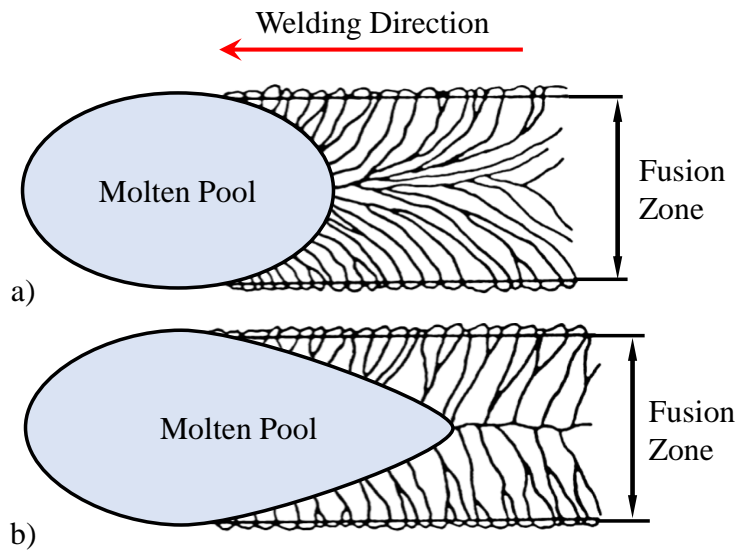


**Fig. 2.13.** (a) The distribution of the different zones in a welded joint as a function of temperature in relation to (b) the iron-carbon phase equilibrium

### 2.6.1.1 Fusion Zone

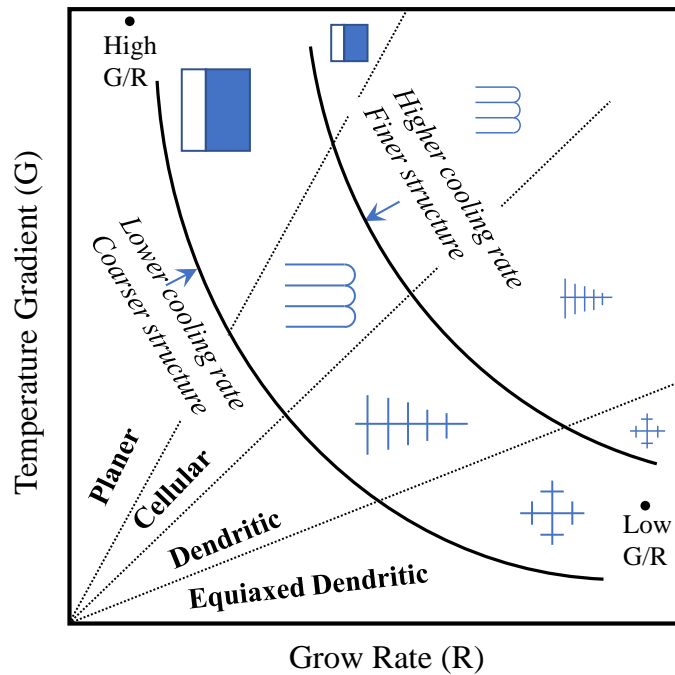
The microstructure in the fusion zone is influenced by the solidification conditions and process parameters. During the solidification process, grains tend to grow in the direction perpendicular to the molten pool boundary because this is the direction of the maximum temperature gradient. At high welding speeds and

power intensity, the molten pool becomes teardrop shape and grains are essentially straight in order to grow perpendicular to the pool boundary. On the other hand, the molten pool becomes elliptical shape at lower welding speed and power intensity, and grains are curved to grow perpendicular to the pool boundary. Figure 2.14 shows the grain structure of the fusion zone (at top view) for both high and low welding speeds.



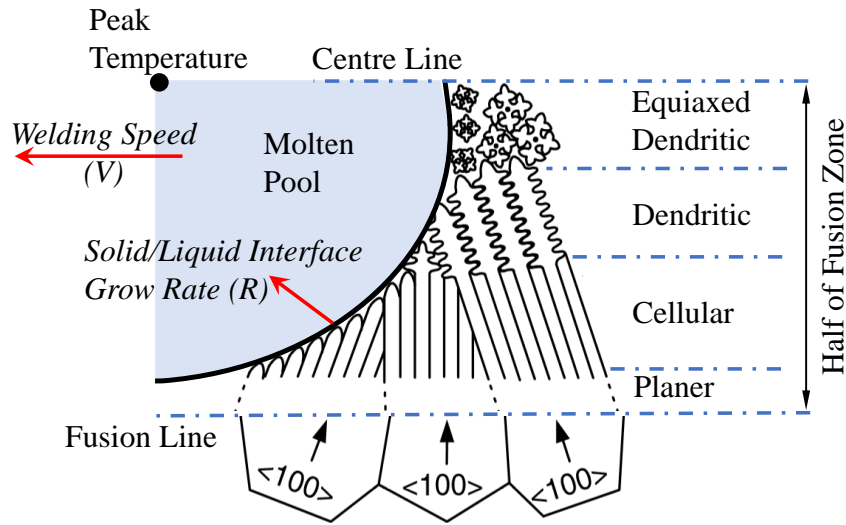
**Fig. 2.14.** Top view of the fusion zone structure at different welding speeds (a) elliptical molten pool, (b) teardrop shape molten pool [Adopted from Lienert et al. (2011)]

The temperature gradient ( $G$ ), solid/liquid interface growth rate ( $R$ ), and cooling rate ( $e$ ) are the important parameters for the solidification process. Kou (2010) identified four possible solidification modes depending on these parameters. The identified modes are listed as follows: (i) planar, (ii) cellular, (iii) dendritic, and (iv) equiaxed dendritic. It is highlighted that the ratio of the temperature gradient and the growth rate ( $G/R$ ) determines the solidification mode, and the product of the temperature gradient and the growth rate ( $G \cdot R$ ) determines the size of the solidified microstructure. The effect of the temperature gradient ( $G$ ) and the growth rate ( $R$ ) on the solidified microstructure is depicted in Fig. 2.15.



**Fig. 2.15.** Effect of temperature gradient  $G$  and growth rate  $R$  on the morphology and size of solidification microstructure [Adopted from Kou (2003)]

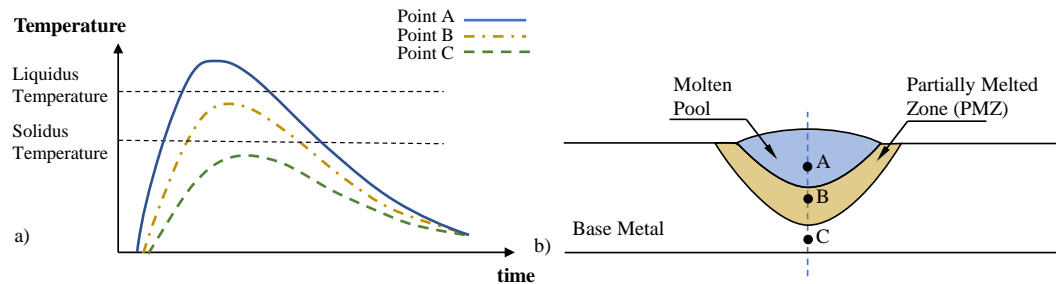
The temperature gradient ( $G$ ) is relatively high at the fusion line (FL) because the molten pool is in contact with the metal that has not been melted. An opposite trend exists for the interface growth rate ( $R$ ), it is maximum at the fusion line and reaching almost zero at the fusion line. Therefore, the solidification mode change continuously in the fusion zone since the ratio  $G/R$  decreases from the fusion line toward the centre line, as indicated in Fig. 2.16.



**Fig. 2.16.** Variation in solidification mode across the fusion zone [Adopted from Kou (2003)]

### 2.6.1.2 Partially Melted Zone

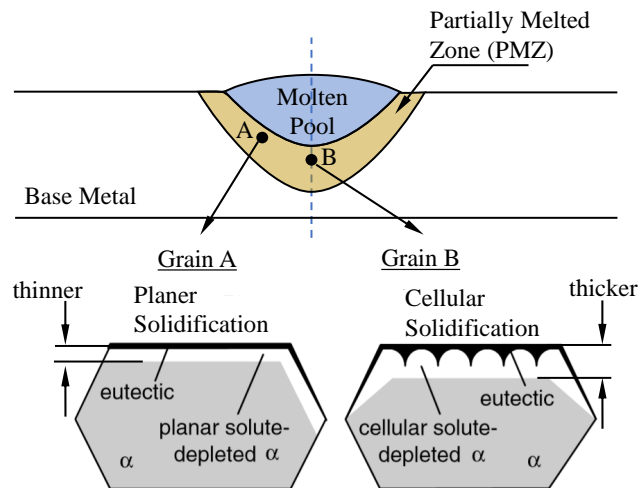
Temperature profile and history can be used to characterize a welding process. The temperature profile indicates temperature distribution at a certain time, and the temperature history represents the instantaneous temperature of a certain point in the welded material. The partially melted zone (PMZ) is defined as the region that experiences temperatures in the freezing range (between liquidus and solidus temperature). This zone separates the FZ and the HAZ (See Fig. 2.17). The width of the partially melted zone is determined by the size of the freezing range and cooling rate. In laser welding, the PMZ is very narrow due to higher cooling rates.



**Fig. 2.17.** A schematic representation of a) the partially melted zone, and b) temperature history for given points in the welded material

The fraction of liquid inside the grain in this zone depends on the local temperature gradient. It is fully liquid at the edge of the molten pool. Consider an

alloy of A and B that has an overall composition that places it to the left of the eutectic point. The liquation will take place when the base metal is heated to the eutectic temperature. At this temperature, the alpha phase and the beta phase react with each other and forming the liquid of the eutectic composition. The liquation occurs particularly along grain boundaries and to a lesser extent in the interior of the grains. During solidification, grains have a tendency to solidify essentially upward and toward the molten pool. However, if the grains are long and thin, the direction of solidification is only upward (Huang et al., 2001). It is observed that the solidification mode is predominantly planer in this zone. However, the cellular mode is seen near the weld bottom because PMZ is thicker in this area resulting in a lower temperature gradient. These two modes are depicted in Fig. 2.18.



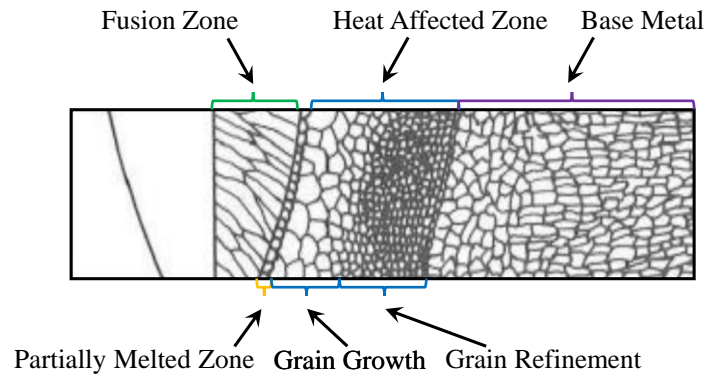
**Fig. 2.18.** The solidification modes of grain boundary liquid in the PMZ [Adopted from Huang et al. (2001)]

### 2.6.1.3 Heat Affected Zone

The heat-affected zone (HAZ) lies outside the PMZ, and it begins where the peak temperature is just below the solidus temperature of the alloy and extends to a point where the temperature is high enough to alter the microstructure of the base material. The HAZ is generally divided into two regions: (i) the grain growth region, which lies adjacent to the PMZ, and (ii) the grain-refined region, which is farther away from the weld. The grain growth is a function of the temperature, and it decreases with increasing distance from the FZ. Thus, the coarser grains (the maximum grain size) always occur along the PMZ. Due to the coarser grains, this region will be softer and have lower strength. The heat applied during welding recrystallizes grains that are away from the weld metal into fine, equiaxed grains.



The typical grain structure for the fusion welded joint is shown in Fig. 2.19.

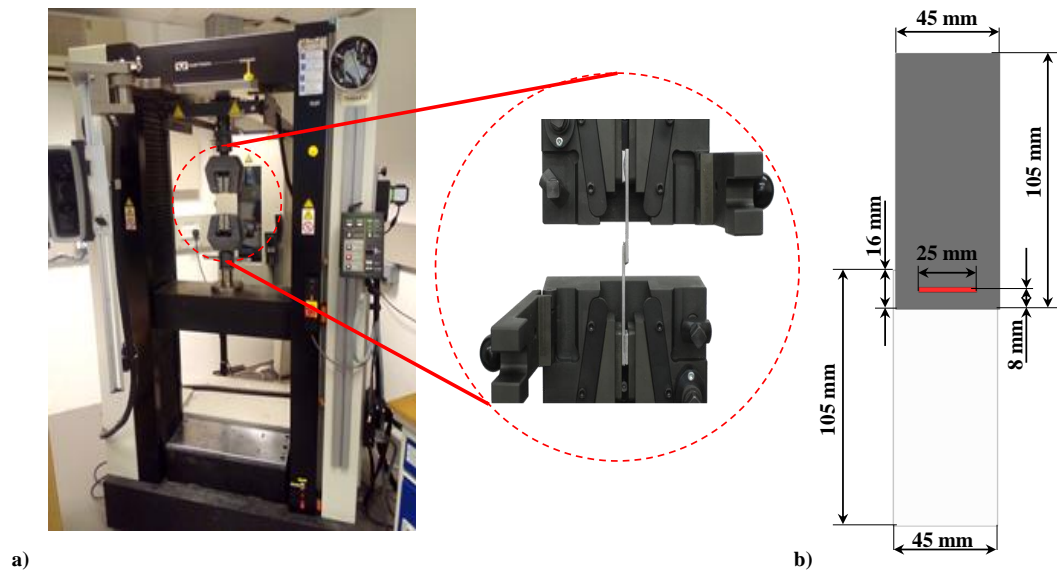


**Fig. 2.19.** The different microstructural regions in a steel weld highlighting the grain growth and the grain refinement regions inside the HAZ [Adopted from Layus et al. (2018)]

### 2.6.2 Mechanical Weld Quality

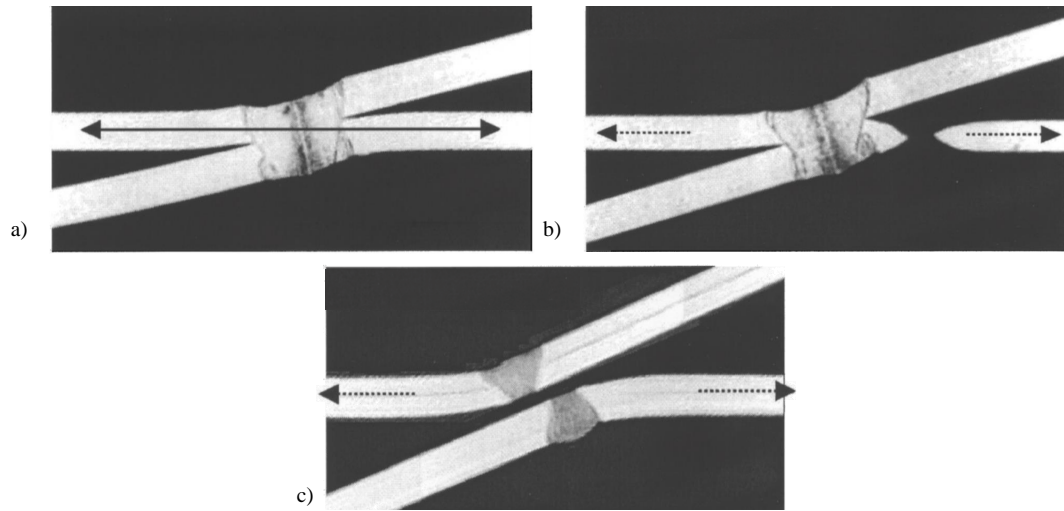
The mechanical-based weld quality quantifies the ability of the weld to perform the functional requirements during the service life. These requirements could be either strength in static loading and/or durability in dynamic loading. Strength is usually tested through a tensile machine applying a quasi-static force and checking which is the maximum value of the load the joint can stand, and which is the correspondent elongation for that load. Clearly, this characteristic plays a fundamental role in the evaluation of a weld; the joined components are, in fact, utilized for the creation of structural parts of the automotive frame, and they need, for safety issues, to be resistant.

EN ISO 5817 (2014) is a industrial standard for fusion welded joints in steel, nickel, titanium, and their alloys with quality levels and imperfections. The weld quality is defined by quality levels (A, B, C, or D), where A is the highest and D the lowest weld quality, respectively. Tensile-shear tests are widely employed to evaluate tensile strength. It enables to obtain important information about the breaking point, maximum load, fracture position and the percentage elongation of the weld. An example Tensile-Shear testing configuration of a welded structure is shown in Fig. 2.20.



**Fig. 2.20.** a) Instron 100kN tensile testing machine used for the lap shear tensile tests, b) Dimensions of the welded samples to be tested via lap shear tensile test [Prepared based on the industrial standard EN ISO 5817 (2014)]

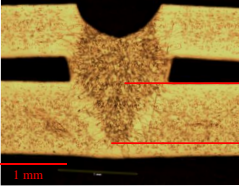
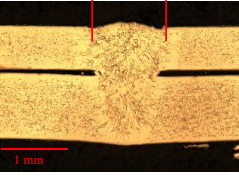
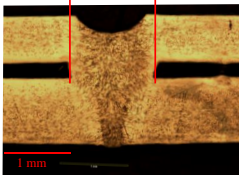
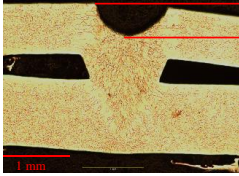
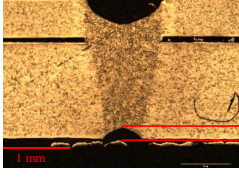
Miyazaki and Furusako (2007) conducted an experimental examination to examine the effects of the bead size on the tensile shear strength of laser welded lap joints. In the tensile shear test of laser welded lap joints, fracture occurred either at the base metal (BM), at the adjacent to the weld or at the weld depending on the strength of the welded joint. When the weld width was 2.0 mm and the weld length was 50 mm across, the fracture occurred at the base metal, and the joint strength was the same as the base-metal strength. In contrast, when the weld width was 0.85 mm and the weld length was 50 mm, the weld metal failed. When the bead width was 2.0 mm and its length was 30 mm, the test pieces failed at the adjacent to the weld, and the joint strength increased as the base metal strength increased. Figure 2.21 illustrates the macro-section images for different welded structures highlighting configuration of breaking point after fracture. It can be summarized that if the weld strength is bigger than the base metal strength, the fracture occurs at the base metal. If the base metal strength is bigger than the weld strength, the fracture occurs at the weld. Depending on the thermal cycle, the fracture occurs at the HAZ.



**Fig. 2.21.** Deformation of the different laser lap welded structures under tensile shear load and configuration of breaking point after fracture a) at the base metal, b) at adjacent to the weld, c) at the weld [Adopted from Miyazaki and Furusako (2007)]

Weld profile is important not only because of its effects on the strength and appearance of the weld but also because it can indicate incomplete fusion, imperfect shape or unacceptable contour. Thus, a significant body of research has been conducted to establish a mapping relation between welding process parameters and fusion zone dimensions to predict the weld quality; and, to find out optimum process parameters to achieve quality requirements determined by the manufacturers or the industrial standards (EN ISO 13919-1, 1997; EN ISO 13919-2, 2001). The top width, interface width, penetration, and bottom concavity are the characteristic fusion zone dimensions (FZDs) that determine the strength of the weld. The allowance limits of FZDs and graphical description are shown in Table 2.6.

**Table 2.6:** Welding quality in terms of Fusion Zone Dimensions (FZDs) and their allowance limits.  $t_{upper}$  indicates the thickness of the upper sheet;  $t_{lower}$  indicates the thickness of the lower sheet

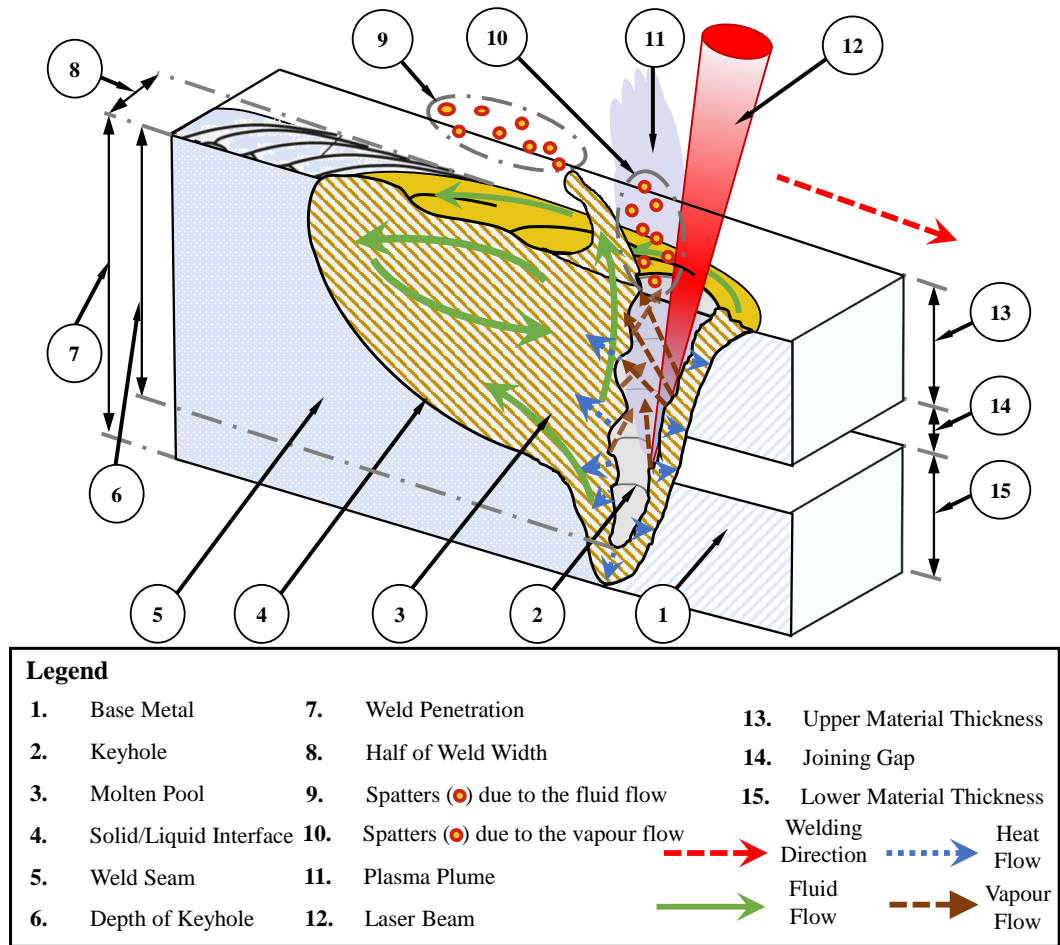
Fusion Zone Dimension	Macro-Section Image Description	Allowance Limit
Penetration (PT)		$0.6 \times t_{lower} \leq PT \leq t_{lower}$
Top Width (TW)		$t_{upper} \leq TW \leq 2 \times t_{upper}$
Interface Width (IW)		$IW \geq 1.1 \times \min(t_{lower}, t_{upper})$
Top Concavity (TC)		$TC \leq 0.5 \times t_{upper}$
Bottom Concavity (BC)		$BC \leq 0.5 \times t_{lower}$

### 2.6.3 Aesthetic Weld Quality

Spatter, which is the ejection of melt droplets from the molten pool, is the main reason for the mass loss. This mass loss can cause weld defects, such as under-filling, an unsteady appearance of the weld seam which deteriorate the aesthetics of the weld seam. It is important to have less amount spatters for Class-A type surface finish (Haider et al., 2007).

The formation of spatter can be explained by two reasons. The first explanation is based on the unstable keyhole. The recoil pressure tries to open the keyhole; on the other hand, the surface tension pressure tries to close (Kägeler and Schmidt, 2010). The keyhole front is slightly tilted in the reverse direction of the welding speed. This means that the upper part of the keyhole front is overheated. Thus, localized evaporation is occurred resulting in intense vapour jets at the keyhole front. These vapour jets impinge on the keyhole rear, and in this case, total pressure that opens the keyhole rear is the superposition of the recoil pressure and the vapour jet pressure. Consequently, the keyhole rear is locally pushed backwards, resulting in waves at the keyhole rear. When these waves are broken at the keyhole opening, spatters are generated (Kaplan and Powell, 2011).

The second explanation relates to the flow conditions within the molten pool. The keyhole opening fluctuates in diameter periodically. Any increase in diameter narrows the distance between the keyhole and the liquid-solid interface. This narrowing increases local flow around the keyhole opening, and the molten pool around the keyhole rear was elongated vertically. A droplet can break from the vertically elongated molten pool when the energy of the fluid element with the vertically elongated molten pool overcomes the surface energy of the melt and the energy of the escaping fluid element (Nagel et al., 2018). The flow conditions in the molten pool around the keyhole and the localized evaporation of the metal in the keyhole front are illustrated in Fig. 2.22.



**Fig. 2.22.** A schematic description of spatter formation based on the localized evaporation of metal in the keyhole front, and the flow conditions in the molten around the keyhole

Also, corrosion has been recognized to have an influence on the aesthetics of the weld. Beyond visual aspects, sealing capabilities must be ensured. Although sealants are widely used for this purpose, welds must still be free of any defect that could allow this to happen. Therefore, defects like burn-through and cracks should be completely avoided.

## 2.7 Summary

This chapter presents a general overview of the background information of the laser beam and the laser welding process. The first part of this chapter briefly described the fundamentals of a laser beam. The second part gives information related to laser-material processing specifically welding.

The laser beam is generated based on the stimulated emission of electromagnetic radiation and it consists of electromagnetic waves. The fundamental characteristics are *(i)* coherent (i.e. travel in the same direction), *(ii)* monochromatic (i.e. single colour), *(iii)* transverse electric mode (i.e. defines the intensity distribution of the laser), *(iv)* polarization (i.e. a phase difference between electric and magnetic fields), and *(v)* a unique wavelength. An ideal laser beam has a  $TEM_{00}$  mode where laser intensity distribution shows a Gaussian profile. The laser beam geometry depends on the following parameters: *(i)* beam waist radius, *(ii)* beam divergence angle, and *(iii)* Rayleigh length. Furthermore, the quality of the laser beam is expressed with two metrics: *(i)*  $M^2$  value, and *(ii)* beam parameter product (BPP).

The main parameters that affect the shape of the weld can be listed as *(i)* laser power, *(ii)* welding speed, *(iii)* focal offset, and *(iv)* incidence angle. These process parameters can be gathered into the spatial and temporal distribution of the laser energy on the surface of the workpiece as laser intensity and interaction time, respectively. Depending on these two distributions, different welding regimes occur in laser processing, identified as conduction and keyhole modes. The shape of the weld is in bowl shape (i.e. shallow penetration and wide width) in conduction mode; whereas, it is in goblet shape (i.e. deep penetration and narrow width) in keyhole mode.

# Chapter 3

## Literature Review

The laser welding process is a recent welding method which is capable of assembling several pieces of sheet metals using a laser beam. The laser beam is a highly concentrated heat source, and its diameter ranges from 0.2 *mm* to 10 *mm* in the knowledge that only the smaller diameters are employed. Furthermore, the welding is often performed without using filler material and there is no physical contact between the laser beam and the material. The main advantages are listed as *(i)* the high laser intensity ( $I \geq 10^6 W/cm^2$ ) which is capable of producing deep penetration welding in a fraction of a second, *(ii)* high energy input in a short time creates narrow heat affected zone (HAZ) resulting low thermal distortion, and *(iii)* non-contact welding leads to joining materials by single side access gives an ability to design thinner flanges in the automotive industry (Sinha et al., 2013; Enz et al., 2017).

Despite numerous advantages of laser welding, it is difficult to laser weld *(i)* steels especially galvanized steels due to the mitigation problem of zinc vapour (Kim et al., 2015), *(ii)* aluminium due to the lower absorption of the laser beam at the surface and hot cracking (Hu and Richardson, 2006), and *(iii)* magnesium due to oxidation and pore formation (Cao et al., 2006). Furthermore, the pieces to be welded need to be closely adjusted since it is non-contact welding and filler material is not used (Li et al., 2003; Franciosa et al., 2014). Therefore, inaccurate beam positioning can result weld defects such as lack of fusion, and other weld defects, such as porosity and spatters may also result due to high cooling rates with insufficient de-gasification metallic vapour from the welding medium.

The overall goal of this thesis is to emulate the RLW process to directly measure the aforementioned FZDs (i.e. penetration, top width, interface width). Furthermore, the developed model is a necessary enabler for the proposed closed-loop quality assurance framework (See Fig. 1.5) for the RLW process. The strategy



is to integrate the data gathered from the process to the physics-driven welding model to obtain FZDs during the welding process. To accomplish this goal, it is necessary to have control over process parameters that affect the weld quality as well as a fast and accurate model which emulates the welding.

The remaining part of this chapter is organized as follows: (i) Section 3.1 summarizes the mitigation methods of zinc vapour in laser welding of galvanized steel, (ii) Section 3.2 reviews on state-of-the-art of the in-process monitoring methods used in the laser welding process, and (iii) a brief overview the driving physical phenomenon involved in laser welding is presented in Section 3.3.

### 3.1 Related Work on the Mitigation Methods of Zinc Vapour in Laser Welding of Galvanized Steels

The galvanization is a process in which steels are coated with zinc. The coating protects the metal against corrosion, also it allows the paint to adhere better to the surface of the metal. Two most commonly used processes for galvanization are “*hot-dip galvanization*” and “*electrogalvanizing*”.

Hot-dip galvanizing means immersing the steel in a molten zinc bath of about 450 °C. The zinc is metallurgically bonded to the steel due to the diffusion reaction between the zinc and the iron in the steel. When the steel is removed from the zinc bath, the coating is made up of different layers of zinc-iron alloys with a top layer of pure zinc (Krauss et al., 1990). The immersion time varies according to the dimension of the base metal and thickness of the coating. Depending on the immersion time, the coating may be silvery and shiny (thinner layers) or dark grey and matt (thicker layers) (Porter, 1991). Another commonly used method of zinc coating is electrogalvanizing. It is an electroplating technique that uses electricity to coat an object with a layer of metal. The coating is carried out immersing the object being coated (cathode) and a bar of coating metal (anode) into an electrolytic bath and connecting the anode and the cathode into a circuit with a battery or other power supply. When the electricity flows through the circuit, the bar dissolves in the electrolytic bath, and plates out on the object, forming a thin but durable coating. Compared to hot-dip galvanization, electrogalvanizing provides a thinner coating and more aesthetic appearances (Thiery and Frédéric, 2007; Duprat and Kelly, 2009).

The most utilized welding technique in the automotive industry is resistance spot welding (RSW). The main limitations of this process can be listed as (i) the need for higher current, (ii) the longer welding time, and (iii) the tendency of zinc

coating to stick to the electrodes (Holliday et al., 1996). With the advancement of laser technology, RSW has been steadily taken over by RLW because it offers better weld quality, cheaper and faster manufacturing process (Ribolla et al., 2005; Kawahito et al., 2007; Ceglarek et al., 2015). However, laser welding of galvanized steels is still challenging. Due to the difference between the melting temperature of steel ( $1500\text{ }^{\circ}\text{C}$ ) and the vaporizing temperature of zinc ( $907\text{ }^{\circ}\text{C}$ ), the zinc vapour at faying surfaces might be trapped within the molten pool (i.e. degrade mechanical and metallurgical quality) or might cause disruption of keyhole stability leading spatters (i.e. degrade aesthetic quality).

This section reviews past research on the mitigation methods of zinc vapour that are utilized in laser welding of galvanized steel. Moreover, limitations of the existing methods are highlighted in the context of the welding process and they can be classified into three categories as *(i)* removal of zinc coating, *(ii)* reduction in zinc vapour pressure, and *(iii)* ventilation of zinc vapour.

### 3.1.1 Removal of Zinc Coating

The simple solution is to eliminate the root cause of the problem which is removal of zinc coating. The removal process is based on adequately controlling the heating, melting and vaporization processes of the zinc coating.

Yang and Kovacevic (2009) achieved zero defect welding in overlap welding of galvanized DP 980 steel by utilizing a hybrid process combining gas metal arc welding (GMAW) and fibre laser welding. In this research, the auxiliary heat source (GMAW) was used to preheat the surface of metal to transform the zinc coating to zinc oxide. It was pointed out that the formed zinc oxide was higher vaporization temperature ( $T_{vapZnO} = 2248\text{ K}$ ) than atomic zinc ( $T_{vapZn} = 1180\text{ K}$ ). After pre-process, the actual weld was accomplished using the fibre laser.

Similarly, Milberg and Trautmann (2009) proposed a bifocal hybrid laser welding (BHLW) which was a superposition of high-power diode laser (HPDL) and Nd:YAG laser systems. The HPDL system was utilized for the zinc removal and welding is performed using an Nd:YAG laser system. The BHLW enables increased top width due to the larger area was irradiated by the HPDL beam spot. Furthermore, Ma et al. (2013) utilized a 4 kW fibre laser for both pre-heating and welding processes. In pre-heating, the laser intensity was diminished by defocusing the laser beam. The welding was conducted after the zinc layer had been removed. The Energy Dispersive Spectroscopy (EDS) was used to measure the zinc coating. Despite obtaining better weld quality using this method, it allows the material to corrode. Thus, it has been proposed that a nickel painting after removing the zinc coating

provides good corrosion resistance without causing the same problem with zinc since nickel has a higher melting temperature ( $T_{melt_{Ni}} = 1728 \text{ K}$ ).

### 3.1.2 Reduction in Zinc Vapour Pressure

This section summarizes the conducted research on the reduction of the zinc vapour pressure accumulated at faying surfaces. The highly pressurized zinc vapour is decreased by introducing active elements (e.g. Cu and Al) on faying surfaces or adopting suction mechanisms.

Dasgupta and Mazumder (2008) suggested inserting an additional copper (*Cu*) layer in joining gap. Hence, it was filled with this additional layer of copper. During welding, zinc-copper alloy was formed that would prevent the violent behaviours of zinc vapour and would reduce the amount of porosity from 10% to 2%. Furthermore, the experimental results indicated that the fatigue life of the welded joint was 25% higher than a standardised spot weld for the same strain energy release rate. Likewise, Li et al. (2007) suggested inserting an aluminium (*Al*) foil. The authors pointed out that 80% improvement in the shear strength was achieved due to the less amount of porosities and deeper penetration. However, the placement of additional metal is the most crucial parameter of the stability of the molten pool. Thus, sufficient clamping force was required to tightly close sheet metals and additional material to produce decent welds.

Chen et al. (2014) employed a novel method to reduce the zinc vapour by using a suction device which was specifically designed to create a negative pressure zone. A high-speed video camera was used to monitor the dynamic behaviour of the plasma plume and the zinc vapour. According to the results, porosities and blow holes were avoided, and the best surface quality was obtained using laser power of  $3.4 \text{ kW}$ , welding speed of  $2.4 \text{ m/min}$  and vacuum suction. However, undercuts were observed on the top and bottom of the weld due to a small portion of liquid metal is also sucked along with zinc vapour.

The limitation of inserting an additional metal is that inter-metallic compounds will be created at the joint interface. These compounds lower the mechanical quality of the joint. Furthermore, inserting additional metal is difficult to implement and automate during the welding process. Similarly, the suction method requires dedicated equipment which increases the complexity of the process.

### 3.1.3 Ventilation of Zinc Vapour

The summarized methods in this section are based on de-gasification of zinc vapour from the welding medium without causing any weld defects either by (i) using pre-drilled “*vent holes*” inside base material for ventilation, (ii) stabilizing the keyhole by employing shielding gas in which zinc vapour escapes through, (iii) using a leading beam to cut ventilation channels along with the main welding beam, and (iv) creating an appropriate joining gap between faying surfaces. The required joining gap can be obtained by inserting calibrated metal shims in faying surfaces or creating surface features such as dimple that work as a spacer between sheet metals.

Chen et al. (2009) studied the “*vent hole*” approach and investigated the optimum distance between holes. In this work, the vent holes are drilled by using a pulsed mode Nd:YAG laser with an average power of 200 W and a pulse duration of 1 ms. The vent holes were aligned with the weld line, and welds were conducted using CW mode CO<sub>2</sub> laser. The material used in this experimental work was 0.7 mm thickness and 7 μm zinc coating. The results indicated that the optimum distance between two vent holes was dependent on the welding speed and it should be 0.14 mm for 9 m/min. However, the additional drilling procedure increases the production cost and cycle time.

Carlson et al. (2011) investigated the effect of shielding conditions on the weld quality. In this research, welding took place under different shielding conditions such as; the mixture of argon and carbon dioxide as well as argon and oxygen. The authors concluded that the shielding gas not only blew away the plasma plume, but also reacted with the zinc vapour and stabilized the molten pool. The experimental results demonstrated that for a given laser power of 3.6 kW, decent welds were achieved at welding speeds up to 30 mm/s with mixtures of 75% Ar and 25% CO<sub>2</sub> as well as 98% Ar and 2% O<sub>2</sub>. The lower processing speed is the main limitation of this method.

Iqbal et al. (2010) offered the utilization of dual the laser beams which involved a leading the laser beam for cutting exhaust slots in which zinc vapour vented out; and followed by the main the laser beam for welding. The exhaust slots were aligned with the welding line. Moreover, a specific offset distance between these two the laser beams was needed in order to not to merge these two the laser beams.

The simple approach can be to create an appropriate joining gap between faying surfaces in which the zinc vapour mitigated from the welding medium. Akhter (1990) developed a model to calculate the joining gap size for CO<sub>2</sub> lasers. The model was derived from the volume rate balance of generated zinc vapour and escaping through the joining gap. The minimum joining gap size ( $g_{min}$ ) is calculated in

Eq. (3.1).

$$g_{min} = K \times W_S \times t_{Zn} \times t_p^{-1/2} \quad (3.1)$$

where  $t_p$  is the thickness of the sheet,  $v$  is the welding speed,  $t_{Zn}$  is the thickness of zinc coating; and,  $K$  is a material constant depending on laser power which is  $18.25 \text{ sm}^{-1/2}$  for  $CO_2$  lasers. On the other hand, the maximum joining gap size should be 35% of the thickness of the sheet for decent weld.

Graham et al. (1994) conducted experimental research on the weldability of galvanized sheet metals by using 2 kW of Nd:YAG laser in a lap joint configuration. The authors investigated the effect of the joining gap size on the weld quality. In order to create the pre-set joining gap size, calibrated metallic shims were inserted between faying surfaces. The authors concluded that high-quality weld could be achieved at welding speed up to 2.7 m/min by using joining gap size in between 0.10 to 0.20 mm. In order to easily remove the zinc vapour from the medium, the gap to be formed must be close enough to the welding area. However, it is very difficult to adjust the position of shims since they are only contact with the workpiece not bounded and they easily dislocate during the welding process.

The required gap can be obtained by surface features such as dimples generated by the stamping process. It is evident that the stamping process requires additional equipment than the welding process. Moreover, it is difficult to create such a small dimple, whose height is around  $0.15 \sim 0.20 \text{ mm}$ , because the workpiece might be damaged during the process. Dimples are also created by the rapid movement of the laser beam on the surface of the material in a short distance. In addition, there is no need for any additional equipment and the same laser source as well as the fixture that is designed for the welding process can be utilized. This process is called the “*laser dimpling process*”. It is a promising solution to generate dimples near the welding area. These dimples work as a spacer between the faying surfaces to obtain the required joining gap. During the welding, the zinc vapour ventilated through this obtained joining gap. Each dimple is individually manufactured, and its shape, height, and position are determined locally by changing the process parameters which gives flexibility in production. However, little data is available in literature about the laser dimpling process.

An experimental study conducted by Gu (2010) in which dimples are generated on the bottom surface of the zinc coated sheet metal of 0.76 mm thickness. During experimental studies, the laser beam focus position was varied between  $\mp 3 \text{ mm}$  above the top surface of the specimen, whilst both laser power and travel speed were kept constant. Furthermore, Gu and Shulkin (2011) also developed dimples on

the top surface of the same material at varying scanning speed and incidence angle, while other parameters such as focal offset were kept constant. In these studies, the laser power was kept constant at 4 kW. The results indicated that dimple height monotonically decreased with increasing both scanning speed and incidence angle; whereas, the dimple height firstly, increased and then decreased whilst increasing the focal offset.

In a more recent study conducted by Colombo and Previtali (2014) applied univariate linear regression model to determine the influence of scanning speed on the dimple height keeping constant laser power, focal offset, and laser track. They found that linear energy, which is the amount of energy supplied per unit time, was the primary factor affecting the dimple height. Furthermore, it was stated that obtained dimples have a negative – positive profile due to conservation of volume flow around keyhole. However, this study has limitation as authors considered only the influence of a single process parameter without exploring other important process parameters and their interactions.

The existing literature has focussed mainly on a single-input-single-output (SISO) scenario which is necessary but not sufficient to give a complete characterisation of the dimpling process. The dimple quality is evaluated by one KPI, which is dimple height. Thus, it is important to take into consideration a multi-input-multi-output (MIMO) based scenario and to include the following multi-inputs: scanning speed ( $S_S$ ), focal offset ( $F_O$ ), incidence angle ( $\alpha$ ), and laser track ( $L_T$ ). The following three KPIs are addressed as multi-outputs: dimple height ( $D_H$ ), dimple upper surface area ( $D_U$ ), and dimple lower surface area ( $D_L$ ). Another limitation associated with the current literature is the lack of modelling variation in the dimpling process. The current models are developed under the assumption of ideal process performance neglecting process variation. Due to lack of understanding process variation, the measurement of a KPI (e.g. dimple height) for given process parameters might violate the given allowance limits and it will lead to the inaccurate selection of process parameters. However, no comprehensive research work has been reported in the laser dimpling process that considers MIMO-based scenario with process variation. Table 3.1 summarizes related research addressing the laser dimpling process and highlights the contributions of the proposed modelling approach.

**Table 3.1:** Related work on the selection of optimum laser dimpling process parameters

	Process Characterization	Process Synthesis
SISO	Gu (2010) Gu and Shulkin (2011) Colombo and Previtali (2014)	Proposed in this thesis (See <b>Chapter 4</b> )
MIMO	-	

### 3.2 Related Work on the Process Monitoring

A critical requirement for any manufacturing process to produce products within defined specification limits. The term weld quality assurance generally refers to use of technological methods and actions to guarantee quality by *(i)* gathering process information, *(ii)* understanding of the occurring physical phenomena based on the gathered information, and *(iii)* creating quality control methods to reduce weld defects.

The process information is obtained by off-line inspection and in-process monitoring. Traditional off-line inspection builds a relationship between process parameters/conditions to the weld quality through statistical methods, such as Response Surface Methodology (RSM). To build such relationships, a large quantity of data should be required which can be gathered by conducting destructive and non-destructive experiments (Moradi and Ghoreishi, 2011; Gao et al., 2016; Zhang et al., 2015) or running comprehensive numerical simulation of laser welding (Geiger et al., 2009; Otto et al., 2011; Courtois et al., 2016; Pang et al., 2016). Furthermore, off-line monitoring is expensive (i.e. time and material consuming), reduces productivity, and the lack of effective implementation with automation. In comparison with experimental studies, a numerical simulation can give detailed information about the weld quality concerning the weld profile (i.e. fusion zone dimensions) and their relationships with the welding process parameters. However, creating such a computer simulation is not possible, unless the process parameters and their effects on the weld quality are fully understood.

To reduce manual expensive off-line inspection, in-process monitoring of laser welding has been studied in recent years. In-process monitoring requires sensors which convert the process emissions (e.g. optical emissions, acoustic emissions, electric and magnetic fields) into electrical signals. A signal conditioner which converts the electrical signals to measurable variables. These variables are related to the

weld quality. It is common practice defined by the industrial standards that the weld profile is measured by FZDs.

The most commonly used sensors for capturing different process emissions are given in Table 3.2. According to the monitoring target, in-process monitoring methods are divided into two categories as a single-sensor, single-target monitoring, and a multi-sensor, multi-target monitoring. Generally, a single sensor is not sufficient to describe the complete welding process so that multi-sensors are utilized to gain more comprehensive information.

**Table 3.2:** Process signals and detectors used in process monitoring for the laser welding

		Sensor						
		CMOS/CCD camera	IR camera	Thermocouple	Pyrometer	Photodiode	Spectrometer	Microphone
Process Emission	Molten pool image	✓	✓					
	Plasma plume image	✓	✓					
	Workpiece temperature		✓	✓	✓			
	Photo-emissions					✓	✓	
	Back scattered beam					✓	✓	
	Airborne acoustics							✓

High-speed cameras (e.g. Complementary metal oxide semiconductor (CMOS) and charge coupled device (CCD)) are widely employed to study the evolution of a very fast process. In the laser welding process, the weld takes place in a few milliseconds (*ms*) and this kind of device becomes basically mandatory if the objective is to understand the behaviour of the process. Three kinds of high-speed cameras can be found in the literature, namely: *(i)* visible detection (350 - 750 *nm*), *(ii)* infra-red (IR) detection (thermal camera (740 - 1170 *nm*)), and *(iii)* auxiliary light source detection (high-frequency stroboscopic light and waveband within 800 - 990 *nm*). Abt et al. (2011) developed a closed loop control system of obtaining full penetration by controlling laser power and welding speed. The methodology was based on the analysing blind and open keyholes by controlling dark and bright areas in captured images. If the keyhole is blind the laser light is back reflected from the keyhole walls resulting in a bright area in the captured image so that it is



possible to distinguish between the blind keyhole and the open keyhole (i.e. partial and full penetration), but it is difficult to directly measure the actual penetration. Similarly, Luo and Shin (2015) proposed an edge detection algorithm to monitor the molten pool shape to obtain the top width and the molten pool length. The authors used a co-axial CMOS camera and off-axial green illumination. According to the authors, the molten pool dimensions are sensitive to the process parameters in the blind keyhole mode; whereas, they are almost insensitive to power variation in the open keyhole. Images obtained from the high-speed camera contain information on the two-dimensional spatial distribution, but they have a low temporal resolution.

Recent investigations have focussed on IR thermography to provide information on the temperature profile and history of the molten pool and the surrounding metal. Thermal images are recorded on-line and temperature profile and history are computed by using image processing methods. Weld external KPIs (quality indicators), such as spatters, weld bead, molten pool dimensions, and cooling rates can be identified (Chen and Gao, 2014; Speka et al., 2008). It is monitored cooling rates using an infrared camera to detect weld defects during arc welding of steel. Specific weld defects, such as variations in the joint gap, arc misalignment, and impurities were found. The resulting surface isotherms were recorded to measure the weld bead width in real time. Results showed that torch offset and bead width perturbations could be separated and monitored simultaneously. However, the main drawbacks of IR thermography are the low sampling frequency, the high price and the limited field of view.

To detect and acquire signals from the welding process different technical solutions can be adopted, using different types of sensors. The extensively used sensor in the laser welding process is photodiodes because of their low cost and high sampling frequency. The use of different combinations of optical filters have shown that three types of optical radiation are of interest in laser welding which are listed as: *(i)* ultraviolet and visible light emission generated from the plume (P-Sensor), *(ii)* laser light emission from the beam reflection (R-Sensor), and *(iii)* thermal radiation coming from the molten pool surface (T-Sensor). The optical radiations are converted into electrical signals and analysed using signal processing techniques. Apart from the signal analysis of particular spectral bands, analysis of the full spectral waveband during the welding process can also be carried out by using a spectrometer.

Olsson et al. (2011) demonstrated that UV signal could be a good quality indicator in  $CO_2$  laser welding since the plume on the weld pool absorbed the great amount of laser radiation and was heated to an ionized state. However, the plume

in Nd:YAG lasers was transparent to the laser and did not get heated to a plasma state. It radiated as a black body radiator over a continuous spectrum. Eriksson et al. (2010) have pointed out that, since the infrared radiation coming from the pool is picked up by the T-sensor, to study this signal thinking of getting information from the pool is misleading. Better results were achieved if the analysed signal is the difference between the T-sensor and the P-sensor.

An important aspect has been the study of the weld pool and keyhole frequency oscillation. Schmidt et al. (2008) have found, in their process conditions, that the weld pool oscillations occurred within 300-500  $Hz$ , the keyhole ones within 2000-2500  $Hz$ . Baik et al. (2000) employed photodiodes in a control system that was able to detect separately power changes and focal shifts of the beam. The study took advantage of chromatic filtering; the radiation from the melt pool was measured at two or more wavelengths and analysed using chromatic aberration of the optics.

Photodiode based in-process monitoring systems have been commercialized for several years (e.g. Laser Welding Monitor from Precitec, Welding Monitor PD 2000 from Prometec, Weldwatcher from 4D Porosearch) (Bardin et al., 2005). In photodiode based in-process monitoring, a reference signal with lower and upper allowance limits have been pre-defined for a decent weld for each P, R and T sensors. If the welding process is in control without any defects, the gathered signals will fall between the allowance limits. If a weld defect occurs, there is a sudden change in the gathered signal; and hence, the allowance limits are violated. Any observations outside the allowance limits suggest that weld defects have occurred. The limitations of sensor/data-driven process monitoring are the indirect measurement of FZDs, the limited field of view since process emissions gathered mainly from the keyhole, and unable to distinguish between many possible defects such as porosities, lack of penetration, *etc.*

Laser welding is a highly automated process that is being used more and more in the automotive industry. The advantages of laser welding include high speed, deep penetration, high aspect ratio, and low thermal distortion. To further improve the efficiency of the laser welding systems, quality assurance measures are required. Traditional off-line inspection of welds is expensive, reduces productivity, and requires dedicated test equipment. Therefore, the development of an automated on-line monitoring method for laser welding defect detection and closed-loop control systems have been an open field of research in the last years. Several solutions have been proposed to estimate the weld profile.

The weld profile is important because the weld should have a desired weld

profile for achieving the maximum strength. The weld profile is determined by the fusion zone dimensions (FZDs) and their allowance limits are defined in the industrial standards (EN ISO 13919-1, 1997; EN ISO 13919-2, 2001). It must be pointed out that the FZDs are difficult to measure directly during the welding process unless production is stopped which is nearly infeasible as it is economically unjustified; whereas, it is monitored by process signals (e.g. autistic, optical, thermal) and relating these signals to relevant FZDs. The limitation of the current in-process monitoring methods is an indirect measurement of the FZDs. To overcome this limitation, a low coherence interferometer has been recently implemented to direct measurement of the keyhole depth (penetration is slightly longer than the keyhole depth), but most of the implementation is in the laboratory environment (Authier et al., 2016; Kogel-Hollacher et al., 2017). Therefore, a fast and accurate physics-based model is proposed in this study which is suitable for in-process monitoring of multi FZDs (i.e penetration, top and interface widths). The proposed model combines computer numeric simulation with process information. Therefore, the occurring physics in the laser welding process are considered. The equations and assumptions needed for the numerical simulation of the occurring physics in the laser welding process are reviewed in Section 3.3. Table 3.3 summaries the direct in-process monitoring of FZDs.

**Table 3.3:** In-process monitoring of KPIs highlighting the proposed monitoring approach

KPI	Monitoring Method		
	Current		Proposed
Penetration	Direct: Interferometer	Only	Multi KPIs with capability to process adjustment
Top Width	Direct: High Speed Camera	single	
Interface Width	Direct: N/A	KPI	

### 3.3 Related Work on Numerical Simulation Modelling of Laser Welding

Experiment-based statistical models in laser welding have received noticeable attention during the last 20 years (Moradi and Ghoreishi, 2011; Gao et al., 2016; Zhang et al., 2015). These models gather data from conducting destructive and non-destructive physical experiments, then statistical methods such as Response Surface Methodology (RSM), Artificial Neural Network (ANN), Taguchi approach have been widely used to find out optimum process parameters in order to achieve high weld quality.

Simulation-based numerical models (Geiger et al., 2009; Otto et al., 2011; Courtois et al., 2016) give detailed knowledge concerning the formation of the keyhole, fluid flow around the keyhole, the interaction of laser beam with the plasma plume. Such complex models enabled researchers to study welding process in detail. Owing to the growth in computer performance, welding processes have been simulated by numerical models, especially Finite Element Methods (FEM) to: (i) design manufacturing production sequences, (ii) find out optimum process parameters (Rai et al., 2007; Saldi et al., 2013), and (iii) calculate the mechanical quality of weld in terms of strength, residual stress and thermal distortion (Tsirkas et al., 2003; Salonitis et al., 2010; Pang et al., 2016). Nonetheless, the numerical modelling of laser welding is not easy, since the laser welding process is a multi-phase and multi-physics process involving the interaction of heat transfer, fluid flow, and mass transport.

This section represents reviews on the occurring physical phenomenon in the laser welding process that determine the final weld shape as follows: (i) The heat transfer to the surrounding area welding area, (ii) the fluid flow in the molten pool, and (iii) the keyhole surface generation.

### 3.3.1 Heat Transfer

In order to evaluate the temperature distribution on the material, the heat transfer is computed by solving the conservation of energy equation whose general closed form is given in Eq. (3.2).

$$\rho c_p^{eq} \left[ \frac{\partial T}{\partial t} + \mathbf{u} \cdot \nabla T \right] = \nabla \cdot (\lambda \nabla T) + Q_{vol} \quad (3.2)$$

where  $T$  is temperature,  $\rho$  is density,  $\lambda$  is the thermal conductivity,  $\mathbf{u}$  is the fluid velocity vector; and,  $c_p^{eq}$  is effective specific heat capacity considering phase change. It is given in Eq. (3.3) (Bachmann et al., 2014; Courtois et al., 2016).

$$C_p^{eq}(T) = C_{p_{solid}} + L_f \frac{\exp\left(-\left(\frac{T-T_m}{\Delta T}\right)^2\right)}{\sqrt{\pi \Delta T^2}} \quad (3.3)$$

where  $L_f$  is latent heat of fusion,  $T_m$  is melting temperature; and,  $\Delta T$  is the difference between solidus and liquidus temperature of the material. The phase change can be also represented in the energy equation in terms of enthalpy ( $H$ ) (He et al., 2003; Shaibu et al., 2015). The main difference is the consideration of latent heat of fusion which is implicit with enthalpy.

It should be noted that the source term  $Q_{vol}$  on the right-hand-side of Eq. (3.2) refers to the volumetric heat source. Furthermore, the heat influx from

the laser and the heat outflux on the surface are not incorporated in the energy equation, instead, they are given as boundary conditions.

### 3.3.1.1 Heat influx on the surface

The heat flux into the material is determined by the laser. The geometry of an ideal laser beam is defined in Eq. (2.7) and its intensity distribution is assumed to be Gaussian distribution which is given in Eq. (3.4).

$$I(x, y, z) = S_{abs} \frac{\chi \cdot P_L}{\pi w(z)} \exp\left(-\chi \left(\frac{x^2 + y^2}{w(z)}\right)\right) \quad (3.4)$$

where  $S_{abs}$  is the material absorption coefficient which depends on the wavelength of the laser,  $P_L$  is laser power,  $w(z)$  is the laser beam waist radius in the propagation direction of the laser beam,  $\chi$  is the laser beam distribution coefficient; and,  $x, y, z$  are the Cartesian coordinates attached to the laser beam. The peak intensity is obtained in the centre and it is constant depending on the laser power and the laser beam waist radius.

### 3.3.1.2 Heat outflux on the surface

The total heat flux out of the material is composed of three different mechanisms: energy radiation, free convection and evaporation flux due to the evaporation of material. The energy radiation ( $Q_{rad}$ ) is given by the Stefan-Boltzmann law.

$$Q_{rad} = \epsilon \sigma (T_{surface}^4 - T^4) \quad (3.5)$$

where  $\sigma$  is the Stefan-Boltzmann constant and  $\epsilon$  is the emissivity of the material. The convective heat loss ( $Q_{con}$ ) is calculated as:

$$Q_{con} = h_c (T_{surface} - T) \quad (3.6)$$

where  $h_c$  is the convection heat transfer coefficient expressing the heat exchange between the material surface and the environment. Frewin and Scott (1999) developed an empirical relation between temperature and heat transfer coefficient to combine the effects of radiative and convective heat flux. It is given in Eq. (3.7).

$$h_c = 2.4 \times 10^{-3} \epsilon T^{1.61} \quad (3.7)$$

The heat outflux associated with the evaporation of material is expressed as:

$$Q_{evap} = \dot{m}_{evap} L_v \quad (3.8)$$

where  $\dot{m}_{evap}$  denotes the evaporation mass flux and  $L_v$  is the heat of evaporation.  $\dot{m}_{evap}$  is approximated using Eq. (3.9) defined by Winkler et al. (1997) as:

$$\dot{m}_{evap} = A_1 + \log(p_{atm}) - 0.5\log(T) \quad (3.9)$$

where  $A_1$  is the material-dependent constant parameter and taken as 2.52 for hot-rolled steel plates.

### 3.3.1.3 Volumetric heat source

As aforementioned, occurring multi-physics phenomenon are highly coupled resulting in longer calculation times. Therefore, the simple approach is to bring some phenomenon together and others are decoupled. The Eq. (3.2) can be used as its own to simulate the conduction mode laser welding, where the heat is transferred uniformly from the surface. However, in the keyhole mode welding, the volumetric heat source term ( $Q_{vol}$ ) is required to define according to the characteristic dimensions of keyhole to obtain the same weld shape as in the experiments. Indeed, the fluid flow and surface deformation are neglected in this type of modelling approach.

Goldak et al. (1984), who was one of the pioneers of the volumetric heat source modelling approach, established a source term, known as “*double ellipsoidal model*”, based on the real molten pool dimensions to investigate the temperature field. Although this model has been successfully applied to arc welding, it is less appropriate for laser welding applications since keyhole cannot be accurately simulated. In this model, a Gaussian distribution is spread across a three-dimensional double ellipsoidal shape and it is written as:

$$Q_{vol_f}(x, y, z) = \frac{6\sqrt{3}f_f\eta P_L}{a_fbc\pi\sqrt{\pi}} \exp\left(-3\frac{x^2}{a_f^2} + \frac{y^2}{b^2} + \frac{z^2}{c^2}\right) \quad (3.10)$$

$$Q_{vol_r}(x, y, z) = \frac{6\sqrt{3}f_r\eta P_L}{a_rbc\pi\sqrt{\pi}} \exp\left(-3\frac{x^2}{a_r^2} + \frac{y^2}{b^2} + \frac{z^2}{c^2}\right) \quad (3.11)$$

where  $a_f$  and  $a_r$  are the front and the rear semi-axes of the heat source; as well as  $f_f$  and  $f_r$  are the front and the rear fraction of the deposited heat, respectively.

Wu et al. (2006) proposed another volumetric heat source term, known as the “*conical Gaussian model*”, which can be applicable to the keyhole mode laser welding. According to the model, the keyhole is linearly decreased along the z-axis and the laser intensity distribution at any plane perpendicular to this axis is Gaussian distribution. The conical Gaussian model is described in polar coordinated as:

$$r(z) = r_e - (r_e - r_i) \times (z_e - z)/(z_e - z_i) \quad (3.12)$$

$$Q_{vol}(r, z) = Q_0 \exp\left(-3\frac{r^2}{r^2(z)}\right) \quad (3.13)$$

where  $Q_0$  is the peak laser intensity,  $r(z)$  is the effective radius of keyhole; and,  $r_e$  and  $r_i$  are radii of the keyhole at the top and bottom of the workpiece, respectively.

Wu et al. (2009) established a more realistic volumetric heat source model, known as the “*rotary Gaussian model*”. In essence, it is similar to the previous model proposed by the same authors. However, in this model, the attenuation of the laser intensity inside the keyhole is modelled as a logarithmic function along the thickness. The rotary Gaussian heat source model is defined in Cartesian coordinates as:

$$Q_v(x, y, z) = \frac{9S_{abs}P_L}{\pi w_0^2 H} \exp\left(\frac{9}{\log(z/H)}\left(\frac{x^2}{w_0^2} + \frac{y^2}{w_0^2}\right)\right) \quad (3.14)$$

where  $P_L$  is the laser power,  $S_{abs}$  is the surface absorption coefficient,  $w_0$  is the on-surface spot radius of the laser beam,  $x$  is the axis in the welding direction,  $y$  is the axis in perpendicular to the welding direction; and,  $z$  is the axis in the laser beam propagation direction.  $H$  is defined as the depth of the keyhole. Ma et al. (2012) applied the rotary Gaussian model to predict the temperature profile and the vaporized zinc area in laser welding of zinc coated steels in a zero-gap lap joint configuration. It was found that the vaporized zinc area was increased with increasing laser power and decreasing welding speed.

### 3.3.2 Fluid Flow

In order to evaluate the velocity field on the material, the fluid flow is computed by solving the conservation of momentum whose general closed form is given in Eq. (3.15). The liquid region in the molten pool is assumed as Newtonian, laminar flow and constant thermodynamic and transport properties.

$$\rho \left[ \frac{\partial \mathbf{u}}{\partial t} + (\mathbf{u} \cdot \nabla) \mathbf{u} \right] = \nabla \cdot [-p\mathbf{I} + \mu (\nabla \mathbf{u} + (\nabla \mathbf{u})^T)] + \rho \mathbf{g} + \vec{F}_{Buoyancy} + \vec{F}_{Darcy} \quad (3.15)$$

where  $\mathbf{u}$  is fluid velocity vector and coupled with thermal field,  $p$  is pressure,  $\mathbf{I}$  is the identity matrix; and,  $\mu$  is the viscosity of the liquid.

The first source term in the right-hand side of Eq. (3.15) is Boussinesq’s approximation to account for the lifting force due to thermal expansion. It is defined

as:

$$\vec{F}_{Buoyancy} = \rho\beta_l\mathbf{g}(T - T_{melt}) \quad (3.16)$$

where  $\beta_l$  is the coefficient of thermal expansion,  $\mathbf{g}$  is the gravitational acceleration, and  $T_{melt}$  is the melting temperature of the material. The second source term is the drag force associated with the frictional dissipation to cancel the fluid flow inside the solid region where the temperature is lower than the melting temperature. It is derived from the Carman-Kozeny equation, and it is given as:

$$\vec{F}_{Darcy} = K_d \frac{(1 - f_l)^2}{f_l^3 + \varepsilon} \mathbf{u} \quad (3.17)$$

where  $K_d$  is the volume force damping constant,  $f_l$  is the volume fraction of liquid; and,  $\varepsilon$  represents arbitrary constants to avoid division by zero. The velocity boundary conditions are defined in Eq. (3.18) to solve Eq. (3.15).

$$\begin{aligned} \mu \frac{\partial u}{\partial z} &= -f_l \frac{\partial \gamma_t}{\partial T} \frac{\partial T}{\partial x} \\ \mu \frac{\partial v}{\partial z} &= -f_l \frac{\partial \gamma_t}{\partial T} \frac{\partial T}{\partial y} \\ \mu \frac{\partial w}{\partial z} &= -f_l \frac{\partial \gamma_t}{\partial T} \frac{\partial T}{\partial z} \end{aligned} \quad (3.18)$$

where  $u$ ,  $v$ , and  $w$  are the fluid velocity components along the  $x$ ,  $y$ , and  $z$  directions, respectively. The  $w$  velocity is equal to zero since there is no outward flow at the pool top surface. As shown in this equation  $\frac{\partial \gamma_t}{\partial T}$  is the temperature coefficient of surface tension known as the Marangoni effect. Cho et al. (2012) proposed that the Marangoni effect could be neglected and the fluid flow was mainly driven by the buoyancy force if the Grashof number was high.

### 3.3.3 Keyhole Surface Generation

In order to take into account the mass flux, the conservation of mass is computed in Eq. (3.19).

$$\frac{\partial \rho}{\partial t} + \nabla \cdot (\rho \mathbf{u}) = \dot{m}_{evap} \quad (3.19)$$

In general, the fluid flow in the laser welding is assumed as incompressible Newtonian and terms associated with  $\rho$  is omitted. Furthermore, the source term in the right-hand side of the Eq. (3.19) is set zero if the solid/liquid boundary is considered. However, evaporation mass flux is introduced as a source term while



considering the liquid/gas interface (i.e. keyhole boundary) (Zhou et al., 2006; Dasgupta et al., 2007).

During the phase change, the evaporation mass flux produces vaporization pressure, known as recoil pressure which is the driving force of keyhole generation. The recoil pressure ( $p_{rec}$ ) keeps the keyhole open whereas surface tension and other forces try to close it. Thus, the keyhole vibrates during the welding at around 2 - 4  $kHz$  depending on the process parameters (Kaplan, 2012). A pressure balance can be written to obtain keyhole surface as:

$$p = p_{rec} + p_g - p_{amb} + p_{surf} \quad (3.20)$$

where  $p_{amb}$  the atmospheric pressure far from the keyhole,  $p_g$  the partial pressure of surrounding gas, and  $p_{surf}$  is surface tension pressure. The formulation of the recoil pressure  $p_{rec}$  is based on the Clausius-Clapeyron equation defined as:

$$p_{rec} = p_0 \exp \left[ \frac{\Delta H_v}{R} \left( \frac{1}{T_{evap}} - \frac{1}{T} \right) \right] \quad (3.21)$$

where  $p_0$  is the surrounding gas pressure,  $\Delta H_v$  is enthalpy of vaporization,  $R$  is the gas constant; and,  $T_{evap}$  is the evaporation temperature. On the other hand, surface tension pressure  $p_{surf}$  is expressed as:

$$p_{surf} = \kappa \cdot \gamma_t \quad (3.22)$$

The surface tension ( $\gamma_t$ ) typically changes due to variations in temperature along the keyhole. A small increment of surface tension is defined as:

$$\gamma_t = 1.2 - 4.3 \times 10^{-4}(T - 1720) \quad (3.23)$$

where  $T$  refers to a temperature in the Kelvin scale.

The numeric simulation of the laser welding process involves the interaction of the aforementioned physical phenomenon. Furthermore, the welding process has the transient characteristic where the heat source (i.e. the laser beam) moves with a constant welding speed. Thus, a very dense mesh is obtained near the on-surface spot of the laser beam and elsewhere coarse mesh can be employed for the numeric simulation. Table 3.4 presents occurring multi-physics phenomenon and their interactions.

**Table 3.4:** Interactions of occurring physical phenomenon in laser welding

		Physical phenomenon		
		Keyhole Surface Generation	Heat Transfer	Fluid Flow
Physical phenomenon	Keyhole Surface Generation	Conservation of Mass	Recoil Pressure	Surface Tension Marangoni
	Heat Transfer	-	Conservation of Energy	Buoyancy Force Darcy Force
	Fluid Flow	-	-	Conservation of Momentum

A deeper understanding of laser welding allows improving weld quality, process control and process efficiency. Many realistic welding models have been developed considering the aforementioned physical phenomenon, but the challenge is the long computational time.

Some of the earlier models consider mainly the heat transfer phenomena and they compute the temperature distribution by applying volumetric heat source modelling. In this approach, the keyhole is modelled as a 3D geometric shape with certain arbitrary values. These values are parametrized to get an actual representation of the keyhole. For example, Tsirkas et al. (2003) employed a 3D conical Gaussian volumetric heat source model to obtain temperature distribution in the laser welding of AISI304 stainless steel. In the model, temperature-dependent thermal properties were used, and thermo-mechanical analysis was performed. In this study, the computational domain of 150 x 300 x 4 mm is mesh with uniform grid and the computational time took about 2 h using Intel X5355 2.66 GHz single-core CPU Linux machine.

In later models, the multi-physical coupling between heat transfer and fluid flow has been widely used. The laser energy deposited on the workpiece is given as a heat influx on the surface and formation of keyhole (liquid/gas interface) is tracked with either volume-of-fluid (VoF) or level-set (LS) methods. The molten pool (solid/liquid interface) is the outcome of these multi-physics models. For example, Zhou et al. (2006) modelled pulsed mode Nd:YAG laser welding for stainless steel in 2D. The keyhole boundary was tracked with the volume-of-fluid (VoF) method. A non-uniform grid system with 202 x 252 points is used for the total computational domain of 5.0 mm x 6.25 mm. According to the authors, the calculation time took 7 h of CPU time to simulate 100 ms of welding. Calculations were executed on the DELL OPTIPLEX GX270 workstations with LINUX-REDHAT 9.0 OS.

Geiger et al. (2009) simulated transient behaviour of CW mode Nd:YAG laser welding of stainless steel. In this model, the enthalpy form of the heat transfer equation was employed and energy loss due to conductive, radiative and evaporative flux was assumed. The computational domain consisted of 216,000 tetrahedral elements and the calculation time took 8 h for 40 ms of welding process. The simulation run in a personal computer whose configuration was Intel Core2 CPU 6700 at 2.66 GHz, 3.86 GB RAM.

Laser welding models are becoming very sophisticated using a free liquid/gas interface method. Nevertheless, the recent trend in modelling of laser welding involves calculation of the flow inside the vapour region. Thus, the heat dissipation in the solid part, the fluid flow in the molten pool, and the plume dynamics inside keyhole can be examined. For instance, Bailey et al. (2015) conducted experimental study and numerical simulation on laser welding of magnesium alloy AZ31. The mass transport phenomena between the liquid and the vapour phases modelled with diluted transfer species. The liquid/gas interface is tracked with the level-set (LS) method. It was reported that the computational time was roughly 80 h on a 24-core cluster.

Another multi-physics study conducted by Courtois et al. (2016) by coupling heat and fluid equations. In this case, the specific heat ( $c_p$ ) was temperature dependent and a jump condition was denoted between the solidus and the liquidus temperatures of the material. The model had 30,000 quadratic triangular elements and 20,000 linear triangular elements and the solution time took almost 16 h to describe 10 ms of welding. Similarly, Pang et al. (2016) developed a 3D transient numerical model to study the temperature field, molten pool shape and the dynamic behaviour of plume. The computational domain  $3 \times 1.5 \times 3$  mm meshed with a maximum element size of  $2.5 \times 10^{-5}$  mm and it took almost 14 h for 10 ms welding

time. Furthermore, the author pointed out that an increase in welding speed results increase in the inclination of the front edge of the keyhole.

The whole physical phenomenon occurring during the laser welding process are highly coupled and it is difficult to handle. Thus, an alternative way is to decouple the occurring phenomenon and solve them in sequential order. In this case, numeric simulation models will use the experimental data to adjust process parameters in the simulation model. Rai et al. (2007) employed an analytical method to calculate the keyhole shape based on energy balance at the keyhole (Kaplan, 1994). The conservation of energy, and momentum equations were then solved in three dimensions assuming that the boiling temperature was constant at the keyhole. The solution domain was meshed with uniform grid (1.09 million grid points) and the computational time was about 20 *min*. The simulation was stopped after 1500 iterations and the conservation of momentum was solved only in the molten pool region. A desktop computer with 3.2 *GHz* Pentium 4 processor and 1 *GB* RAM was used for the execution of the computer program.

Another decoupled analysis was performed by Bachmann et al. (2014) to investigate the effect of electromagnetic fields on the molten pool shape. For this purpose, the author used a pre-defined keyhole shape. It was concluded that the hydrodynamic pressure inside the molten pool was compensated by the generated magnetic field. By increasing magnetic force, a smooth molten pool shape is obtained.

Similarly, Fetzer et al. (2017) suggested a model based on an experimentally calibrated keyhole geometry in the solution domain. Only the conservation of energy equation was solved using FEM to predict only penetration in lap welding. According to the results of the authors, there was a good correlation between simulated and measured penetration values, but it was highlighted that the most significant deviation up to 55% between simulated and measured values occurred at low welding speed and high laser power. The simulation was performed with an Intel Core i5-4570 CPU and 8 *Gb* of RAM, and the computational time took 8 *min*.

These publications are concerned with numeric simulation of laser welding using mainly heat transfer and fluid flow to predict the final shape of the weld. The aim is to understand the relation between process parameters and the occurring physical phenomenon. A summary of these modelling approaches with their main properties are given in Table 3.5.

**Table 3.5:** Computational time for different modelling approaches and their main properties

Author	Domain of study	Heat source	Phase change	Keyhole free surface generation	Moving heat source	Fluid flow	Plume dynamics	Computational time
Tsirkas et al. (2003)	3D	Volumetric heat source	Effective heat capacity	-	Yes	No	No	2 h
Zhou et al. (2006)	2D	Heat influx	Enthalpy	LS	No	Yes	No	7 h
Geiger et al. (2009)	3D	Heat influx	Enthalpy	VoF	Yes	Yes	No	8 h 40 ms
Bailey et al. (2015)	3D	Heat influx	Enthalpy	LS	Yes	Yes	Yes	80 h
Courtois et al. (2016)	3D	Heat influx	Effective heat capacity	LS	Yes	Yes	Yes	16 h
Pang et al. (2016)	3D	Heat influx	Effective heat capacity	LS	Yes	Yes	Yes	14 h
Rai et al. (2007)	2D	Constant temperature	Enthalpy	Analytical keyhole	No	Yes	No	20 min
Bachmann et al. (2014)	3D	Constant temperature	Effective heat capacity	Analytical keyhole	No	Yes	No	
Fetzer et al. (2017)	2D	Constant temperature	Effective heat capacity	Analytical keyhole	No	No	No	8 min

The most studied process parameters can be listed as *(i)* laser power, *(ii)* welding speed, and *(iii)* focal offset. However, the effect of the laser beam incidence angle and the joining gap have not been intensively investigated. Since, the presence of a gap between the sheet metals influences the thermal deformation and weld quality as well as the incidence angle determines the accessibility of the laser beam to the welding area. It is important because the laser beam is usually not perpendicular to the material surface for practical application. The main aim is to develop a fast model to estimate internal FZDs and the model has a capability to utilize as an in-process monitoring method. Table 3.6 groups the listed publications in terms of joining gap and incidence angle, and highlights the contributions of the proposed modelling approach.

**Table 3.6:** The multi-physics and decoupled multi-physics modelling approaches

		Not Considering Joining Gap	Considering Joining Gap
Multi-physics modelling	Not Considering Incidence Angle	Tsirkas et al. (2003) Geiger et al. (2009) Pang et al. (2016)	Zhou et al. (2006) Bailey et al. (2015)
	Considering Incidence Angle	Courtois et al. (2016)	-
Decoupled multi-physics modelling	Not Considering Incidence Angle	Rai et al. (2007) Bachmann et al. (2014) Fetzer et al. (2017)	Proposed in this thesis (See <b>Chapter 5</b> )
	Considering Incidence Angle	-	

### 3.4 Summary

In Section 3.1, a comprehensive summary of zinc vapour mitigation methods in literature is presented. Despite several approaches, currently, the best solution for welding of galvanized steels is in an overlap configuration with a joining gap between faying surfaces. However, it is challenging since a small gap results in explosive zinc ejections; whereas, a very large gap causes inability to weld pieces. Although the joining gap is one of the process parameters, it cannot be controlled during the welding process. However, the joining gap can be controlled in a downstream process. Nonetheless, the selection of optimum process parameters to achieve the target joining gap in the process variation is not highlighted in the existing literature.

Section 3.2 focuses on quality monitoring and inspection methods in laser

welding. In-process monitoring refers to the acquisition of signal during the process through sensors; and then, correlating detected signal to defined KPIs, especially FZDs. Process control refers to regulating the process parameters with knowledge gain by the process monitoring to assure weld quality by avoiding defects. The state-of-art in-process monitoring methods are mostly data-driven, implying that predictive models are trained on gathered data using secondary information and cannot be fully exploited outside of the training data set. Furthermore, the signals are only an indirect measurement of FZDs. The drawback is the indirect measurement because FZDs (for example: penetration and interface width in the overlap joint) are inside the weld seam and cannot be directly measurable during the welding process.

Section 3.3 reviews the driving physical phenomenon involved in laser welding. Most numerical laser welding processes consider heat transfer, fluid flow and keyhole surface generation as the driving physical phenomenon. Complex models have a realistic emulation of the welding process, but their computational times are very costly so they cannot be directly used for the determining fusion zone during the welding.

## Chapter 4

# Laser Dimpling Process Parameters Optimization Using Surrogate-Driven Process Capability Space<sup>1</sup>

Remote Laser Welding (RLW) is a fusion-welding process in which the heat for welding is delivered by a focussed laser beam. Due to high power intensity and low heat input, deep and narrow welds can be obtained with a high welding speed. In the automotive industry, zinc-coated steel metals are widely utilized because zinc coating improves corrosion resistance. Despite the benefits of laser welding, it is challenging to laser weld of zinc coated steels (i.e. galvanized steels) since the boiling point of zinc ( $907\text{ }^{\circ}\text{C}$ ) is significantly lower than the melting point of steel ( $\sim 1500\text{ }^{\circ}\text{C}$ ), resulting in highly pressurized zinc vapour on the faying surfaces during the welding process (Nicolosi et al., 2012). Left unaddressed, such zinc vapour can easily be trapped inside the molten pool which can lead to welding defects such as porosity, spatter, burn-through, and severe undercuts (Norman et al., 2009; Chen et al., 2013).

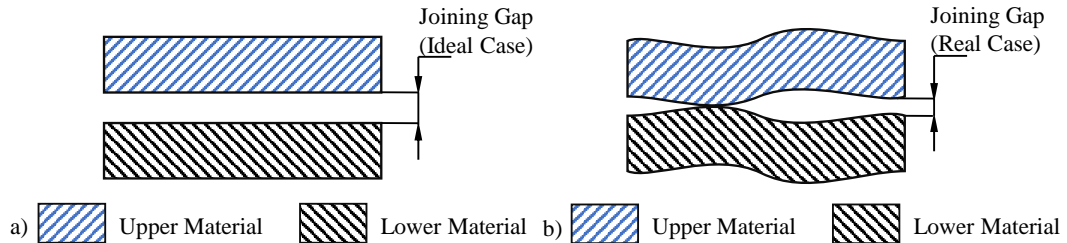
According to the reviewed literature in Section 3.1, the predominantly used technique to overcome the problem caused by the zinc vapour is to create a ventilation channel where the zinc vapour freely escapes from the welding area. An adequate channel can be the joining gap between metal parts because there is no need for installing additional equipment, which increases production cost as well as cycle time (Sinha et al., 2013). However, the major challenge is the tight control of the joining gap in the welding area. Since RLW is non-contact welding, the precise part-to-part fit-up is essential. The parts that are welded must fit together in such

---

<sup>1</sup>This section was published in the “*Journal of Optics and Laser Technology*” on 14 February 2017 with a DOI number of <http://dx.doi.org/10.1016/j.optlastec.2017.02.012>. A copy of the publication is also presented in Appendix E



a way that the joining gap between the parts must be controlled in a certain range. However, the joining gap is not constant due to the geometrical variation of the sheet metal part which is induced during their fabrication process, as depicted in Fig. 4.1.



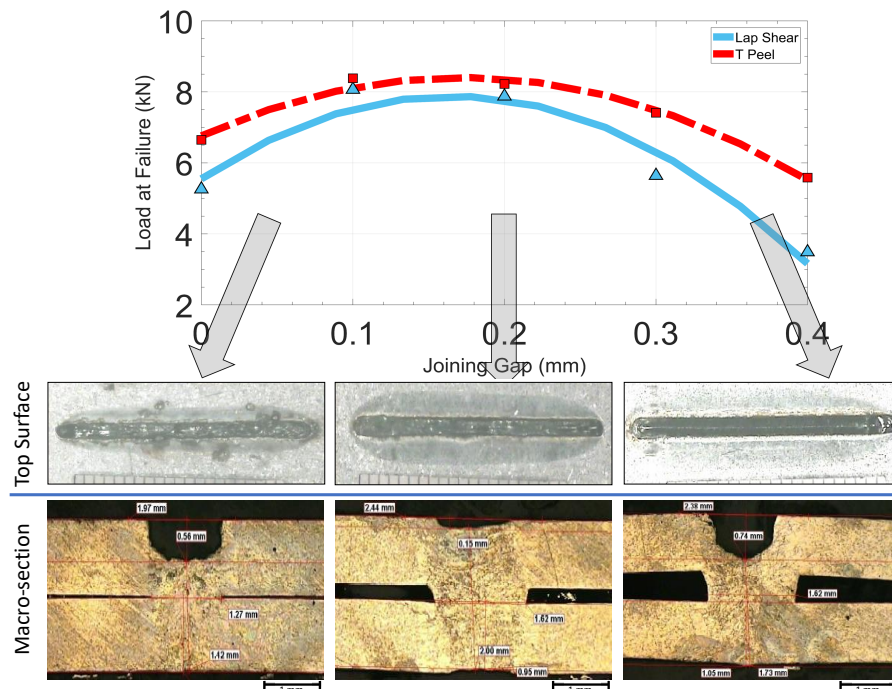
**Fig. 4.1.** A schematic diagram of the joining gap between two sheet metals a) ideal case  
b) real case

According to Jou (2003), the highly utilized welding method in the BIW manufacture is Resistance Spot welding (RSW). In the RSW process, spot guns apply pressure on the welding area to clamp metal parts. Therefore, the joining gap can be controlled in the RSW process. However, there is not any physical contact between the welding robot and metal parts in the RLW process. Therefore, controlling the joining gap is challenging. The control of the minimum gap can be obtained by the laser dimpling process (Gu, 2010). It is an upstream process where adequate dimples are produced on the surface of the material by the rapid movement of the laser beam in a short distance. Moreover, there is no need for additional equipment, the same welding robot, laser source and fixture that are going to be utilized in the welding process can be employed for the dimpling process (Colombo and Previtali, 2014).

The maximum joining gap which allows the formation of a weld is controlled by the fixture (Das et al., 2015). Fixtures are designed to hold the part(s) in an accurate position and to secure the defined position during the process. The major component of a fixture is the clamp. The economical design of a fixture aims to minimize the number of clamps used while considering the part variation. The joining gap along the weld changes as clamps are moved from one position to another position. Therefore, clamps must be located in an optimal position to ensure that the joining gap along the weld does not violate the minimum and the maximum joining gap requirements (Das et al., 2015).

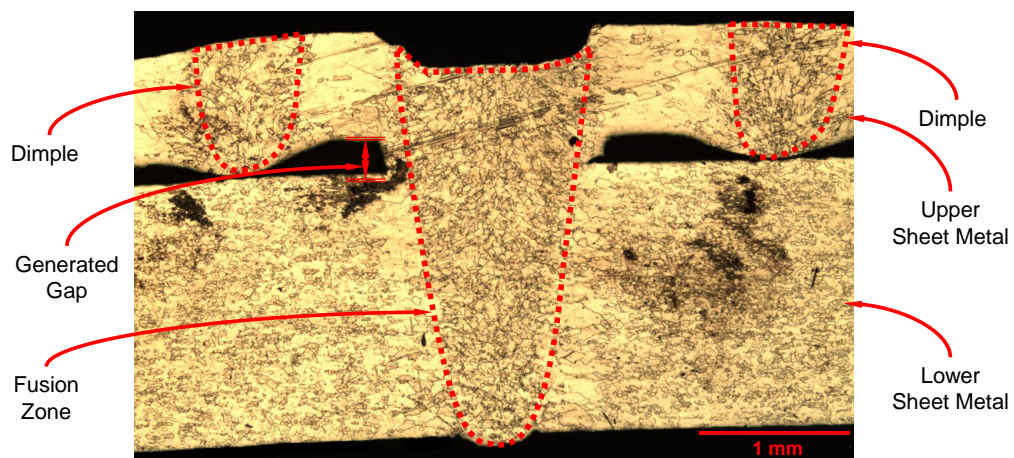
Alexander and Izquierdo (2010) conducted an experimental study using an Nd:YAG laser with a laser power of 4 kW and a welding speed of 2.7 m/min to investigate the effect of the joining gap size on the weld quality. The welding

experiments were conducted on the lap joint configuration of two galvanized plates of steel (DX54D+Z). The dimensions of metals were  $130\text{ mm} \times 30\text{ mm} \times 1\text{ mm}$ , and weld length was  $25\text{ mm}$ . The results showed that when the joining gap was too small ( $0.05\text{ mm}$ ), the zinc vapour could only emerge through the keyhole. As a result, some liquid material was expelled from the molten pool resulting in excessive spatters on the surface of the metal. Due to the material ejection, the top surface concavity was observed. When the joining gap was too large ( $0.40\text{ mm}$ ), the zinc vapour escaped through the joining gap, without causing any disturbance to the molten pool. The weld seam was consistent and smooth, and spatters did not appear at the top surface. However, the liquid material inside the molten pool filled up the joining gap in order to create the weld, resulting in the top surface concavity. Moreover, partial penetration was observed because most of the laser power was dissipated during the bridging the gap. Based on the tensile test results and macro-section images, the maximum joining gap (i.e. control by the fixture design and clamp location), which allows the formation of a weld, was given as  $0.30\text{ mm}$ ; whereas, the minimum joining gap (i.e. control by dimples) was determined as  $0.10\text{ mm}$ . The authors also suggested that the optimum joining gap should be in the range of  $0.10\text{ mm} - 0.20\text{ mm}$ . The key macro-section images and mechanical test result are given in Fig. 4.2.



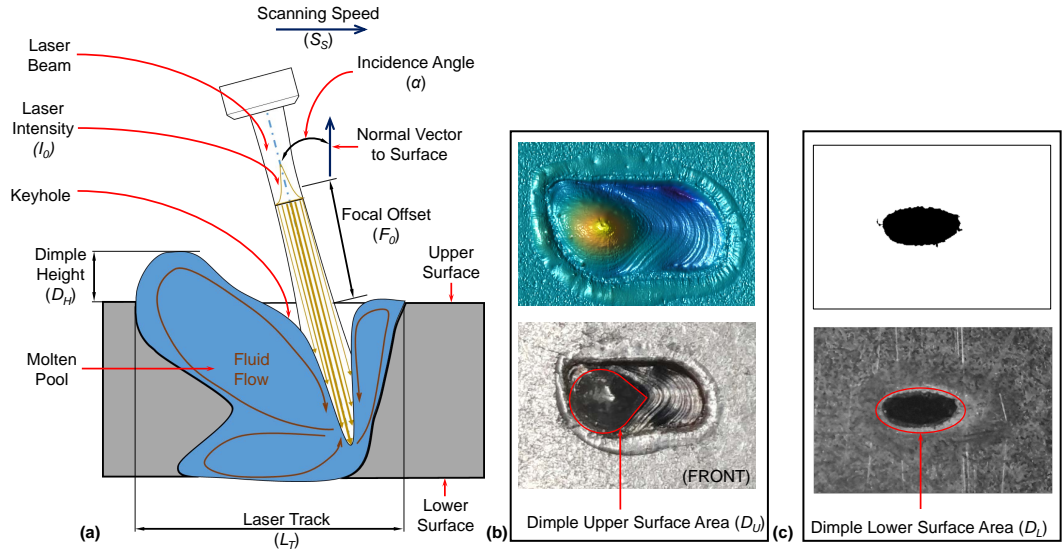
**Fig. 4.2.** The effect of joining gap variation on the weld quality (a) the strength at the failure (b) macro-section image showing weld shape and contour

This chapter reports on an experimental investigation carried out to understand and subsequently control the dimple in the “*laser dimpling process*”. Dimples are generated near the welding area in the upper sheet metal. The lower sheet metal is placed on top of the upper sheet metal to form a lap joint. Dimples work a spacer to create the joining gap between sheet metals. Furthermore, dimples can be created by the rapid movement of the low power on-focus laser beam in a short distance. The same laser source and the fixture designed for laser welding are utilized for the laser dimpling process. Thus, there is no need for any additional equipment. The generated gap, dimples and fusion zone of the weld are illustrated in Fig. 4.3.



**Fig. 4.3.** A macro-section image of a laser welded joint highlighting the fusion zone of the weld, the generated gap, and two dimples

The physical principle behind the laser dimpling process is explained by the “*humping effect*” which is influenced by the heat and mass transfer in the molten pool (Gu, 2010; Gu and Shulkin, 2011; Colombo and Previtali, 2014). In general, humps occur periodically along the weld bead which deteriorates the homogeneity of the molten pool. In the laser welding process, when the beam hits the workpiece, it creates a deep narrow cavity, known as the “*keyhole*”. While the laser beam is moving, the liquid material at the bottom of the keyhole flows upwards to the rear of the molten pool and generates a backward trail of a thin jet due to the surface tension on the keyhole. The solidification of this jet on the surface forms the hump at the rear and a valley at the front which is depicted in Fig. 4.4.



**Fig. 4.4.** (a) Illustration of humping effect during a dimpling process, (b) dimple upper surface, (c) dimple lower surface

The accurate characterization of a dimple is critical since the joining gap generated by the dimple determines the weld quality. Furthermore, dimples obtained by the laser dimpling process are often subjected to stochastic variations which can be uncontrollable factors. Therefore, it is crucial to determine the optimum laser dimpling process parameters, so that dimples are as close as possible to the desired quality criteria, and the variability around the desired dimple quality criteria is minimized in the presence of the process variation.

The existing literature has focussed mainly on a single-input, single-output (SISO) scenario which is necessary, but not sufficient to give a complete characterisation of the dimpling process. Furthermore, the dimple quality is evaluated by one key performance indicator, which is dimple height. Thus, it is important to take into consideration a multi-input, multi-output (MIMO) based scenario and to include the following multi-inputs parameters for a dimpling process: scanning speed ( $S_S$ ), focal offset ( $F_O$ ), incidence angle ( $\alpha$ ), and laser track ( $L_T$ ) as well as the following three dimple quality criteria to be addressed as multi-outputs parameters: dimple height ( $D_H$ ), dimple upper surface area ( $D_U$ ), and dimple lower surface area ( $D_L$ ).

Another limitation associated with the current literature is the lack of modelling variation in the laser dimpling process. The current models are developed under the assumption of ideal process performance, neglecting process variation. As a result of lack of understanding process variation, the dimple quality criteria (i.e. dimple height, dimple upper surface area, and dimple lower surface area) for

given process parameters might violate the given allowance limits, and it will lead to erroneous process parameters selection. However, there is a lack of comprehensive characterization of dimple by considering inherent changes in variability of the laser dimpling process parameters.

Therefore, this chapter introduces a methodology to develop *(i)* a surrogate model for dimpling process characterization considering a MIMO-based scenario by conducting physical experimentation and using statistical modelling, *(ii)* process capability space based on the developed surrogate model that allows the estimation of a desired process fallout rate in the case of violation of process requirements in the presence of stochastic variation, and *(iii)* the selection and the optimization of the process parameters based on the developed process capability space. The proposed methodology provides a unique capability to *(i)* simulate the effect of process variation as generated by a manufacturing process, *(ii)* model quality requirements with multiple and coupled quality requirements, and *(iii)* optimize process parameters under competing quality requirements, such as maximizing the dimple height while minimizing the dimple lower surface area. The methodology is demonstrated using a case study from the door assembly process in the automotive industry, where dimples are determined based on the desired process fallout rate.

The rest of the chapter is organized as follows: Section 4.1 defines Key Control Characteristics and Key Performance Indicators. Section 4.2 presents the problem formulation of *(i)* surrogate modelling for the laser dimpling process characterization, *(ii)* the deterministic and the stochastic process capability spaces, and *(iii)* the laser dimpling process parameters optimization using calculated surrogate models. Section 4.3 explains *(i)* experimental campaign by introducing materials and experimental setup, *(ii)* the development of the deterministic and the stochastic surrogate models, and *(iii)* the development of the deterministic and the stochastic process capability spaces. Section 4.4 describes the proposed methodology for the multi-objective optimization problem to obtain robust KCCs. Section 4.5 demonstrates the results of *(i)* the laser dimpling process characterization, *(ii)* the deterministic and the stochastic process capability spaces, and *(iii)* the optimization results with validation experiments. A sensitivity analysis is performed in Section 4.6 to understand the effect of the change in mean and standard deviation on the results. Section 4.7 summarises the research presented in this chapter.

## 4.1 Definition of Key Control Characteristics & Key Performance Indicators

The dimple quality criteria are evaluated by multi-outputs called Key Performance Indicators (KPIs), which are delivered by multi-inputs (process parameters) called Key Control Characteristics (KCCs). As shown in Fig. 4.4, KCCs considered in this study are:

- ▶ *Scanning Speed* ( $S_S$ ) – The travelling speed of the laser beam along the upper surface of the workpiece;
- ▶ *Focal Offset* ( $F_O$ ) – The distance along the beam axis between the focal point and the interaction of the laser beam and the upper surface of the workpiece;
- ▶ *Incidence Angle* ( $\alpha$ ) – The angle along the beam movement between the beam axis and the normal vector to the upper surface of the workpiece;
- ▶ *Laser Track* ( $L_T$ ) – The linear distance of the beam movement to make a dimple which is parallel to the upper surface of the workpiece.

It was observed that the aforementioned KCCs affect not only the selected KPIs but also KPIs of other downstream processes. For example, scanning speed and laser track can affect process cycle time and fixture clamp layout design. Moreover, focal offset and incidence angle can be related to not only dimple height or dimple upper surface area but also, they can affect detailed 3D fixture design includes the beam visibility, accessibility and offline programming of the robotic scanner head. This is caused by the fact that the robotic system used to make dimples needs to gain access to the workpiece with no collision between the workpiece/fixture and the laser beam. These examples illustrate the importance analysing dimpling process as a MIMO-based system and also to develop a methodology which can be expanded to include additional KPIs as required by downstream processes.

Let us define that four KCCs ( $S_S$ ,  $F_O$ ,  $\alpha$  and  $L_T$ ) are gathered as in Eq. (4.1), where  $i$  and  $k$  represent the index of KCC and experimental configuration; whereas,  $N_i$  and  $N_k$  are the total number of KCCs and experimental configurations, respectively.

$$\mathbf{KCCs} = \begin{bmatrix} KCC_1^{(1)} & \cdots & KCC_{N_i}^{(1)} \\ \vdots & KCC_i^{(k)} & \vdots \\ KCC_1^{(N_k)} & \cdots & KCC_{N_i}^{(N_k)} \end{bmatrix} \quad (4.1)$$

The following KPIs are proposed to measure the functionality, strength and aesthetic quality requirements of the dimple which are illustrated in Fig. 4.4.

- ▶ *Dimple height ( $D_H$ )* – This KPI is needed to evaluate the required and pre-determined gap between sheet metals. It is reported in the literature that dimple height needs to be in the range of  $[0.1, 0.3]$  mm to have a weld with satisfactory quality (Akhter et al., 1991; Colombo and Previtali, 2014).
- ▶ *Dimple upper surface area ( $D_U$ )* – This KPI assesses (i) strength of the dimple to prevent excessive deformation of the dimple height under compression of clamping force applied during welding process, and (ii) uncertainty as measured by difference between dimple height and the required gap between the faying surfaces during consecutive welding process and caused by geometric surface defects, such as roughness, scratches, lines, etc. In essence, the larger dimple upper surface area generates stronger and higher dimples, but it creates unwanted surface feature such as dark spots in the lower surface of the workpiece. According to initial screening experiments, dimple upper surface area should be in the range of  $[1.0, 5.0]$  mm<sup>2</sup> in order to generate sufficient a gap between faying surfaces to achieve a decent weld.
- ▶ *Dimple lower surface area ( $D_L$ )* – The dark spot appeared in the dimple lower surface is an aesthetic quality requirement which is an unwanted feature in Class-A surfaces in the automotive industry (Haider et al., 2007). Thus, the objective is to determine dimple lower surface area which minimizes dimple height variation under compression clamping force in the lap joint. According to initial screening experiments, dimple lower surface area should be in the range of  $[0, 1.5]$  mm<sup>2</sup>.

Let us define three KPIs ( $D_H$ ,  $D_U$  and  $D_L$ ), as shown in Eq. (4.2), where  $j$ ,  $k$  and  $l$  represent the index of KPI, experimental configuration number and its replication ( $KPI_j^{(k,l)}$ ); whereas,  $N_j$ ,  $N_k$  and  $N_l$  are the total number of KPIs, experimental configurations and replicates, respectively.

$$\begin{aligned}
 \mathbf{KPIs} &= \{\mathbf{KPI}_j \mid \forall j = 1, \dots, N_j\} \\
 \mathbf{KPI}_j &= \begin{bmatrix} \mathbf{KPI}_j^{(1)} \\ \mathbf{KPI}_j^{(k)} \\ \mathbf{KPI}_j^{(N_k)} \end{bmatrix} = \begin{bmatrix} KPI_j^{(1,1)} & \dots & KPI_j^{(1,N_l)} \\ \vdots & KPI_j^{(k,l)} & \vdots \\ KPI_j^{(N_k,1)} & \dots & KPI_j^{(N_k,N_l)} \end{bmatrix} \quad (4.2)
 \end{aligned}$$

The lower limits (LL) and upper limits (UL) for each KCC and KPI are defined in Tables 4.1 and 4.2, respectively.

**Table 4.1:** KCCs and their corresponding allowance limits

KCC	Unit	KCC <sup>LL</sup>	KCC <sup>UL</sup>
Scanning speed	<i>m/min</i>	2	4
Incidence angle	°	0	20
Laser track	<i>mm</i>	2	4
Focal offset	<i>mm</i>	25	55

The lower and upper limits of all KCCs have been defined by considering technological constraints, such as the maximum scanning speed of the laser beam, the minimum required laser power intensity on the upper surface of the workpiece to create a dimple. These limits were determined by conducting initial laser dimpling experiments, the results of which are not reported. The lower and upper allowance limits of all KPIs are determined based on the quality requirements. The set of all possible KCCs within the allowance limits defines the process parameters space (KCC-space).

**Table 4.2:** KPIs and their corresponding allowance limits

KPI	Unit	KPI <sup>LL</sup>	KPI <sup>UL</sup>
Dimple height	<i>mm</i>	0.1	0.3
Dimple upper surface area	<i>mm</i> <sup>2</sup>	1.0	5.0
Dimple lower surface area	<i>mm</i> <sup>2</sup>	0.0	1.5

## 4.2 Problem Formulation for the Proposed Research Approach

A methodology is provided to select optimum process parameters (KCCs) in the presence of process variation so that the observable quality indicators of the product (KPIs) are as close as possible to their desired target values and the variability around this target is minimized.

Let us consider one KPI, dimple height ( $D_H$ ), and one KCC, scanning speed ( $S_S$ ) in order to explain the proposed methodology. The upper and the lower limits of a KPI are determined by the quality requirements. For example, dimple works a spacer between two sheet metals in order to create the joining gap. The gap should be controlled within a certain range in order to have a decent weld. The upper and the lower limits of a KCC are defined by considering the technological constraints,



such as the maximum scanning speed that allows making a dimple.

The space determined by the upper and the lower limits of a KCC is called the “**Design Space**” or the “**KCC-space**”. The “*process capability space ( $C_p$ —space)*” defines a region inside the **KCC-space** where selected KCCs will produce acceptable KPIs. The  $C_p$ —space is obtained for both deterministic and stochastic scenarios.

Initially, experimental configurations inside the KCC-space are defined by the DoE methods. Then, experiments, as well as measurements of the KPI, are conducted at the defined experimental configurations. Generally, experiments are subject to the process variation. Thus, each experimental configuration is replicated to help identify the sources of variation. For example, there is not one measured KPI value for a given experimental configuration, instead, there are replicates, and the mean value of these replicates is calculated for each experimental configuration. Hence, two sets can be obtained. The first set is the set of mean values, which contains the mean value for each experimental configuration. The second set is the set of KCCs, which contains the KCC value for each experimental configuration.

In the deterministic scenario, a surrogate model is computed between these two sets to estimate the KPI value over the **KCC-space** (See Fig. 4.5a in the deterministic scenario). The model that might describe this relationship is given as:

$$\hat{\mu}_{KPI} = \mathbf{F}_{\mu_{KPI}}(KCC) \quad (4.3)$$

If the estimated KPI value is within the allowance limits of the KPI, the KCC is said to be feasible and the success rate (SR) gets the value 1. If the estimated KPI value violets the allowance limits, KCC is considered as unfeasible and the SR gets the value 0 (See Fig 9.1b in the deterministic scenario). Thus, the SR in the deterministic scenario is a binary function, and the “*Deterministic  $C_p$ —space*” envelops all the feasible KCC values inside the **KCC-space**. The largest feasible KCC value is called the “*upper specification limit*” (USL), and the smallest feasible KCC value is called the “*lower specification limit*” (LSL) (See Fig. 4.5b in the deterministic scenario).

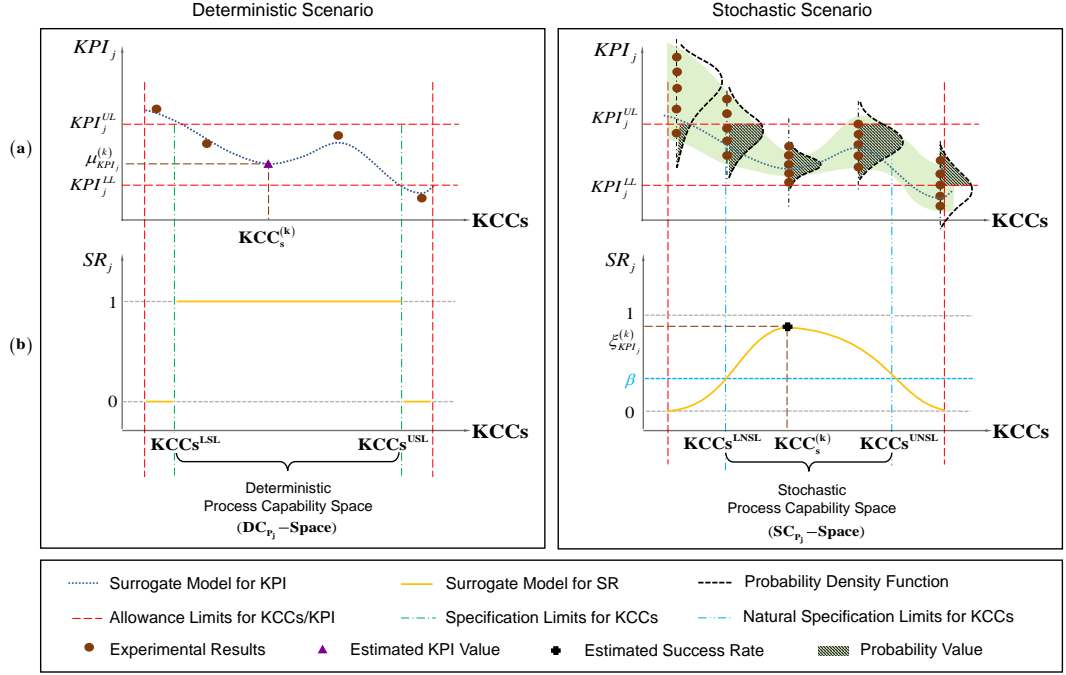
This modelling approach has its own limitation. For example, the estimated KPI value using the developed surrogate model might not violate the allowance limits of the KPI, but one of the replicates might violate the allowance limits. The opposite situation might be also possible. The estimated KPI value might violate the allowance limits, but one of the replicates might be within the allowance limits. Therefore, it is important to consider mean and variance together.

In the stochastic scenario, mean and variance are considered together. The

success rate (SR) is calculated as the probability value of satisfying the allowance limits of the KPI. Initially, the probability density function (PDF) is developed based on replicates. Afterwards, the SR is computed which is the probability value of satisfying the allowance limits as illustrated shaded regions in Fig. 4.5a in the stochastic scenario. Finally, a surrogate model is computed to estimate the SR over the **KCC-space**, which is written as:

$$\hat{\xi}_{KPI} = \mathbf{F}_{\xi_{KPI}}(KCC) \quad (4.4)$$

The developed surrogate model for estimating the SR over the **KCC-space** is a non-binary function, and it gets any value between 0 and 1. Thus, the effect of variation can be presented in the form of the SR model. For example, the low SR means that most of the replicates are outside of the allowance limits of the KPI; whereas, the high SR means that most of the replicates are between the limits (See Fig. 4.5b in the stochastic scenario). It is also noted that an acceptable KPI might be generated in the low SR conditions (e.g.  $SR \leq 0.1$ ) due to high variation. In order to select the robust KCC that produce the replicates with less variation, a threshold value ( $\beta$ ) is defined. Thus, the space inside the **KCC-space** where the KCC values give the SR equal to or higher than the defined ( $\beta$ ) value is called the “*Stochastic  $C_p$ —space*”. The maximum KCC value inside the **Stochastic  $C_p$ —space** is called the “*upper natural specification limit*” (UNSL); whereas, the minimum KCC value inside the **Stochastic  $C_p$ —space** is called the “*lower natural specification limit*” (LNSL). The allowance limits for both KCC and KPI, specification limits, the natural specification limits, the KCC-space, the deterministic and the stochastic process capability spaces are illustrated in Fig. 4.5.



**Fig. 4.5.** The conceptual representation of (a) Experimental results, (b) Success rate models for the deterministic and the stochastic scenarios. The tolerance limits that determine the process capability space in each scenario are also presented.

An analogy can be given from the set theory in mathematics. The **KCC-space** can be considered as the universal set, which contains all KCC values. The **Deterministic  $C_p$ -space** is the subset of the **KCC-space** which contains feasible KCC values. The **Stochastic  $C_p$ -space** is the subset of the **Deterministic  $C_p$ -space**, which contains robust KCC values. They are selected from the feasible KCC values which are less sensitive to process variation. Therefore, selecting robust KCC values is accomplished in two steps. In the first step, feasible KCCs are determined using the **Deterministic  $C_p$ -space**. In the second step, the robust KCCs are selected among the feasible KCCs using the **Stochastic  $C_p$ -space**. However, robust KCCs do not always guarantee to obtain the maximum KPI. For example, the estimated KPI value ( $\mu_{(KPI_j)}^{(k)}$ ) and the estimated SR value ( $\xi_{(KPI_j)}^{(k)}$ ) for the same given KCC are illustrated in Fig. 4.5. At this given KCC, the SR is very high, which means that the variation is less, but the estimated KPI value is not the maximum value in the allowance limits of the KPI. Therefore, these two competing objectives (i.e. maximizing the KPI and the SR values) have to be taken into account during the optimization. In this case, the process engineer has to determine initially the process fallout rate (i.e. how much scraps can be tolerated?) because the  $\beta$  value (a threshold value for the minimum SR) is also referred to 1-process fallout rate

in the manufacturing terminology. A high  $\beta$  value results in a small **Stochastic**  $C_p$ —**space**; whereas, a low  $\beta$  value results in a large **Stochastic**  $C_p$ —**space**. In a small **Stochastic**  $C_p$ —**space**, it is more likely to find out the robust KCCs, but not the maximum KPI; on the other hand, in the large **Stochastic**  $C_p$ —**space**, it is more likely to find out maximum KPI, but the variation around this value is high.

The proposed approach addresses two key limitations of the currently available models for dimpling process characterization as discussed in the introduction section by taking into consideration (i) approximation of a comprehensive multivariate relations between multi-inputs (KCCs) and multi-outputs (KPIs) of the dimpling process, and (ii) process variation over the KCC-space which can be either homoscedasticity (all KPIs across the KCC-space have the same variance) or heteroscedasticity (variability of a KPI is unequal across the KCC-space). The process capability space ( $C_p$ -space) is then presented to address both limitations by defining a set of KPIs comprehensively evaluate dimpling process and identifying process parameters inside the KCC-space that satisfy the given quality requirements.

#### 4.2.1 Formulation of Surrogate Modelling for the Process Characterization

The first objective is to compute the deterministic and stochastic surrogate model capable of analytically formulate relationships between multi-inputs (KCCs) and multi-outputs (KPI ( $\mu_{KPI_j^{(k)}}$ ) and SR ( $\xi_{KPI_j^{(k)}}$ )). The mean value of the  $k^{th}$  experimental configuration of the  $j^{th}$  KPI is defined in Eq. (4.5), where  $N_s^{(k)}$  is the sample size in the  $k^{th}$  experimental configuration.

$$\mu_{KPI_j^{(k)}} = \frac{1}{N_s^{(k)}} \sum_{l=1}^{N_s^{(k)}} KPI_j^{(k,l)} \quad (4.5)$$

$$\mu_{\mathbf{KPI}_j} = \left[ \mu_{KPI_j^{(1)}}, \dots, \mu_{KPI_j^{(k)}}, \dots, \mu_{KPI_j^{(N_k)}} \right]^T \quad \forall j = \{1, \dots, N_j\}$$

The range statistics and corrective coefficient ( $d_2$ ) are used to estimate the standard deviation because the sample size is quite small to directly calculate the standard deviation. It is computed in Eq. (4.6).

$$\sigma_{KPI_j^{(k)}} = \frac{\max(\mathbf{KPI}_j^{(k)}) - \min(\mathbf{KPI}_j^{(k)})}{d_2} \quad (4.6)$$

$$\sigma_{\mathbf{KPI}_j} = \left[ \sigma_{KPI_j^{(1)}}, \dots, \sigma_{KPI_j^{(k)}}, \dots, \sigma_{KPI_j^{(N_k)}} \right]^T \quad \forall j = \{1, \dots, N_j\}$$

where  $d_2$  is determined according to the sample size in each experimental configuration. Furthermore, the Shapiro-Wilk normality test, which provides better

results than other normality tests for small sample size (between 3 and 10) (Thode, 2002), is applied to assess the normality assumption for each experimental configuration; hence, the PDF is given as a normal distribution. The KPIs might not be independent of each other and their joint relationship becomes important to define the PDF. Therefore, the Pearson correlation coefficient test has been initially conducted to measure dependence among all KPIs, which is written in Eq. (4.7).

$$\rho_{mn} = \frac{\text{cov}(\mathbf{KPI}_m, \mathbf{KPI}_n)}{\sigma_{\mathbf{KPI}_m} \sigma_{\mathbf{KPI}_n}} \quad \forall m, n = \{1, \dots, N_j\} \quad (4.7)$$

The correlation result indicates the linear relationship among KPIs which takes a value between -1 and +1. Even though correlation and dependency are statistically different terms, if KPIs are linearly correlated, it can be deduced that they are interdependent. As a result, the dependence among KPIs changes the form of the PDF. The function describes the simultaneous behaviour of the dependent KPIs is the “*joint probability density function*” that is given in Eq. (4.8).

$$PDF_{KPI_1^{(k)} \dots KPI_d^{(k)}} = \frac{1}{\sqrt{(2\pi)^d |\Sigma^{(k)}|}} \times \exp\left(-\frac{1}{2}(\mathbf{KPI}_d - \mu_{\mathbf{KPI}_d^{(k)}})^T (\Sigma^{(k)})^{-1} (\mathbf{KPI}_d - \mu_{\mathbf{KPI}_d^{(k)}})\right) \quad (4.8)$$

where  $d$  is the number of dependent KPIs. If all KPIs are interdependent, it will equal to the number of KPIs ( $N_j$ ). Moreover, the symmetric covariance matrix in the  $k^{th}$  experimental configuration is given as  $\Sigma^{(k)}$ . The PDF for each univariate independent KPI is represented as a function of mean value ( $\mu_{KPI_j^{(k)}}$ ) and standard deviation ( $\sigma_{KPI_j^{(k)}}$ ), which is given in Eq. (4.9).

$$PDF_{KPI_j^{(k)}} = \frac{1}{\sqrt{2\pi\sigma_{KPI_j^{(k)}}}} \exp\left(-\frac{1}{2} \frac{(KPI_j - \mu_{KPI_j^{(k)}})^2}{\sigma_{KPI_j^{(k)}}^2}\right) \quad (4.9)$$

The success rate is determined by the integral of the PDF over the given allowance limits, and it is written in Eq. (4.10) for dependent KPIs; whereas, in Eq. (4.11) for each independent KPI.

$$\begin{aligned} \xi_{KPI_1^{(k)} \dots KPI_d^{(k)}} = & \int_{KPI_1^{LL}}^{KPI_1^{UL}} \dots \int_{KPI_d^{LL}}^{KPI_d^{UL}} PDF_{KPI_1^{(k)} \dots KPI_d^{(k)}}(KPI_1^{(k)} \dots KPI_d^{(k)}) dKPI_1^{(k)} \dots dKPI_d^{(k)} \\ & \forall k = \{1, \dots, N_k\} \end{aligned} \quad (4.10)$$

$$\xi_{KPI_j^{(k)}} = \int_{KPI_j^{LL}}^{KPI_j^{UL}} PDF_{KPI_j^{(k)}}(KPI_j^{(k)}) dKPI_j^{(k)} \quad \forall j = \{d+1, \dots, N_j\}, \forall k = \{1, \dots, N_k\} \quad (4.11)$$

The general forms of deterministic and stochastic surrogate models for estimating the KPI and the SR values for dependent and independent KPIs are given in Eqs. (4.12) to (4.14), respectively.

$$\hat{\mu}_{KPI_j} = \mathbf{F}_{\mu_{KPI_j}}(KCC_1, \dots, KCC_{N_i}) \quad \forall j = \{1, \dots, N_j\} \quad (4.12)$$

$$\hat{\xi}_{KPI_1 \dots KPI_d} = \mathbf{F}_{\xi_{KPI_1 \dots KPI_d}}(KCC_1, \dots, KCC_{N_i}) \quad (4.13)$$

$$\hat{\xi}_{KPI_j} = \mathbf{F}_{\xi_{KPI_j}}(KCC_1, \dots, KCC_{N_i}) \quad \forall j = \{d+1, \dots, N_j\} \quad (4.14)$$

## 4.2.2 Formulation of Deterministic & Stochastic Process Capability Spaces

The **KCC-space** can be considered as the universal set, which contains all KCC values. The **Deterministic  $C_p$ -space** is the subset of the **KCC-space** which contains feasible KCC values. The **Stochastic  $C_p$ -space** is the subset of the **Deterministic  $C_p$ -space**, which contains robust KCC values. For the  $j^{th}$  KPI, the deterministic process capability space (**DC $_{p_j}$ -space**) is expressed in Eq. (4.15).

$$\begin{aligned} \mathbf{DC}_{p_j} - \mathbf{space}(KCC_1, \dots, KCC_{N_i}) = & \\ \begin{cases} 1 & \text{if } KPI_j^{LL} \leq \mathbf{F}_{\mu_{KPI_j}}(KCC_1, \dots, KCC_{N_i}) \leq KPI_j^{UL} \\ 0 & \text{otherwise} \end{cases} & \quad (4.15) \\ \forall j = \{1, \dots, N_j\} & \end{aligned}$$

The stochastic process capability spaces are defined in Eqs. (4.16) and (4.17) for dependent and independent KPIs, respectively.

$$\begin{aligned} \mathbf{SC}_{p_{KPI_1 \dots KPI_d}} - \mathbf{space}(KCC_1, \dots, KCC_{N_i}) = & \\ \begin{cases} \hat{\xi}_{KPI_1 \dots KPI_d} & \text{if } \beta \leq \mathbf{F}_{\xi_{KPI_1 \dots KPI_d}}(KCC_1, \dots, KCC_{N_i}) \leq 1 \\ 0 & \text{otherwise} \end{cases} & \quad (4.16) \end{aligned}$$

$$\begin{aligned} \mathbf{SC}_{p_j} - \mathbf{space}(KCC_1, \dots, KCC_{N_i}) = & \\ \begin{cases} \hat{\xi}_{KPI_j} & \text{if } \beta \leq \mathbf{F}_{\xi_{KPI_j}}(KCC_1, \dots, KCC_{N_i}) \leq 1 \\ 0 & \text{otherwise} \end{cases} & \quad (4.17) \\ \forall j = \{d+1, \dots, N_j\} & \end{aligned}$$

where  $\beta$  is the minimal desirable success rate. The identification of the final deterministic and stochastic process capability spaces is done by aggregation of individual deterministic (**DC<sub>p</sub>-space**) and stochastic (**SC<sub>p</sub>-space**) process capability spaces, and they are obtained from Eqs. (4.18) and (4.19), respectively.

$$\mathbf{DC}_p - \mathbf{space} = \bigcap_{j=1}^{N_j} \mathbf{DC}_{p_j} - \mathbf{space} \quad (4.18)$$

$$\mathbf{SC}_p - \mathbf{Space} = \mathbf{SC}_{\mathbf{pKPI}_1 \dots \mathbf{KPI}_d} - \mathbf{Space} \cdot \prod_{j=d+1}^{N_j} \mathbf{SC}_{p_j} - \mathbf{Space} \quad (4.19)$$

It is noteworthy that  $d$  is the number of the dependent KPIs which is determined according to the Pearson correlation coefficient test. The final stochastic process capability space is obtained by the probability theory which is a product of the independent and dependent stochastic process capability spaces. If the all KPIs are dependent, final stochastic process capability is only computed from the dependent stochastic process capability space.

### 4.2.3 Formulation of Process Parameter Optimization Using Calculated Surrogate Models

The aim of this study is to identify optimum KCCs which maximize a KPI (evaluated by deterministic surrogate model) and the probability of satisfying the allowance limits of that KPI (evaluated by stochastic surrogate model) at the same time. Therefore, the multi-objective optimization problem can be formally stated in Eq. (4.20).

$$\begin{aligned} & \mathbf{F}_{\mu_{\mathbf{KPI}_j}}(KCC_1, \dots, KCC_{N_i}) \\ \text{maximize} \quad & \mathbf{F}_{\xi_{\mathbf{KPI}_1 \dots \mathbf{KPI}_d}}(KCC_1, \dots, KCC_{N_i}) \\ & \mathbf{F}_{\xi_{\mathbf{KPI}_j}}(KCC_1, \dots, KCC_{N_i}) \end{aligned} \quad (4.20)$$

$$\begin{aligned} \text{subject to} \quad & KCC_i^{LL} \leq KCC_i \leq KCC_i^{UL} \quad \forall i = \{1, \dots, N_i\} \\ & KPI_j^{LL} \leq \hat{\mu}_{KPI_j} \leq KPI_j^{UL} \quad \forall j = \{1, \dots, N_j\} \end{aligned}$$

## 4.3 Research Methodology to Develop Surrogate-Driven Process Capability Space

### 4.3.1 Materials & Experimental Setup

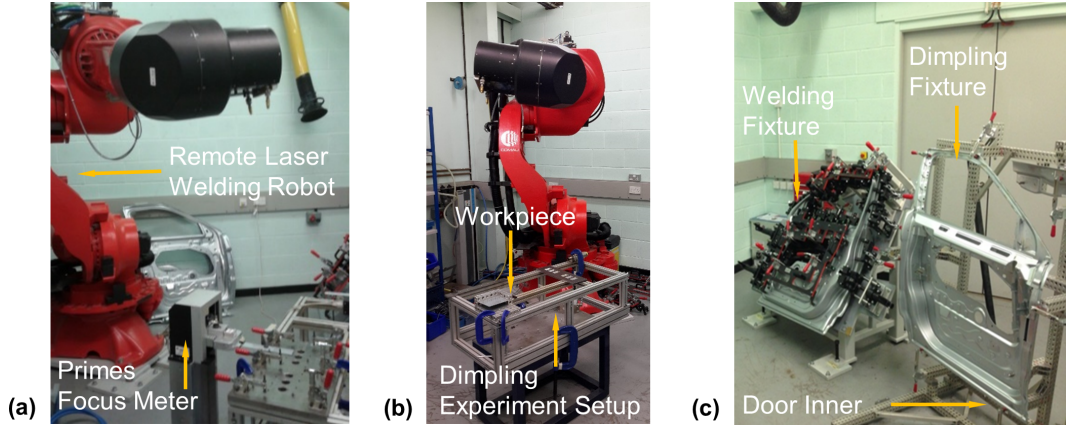
The material used in this study was DX54D+Z hot dip galvanized steel with a thickness of 0.75 *mm*. It has a nominal carbon content of 0.12% and its chemical composition % by mass, mechanical and thermal properties are given in Tables 2.3 to 2.5, respectively. These values are taken from the industrial standard (EN ISO 10327, 2004).

Two series of experiments were carried out. The initial experiments served to characterise the dimpling process and develop the deterministic and stochastic process capability spaces. The second series was used to validate the calculated optimum KCCs based on the process capability spaces by confirmation experiments which were carried out on coupon experiments.

Dimpling experiments were carried out using an IPG Photonics YLR-4000 laser source with a nominal power of 3 *kW*. The laser beam was delivered using an optical fibre, which had a core diameter of 200  $\mu\text{m}$ . The spot diameter of the laser beam on the surface was 900  $\mu\text{m}$ . The laser source generated a multi-mode beam with an  $M^2$  of 31.4 (measured by Primes Focus meter) at a central wavelength of 1064 *nm*. Neither shielding nor backing gases were used during the experiments.

Figure 4.6 shows the experimental setup for the laser beam quality measurement, the Laser Dimpling and the RLW processes. The laser beam is delivered by COMAU SmartLaser robotic system which is a dedicated for the Remote Laser Welding/Laser Dimpling processes and it consists of 4 axes with dynamics and kinematics of a standard industrial robot with an optical system able to deflect the focused beam with high dynamics. The system specifications are given in Table 4.3.



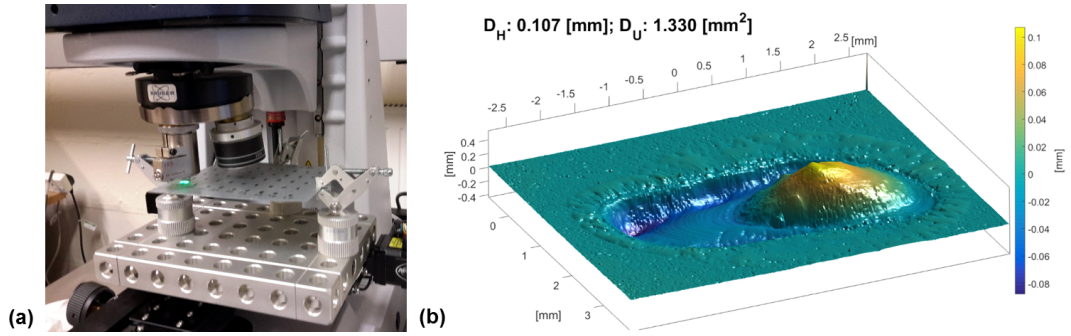


**Fig. 4.6.** An overview of the experimental setup (a) Beam quality measurement (b) Laser Dimpling setup (first series of experiments) (c) Remote Laser Welding setup (second series of experiments)

**Table 4.3:** Laser focusing and repositioning module (SmartLaser)

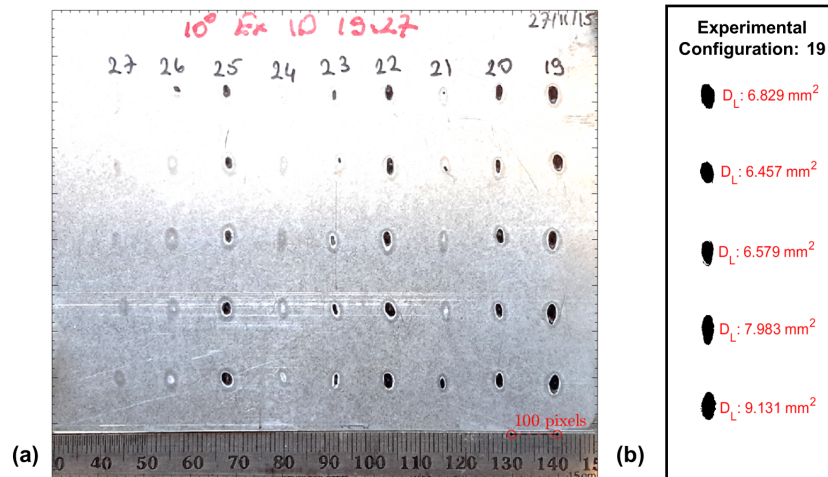
Characteristic Feature	Unit	Specification
Collimating length	$mm$	50
Maximum focal length	$mm$	$1200 \mp 15$
Measured spot size	$\mu m$	$900 \mp 10$
Working area	$mm$	$700 \times 450 \times 400$
Working distance	$mm$	$min\ 894\ max\ 1216$

A 3D optical surface profilometer (Bruker, Contour GT) was used to measure dimple height ( $D_H$ ) and dimple upper spot area ( $D_U$ ). The top surface of the sheet metal was scanned at a speed of  $5\ \mu m/s$  with a vertical resolution of  $10\ nm$  on a rectangle region  $4.5\ mm \times 6.5\ mm$ . The raw data obtained from the optical profilometer was filtered and then reconstructed in 3D using the *Laplacian smoothing filter*. The experimental setup for the profilometer and an example of a scanning result with corresponding process parameters are given in Fig. 4.7.



**Fig. 4.7.** (a) Experimental setup for profilometer, (b) An example of 3D reconstruction. Process parameters:  $S_S: 2 \text{ m/min}$ ,  $\alpha: 20^\circ$ ,  $L_T: 4 \text{ mm}$ ,  $F_O: 35 \text{ mm}$

The dimple lower surface area ( $D_L$ ) was computed by the image segmentation method using MatLab<sup>©</sup>. Each image is captured with a high-resolution camera (3264 pixels  $\times$  2448 pixels). Its focal axis perpendicular to the surface of the workpiece to avoid image distortion. Initially, the number of pixels in a straight line having a length of 10 millimetres is calculated to obtain a scale between pixel length and millimetre. Then, the image was converted into 256 grey levels. After removing the background from the original image, it was binarized (black and white image). The number of black pixels inside the binarized image gives the area in a pixel unit. This is converted into millimetre square using the obtained scale to get the corresponding lower surface area ( $D_L$ ). The reconstructed measurement of ( $D_L$ ) is illustrated in Fig. 4.8.



**Fig. 4.8.** Measurement of the dimple lower surface area (a) Grabbed image with scale bar. (b) Dimple lower surface area for the first right experiment configuration. Process parameters:  $S_S: 2 \text{ m/min}$ ,  $\alpha: 10^\circ$ ,  $L_T: 4 \text{ mm}$ ,  $F_O: 25 \text{ mm}$

### 4.3.2 Design of Experiments

Several methods are available for the design of experiments to establish the relationship between input and output variables, which include, among others, a single-factor by single-factor approach, factorial or fractional factorial approaches, Box-Behnken, Doehlet or Taguchi experimental designs. Even though the full factorial design requires a larger number of experimental configurations than other alternative techniques, it allows to spread out design points uniformly to obtain complete information on an unknown design function with limited sample size for capturing both main factors and interactions. Therefore, a full factorial design approach with 4-factor and 3-level experimental design was adopted. This experimental design requires 81 experimental configurations ( $N_k$ ), and each experiment is replicated 5 times to understand the stochastic nature of the process. Totally, 405 experimental runs were conducted. The DoE table was created in randomized order and it was distributed into 9 batches of sheet metal plates ( $130\text{ mm} \times 110\text{ mm}$ ). Thus, each plate had an equal number of dimples and dimpling experiments were conducted according to the created DoE table. However, this equal division did not guarantee that each replicate was conducted in different metal plates.

**Table 4.4:** Key control characteristics and corresponding levels

KCC	Unit	Level [1]	Level [2]	Level [3]
Scanning speed	m/ min	2	3	4
Incidence angle	°	0	10	20
Laser track	mm	2	3	4
Focal offset	mm	25	35	55

Replication was conducted to detect the variation of the process. 5 replications were selected because they represent the right balance between expected model accuracy and time needed to perform experiments and to collect data (one single dimple experiment, including laser processing, measurement and data collection, took about 2 h). It was intended to provide a general methodological approach, whose accuracy may be enhanced whenever more replications would be available.

### 4.3.3 Development of Surrogate Models

The first objective of this work is to compute surrogate models between multi-inputs (KCCs) and multi-outputs (KPI and SR values). This study applied multivariate adaptive regression spline (MARS) method developed by Friedman

(1991). The MARS method is a non-linear and non-parametric regression that can model complex non-linear relationship among input variables by developing regression models locally rather than globally by the dividing the parameter space into several pieces and then performing piecewise fitting in each piece. Furthermore, it does not require a larger number of training data sets and long training process compared to other methods such as neural networks, support vector machines (Lee et al., 2006).

The piecewise fitting is more appropriate for obtained data in dimpling experiments which are actual measurements and calculated success rates. The behaviour of the obtained data in one region inside the **KCC-space** cannot be easily correlated to its behaviour in other region caused by a sudden change which reduces the goodness of the regression. For instance, the high success rate can be achieved in one experimental configuration, but low success rate might be obtained in the next experimental configuration. This sudden change can be handled by using piecewise fitting methods.

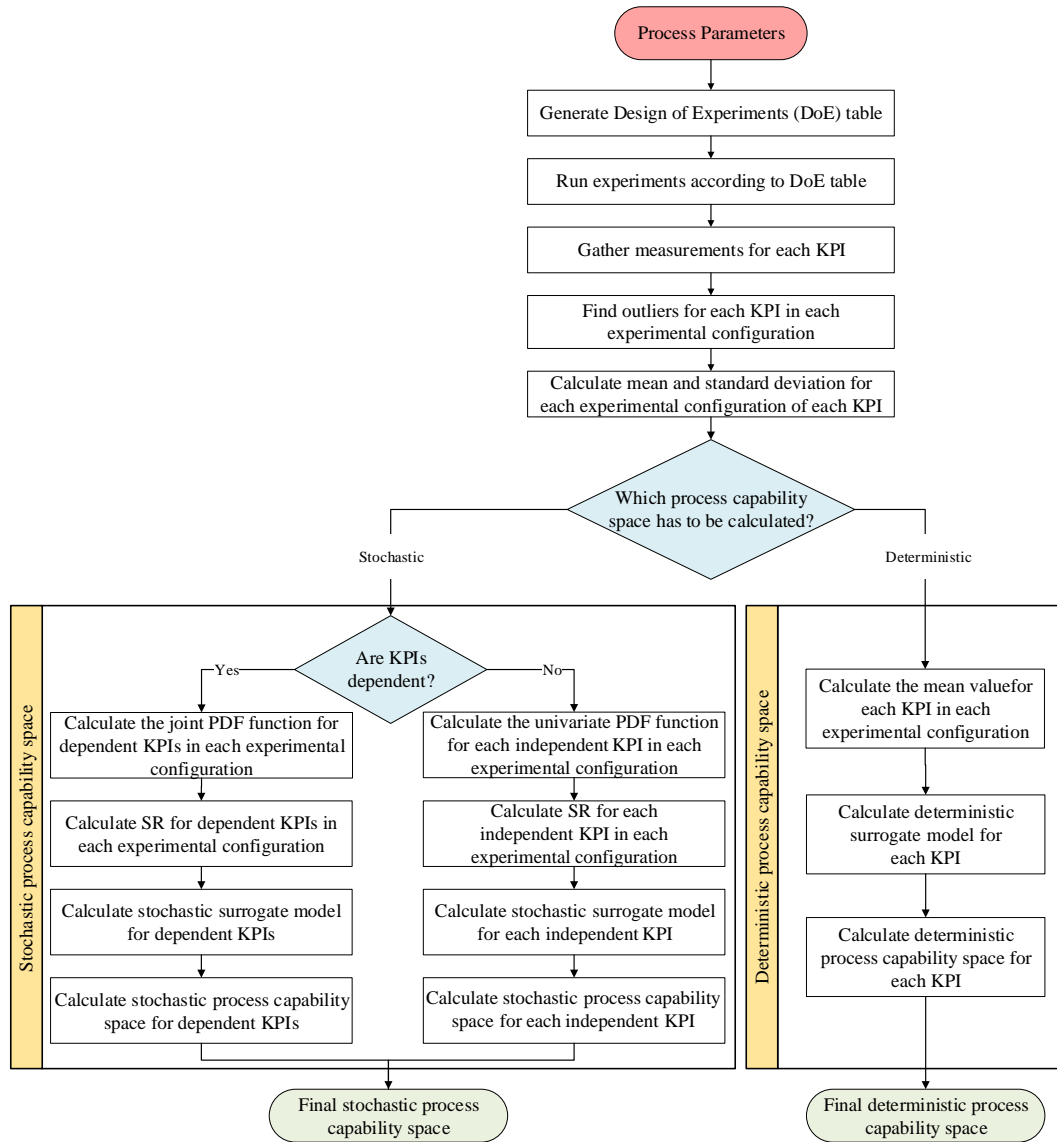
The MARS models were developed using ARESLab<sup>©</sup> (Jekabsons, 2016), a dedicated MatLab toolbox. The parameters used for developing the surrogate models were as follows: *(i)* the maximum number of basis functions that included the intercept terms was set as 101. These functions were necessary to build the model in the forward building phase, *(ii)* the maximum degree of interactions between KCCs was set as 4, *(iii)* piecewise cubic type was chosen, *(iv)* the least important basis functions and high-order interactions were eliminated by feature selection and Generalized Cross-Validation (GCV) score in the backward elimination phase and set as 3, and *(v)* k-fold cross-validation (with 20 k-fold) was used for model validation.

#### 4.3.4 Development of Deterministic & Stochastic Process Capability Spaces

The second objective of this work is to develop deterministic and stochastic process capability spaces. A probabilistic approach was used to develop the stochastic capability space. In some problems, the measured KPIs might be dependent on each other and their simultaneous behaviour defines the probability space. Therefore, the Pearson correlation coefficient test was initially conducted to determine the number of dependent KPIs (d). Consequently, a stochastic surrogate model and a stochastic process capability space were computed for the dependent KPIs; whereas, different stochastic surrogate models and process capability spaces were computed for each independent KPI.

The Dixon's Q test was employed for identification of outliers for each exper-

imental configuration and KPIs since it was designed for small sample size (between 3 and 10 samples) and assumed the normal distribution (Dean and Dixon, 1951). When an outlier detected in one of the dependent KPI, the corresponding values in other KPIs were also considered as an outlier even if the passed were not identified as outliers. The procedure flow for computing final deterministic and stochastic process capability spaces are summarized in Fig. 4.9.



**Fig. 4.9.** The procedure flow for computing process capability spaces

## 4.4 The Laser Dimpling Process Parameter Optimization Using Surrogate-Driven Process Capability Space

The last objective of this work is the optimization of the process parameters based on the deterministic and stochastic process capability spaces. Both deterministic and stochastic  $C_p$ —spaces provide necessary models for selection KCCs to optimize the KPIs using various strategies, reflecting the engineering needs of the laser dimpling process. In general, the optimisation entails two competing objectives: (i) to obtain the maximum KPI value, and (ii) to maximize the probability of satisfying the allowance limits of the selected KPI. It is important to note that the requirements for the laser dimpling process are determined by downstream processes such as assembly fixture design (Franciosa et al., 2016). For example, assembly fixture design for welding which is a downstream process might require a specific KCCs/KPIs configuration which will impose the laser dimpling process to achieve the best success rate in satisfying the requirements of achieving lower allowance limits of KPIs. Therefore, the proposed optimization strategy is based on the  $\epsilon$ -constraint method rather than solving the Pareto Frontier. This involves optimization of success rate in achieving pre-selected KPIs configuration and using the other functions as constraints.

In this study, three design options are defined to optimize all KPIs. The first design option maximizes success rate of the dependent KPIs which addresses the functional and strength requirement of a dimple (i.e.  $D_H$ ,  $D_U$ ) to control simultaneously minimum gap requirement and strength of dimple. Similarly, the second design option evaluates the success rate of the independent KPI which focuses on aesthetic requirements of a dimple (i.e.  $D_L$ ) that is important for Class-A surfaces. The other design option is the combination of these options, and it is handled as a multi-objective optimization problem. Table 4.5 describes the proposed optimization strategies for various pre-defined KCCs/KPIs configurations.

**Table 4.5:** The proposed design option to find out optimum process parameters

Design option	Objective function	Constraint functions		
		Deterministic constraint	Stochastic constraint	Bounded process parameters
1	$\max \mathbf{F}_{\xi_{\text{KPI}_1 \text{KPI}_2}}$	$\mathbf{F}_{\mu_{\text{KPI}_1}} \geq KPI_1^{LL}$	–	
2	$\max \mathbf{F}_{\xi_{\text{KPI}_3}}$	$\mathbf{F}_{\mu_{\text{KPI}_2}} \geq KPI_2^{LL}$ $\mathbf{F}_{\mu_{\text{KPI}_3}} = KPI_3^{LL}$	–	$KCC_i^{LL} \leq KCC_i \leq KCC_i^{UL} \quad \forall i = \{1, \dots, N_i\}$
3	$\max \mathbf{F}_{\xi_{\text{KPI}_1 \text{KPI}_2}}$	$\mathbf{F}_{\mu_{\text{KPI}_1}} \geq KPI_1^{LL}$ $\mathbf{F}_{\mu_{\text{KPI}_2}} \geq KPI_2^{LL}$	$\max \mathbf{F}_{\xi_{\text{KPI}_3}} \geq \beta$	
		$\mathbf{F}_{\mu_{\text{KPI}_3}} = KPI_3^{LL}$		

## 4.5 Results of Surrogate-driven Process Capability Space

### 4.5.1 Statistical Data Analysis

The total number of KCCs, KPIs, experimental configurations, replication and dependent KPIs are determined as  $N_i$ ,  $N_j$ ,  $N_k$ ,  $N_l$  and  $d$ , respectively. The dependency among KPIs are evaluated using the Pearson product-moment correlation coefficient test, and its result ( $\rho$ ) takes a value between +1 and -1, where 1 is the total positive linear correlation, 0 is no linear correlation and -1 is the total negative linear correlation. The result of the Pearson test is given in Eq. (4.21). According to the results, dimple height ( $D_H$ ) and dimple upper surface area ( $D_U$ ) are determined as dependent KPIs and dimple lower surface area ( $D_L$ ) is independent of other KPIs.

$$\begin{aligned} \rho_{mn} &= \frac{\text{cov}(\mathbf{KPI}_m, \mathbf{KPI}_n)}{\sigma_{\mathbf{KPI}_m} \sigma_{\mathbf{KPI}_n}} \quad \forall m, n = \{1, \dots, 3\} \\ &= \begin{bmatrix} 1 & 0.7852 & 0.2409 \\ 0.7852 & 1 & 0.5515 \\ 0.2409 & 0.5515 & 1 \end{bmatrix} \end{aligned} \quad (4.21)$$

The SR in the stochastic case is not a binary value and it gets any value between zero and one. However, its behaviour in one region inside the KCC-space cannot be easily correlated to its behaviour in another region. This change can be handled by using piecewise fitting methods. Thus, the MARS model is implemented in this study. The goodness of a surrogate model is assessed by computing the coefficient of determination ( $R^2$ ) and the root mean square error ( $RMSE$ ). The goodness of the MARS models is compared with the second and the third order polynomial regressions which are reported in Table 4.6. The DoE table, along with measured dimple height ( $D_H$ ), dimple upper surface area ( $D_U$ ) and dimple lower surface area ( $D_L$ ) are given in **Appendix A**.



**Table 4.6:**  $R^2$  & RMSE values for different surrogate models

Surrogate Model	MARS		2nd order polynomial		3rd order polynomial	
	$R^2$	RMSE	$R^2$	RMSE	$R^2$	RMSE
$\mathbf{F}_{\mu_{\text{KPI}_1}}$	0.9281	0.011	0.9527	0.0266	0.9624	0.0235
$\mathbf{F}_{\mu_{\text{KPI}_2}}$	0.9634	0.1219	0.9293	0.3288	0.9358	0.3025
$\mathbf{F}_{\mu_{\text{KPI}_3}}$	0.9874	0.2213	0.9506	0.5621	0.9534	0.5329
$\mathbf{F}_{\xi_{\text{KPI}_1} \xi_{\text{KPI}_2}}$	0.8872	0.1450	0.8068	0.2766	0.8114	0.1866
$\mathbf{F}_{\xi_{\text{KPI}_3}}$	0.9754	0.0684	0.9187	0.2241	0.9039	0.1353

### 4.5.2 Deterministic Surrogate Models

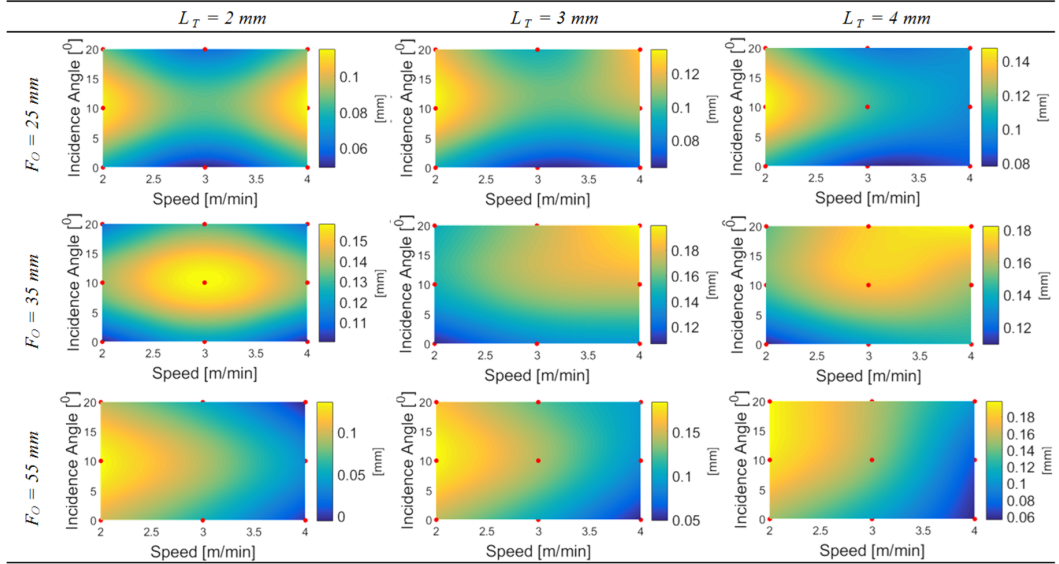
In the deterministic scenario, a different surrogate model is calculated for each KPI to estimate the KPI value over the **KCC-space**. The results of these deterministic surrogate models are illustrated in Figs. 4.10 to 4.12 for varying scanning speed ( $S_S$ ) and incidence angle ( $\alpha$ ) for constant laser track ( $L_T$ ) and focal offset ( $F_O$ ) values. These figures provide two types of information: (i) the effect of the process parameters on KPIs which can be directly used by the automotive industry, and (ii) individual deterministic process capability spaces which lead to final deterministic process capability space.

It is interesting to note that the dimple is formed in the same direction with laser track movement for a high defocus ( $\sim 55 \text{ mm}$ ); whereas, the dimple is formed in the opposite direction of the laser movement for a low focal offset ( $\sim 25 \text{ mm}$ ). This behaviour is one of the findings of this study and is shown in Fig. 4.13. It can be explained by the fact that larger defocusing generates bigger laser beam spot size, which reduces laser intensity. In this case, the molten material is moved forward by the movement of the laser beam. The dimples obtained in this condition are characterized by a cavity in the rear and higher dimple in front, which is highlighted in Fig. 4.4.

#### 4.5.2.1 Characterization of Dimple Height ( $D_H$ )

According to the literature, dimple height decreases with scanning speed. However, as predicted in Fig. 4.10, this can only be obtained for a high focal offset ( $\sim 55 \text{ mm}$ ) and constant incidence angle. For a low focal offset ( $\sim 25 \text{ mm}$ ), the laser track clearly affects the dimple height, whilst a bi-polarized pattern can be observed because of the mutual interaction between speed and incidence angle. At medium focal offset ( $\sim 35 \text{ mm}$ ), scanning speed slightly affects dimple height, whilst

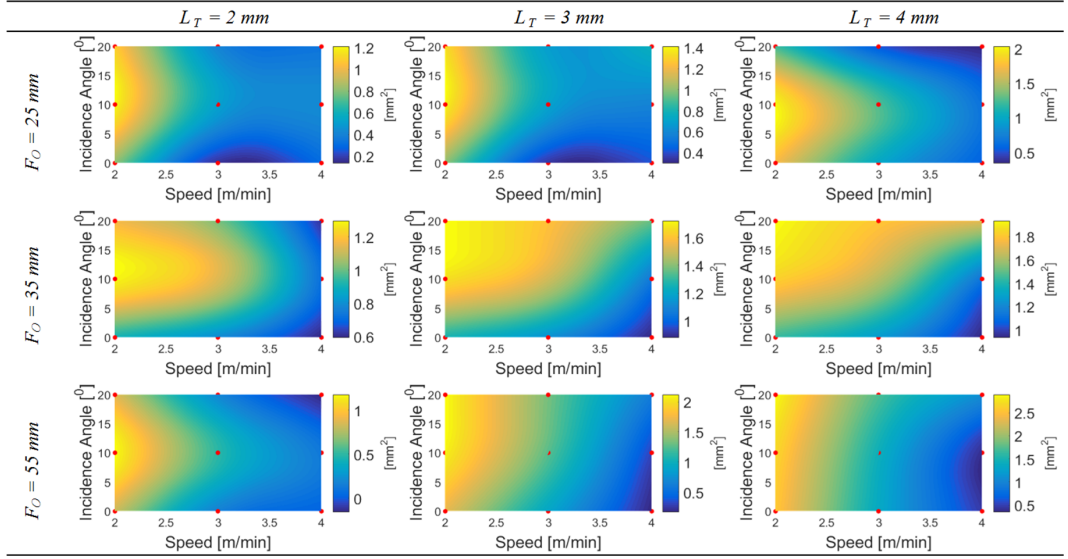
the interaction between laser track and incidence angle generates a unipolar pattern. The highest dimple height is observed around  $5^\circ - 10^\circ$ . The reason for this could be the amount of energy absorbed by the material and tilted keyhole that pushes the melting upwards. It can be deduced that the dimple height increases while increasing laser track, as is also indicated in the literature (Gu and Shulkin, 2011).



**Fig. 4.10.** The estimated dimple height value ( $D_H$ ) over **KCC**-space in the deterministic scenario for varying Scanning Speed ( $S_S$ ) and Incidence Angle ( $\alpha$ ) for constant Laser Track ( $L_T$ ) and Focal Offset ( $F_O$ ) values

#### 4.5.2.2 Characterization of Dimple Upper Surface Area ( $D_U$ )

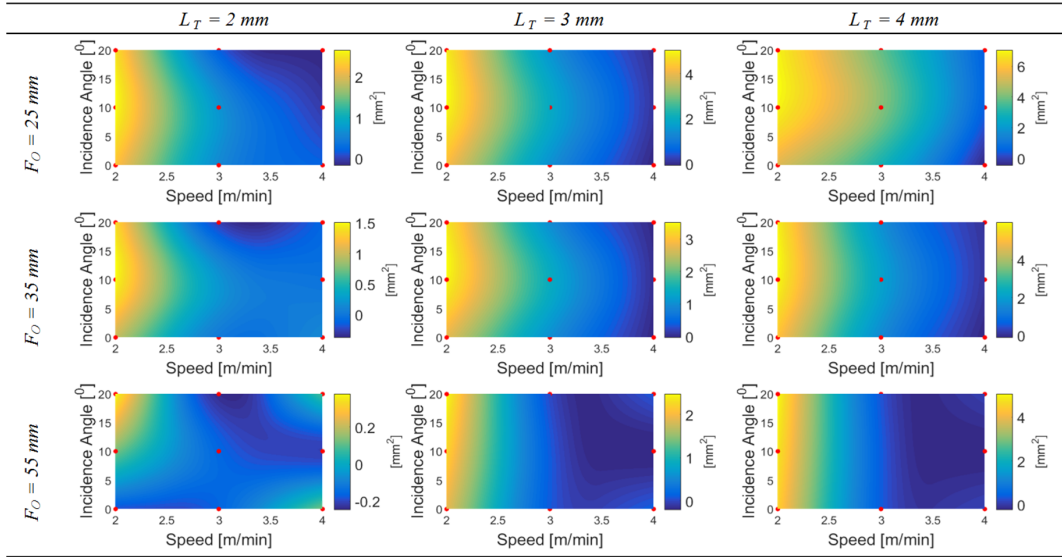
Dimple upper surface area ( $D_U$ ) decreases with only increasing scanning speed ( $S_S$ ) while other parameters are kept constant. The  $D_U$  grows with the increase in both scanning speed ( $S_S$ ) and laser track ( $L_T$ ), but it decreases with increasing both incidence angle ( $\alpha$ ) and focal offset ( $F_O$ ). It is evident that increasing laser track results in higher and larger dimples since the longer displacement creates longer trailing jet on the surface, as is also indicated in the literature (Earl et al., 2012). The correlation patterns exhibit a unipolar shape, which tends to be elongated, moving toward a higher laser track and focal offset.



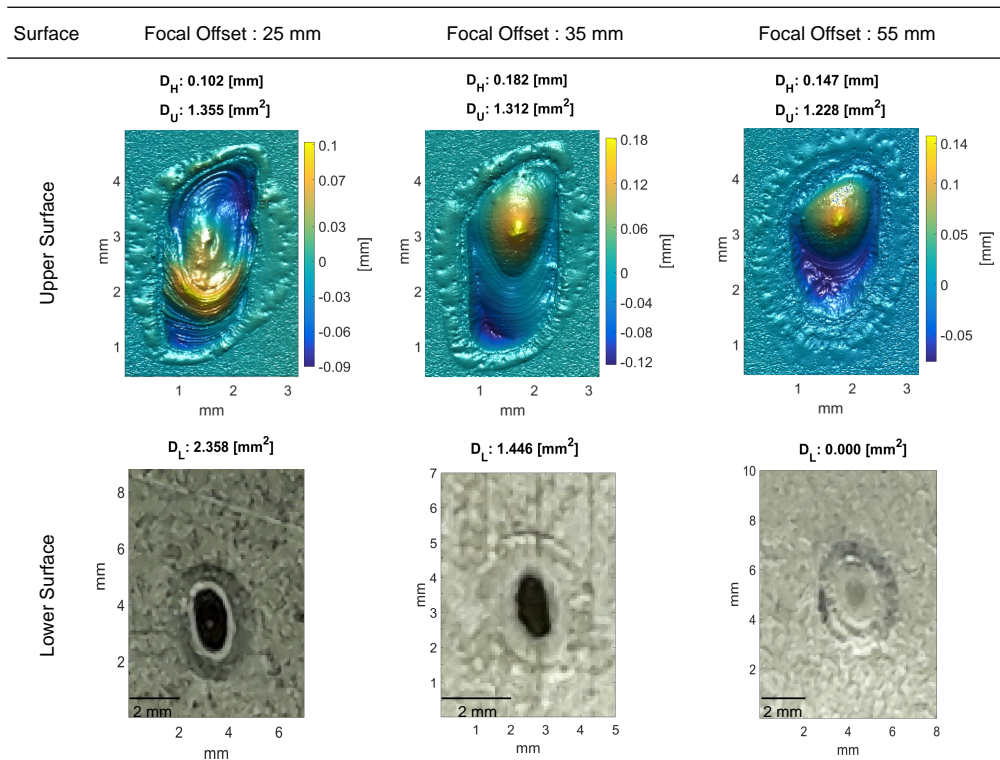
**Fig. 4.11.** The estimated dimple upper surface area value ( $D_U$ ) over **KCC**-space in the deterministic scenario for varying Scanning Speed ( $S_S$ ) and Incidence Angle ( $\alpha$ ) for constant Laser Track ( $L_T$ ) and Focal Offset ( $F_O$ ) values

#### 4.5.2.3 Characterization of Dimple Lower Surface Area ( $D_L$ )

It is interesting to note that the main and interaction effects of incidence angle into dimple lower surface area ( $D_L$ ) can be negligible. This can be seen in Fig. 4.12 that the correlation pattern is almost identical. On the other hand, DL is directly correlated with laser track and inversely correlated with focal offset and scanning speed. The minimum  $D_L$  is observed in the medium ( $\sim 35$  mm) and the high ( $\sim 55$  mm) focal offset for a lower laser track ( $\sim 2$  mm).



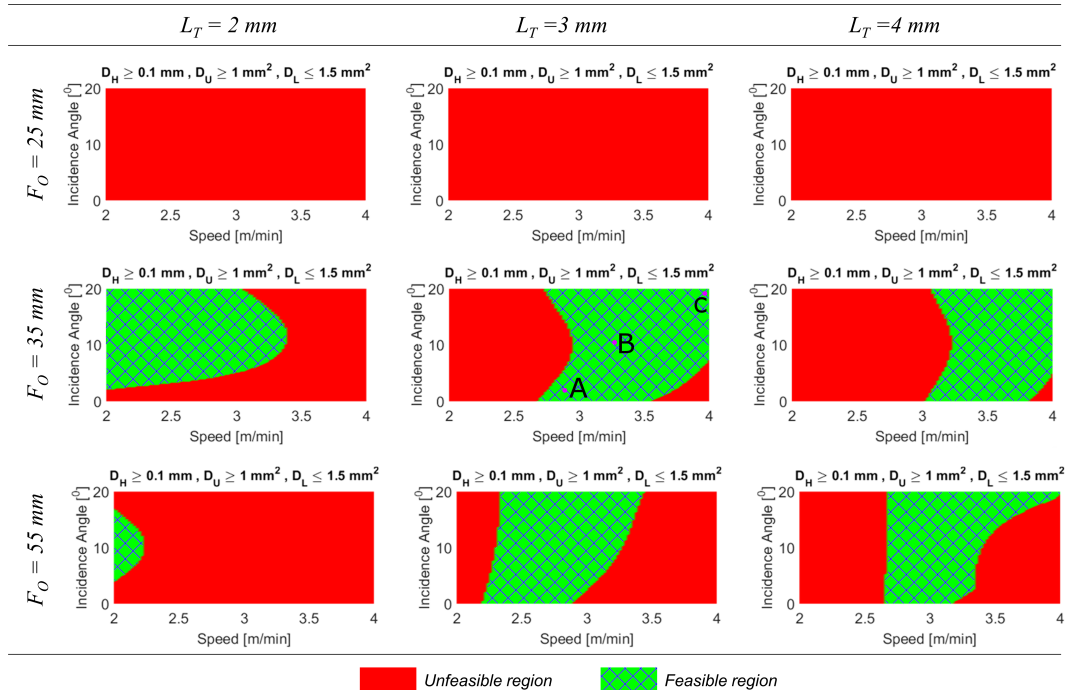
**Fig. 4.12.** The estimated dimple lower surface area value ( $D_L$ ) over **KCC**-space in the deterministic scenario for varying Scanning Speed ( $S_S$ ) and Incidence Angle ( $\alpha$ ) for constant Laser Track ( $L_T$ ) and Focal Offset ( $F_O$ ) values



**Fig. 4.13.** Effect of focal offset on three KPIs when process parameters are constant at:  $S_S$ : 3 m/min,  $\alpha$ : 10°,  $L_T$ : 3 mm. (Upper Surface) Surface profilometer results – (Lower Surface) Image processing results

### 4.5.3 Deterministic Process Capability Space ( $DC_p$ -space)

The deterministic process capability space ( $DC_p$ -space) is illustrated in Fig. 4.14. The shaded area represents the feasible region and any value inside corresponds to feasible process parameters (KCCs) that simultaneously satisfy all quality requirements defined in Table 4.2. According to the  $DC_p$ -space, feasible process parameters cannot be achieved for a lower focal offset ( $\sim 25$  mm) since the  $D_L$  is more likely to exceed its allowance limits that are highlighted in Fig. 4.12. The reason might be that a lower focal offset creates higher laser intensity and thus the more amount of material is molten, which results in a wider and deeper molten pool. The rate of change of the laser intensity determines the occurring physics in the process. For instance, a bigger dimple with a larger  $D_L$  is generated by selecting a slow speed, a short laser track and a low focal offset. Therefore, feasible regions are gathered in the medium levels of each process parameters.



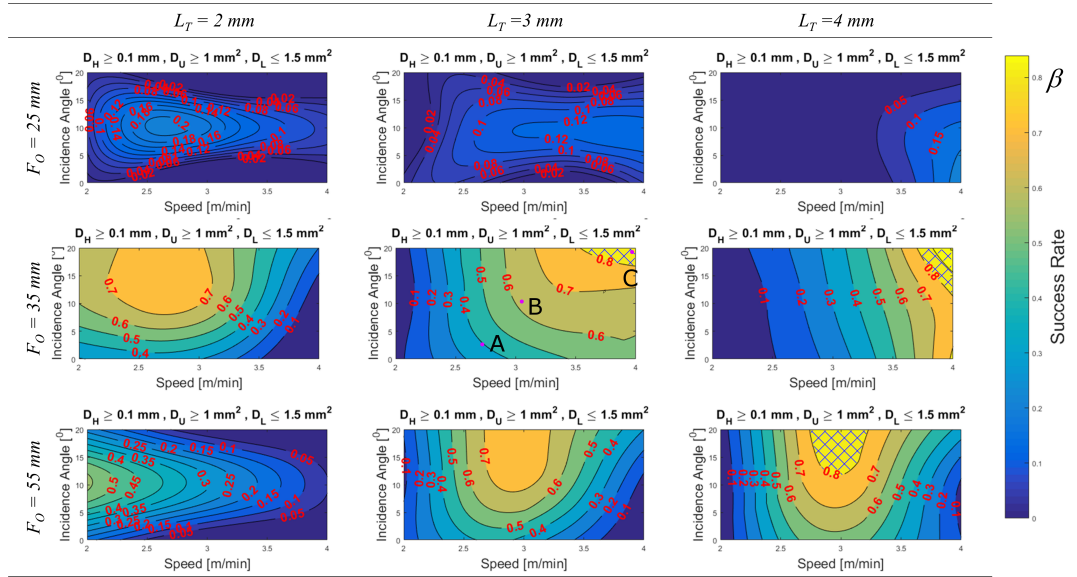
**Fig. 4.14.** Deterministic Process Capability Space ( $DC_p$ -space) over  $KCC$ -space for varying Scanning Speed ( $S_S$ ) and Incidence Angle ( $\alpha$ ) for constant Laser Track Angle ( $L_T$ ) and Focal Offset ( $F_O$ ) values

### 4.5.4 Stochastic Process Capability Space ( $SC_p$ -space)

The calculated stochastic process capability space ( $SC_p$ -space) is presented in Fig. 4.15. The achievable SRs are displayed in the contour plot by initially select-

ing the desirable success rate ( $\beta$ ) at zero. Therefore, it will provide more information to select a set of KCCs. For example, point **A** and point **B** are inside the feasible region in Fig. 4.14 which define two different sets of KCCs that simultaneously satisfy KPIs allowance limits. On the contrary, these points represented in Fig. 4.15 are different SRs since the process variation is less at point **B**. Therefore, point **B** provide more robust process parameters (KCCs). The **SC<sub>p</sub>-space** is utilized to select KCCs according to predefined success rate ( $\beta$ ). Furthermore, the **SC<sub>p</sub>-space** and **DC<sub>p</sub>-space** must follow the same pattern since the probability value is a function of the mean and the standard deviation.

According to the results, the region with the higher SR values is at the medium focal offset ( $\sim 35$  mm). The SR is nearly zero at the lowest focal offset ( $\sim 25$  mm). Thus, it confirms the results obtained by the **DC<sub>p</sub>-space**. The minimum desirable success rate ( $\beta$ ) was set at 0.8, and it was highlighted in the shaded region in Fig. 4.15.



**Fig. 4.15.** Stochastic Process Capability Space (**SC<sub>p</sub>-space**) over **KCC-space** for varying Scanning Speed ( $S_S$ ) and Incidence Angle ( $\alpha$ ) for constant Laser Track ( $L_T$ ) and Focal Offset ( $F_O$ ) values

#### 4.5.5 Process Parameters Optimization

Even though evolutionary algorithms do not guarantee the global optimum, their convergence speeds to the optimal results (nearly global) are better than those of the traditional optimization methods (Anawa and Olabi, 2008; Zhao et al., 2012; Rong et al., 2015; Gao et al., 2016). Thus, evolutionary algorithms have been used

for optimization of real-world problems in many applications instead of traditional techniques. Therefore, the Genetic Algorithm (GA) was implemented to solve the process parameter selection and optimization problem. Population size, the probability of crossover and mutation numbers were selected as 500, 0.60 and 0.12, respectively.

Three design options are defined to find out optimum KCCs under different constraints. These design options are described in Table 4.5 and the optimization results are given in Table 4.7. The results indicate that the optimum configurations are collected between the middle and the high values of each process parameter. This can be explained by the amount of time spent by the laser beam on the workpiece. It can be deduced that by decreasing the interaction time, the less amount of materials was molten, and the molten pool becomes shallow because the less amount of laser energy was absorbed. The design option three is illustrated at Point **C** in Figs. 4.14 and 4.15.

**Table 4.7:** The optimization results showing the proposed design

Design Option	$S_S$	$\alpha$	$L_T$	$F_O$	$\hat{\mu}_{KPI_1}$	$\hat{\mu}_{KPI_2}$	$\hat{\mu}_{KPI_3}$	$\hat{\xi}_{KPI_1KPI_3}$	$\hat{\xi}_{KPI_2}$
1	2.0020	15.0069	3.9692	54.9941	0.198	2.756	4.868	1.000	0.000
2	3.3709	0.2704	3.0229	52.8982	0.092	0.710	0.000	0.283	1.000
3	3.9967	19.9778	3.4845	37.2153	0.199	1.592	0.000	1.000	0.993

The validation experiments were conducted using optimum KCCs given in Table 4.7. Each validation experiment is replicated 5 times. These validation experiments are used to validate optimum KCCs, and the estimated KPI and SR values using the developed surrogate models. The validation experiment results are reported in Table 4.8. The validation experiments were conducted according to the defined methodology in Section 4.3.1. The mean value and the success rate are calculated from the validation experiments (5 replications) for each design option according to the defined methodology in Sections 4.3.3 and 4.3.4. The calculated mean and success rate values are compared against estimated values from the developed surrogate models.

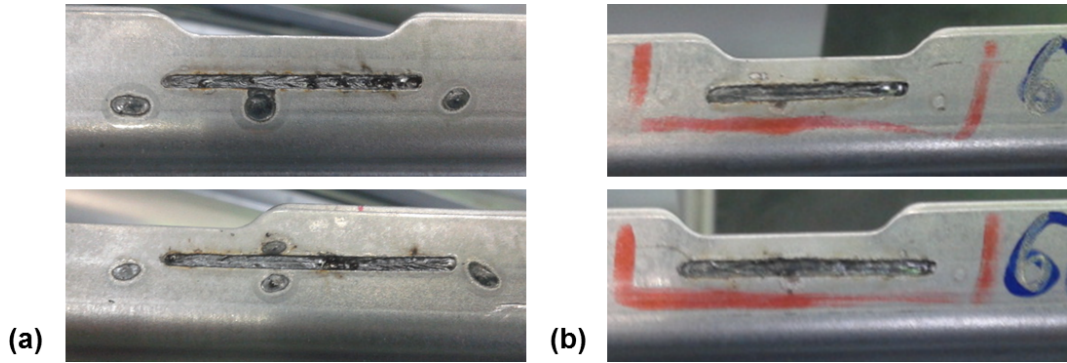
**Table 4.8:** The validation of the optimization results for all design options

Design Option	KPI	Rep. 1	Rep. 2	Rep. 3	Rep. 4	Rep. 5	$\mu_{KPI.}$	$\hat{\mu}_{KPI.}$	$\xi_{KPI.}$	$\hat{\xi}_{KPI.}$
1	$D_H$	0.183	0.190	0.185	2.090	0.189	0.191	0.198	1	1
	$D_U$	2.184	2.055	2.080	2.192	2.154	2.133	2.756	1	1
	$D_L$	4.467	4.318	4.415	5.028	3.417	4.329	4.868	0	0
2	$D_H$	0.124	0.130	0.114	0.084	0.118	0.114	0.092	0.558	0.283
	$D_U$	1.123	1.186	1.037	0.776	1.076	1.039	0.710	0.588	0.283
	$D_L$	0.000	0.000	0.000	0.000	0.000	0.000	0.000	1	1
3	$D_H$	0.207	0.198	0.184	0.179	0.179	0.1894	0.199	0.996	1
	$D_U$	1.741	1.707	1.647	1.261	1.438	1.513	1.592	0.996	1
	$D_L$	0.000	0.000	0.000	0.000	0.000	0.000	0.000	1	0.993

These design options are offered to find robust KCCs which are least affected by process variation. The first option is to find the robust KCCs that maximize the  $D_H$  and  $D_U$ . The second option considers obtaining robust KCCs for achieving only the minimum  $D_L$ . The third option is the combination of both. According to the results, the calculated and the estimated mean and success rates are quite similar for the first design option. However, this similarity is not achieved for the second design option. This is because the variation of the validation experiments is more than the conducted experiments to develop the deterministic and stochastic surrogate models. Therefore, the estimated mean and the success rate using the developed surrogate models is less than the mean and the success rate calculated from the validation experiments.

The laser dimpling process is currently utilized for the laser welding of zinc coated steels in the automotive industry. The dimple generate a small gap between faying surfaces where the zinc vapour is vented out through. However, obtaining a constant gap without having a darker spot at the back side of the steel is the major challenge of the laser dimpling process. An optimum set of KCCs was validated by welding experiments, and the results are given in Fig. 4.16. The figure shows images of the welded specimen before and after the optimization of the laser dimpling process. The dark spots are not visible on the lower surface, and there are no spatters around the stitch after implementing optimum KCCs. Likewise, the quality of the weld seam is improved, and no blow holes are detected in the weld seam.



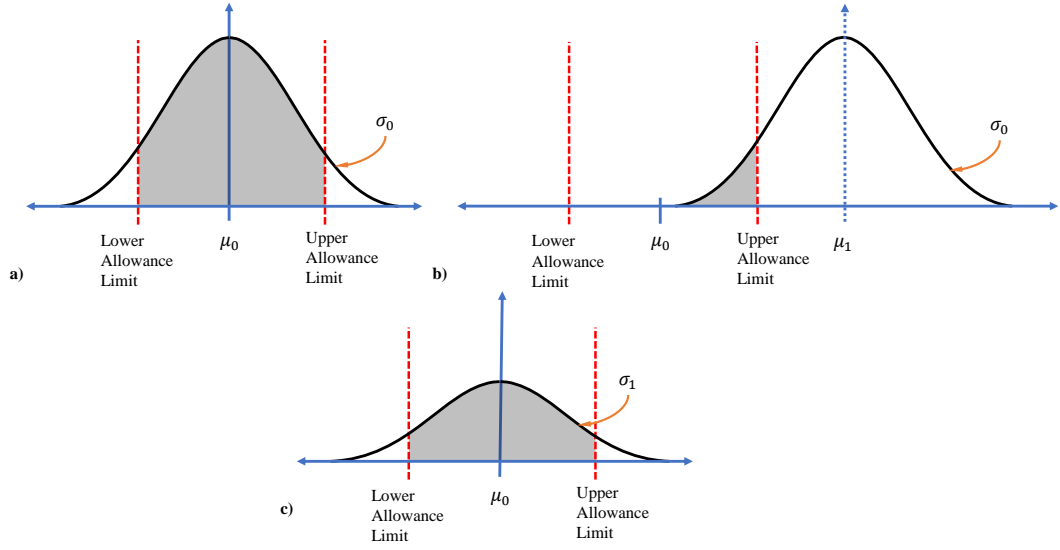


**Fig. 4.16.** Remote laser welded joint looking from the backside. **(a)** Trial-and-error method before optimization. **(b)** Optimized configuration based on the proposed methodology

## 4.6 Sensitivity Analysis

In an experimental design problem, the choice of the number of replicates to use is important due to the cost. The cost can be associated with the amount of material used and the time spent to complete all the planned experiments. The proposed methodology was applied to find out the optimum KCCs for the laser dimpling process. The number of KPIs was set as 3, and the number of KCCs was set as 4. The full factorial design was employed and each KCC was run at 3 levels, resulting in 81 ( $3^4$ ) experimental configurations ( $N_k$ ). Each experimental configuration was replicated 5 times. Totally, 405 experiments, as well as 1215 (405x3 for each KPI) measurements, were conducted.

The probability density function (PDF) is the function of the mean and the standard deviation of replicates. The increase in the replicates results in a change in the mean and the standard deviation as well as the PDF function, as illustrates in Fig. 4.17. Depending on the change, the PDF will be shifted without changing its form (i.e. change in the mean only), or PDF change its form (i.e. change in the standard deviation only). The exact change cannot be understood without conducting physical experimentation. Therefore, a sensitivity analysis is performed to understand the effect of the change in the mean and the standard deviation on the results.



**Fig. 4.17.** The schematic illustration of shifting mean and standard deviation on the PDF  
(a) The original mean and standard deviation, (b) The new mean  $\mu_1$  is bigger than the original mean  $\mu_0$ , (c) The new standard deviation  $\sigma_1$  is bigger than the original standard deviation  $\sigma_0$

A full factorial design is used to determine the effect of the change in the mean and the standard deviation to the results. The results include (i) the optimum KCCs that are the least sensitive to process variation, and (ii) success rate at the optimum KCCs. The maximum and the minimum change in the mean and the standard deviation (2 factors) is considered as  $\pm 10\%$  from the original values, and each factor is run at 21 levels. Thus, the total number of sampling points (SP) is 441 ( $21^2$ ). Let us assume that the % change in the mean from the original value for the  $i^{th}$  level is defined as  $c_{(m,i)}$ . Similarly, the % change in the standard deviation from the original value for the  $j^{th}$  level is defined as  $c_{(s,j)}$ . Thus, the sampling points defined by the full factorial design can be gather as:

$$SP_{(i,j)} = c_{(m,i)}c_{(s,j)} \quad \begin{array}{l} \forall i = 1, \dots, N_m \\ \forall j = 1, \dots, N_s \end{array} \quad (4.22)$$

where  $N_m$  and  $N_s$  are numbers of levels for % change in the mean and % change in the standard deviation, respectively. As explained before, 81 experimental configurations were defined for the laser dimpling process characterization. Each experimental configuration has its own original mean ( $\mu_0^{(k)}$ ) and standard deviation ( $\sigma_0^{(k)}$ ). Both the mean and the standard deviation values for each experimental configuration can be grouped as:

$$\boldsymbol{\mu_0} = \left\{ \mu_0^{(1)}, \dots, \mu_0^{(k)}, \dots, \mu_0^{(N_k)} \right\} \quad (4.23)$$

$$\boldsymbol{\sigma}_0 = \left\{ \sigma_0^{(1)}, \dots, \sigma_0^{(k)}, \dots, \sigma_0^{(N_k)} \right\} \quad (4.24)$$

where  $N_k$  is the number of experimental configurations. Let us take a sampling point ( $SP_{(i,j)}$ ), and calculate the scaled mean and the scaled standard deviation for each experimental configuration.

$$SP_{(i,j)} = c_{(m,i)} c_{(s,j)} \quad (4.25)$$

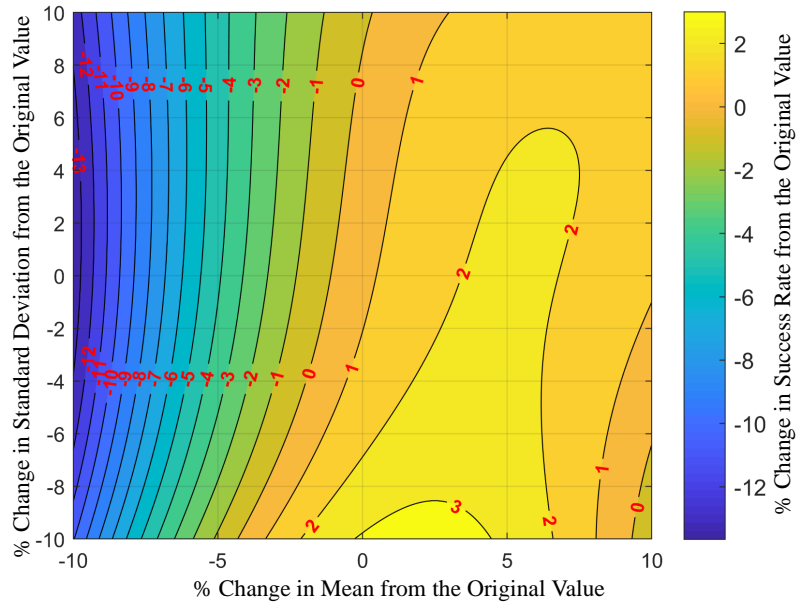
$$\boldsymbol{\mu}_i = c_{(m,i)} \times \boldsymbol{\mu}_0 = \left\{ c_{(m,i)} \times \mu_0^{(1)}, \dots, c_{(m,i)} \times \mu_0^{(k)}, \dots, c_{(m,i)} \times \mu_0^{(N_k)} \right\} \quad (4.26)$$

$$\boldsymbol{\sigma}_j = c_{(s,j)} \times \boldsymbol{\sigma}_0 = \left\{ c_{(s,j)} \times \sigma_0^{(1)}, \dots, c_{(s,j)} \times \sigma_0^{(k)}, \dots, c_{(s,j)} \times \sigma_0^{(N_k)} \right\} \quad (4.27)$$

Based on the scaled means ( $\boldsymbol{\mu}_i$ ) and the scaled standard deviations ( $\boldsymbol{\sigma}_j$ ), the new results are obtained according to the defined methodology (See Fig. 4.9). The new results include: (i) the new optimum KCCs that are the least sensitive process parameters to process variation, and (ii) the new success rate ( $SR_{i,j}$ ) at the new optimum KCCs. The major objective of the **Chapter 4** is to find out the optimum KCCs that are the least sensitivity to the process variation while maximizing the KPIs. Therefore, the effect of the change in the mean and the standard deviation is analysed by looking into % change in SR from the original value ( $SR_{0,0}$ ), which is formulated as:

$$\% \text{ change } SR_{i,j} = \frac{(SR_{i,j} - SR_{0,0})}{SR_{0,0}} \times 100 \quad \begin{array}{l} \forall i = 1, \dots, N_m \\ \forall j = 1, \dots, N_s \end{array} \quad (4.28)$$

After calculating all % change in SR, the change is determined as a function of % change in the mean and % change in the standard deviation using a second order polynomial fitting. The fitting results are provided as a contour plot in Fig. 4.18.



**Fig. 4.18.** The two-dimensional design space showing the effect of % change in the mean and the standard to the change in success rate. The change in the mean value is much more significant than the change in the standard deviation.

The SR is the probability value under the PDF function. A change in the mean and the standard deviation changes the PDF function as well as the obtained SR. Depending on the original values, this change either increases or decreases the SR. For example, up to 5% change in the mean without changing the standard deviation causes 2% increase in the SR. It can be explained that the allowance limits of KPIs do not centre the PDF so that some part of the PDF is not considered while calculating the SR rate. Another example, a decrease in the standard deviation while keeping the same mean value, up to 3% increase in SR is observed because a narrow PDF function will be developed when the standard deviation is decreased. The best-case and the worst-case scenarios are chosen to demonstrate the effect of % change in mean and standard deviation on the results. The obtained results for both scenarios are compared to each other in Table 4.9.

**Table 4.9:** The effect of % change in mean and standard deviation into the results

Scenario	% Change in $\mu$	% Change in $\sigma$	SR	KCC <sub>1</sub>	KCC <sub>2</sub>	KCC <sub>3</sub>	KCC <sub>4</sub>	KPI <sub>1</sub>	KPI <sub>2</sub>	KPI <sub>3</sub>
The best case	5	-10	0.922	3.489	15.637	3.271	39.680	0.191	1.594	0.119
The worst case	-10	6	0.727	3.502	11.260	2.745	32.212	0.146	1.008	0.420

## 4.7 Summary of the Chapter

This chapter presents a novel methodology to select process parameters for the laser dimpling process. It is based on the process capability space which allows the estimation of a desired process fallout rate in the case of quality failures or violation of process requirements. The success rate is offered to measure the process fallout rate using a probabilistic approach. First, two surrogate models are developed to estimate the mean and the success rate over the **KCC-space**. Then, the process capability spaces are computed using the developed surrogate models. Finally, an optimization strategy was proposed to find out the robust KCCs. Furthermore, the mean value is illustrated in the deterministic process capability space (**DC<sub>p</sub>-space**); whereas, success rate, indirectly process variation, is in the stochastic process capability space (**SC<sub>p</sub>-space**). It is noteworthy that the robust KCCs, which are the least sensitive to process variation, does not guarantee to maximize the mean value. Thus, the optimization problem is considered as a multi-objective optimization with two competing objectives.

The industrial needs are also addressed and two new key performance indicators ( $D_U$ ,  $D_L$ ) which are first time offered for the laser dimpling process.  $D_U$  is required to control the gap between faying surfaces, whereas  $D_L$  affects post-weld operations. For example, a large  $D_L$  (a dark black spot) is unwanted for the downstream process. Thus, it requires an additional process to cover these dark spots. Furthermore, four process parameters ( $S_S$ ,  $\alpha$ ,  $L_T$ ,  $F_O$ ) are offered to have a more comprehensive characterization of the process and to determine their effect on the proposed KPIs. These parameters are selected because scanning speed and laser track can affect the process cycle time, and focal offset and incidence angle can be related to the beam visibility, accessibility and offline programming of the robot scanner head.

The following guidelines have been pointed out: a dimple is formed in the opposite direction of the laser beam movement for a low focal offset; whereas, it is generated in the same direction for a large defocus. In addition to that, a larger defocus will lead to a reduction in the dimple lower surface area. Conversely, increasing laser track will result in a reduction of the dimple lower surface area. It can be concluded that laser intensity and the rate of change of the laser intensity are the key factors affecting the formation of the laser dimple.

The current best practice for process parameters selection is based on the costly and time-consuming trial-and-error method (up to 2-3 weeks to set up the proper combination of process parameters for the door assembly process). The pro-

posed methodology offers the following opportunity and applicability: *(i)* selection and optimization of process parameters at the early design stage, and *(ii)* identification of risky areas and low reliable process parameters which help to speed up the process of detecting and correcting defects. This will lead to shorten the time for design and commissioning and reduce production scraps.

The proposed methodology offers a unique simulation tool which is generic and can be applied not only to the laser dimpling process but also can be exploited in the context of selection and optimization of process parameters with heteroscedasticity. This research will be further expanded to integrate the developed surrogate models with task planning and sequencing algorithms in order to simultaneously optimize quality, cost and cycle time of robotic remote laser welding systems.

## **Acknowledgements**

This study was partially supported by the EU research project EU-FP7 FoF-ICT-2011.7.4: RLW Navigator, by the UK EPSRC project EP/K019368/1: Self-Resilient Reconfigurable Assembly Systems with In-process Quality Improvement; and, by the Republic of Turkey Ministry of National Education Post-Graduate Scholarship Scheme. Furthermore, this section was submitted to the “Journal of Optics and Laser Technology” on the 1st September 2016 and accepted for publication on the 14th February 2017 with a DOI number of <http://dx.doi.org/10.1016/j.optlastec.2017.02.012>.

## Chapter 5

# Decoupled Multi-physics Multi-Fidelity Modelling of Laser Welding for In-process Monitoring<sup>2</sup>

Chapter 4 presents a methodology to select robust process parameters in the laser dimpling process so that a constant joining gap can be achieved in the presence of process variation. The joining gap is required in the laser welding of zinc-coated (galvanized) steel to expel the zinc vapour away from the welding area. If the joining gap is too wide, no welding occurs; whereas, if it is too narrow, welding takes place with defects such as explosions, spatters and porosities (See Fig. 4.2). The maximum joining gap size is controlled by the welding fixture; on the other hand, the minimum joining gap is controlled by dimples which are generated by the laser dimpling process.

Chapter 5 focusses on the developing a physics-driven model which can be used as a process model in the proposed closed-loop control system (See Fig. 1.5). RLW is a highly automated process that is being used more and more in the automotive industry. The advantages of RLW are deep penetration, high speed, high aspect ratio, and low thermal distortion. To further improve the efficiency of the RLW process, quality assurance measures are required. Traditional off-line inspection of welds is expensive, reduces productivity. Therefore, the development of an automated in-process monitoring method for laser welding defect detection and a closed-loop control system have been an open field of research in the last years (Ancona and Sibillano, 2008).

Several solutions have been proposed to estimate the weld profile. The weld

---

<sup>2</sup>This section was partially published in the “*Journal of Laser Application*” on 28 March 2017 with a DOI number of <http://dx.doi.org/10.2351/1.4983234>. A copy of the publication is also presented in Appendix F

profile is important because the weld should have a desired profile for achieving the maximum strength. The weld profile is determined by the Fusion Zone Dimensions (FZDs) and their allowance limits are defined in industrial standards EN ISO 13919-1 (1997); EN ISO 13919-2 (2001). It must be pointed out that the FZDs are difficult to measure directly during the welding process unless production is stopped which is nearly unfeasible as it is economically unjustified; whereas, it is monitored by process signals (e.g. acoustic, optical, thermal) and relating these signals to relevant FZDs. The limitation of the current in-process monitoring methods is an indirect measurement of the FZDs. Therefore, an accurate model to perform non-destructive measurement of the FZDs is essential for on-line monitoring of laser welding as a part of quality assurance.

Simulation-based numerical models are developed using the Finite Element Method (FEM) to predict the weld profile and FZDs to develop a better understanding of the process behaviour. Many studies related to this topic have focused on modelling (i) the dynamic behaviour of the keyhole (Ye and Chen, 2002; Pang et al., 2015), (ii) heat transfer and fluid flow in the molten pool (Montalvo-Urquiza et al., 2009; Longuet et al., 2009), and (iii) the laser absorption mechanisms (Jin et al., 2012; Courtois et al., 2013). Due to this complexity, no model can fully explain and correlate all the occurring physics with process parameters. Furthermore, high computational resources are required depending on the complexity of the considered physics. Therefore, it is still impracticable to utilize the FEM models directly in the in-process monitoring because the computational time is much longer than the processing time of the weld. Thus, experimental design methods have been applied to build a model of the system being modelled by the FEM models. This new model is called the “*meta-model*”, the model of the model. Then, the meta-model is utilized as a process model in the in-process monitoring or the closed-loop control system. The assumption is that if the FEM model is a faithful representation of the real system, the meta-model will result in an adequate determination of the optimum conditions for the real system.

The term “*fidelity*” refers to the degree of exactness to reality. An experiment-based model or a simulation-based numeric model (i.e. the FEM model) can be either high-fidelity (HF) or low-fidelity (LF) depending on their predicted results. The creation of this high-fidelity model and the solution of this model definitely takes a lot of time. To overcome the conflict between high accuracy and low computational time requirements for in-process monitoring, a multi-fidelity (MF) modelling approach is proposed based on the interaction between high-fidelity (HF) and low-fidelity (LF) models. An HF model is able to accurately describe the weld-



ing process; whereas, an LF model is one that is able to reflect the most prominent physical phenomena at a less computational cost. In the case of physical experiment, the HF model is the experiment.

As a result, the occurring physics in the laser welding process are decoupled by sequential modelling which consists of three steps as follows: (i) calculating the laser intensity acting on the material, (ii) calculating the keyhole (KH) profile by using an analytic method, and (iii) solving the heat equation using the FEM to calculate the temperature distribution. After obtaining the temperature distribution (TD), the fusion zone (FZ) profile is defined by selecting an isotherm. Then, the aforementioned FZDs (i.e. Penetration, Top Width, Interface Width) are measured from the calculated the FZ profile according to the industrial standard.

Even though the sequential model (low-fidelity (LF) model) has fast computational time, it suffers from low accuracy. Therefore, scaling functions, which are derived from the experiments (high-fidelity (HF) model), are introduced to increase the accuracy without increasing computation time. These functions are initially calculated off-line. Then, they are embedded in the LF model. The proposed modelling approach is computationally efficient and it is suitable for the closed-loop quality control system.

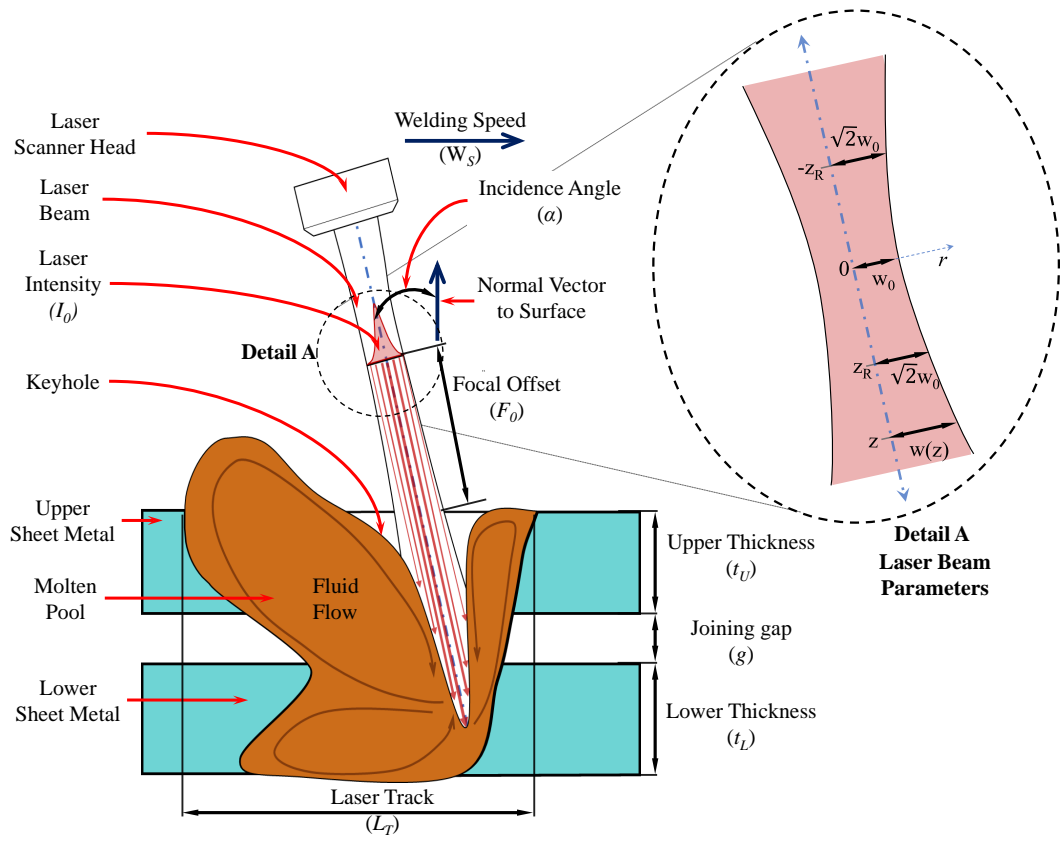
The rest of the chapter is organized as follows: Section 5.1 defines Key Control Characteristics and Key Performance Indicators. Section 5.2 presents the problem formulation of the proposed approach which includes: (i) formulation of the laser intensity ( $I_0$ ), (ii) formulation of the keyhole (KH) profile, (iii) calculation of the temperature distribution (TD), and (iv) extraction of FZDs from the FZ profile. Section 5.3 explains (i) experimental campaign by introducing materials and experimental setup, (ii) the development of scaling functions, and (iii) the development of the multi-fidelity model. Section 5.4 demonstrates the results of (i) the laser welding process characterization, (ii) the scaling functions, and (iii) the validation experiments. Section 5.5 summarises the research presented in this chapter.

## 5.1 Definition of Key Control Characteristics & Key Performance Indicators

The key parameter that influences the laser welding process is the laser intensity ( $I_0$ ). When the laser intensity exceeds a critical value ( $I_0 \geq 10^6 \text{ W/cm}^2$  for steels), instantaneous vaporization occurs along with melting on the surface of the workpiece. Such vaporization generates a pressure which pushes the molten

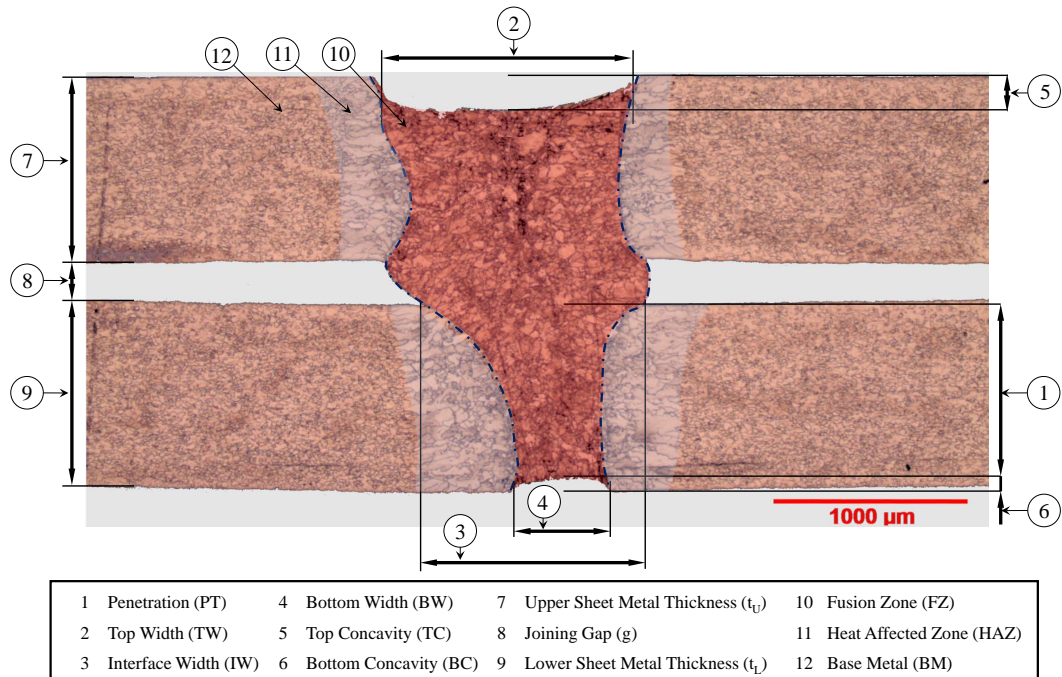
material downwards resulting in the keyhole. The laser intensity ( $I_0$ ) is a function of the laser power and the on-surface spot area ( $A_{spot}$ ) of the laser beam which is correlated to focal offset ( $F_O$ ) and incidence angle ( $\alpha$ ). Furthermore, the interaction time ( $t_i$ ) is also considered as an important process parameter since it controls how long the laser beam will be located at a point on the surface of the workpiece. In addition to these parameters, the joining gap ( $g$ ) is important because it influences the weld profile/weld quality. Generally, the laser beam is focussed on the surface of the workpiece and the maximum laser power is delivered to obtain the maximum laser intensity ( $I_0$ ), so that the keyhole mode is guaranteed. Therefore, the incidence angle, the joining gap, and the welding speed are selected as Key Control Characteristics (KCCs) in this study.

In optics, a beam of light is called Gaussian when its intensity profile on a plane perpendicular to the propagation direction ( $z$ ) follows a Gaussian distribution. In addition, the Gaussian beam tapers approximately linearly until it reaches the narrowest point, called the focus or waist, and then grows again as well. The shape of a Gaussian beam at a given wavelength ( $\lambda$ ) is governed solely by the beam waist ( $w_0$ ). This is a measure of the beam size at the point of its focus ( $z = 0$ ). The Rayleigh length ( $z_R$ ) is the distance along the propagation direction of the beam where the variation of the beam waist is not larger than  $\sqrt{2}$ . The listed process and laser beam parameters are given in Fig. 5.1.



**Fig. 5.1.** A schematic diagram showing laser welding process parameters and laser beam parameters

In the mechanics of materials, the strength is defined as the intensity of the internal forces acting perpendicular to a plane which is created by external loadings. The ultimate tensile strength is the maximum stress that a material can withstand before it breaks. It is usually calculated as force per unit area. For this reason, the welded area is important in any welding process, and the area is represented as the Fusion Zone Dimensions (FZDs). Their allowance limits are defined in industrial standards. Figure 5.2 presents a macro-section of the weld that is obtained by laser welding the steel used in this study. The figure shows all the FZDs and distinct zones in the weld. In this study, Key Performance Indicators are selected as top width ( $TW$ ), interface width ( $IW$ ), and penetration ( $PT$ ) which can represent the welded area and the weld profile.



**Fig. 5.2.** The distinct regions and the fusion zone dimensions to assess the weld quality

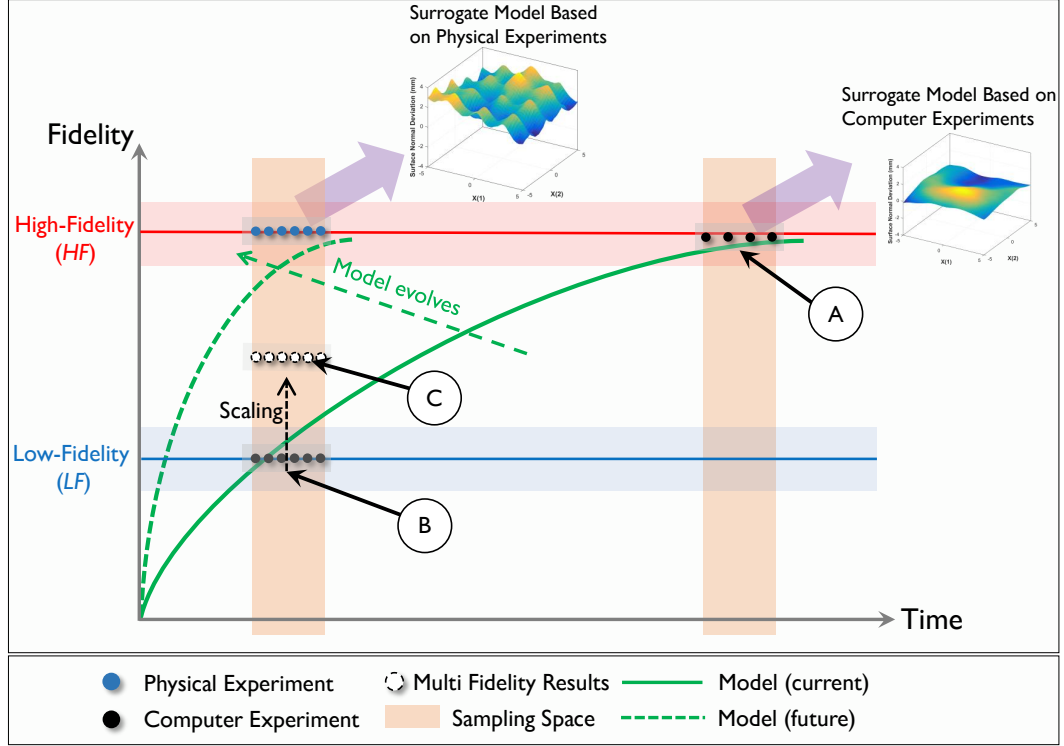
## 5.2 Problem Formulation for the Proposed Research Approach

The term “*fidelity*” refers to the degree of exactness to reality. An experiment-based model (i.e. surrogate model) or a simulation-based numeric model (i.e. the FEM model) can be either high-fidelity (HF) or low-fidelity (LF) depending on their predicted results. The engineering problem that needs to be addressed in the field of in-process monitoring is to develop a process model that accurately and rapidly predicts the outcome (e.g. quality criteria, KPIs, FZDs, *etc.*) of the process.

To overcome the conflict between high accuracy and low computational time requirements for in-process monitoring, a multi-fidelity (MF) modelling approach is proposed based on the interaction between high-fidelity (HF) and low-fidelity (LF) models. The core idea of the MF modelling approach is that the LF model is employed to provide an overall behaviour of the process, while physical experiments with high-fidelity are used to guarantee the accuracy of the prediction of the MF model.

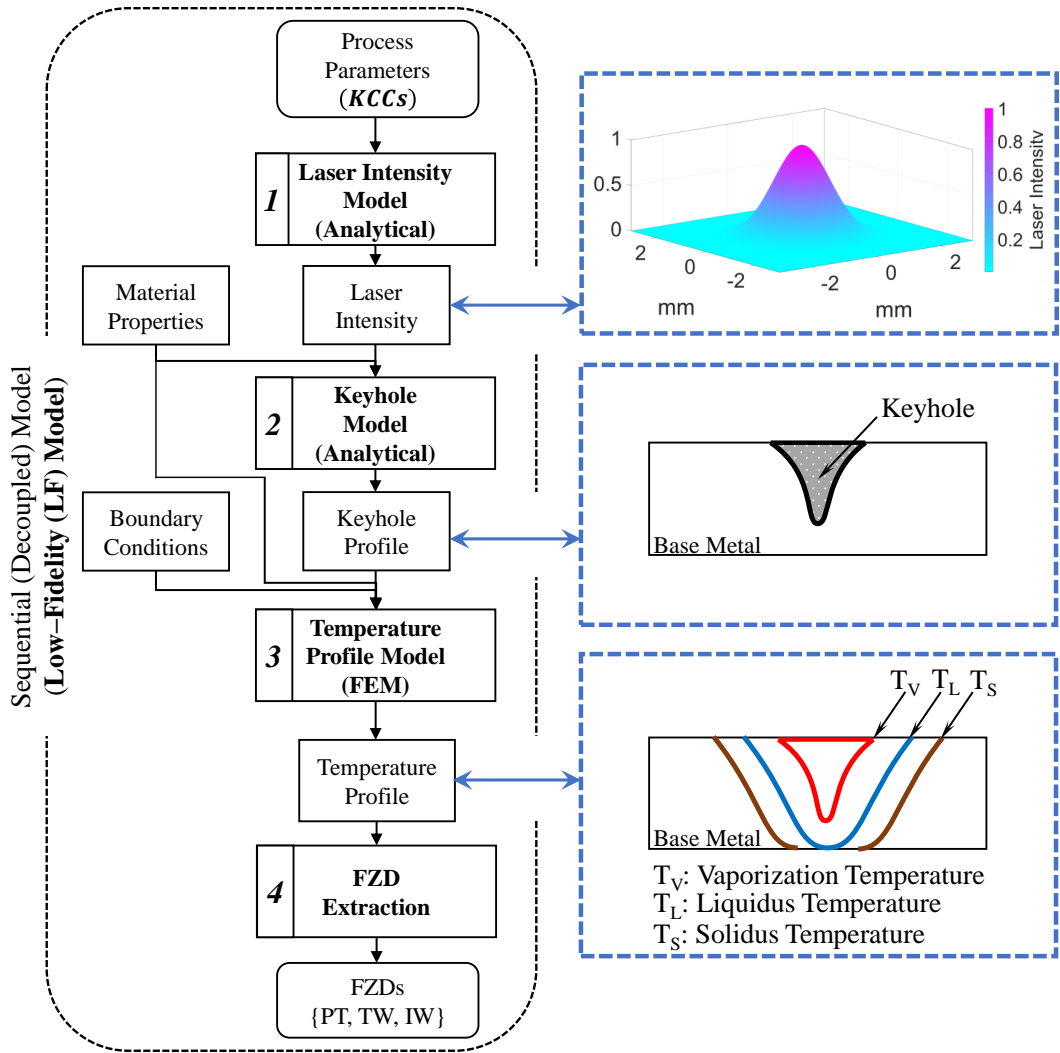
There are three common methods downgrading an HF model to an LF model (See Fig. 5.3 - Moving from Point **A** to Point **B**). These methods can be summarized as follows: (i) simplifying the analysis (e.g. by using a coarse finite element mesh

instead of a refined finite element mesh), *(ii)* simplifying the modelling concept (e.g. by using a two-dimensional (2D) model instead of a three-dimensional (3D) model), and *(iii)* simplifying the mathematical or physical description (e.g. by using the most prominent physical phenomena. It is heat transfer in the laser welding).



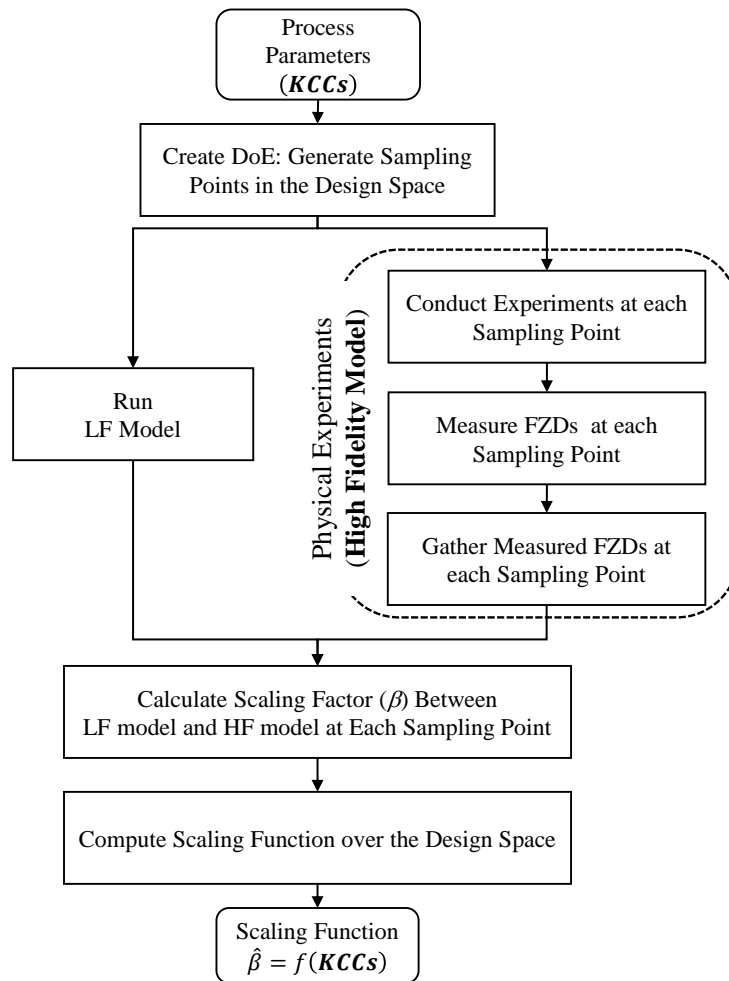
**Fig. 5.3.** The overall representation of the proposed methodology in multi-fidelity modelling. It highlights the high-fidelity model (Point A), the low-fidelity model (Point B), the low-fidelity model with scaling, called the multi-fidelity model (Point C), and physical experimentation with high-fidelity

The occurring physical phenomenon in laser welding is downgraded into an LF model by the sequential modelling (decoupled multi-physics) approach. It consists of three steps: *(i)* calculating the laser intensity acting on the material, *(ii)* calculating analytically the keyhole profile, and *(iii)* calculating the temperature profile by applying FEM to the heat equation. FZDs are extracted from the temperature profile which depends on the choice of a reference temperature, such as the liquidus temperature ( $T_L$ ), then the area enclosed by this isotherm ( $T = T_L$ ) represents the weld. The FZDs are computed from this area according to the industrial standards (EN ISO 13919-1, 1997; EN ISO 13919-2, 2001). The framework of the proposed LF model is depicted in Fig. 5.4.



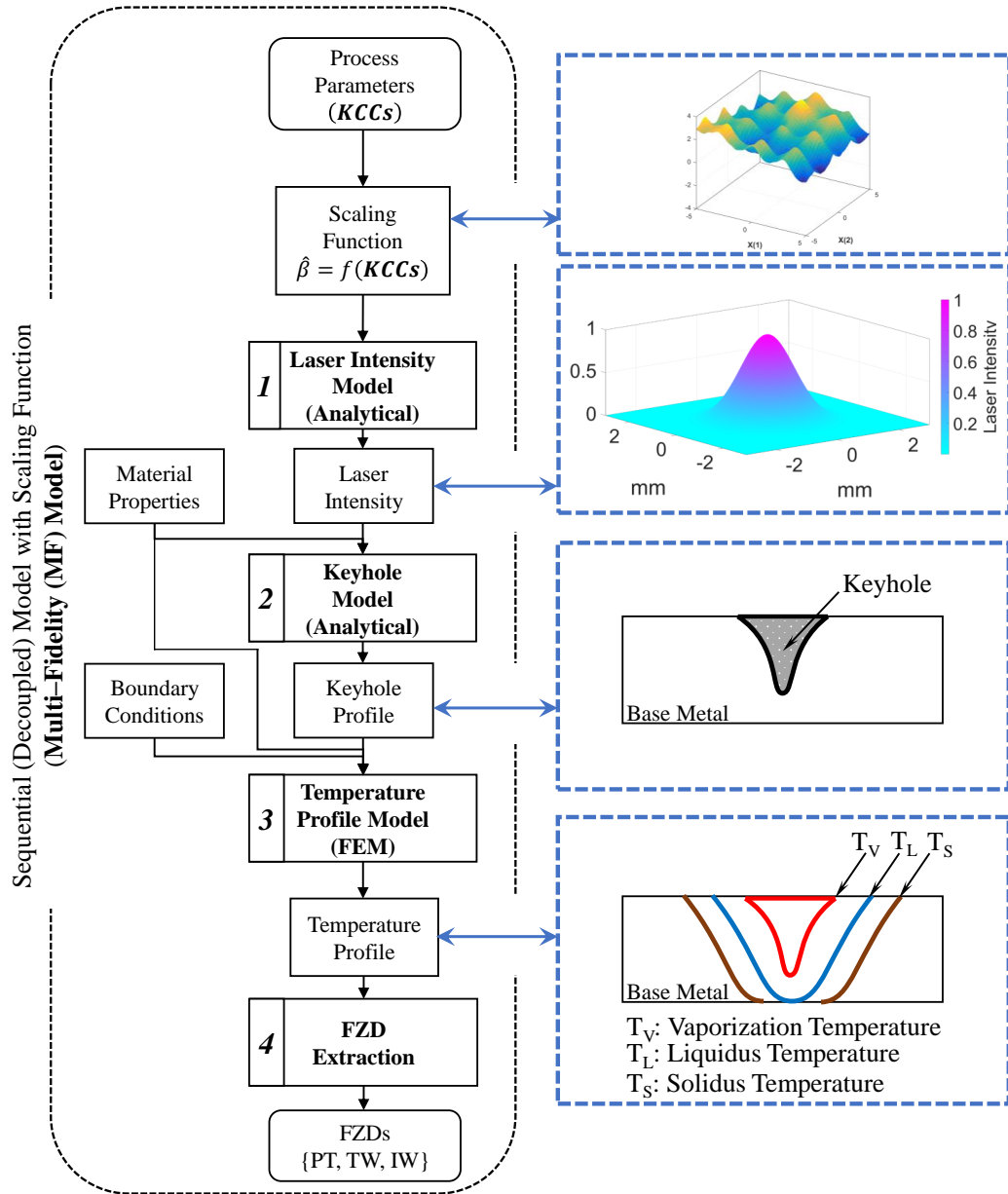
**Fig. 5.4.** The framework of the proposed sequential decoupled model (Low-Fidelity (LF) model – Moving from Point A to Point B in Fig. 5.3)

The proposed LF model has a fast-computational time, but it suffers from low accuracy. Therefore, a correction function is introduced to increase accuracy without increasing computational cost. In the literature (Fernández-Godino et al., 2016), the chosen correction function can either output (i) the scaling factor ( $\beta$ ) which is the ratio between the results of the HF and the LF models, (ii) the discrepancy factor ( $\delta$ ) which is the difference between the results of the HF and the LF models, or (iii) a mix of both. In this research, the correction function is expressed based on the scaling factor (also called the scaling function due to the chosen method), and the methodology to compute the scaling function is given in Fig. 5.5.



**Fig. 5.5.** The methodology of computing the scaling function over the design space

The laser intensity is the most important parameter for the keyhole model. Therefore, the scaling factor is applied before the laser intensity model to ensure that it is being used within the laser model and that henceforth its effect is propagated throughout. The methodology for multi-fidelity (MF) is given in Fig. 5.6.



**Fig. 5.6.** The flow chart of the sequential decoupled model with scaling function (Multi-Fidelity (MF) Model – Moving from Point B to Point C in Fig. 5.3)

The formulation of each sub-models presented in the LF model is given in the following sections.

### 5.2.1 Formulation of the Laser Intensity

In this section, the peak laser intensity ( $I_0$ ), the laser intensity absorbed by the material surface ( $I_1$ ) and the laser intensity acting on the keyhole wall ( $I_2$ ) are



defined. The beam radius ( $w(z)$ ) for a given distance ( $z$ ) from the beam waist radius ( $w_0$ ) is expressed as:

$$w(z) = w_0 \sqrt{1 + \left( \frac{z \mp FO}{z_R} \right)^2} \quad (5.1)$$

where  $z_R$  is the Rayleigh length. The laser intensity is simply the laser power ( $P_L$ ) divided by the spot area of the laser beam ( $A_{spot}(z)$ ). The laser intensity for a given laser power and beam radius is defined as:

$$I(x, y, z) = \frac{2P_L}{\pi w(z)^2} \exp \left[ -2 \left( \left( \frac{x}{w(z)} \right)^2 + \left( \frac{y}{w(z)} \right)^2 \right) \right] \quad (5.2)$$

where  $x$  is the coordinate in the direction of welding,  $y$  is perpendicular to the direction of weld, and  $z$  is the propagation direction of the laser beam. Equation 5.2 considers the on-surface spot of the laser beam is a circle. However, when the laser beam hits the surface with an incidence angle ( $\alpha$ ), the on-surface spot is no longer a circle, instead, it is an ellipse, and its the semi-major ( $w_{x_0}$ ) and the semi-minor axes ( $w_{y_0}$ ) can be found using the intersection of a hyperboloid with a plane. The calculation of these dimensions is explained in **Appendix B**. In this case, the laser beam intensity can be calculated as:

$$I(x, y, z) = \frac{2P_L}{\pi \cdot w_x(z) \cdot w_y(z)} \exp \left[ -2 \left( \left( \frac{x}{w_x(z)} \right)^2 + \left( \frac{y}{w_y(z)} \right)^2 \right) \right] \quad (5.3)$$

The maximum laser intensity ( $I_0$ ) is achieved at the beam waist radius ( $w_0$ ) which is written as:

$$I_0 = \frac{2P_L}{\pi \cdot w_{x_0} \cdot w_{y_0}} \exp \left[ -2 \left( \left( \frac{x}{w_{x_0}} \right)^2 + \left( \frac{y}{w_{y_0}} \right)^2 \right) \right] \quad (5.4)$$

The laser-material absorption mechanisms play a fundamental role in determining the occurring physics in the laser welding process. The mechanisms are divided into two categories as follows: (i) absorption outside the keyhole which involves the plasma plume absorption ( $\alpha_{plasma}$ ) and the surface absorption ( $\alpha_{surf}$ ), and (ii) absorption inside the keyhole which involves the inverse Bremsstrahlung ( $\alpha_{in-Bre}$ ) and the Fresnel absorption ( $\alpha_{Fre}$ ).

Step 1: Calculating the laser intensity absorbed at the material surface

The first mechanism involves the transfer of laser intensity between the laser source and the surface of the work. It defines the actual laser intensity received

by the base metal from the total laser intensity generated at the laser source. The laser beam has an initial laser intensity of  $I_0$ . When the laser beam passes through the plasma plume, a part of its energy is absorbed by the plume ( $\alpha_{plasma}$ ) and the remaining  $(1 - \alpha_{plasma})$  is transferred to the base metal. Then, the laser beam is absorbed according to the surface absorption mechanism ( $\alpha_{surf}$ ) to melt the base metal and to form the keyhole. The surface absorption mechanism is generally dependent on the wavelength of the laser beam (See Fig. 2.4). To sum up, the laser intensity that is absorbed by the material surface is given as:

$$I_1 = I_0 \cdot \alpha_{surf} \cdot (1 - \alpha_{plasma}) \quad (5.5)$$

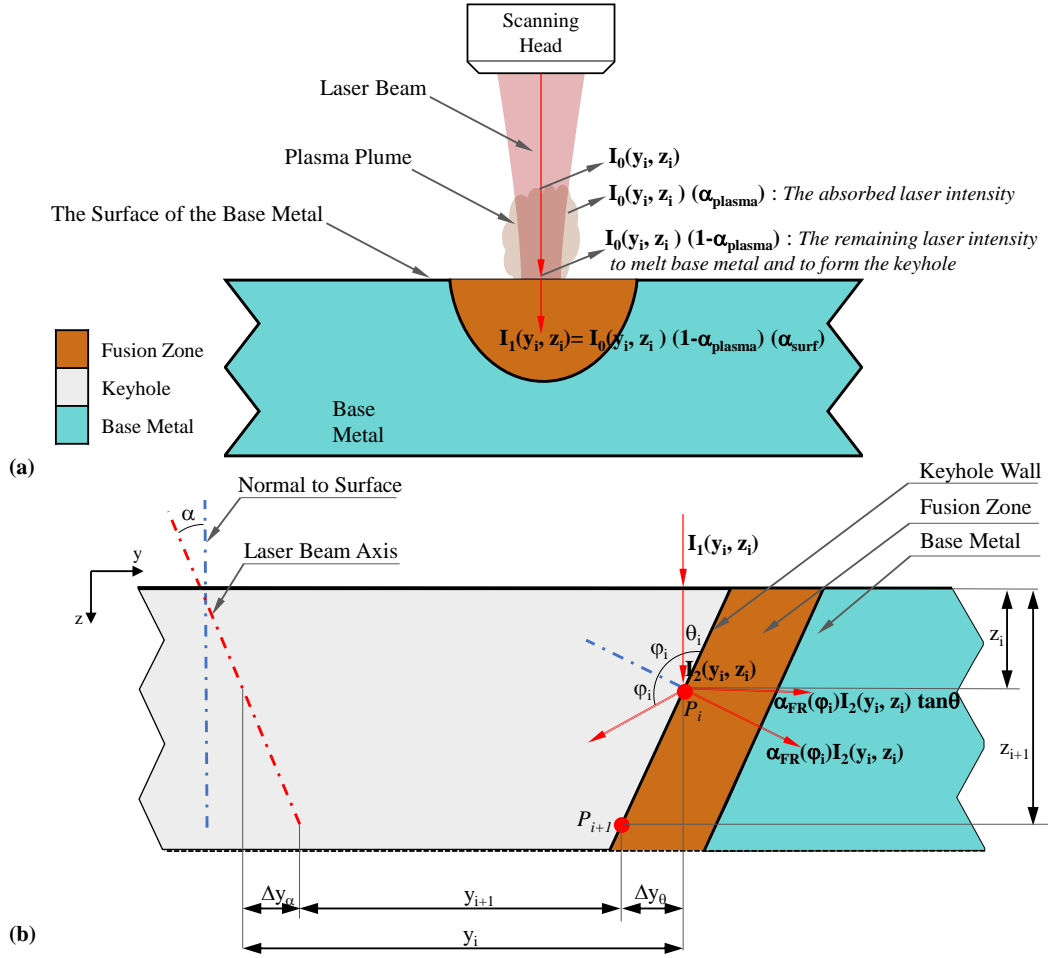
Step 2: Calculating the laser intensity absorbed at the keyhole wall

The absorbed laser intensity ( $I_1$ ) is further decreased along the keyhole depth direction which obeys the inverse Bremsstrahlung absorption ( $\alpha_{inBre}$ ). Finally, the laser intensity that reaches the keyhole wall ( $I_2$ ) is absorbed at the keyhole wall according to the Fresnel absorption ( $\alpha_{Fre}$ ) are given in Eqs. (5.6) and (5.7), respectively.

$$I_2 = \begin{cases} I_1 \cdot \exp(-\alpha_{inBre} \cdot \Delta z) & z \leq t_u \\ I_1 \cdot \exp(-\alpha_{inBre} \cdot \Delta z) \cdot \exp(-\alpha_{gap} \cdot g) & z \geq t_u + g \end{cases} \quad (5.6)$$

$$I_{2abs} = I_2 \cdot \alpha_{Fre} \quad (5.7)$$

where  $I_{2abs}$  is the absorbed laser intensity at the keyhole wall, and  $\Delta z$  the distance that the laser beam travels inside the keyhole before hitting the keyhole wall. All these absorption mechanisms are shown in Fig. 5.7.



**Fig. 5.7.** A schematic description of the absorption mechanism in the laser welding process (a) outside the keyhole: the plasma absorption ( $I_0 \cdot (1 - \alpha_{plasma})$ ) and the surface absorption ( $I_1 = I_0 \cdot \alpha_{surf} \cdot (1 - \alpha_{plasma})$ ) (b) inside the keyhole: the inverse-Bremsstrahlung absorption ( $I_2 = I_1 \cdot \exp(-\alpha_{inBre} \cdot \Delta z)$ ) and the Fresnel absorption ( $I_{2_{abs}} = I_2 \cdot \alpha_{Fre}$ )

## 5.2.2 Formulation of the Keyhole Profile

The energy balance method was developed by Kaplan (1994). It is assumed in this method that the heat flow through the keyhole wall is equal to the heat loss at the keyhole. The heat loss depends on the absorbed laser intensity which is given in Eqs. (5.5) to (5.7). The heat flow is determined by applying Fourier's law of heat conduction by substituting the Rosenthal's moving line source solution. Then, the following equation is obtained in the polar coordinates  $(r, \phi)$  as:

$$q(r, \phi) = \frac{1}{r} (T_v - T_0) kPe \left( \cos(\phi) + \frac{K_1(Pe)}{K_0(Pe)} \right) \quad (5.8)$$

where  $q$  is the heat flow,  $T_v$  is the vaporization temperature,  $T_0$  is the ambient temperature,  $Pe$  is the Peclet number,  $K_1$  and  $K_0$  is the modified Bessel function of the second kind the first order and the second kind the zero order, respectively. As mention before the plane of interest is perpendicular to the welding direction (the  $YZ$  plane) because it is the transverse cross-section of the weld in which FZDs are measured. Therefore, the  $r$  is equal to  $y$ , and the  $\phi$  is equal to  $\pi/2$ . Furthermore, it is assumed in the energy balance method that the laser beam is perpendicular to the workpiece surface and the keyhole opening radius ( $r_{KH_0}$ ) is pre-determined. In this study, the method is generalized by considering the incidence angle and the keyhole opening radius ( $r_{KH_0}$ ) based on the pressure balance.

Step 1: Calculating keyhole opening radius ( $r_{KH_0}$ )

When the keyhole has fully developed, pressures acting on the keyhole wall are in balance. In this quasi-steady state, the ablation pressure ( $p_{abl}$ ) of the vaporized material counteracts mainly against the pressure due to the surface tension ( $p_\gamma$ ) of the melt around the keyhole. When these two pressures are in balance the keyhole is widely opened. The pressure due to the surface tension is described as:

$$p_\gamma = \frac{\gamma_{surf}}{r_{KH_0}} \quad (5.9)$$

where  $\gamma_{surf}$  is the surface tension coefficient and  $r_{KH_0}$  is the keyhole opening radius. The ablation pressure is written as:

$$p_{abl} = \left( \frac{I_v}{L_v} \right) \sqrt{\left( \frac{\gamma \cdot R \cdot T_s}{M} \right)} \quad (5.10)$$

where  $I_v$  is expressed as:

$$I_v = I_1 - k \frac{(T_v - T_m)}{\left( \frac{\kappa}{W_s} \right)} \quad (5.11)$$

where  $T_v$  and  $T_m$  are the evaporation and melting temperatures of the material,  $\kappa$  is the thermal diffusivity,  $W_s$  is the welding speed,  $k$  is the thermal conductivity, and  $I_1$  is the laser beam intensity that is absorbed by the material surface. The keyhole opening radius ( $r_{KH_0}$ ) is calculated by solving Eqs. 5.9 to 5.11 (Volpp and Vollertsen, 2016).

Step 2: Calculating the keyhole (KH) profile

The energy balance method calculates the KH profile at the defined 2D plane. The plane of interest in this study is the  $YZ$  plane which is perpendicular to the

direction of the weld. It is the transverse cross-section of the weld which corresponds to the same plane with macro-section images of the weld.

Let us consider an infinitesimally thin layer of thickness  $dz$ , and a point  $\mathbf{P}_i = [y_i, z_i]$  at the keyhole (See Fig. 5.7b). The local incoming laser intensity ( $I_2(y_i, z_i)$ ) at this point is absorbed according to the Fresnel absorption in the direction perpendicular to the keyhole wall (See Fig. 5.7b). The absorbed intensity ( $I_{2_{abs}}$ ) at the point  $\mathbf{P}_i$  is defined in Eq. (5.7). Within the infinitesimally thin layer  $dz$ , it is assumed that the tangential component of the absorbed beam intensity is much larger than those parallel to the incoming beam direction. Therefore, the absorbed laser intensity is mainly transported along horizontally to the base material. The energy balance at the point  $\mathbf{P}_i$  is described as:

$$\begin{aligned}
I_{2_{abs}} \cdot \tan(\theta(y_i, z_i)) &= q(y_i, z_i) \\
\alpha_{FR}(\varphi(y_i, z_i)) \cdot I_2(y_i, z_i) \cdot \tan(\theta(y_i, z_i)) &= q(y_i, z_i) \\
\tan(\theta(y_i, z_i)) &= \frac{\frac{1}{y_i} (T_v - T_0) kPe \left( \frac{K_1(Pe)}{K_0(Pe)} \right)}{\alpha_{FR}(\varphi(y_i, z_i)) \cdot I_2(y_i, z_i)}
\end{aligned} \tag{5.12}$$

The position of the next point ( $\mathbf{P}_{i+1}$ ) at the keyhole is found updating coordinates as:

$$\begin{aligned}
z_{i+1} &= z_i + dz \\
y_{i+1} &= y_i - \Delta y_\alpha - \Delta y_\theta \\
\Delta y_\alpha &= dz \cdot \tan(\alpha) \text{ and } \Delta y_\theta = dz \cdot \tan(\theta(y_i, z_i))
\end{aligned} \tag{5.13}$$

The solution of Eq. 5.13 requires initial coordinates of the point  $\mathbf{P}_0 = (y_0, z_0)$ . The  $y_0$  equals to the keyhole opening radius and the  $z_0$  equals to zero to indicate the surface of the material. The energy balance method defined by Kaplan (1994) assumes that the keyhole opening radius equals to the on-spot radius of the laser beam. In this study,  $y_0$  equals to  $r_{KH_0}$ , which is computed based on Eqs. 5.9 to 5.11. The KH profile is calculated point-by-point starting from the surface of material downwards until the  $y_i$  reaches zero (for the blind keyhole) or when the  $z_i$  equals to the metal thickness (for the open keyhole mode).

### 5.2.3 Formulation of the Temperature Profile

The LF-model consists of three sub-models. These models are the laser intensity model, the KH profile model and the temperature distribution model. The first two models are based on analytic solutions. However, the temperature profile is calculated by solving the heat transfer equations using the FEM, after obtaining the

KH profile. The heat transfers from the KH profile into the base metal in conduction for a time duration equal to the interaction time ( $t_i$ ). It is defined as a duration at which a given point is exposed to the laser. Therefore, the heat transfer equation is defined as:

$$\rho c_p^{eq} \left( \frac{\partial T}{\partial t} \right) = k \left( \frac{\partial^2 T}{\partial y^2} + \frac{\partial^2 T}{\partial z^2} \right) \quad (5.14)$$

The phase change from solid to liquid is taken into account by employing the effective specific heat capacity method. The equivalent specific heat capacity is written as:

$$C_p^{eq}(T) = C_{p_{solid}} + L_f \frac{\exp\left(-\left(\frac{T-T_m}{\Delta T}\right)^2\right)}{\sqrt{\pi\Delta T^2}} \quad (5.15)$$

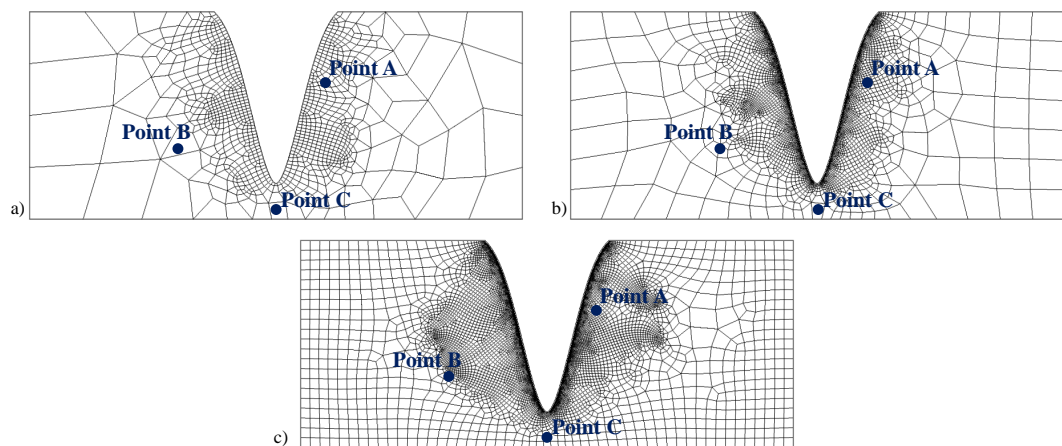
where  $L_f$  is latent heat of fusion,  $T_m$  melting temperature; and,  $\Delta T$  is the difference between solidus and liquidus temperature. Two types of boundary conditions were specified; constant temperature on the keyhole wall and the heat dissipation by convection on the other surfaces. All surfaces are at room temperature as an initial condition. The assumptions employed in this study are listed as follows:

- The heat transfer is the main driving physical phenomena to compute fusion zone shape. The other phenomena are not considered in this study.
- The material thickness and the joining gap are assumed to be constant.
- The temperature of the KH equals to the vaporization temperature ( $T_v$ )
- Two types of boundary conditions are specified: the constant temperature on the keyhole and surface convection on the other boundaries.
- The heat transfer between the material and the welding table is ignored.

The heat transfer problem was numerically solved by utilizing the FEM which was implemented in COMSOL Multiphysics<sup>®</sup> v5.2. The computer specification used in this study was Intel-i7 2.8 GHz CPU and 16 GB DDR3 Memory. In order to determine the optimum mesh configuration, a mesh convergence study was applied in the FEM model where a different temperature profile was obtained using different mesh sizes. The other parameters, such as the KH profile, material properties, and the boundary conditions were kept constant. The computational domain was 5 mm x 2.5 mm. The mesh was constructed using a non-structure grid using (a) 972 elements with the maximum element size of 0.65 mm (coarse mesh), (b) 11549 elements with the maximum element size of 0.335 mm (normal mesh), and (c) 23976 elements with the maximum element size of 0.05 mm (fine mesh). Three different points were selected inside the computational domain. The computational domains generated employing different mesh sizes and three sampling points within these

domains are illustrated in Fig. 5.8. The temperature values at the sampling points within the different computational domains created using different mesh sizes, and the computational time for each domain are recorded in Table 5.1.

It is a known fact that the FEM model with fine mesh (small element size) may give very accurate results but can take longer computational time. On the contrary, the FEM with coarse mesh (large element size) may give to less accurate results but can save more computing time. According to the results, the temperature value at each sampling point converged at a certain temperature value as the mesh size increased. However, the computational time also increased with the increase in the mesh size. The subject of physics in the FEM study is the two-dimensional heat transfer problem which involves one unknown parameter that is temperature ( $T$ ). Therefore, there is no need to have a high computational time. Thus, the computational domain was meshed by the non-structure mapping method with a maximum element size of  $0.3 \text{ mm}$ .



**Fig. 5.8.** The computational domains generated employing different mesh sizes (a) Coarse Mesh, (b) Normal Mesh, (c) Fine Mesh, and three sampling points within these domains

**Table 5.1:** The temperature values at the sampling points and the computational time for each mesh size. The temperature value at each sampling point converges to a certain temperature value as the mesh size is increased. The computational time also increases with the increase in the mesh size

Mesh Size	The Temperature at Point A (K)	The Temperature at Point B (K)	The Temperature at Point C (K)	The Computational Time (s)
Coarse (The maximum element size 0.65 mm)	2625.706	1018.007	2273.003	16
Normal (The maximum element size 0.335 mm)	2619.545	1020.190	2274.190	53
Fine (The maximum element size 0.05 mm)	2619.511	1020.144	2274.011	128

#### 5.2.4 Formulation of FZDs Extraction

In this study, the fusion zone (FZ) profile is extracted from the temperature profile which depends on the choice of a reference temperature, such as the liquidus temperature ( $T_L$ ). Then the area enclosed by this isotherm ( $T = T_L$ ) represents the weld. The FZDs are computed from this area according to the industrial standards (EN ISO 13919-1, 1997; EN ISO 13919-2, 2001).

The FZDs are calculated according to the linear distance between two points which are on the obtained FZ profile. Top Width ( $TW : (FZD_1)$ ) is not yet clearly defined. In most of the cases, it can be considered the width of the weld bead along the top surface. In order to guarantee that the interface width is enough to provide the required strength, the minimum top width should be 50% of top sheet thickness. Interface Width ( $IW : (FZD_2)$ ) characterise the welded area that holds both sheets together. Thus, penetration and interface width are the main FZDs that affect weld strength. Interface width is normally measured as the horizontal distance along the weld interface, and it should be no less than 90% of thinnest sheet thickness. Penetration ( $PT : (FZD_3)$ ) is the most critical parameter, strictly related to the weld strength. In a lap joint, it is the vertical extension of the weld in the lower sheet. For an acceptable weld, the minimum penetration must not be lower than the 60% of the thickness of the lower sheet metal.

The constant parameters used for developing the LF model are given in Table 5.2.



**Table 5.2:** The constant parameters used in the LF model

Parameter	Symbol	Value	Unit
Thermal conductivity	$k$	49.8	$W/(mK)$
Specific heat	$c_p$	435	$kJ/(kgK)$
Latent heat of fusion	$L_f$	2.72e5	$J/kg$
Latent heat of evaporation	$L_v$	6.1e6	$J/kg$
Density	$\rho$	7800	$kg/m^3$
Initial temperature	$T_0$	293	$K$
Vaporisation temperature	$T_v$	3100	$K$
Liquidus temperature	$T_m$	1800	$K$
Solidus temperature	$T_m$	1750	$K$
Temperature difference	$\Delta T$	50	$K$
Wavelength of the laser beam	$\lambda$	1.064	$\mu m$
Molar mass	$M$	24.3	$g/mol$
Surface Tension	$\gamma_{surf}$	0.288	$N/m$
Heat transfer coefficient of air	$h_c$	25	$W/(m^2K)$
Isentropic expansion factor of air	$\gamma$	1.3	-
Upper sheet metal thickness	$t_u$	1	$mm$
Lower sheet metal thickness	$t_l$	1	$mm$

## 5.3 Research Methodology to Develop Multi-Fidelity Model

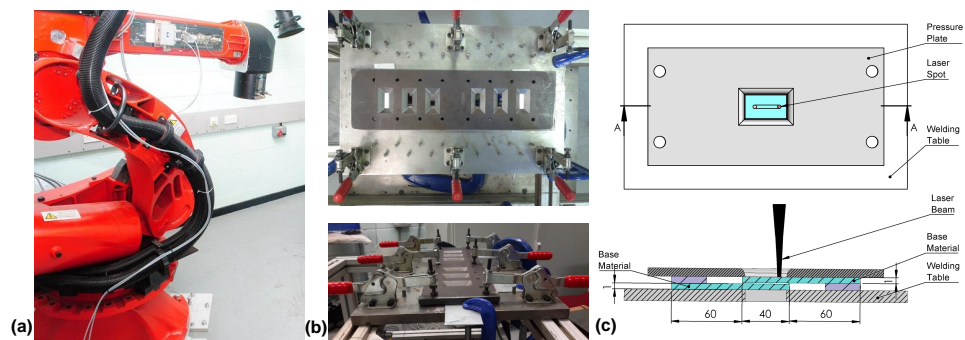
### 5.3.1 Materials & Experimental Setup

The material used in this study was DX54D+Z hot-dip galvanized steel with a thickness of 1.00  $mm$ . It has a nominal carbon content of 0.12% and its chemical composition % by mass, mechanical and thermal properties are given in Tables 2.3 to 2.5, respectively. These values are taken from the industrial standard (EN ISO 10327, 2004).

Two series of experiments were carried out. The first series served to characterise the welding process and to develop the model. The second series was used to validate the developed model by confirmation experiments. Each experiment was conducted on a 100  $mm \times 40 mm \times 1 mm$  sheet metal and a linear weld of 25  $mm$  was performed in an overlap joint configuration. The control of the joining gap size is crucial during welding. Thus, it was created using calibrated metal shims of

required thickness, and a fixture was designed to prevent distortion and to have a uniform joining gap. A pressure plate was put over the sheets and tightly clamped in order to minimize welding distortion and metal strip variation.

Laser welding experiments were carried out using an IPG Photonics YLR-4000 Ytterbium Fibre laser source with a nominal power of 3 kW. The laser was delivered using an optical fibre which had a core diameter of 200  $\mu\text{m}$ . The spot diameter of the laser beam on the surface was 900  $\mu\text{m}$ , while the output wavelength of the laser beam was 1064 nm. In order to vary the position of the laser beam focus in space, a standard industrial robot (COMAU SmartLaser Robotic) was employed. The robot integrated the focusing optics and repositioning scanning head in a single architecture. Thus, the robot could weld on-the-fly. The shielding gas was not employed, but the laser head was equipped with an “air knife” to repulse eventual spatter coming from the material under process. The compressed air also had the function to move away from the plume from the welding area. The welding robot, the top and front images of designed fixture, and its cross-section image highlighting the welding location are given in Fig. 5.9.



**Fig. 5.9.** Experimental setup. (a) The welding robot, (b) The welding table and clamp locations, (c) Top view and cross-section of welding fixture showing laser welding location and direction

After laser welding two sheet metals, the welded sample was initially sectioned in the transverse direction. Then, the cut sample was mounted using a mounting press. Later, the surface of the mounted sample was polished with different abrasive plates. Finally, the polished sample was etched by a mixture of acid to reveal the fusion zone. The image was taken by an optical microscope and fusion zone dimensions were measured by an image processing software. The steps followed for preparation and measurement are described in Table 5.3.

**Table 5.3:** The procedure to be followed for the metallographic analysis of the weld

Operation	Description	Equipment
Sectioning	The test specimens were cut into two pieces	Linear Precision Saw Buehler IsoMet 5000
Sample mounting	Samples mounted at 290 <i>bar</i> 3 minutes of heat and cool time	Automatic Mounting Press Buehler SimpliMet 1000
Surface preparation Phase 1	Polishing Disc: Abrasive disc (Grit 600/P1200) Duration: 1 <i>min</i> Revolution speed: 275 <i>rpm</i> Rotation: Complementary Compressing Force: 25 <i>N</i> Lubricant: Water	Sample Preparation System Buehler Phoenix 4000
Surface preparation Phase 2	Polishing Disc: Grinding Disc 9 $\mu m$ diamond Duration: 3 <i>min</i> Revolution speed: 275 <i>rpm</i> Rotation: Contrary Compressing Force: 25 <i>N</i> Lubricant: 9 $\mu m$ Polycrystalline Diamond Suspension	Sample Preparation System Buehler Phoenix 4000
Surface preparation Phase 3	Polishing Disc: Trident Disc 3 $\mu m$ diamond Duration: 5 <i>min</i> Revolution speed: 275 <i>rpm</i> Rotation: Complementary Compressing Force: 25 <i>N</i> Lubricant: 3 $\mu m$ Polycrystalline Diamond Suspension	Sample Preparation System Buehler Phoenix 4000
Surface preparation Phase 4	Polishing Disc: Micro-cloth Disc 0.05 $\mu m$ Duration: 2 <i>min</i> Revolution speed: 275 <i>rpm</i> Rotation: Contrary Compressing Force: 25 <i>N</i> Lubricant: 20 <i>ml</i> Master Prep. Polishing Suspension	Sample Preparation System Buehler Phoenix 4000
Etching	45 <i>ml</i> of methanol 6 <i>ml</i> of Nitric Acid	-
Inspection	Macro-section pictures were taken for every sample. Fusion zone dimensions were digitally measured.	Optical Microscope LEICA DM 4000 M Buehler OmniMet Image Capturing Software

### 5.3.2 Design of Experiments

The welding process can be performed in many configurations, such as edge welding, butt welding, overlap welding, *etc.* From screening experiments, it was understood that Penetration ( $PT$ ) and Top Width ( $TW$ ) were correlated to each other in overlap welding. However, Interface Width ( $IW$ ) was not correlated with each other FZDs. The proposed LF model simultaneously calculates the defined FZDs (See Fig. 5.4). To increase the accuracy of the LF model, two new ratios are introduced, called the first scaling factor and the second scaling factor. The first scaling factor considers the joint behaviour of Penetration ( $PT$ ) and Top Width ( $TW$ ); whereas, the second scaling factor takes into account only Interface Width ( $IW$ ).

In the manufacturing terminology, process parameters are called “*Key Control Characteristics*” (KCCs). The space determined by the upper and the lower limits of each KCC is called the “*Design Space*” or the “*KCC-space*”. The scaling factors are not constant for given process parameters. Instead, there are varying over the KCC-space. Thus, a mathematical function is obtained over the KCC-space for each scaling factor.

As a pre-process, the design of experiments (DoE) table was generated to define KCCs to be used in each experimental configuration. The first scaling factor was obtained from the bead-on-plate welding experiments. A full factorial design of experiments was generated by considering the blocking effect. It was setup with five levels of welding speed (2.0 *m/min*, 2.3 *m/min*, 2.6 *m/min*, 2.9 *m/min* and 3.2 *m/min*), and three levels of incidence angle ( $0^\circ$ ,  $10^\circ$  and  $20^\circ$ ). Five replications were performed for each experimental configuration. Thus, 75 welding experiments were conducted. After the welding experiments, the post-processing was performed according to the defined procedure (See Table 5.3) to obtain a macro-section image of the weld. Finally, the 2 FZDs (Penetration, Top Width) were measured from the macro-section image. The macro-section image of the weld and the result of each measurement are presented in **Appendix C**.

The second scaling factor is obtained from the overlap welding experiments. Again, a full factorial design of experiments was generated. It was arranged with four levels of joining gap (0.10 *mm*, 0.15 *mm*, 0.20 *mm* and 0.25 *mm*), five levels of welding speed and three levels of incidence angle. The levels used for welding speed and incidence angle in the bead-on-plate experiments were also used in the overlap welding experiments. Seven replications were performed for each experimental design. Thus, 420 welding experiments were conducted, and the same procedure (See Table 5.3) was performed to obtain FZDs. The experimental results for each

replication are presented in **Appendix D**.

### 5.3.3 Off-line Generation of Scaling Functions

The scaling factor is the ratio between the results of the HF and the LF models. The HF model is the physical experiments, and the LF model is the proposed sequential (decoupled) model (See Fig. 5.4). The proposed MF model is basically the LF model with utilizing the scaling factor. However, the scaling factor is not a constant value over the KCC-space. Instead, it is varying, and the mathematical function that estimates the scaling factor over the KCC-space is called the scaling function.

In this research, the scaling factors are developed based on two scenarios: *(i)* mean ( $\mu$ ) only analysis, and *(ii)* mean and standard deviation ( $\mu \mp \sigma$ ) analysis. Therefore, the process variation is represented inside the scaling factor.

Suppose that all KCCs at each experimental configuration can be gathered as:

$$\mathbf{KCCs} = \begin{bmatrix} KCC_1^{(1)} & \cdots & KCC_{N_i}^{(1)} \\ \vdots & KCC_i^{(k)} & \vdots \\ KCC_1^{(N_k)} & \cdots & KCC_{N_i}^{(N_k)} \end{bmatrix} \quad (5.16)$$

where  $i$  is the index of KCC,  $k$  is the index of experimental configuration,  $N_i$  is the total number of KCCs, and  $N_k$  is the total number of experimental configurations. The set of KCCs given in Eq. (5.16) implicitly represents the DoE table. According to the defined experimental procedure, the physical experiments were conducted at each experimental configuration. The measured results of each Fusion Zone Dimension ( $^{HF}FZDs$ ) can be written as:

$$\begin{aligned} \mathbf{^{HF}FZDs} &= \{ \mathbf{^{HF}FZD}_j \mid \forall j=1, \dots, N_j \} \\ \mathbf{^{HF}FZD}_j &= \begin{bmatrix} \mathbf{^{HF}FZD}_j^{(1)} \\ \vdots \\ \mathbf{^{HF}FZD}_j^{(k)} \\ \vdots \\ \mathbf{^{HF}FZD}_j^{(N_k)} \end{bmatrix} = \begin{bmatrix} {}^{HF}FZD_j^{(1,1)} & \cdots & {}^{HF}FZD_j^{(1,N_l)} \\ \vdots & \ddots & \vdots \\ {}^{HF}FZD_j^{(k,l)} & \cdots & \vdots \\ \vdots & \ddots & \vdots \\ {}^{HF}FZD_j^{(N_k,l)} & \cdots & {}^{HF}FZD_j^{(N_k,N_l)} \end{bmatrix} \end{aligned} \quad (5.17)$$

where  $j$  is the index of  $^{HF}FZD$ ,  $l$  is the index of the replication,  $N_j$  is the total number of FZDs, and  $N_l$  is the total number of replications. The mean value of the  $k^{th}$  experimental configuration of the  $j^{th}$  FZD is calculated using Eq. (5.18). The calculated mean values at each experimental configuration can be collected in

a set using Eq. (5.19). Similarly, the standard deviation of the  $k^{th}$  experimental configuration of the  $j^{th}$  FZD is computed using Eq. (5.20). The computed standard deviations at each experimental configuration can be grouped in a set using Eq. (5.21).

$$\mu_{HF FZD s_j^{(k)}} = \frac{1}{N_l} \sum_{l=1}^{N_l} HF FZD s_j^{(k,l)} \quad (5.18)$$

$$\boldsymbol{\mu}_{HF FZD s_j} = \left[ \mu_{HF FZD s_j^{(1)}}, \dots, \mu_{HF FZD s_j^{(k)}}, \dots, \mu_{HF FZD s_j^{(N_k)}} \right]^T \quad (5.19)$$

$$\sigma_{HF FZD s_j^{(k)}} = \sqrt{\frac{1}{N_l - 1} \sum_{l=1}^{N_l} \left( HF FZD s_j^{(k,l)} - \mu_{HF FZD s_j^{(k)}} \right)^2} \quad (5.20)$$

$$\boldsymbol{\sigma}_{HF FZD s_j} = \left[ \sigma_{HF FZD s_j^{(1)}}, \dots, \sigma_{HF FZD s_j^{(k)}}, \dots, \sigma_{HF FZD s_j^{(N_k)}} \right]^T \quad (5.21)$$

Computer experiments are also carried out in parallel with the physical experiments. The same DoE generated for the physical experiments is used for the computer experiments and the computed results of each Fusion Zone Dimension ( $LF FZD$ ) can be written as:

$$\boldsymbol{LF FZD s_j} = \left[ LF FZD s_j^{(1)}, \dots, LF FZD s_j^{(k)}, \dots, LF FZD s_j^{(N_k)} \right]^T \quad (5.22)$$

As aforementioned, the scaling factor is the ratio between the results of the HF and the LF models. The first option is based on the mean value. Let us consider the mean value of the  $j^{th}$  FZD at the  $k^{th}$  experimental configuration ( $\mu_{HF FZD j^{(k)}}$ ), and the computed result according to the LF model at the same configuration ( $LF FZD j^{(k)}$ ). The  $j^{th}$  scaling factor as defined in Eq. (5.23). The calculated factors at all experimental configurations are gathered in a set employing Eq. (5.24).

$$\beta_{j_\mu}^{(k)} = \frac{\mu_{HF FZD j^{(k)}}}{LF FZD j^{(k)}} \quad (5.23)$$

$$\boldsymbol{\beta}_{j_\mu} = \left[ \beta_{j_\mu}^{(1)}, \dots, \beta_{j_\mu}^{(k)}, \dots, \beta_{j_\mu}^{(N_k)} \right]^T \quad (5.24)$$

In general, the scaling factor is developed by using mean-only analysis. Even though the mean value implicitly contains the process variation, it is better to consider the mean value and the standard deviation together. Therefore, the second

and the third options are introduced to consider one standard deviation above and below the mean value of the experimental results ( $\mu \mp \sigma$ ). The  $j^{th}$  scaling factor at the  $k^{th}$  experimental configuration based on these options is formulated in Eq. (5.25).

$$\beta_{j\mu+\sigma}^{(k)} = \frac{\mu_{HF FZD_j^{(k)}} + \sigma_{HF FZD_j^{(k)}}}{LF FZD_j^{(k)}}, \quad \beta_{j\mu-\sigma}^{(k)} = \frac{\mu_{HF FZD_j^{(k)}} - \sigma_{HF FZD_j^{(k)}}}{LF FZD_j^{(k)}} \quad (5.25)$$

The calculated factors at all experimental configurations based on one standard deviation above the mean value are gathered in a set utilizing Eq. (5.26). Similarly, the calculated factors at all experimental configurations based on one standard deviation below the mean value are collected in a set using Eq. (5.27).

$$\beta_{j\mu+\sigma} = \left[ \beta_{j\mu+\sigma}^{(1)}, \dots, \beta_{j\mu+\sigma}^{(k)}, \dots, \beta_{j\mu+\sigma}^{(N_k)} \right]^T \quad (5.26)$$

$$\beta_{j\mu-\sigma} = \left[ \beta_{j\mu-\sigma}^{(1)}, \dots, \beta_{j\mu-\sigma}^{(k)}, \dots, \beta_{j\mu-\sigma}^{(N_k)} \right]^T \quad (5.27)$$

To sum up, 4 different sets are calculated. These sets are as follows: (i) the set of KCCs (Eq. (5.16)), (ii) the set of scaling factors developed considering only the mean value (Eq. (5.24)), the set of scaling factors developed considering one standard deviation above the mean value (Eq. (5.26)), and the set of scaling factors developed considering one standard deviation below the mean value (Eq. (5.27)). Generally, the least squares method is used to develop a regression model (i.e. a mathematical function) between two sets. A mathematical function is computed between the set of KCCs and the chosen set of scaling factors by using the least squares method. The form of the function is selected as the second-degree polynomial. The  $j^{th}$  scaling functions that estimate the  $j^{th}$  scaling factors developed based on the mean value, one standard deviation above the mean value and one standard deviation below the mean value are given in Eqs. (5.28) to (5.30), respectively.

$$\widehat{\beta}_{j\mu} = f_{\beta_{j\mu}}(KCC_1, \dots, KCC_{N_i}) \quad (5.28)$$

$$\widehat{\beta}_{j\mu+\sigma} = f_{\beta_{j\mu+\sigma}}(KCC_1, \dots, KCC_{N_i}) \quad (5.29)$$

$$\widehat{\beta}_{j\mu-\sigma} = f_{\beta_{j\mu-\sigma}}(KCC_1, \dots, KCC_{N_i}) \quad (5.30)$$

Even though the scaling factor ( $\beta_{j\mu}^{(k)}$ ) and the error ( $\varepsilon_j^{(k)}$ ) between the results of the HF and the LF models are different, a mathematical relation between these two terms can be driven in Eq. (5.31).

$$\varepsilon_j^{(k)} = \frac{\mu_{HF FZD_j^{(k)}} - LF FZD_j^{(k)}}{\mu_{HF FZD_j^{(k)}}} = 1 - \frac{LF FZD_j^{(k)}}{\mu_{HF FZD_j^{(k)}}} = 1 - \frac{1}{\beta_{j\mu}^{(k)}} \quad (5.31)$$

### 5.3.4 Development & Validation of Multi-Fidelity Model

The goal of this study is to obtain the FDZs from the FZ profile in the overlap welding. The occurring physics in laser welding is decoupled by initially obtaining laser intensity acting on the surface of the material, then calculating the keyhole profile using an analytic solution. Finally, only heat transfer via heat conduction in the solid is solved using the FEM to obtain a temperature profile. FZDs are extracted from the FZ profile which is the area enclosed by the melting isotherm.

From screening experiments, it was understood that Penetration and Top Width were correlated with each other in overlap welding. However, Interface Width was not correlated to other FZDs. The proposed LF model simultaneously calculates the defined FZDs. To increase the accuracy of the LF model, two new ratios are introduced, called the first scaling factor ( $\beta_{(1/3)_\mu}$ ) and the second scaling factor ( $\beta_{(2)_\mu}$ ). The first scaling factor considers the joint behaviour of Penetration and Top Width; whereas, the second scaling factor takes into account only Interface Width. The procedure flow for developing the multi-fidelity (MF) model that calculates FZDs in the overlap welding is given in Table 5.4.



**Table 5.4:** The methodological steps for computing FZDs using the multi-fidelity (MF) model in the overlap welding

Step	Methodological steps for developing the multi-fidelity (MF) model in the overlap welding
1.1	Obtain the 1 <sup>st</sup> scaling factor ( $\beta_{(1/3)\mu}$ ) for given KCCs using the 1 <sup>st</sup> scaling function (j=1 in Eq. (5.28))
1.2	Obtain the 2 <sup>nd</sup> scaling factor ( $\beta_{(2)\mu}$ ) for given KCCs using the 2 <sup>nd</sup> scaling function (j=2 in Eq. (5.28))
2.1	Calculate the laser intensity ( $I_1$ ) that is absorbed by the surface using Eq. (5.5)
2.2	Scale the calculated laser intensity ( $I_1$ ) with the 1 <sup>st</sup> scaling factor
3	Compute the KH profile in the upper sheet using Eqs. (5.8) to (5.13)
4.1	Calculate the laser intensity ( $I_2$ ) acting on the surface of the lower sheet using Eq. (5.6)
4.2	Scale the calculated laser intensity ( $I_2$ ) with the 2 <sup>nd</sup> scaling factor
5	Compute the KH profile in the lower sheet using Eqs. (5.8) to (5.13)
6	Gather the upper and the lower KH profiles
7	Determine the temperature profile by solving the heat equation given in Eqs. (5.14) and (5.15)
8	Extract FZDs from the temperature profile as defined in the standard (See Table 2.6)

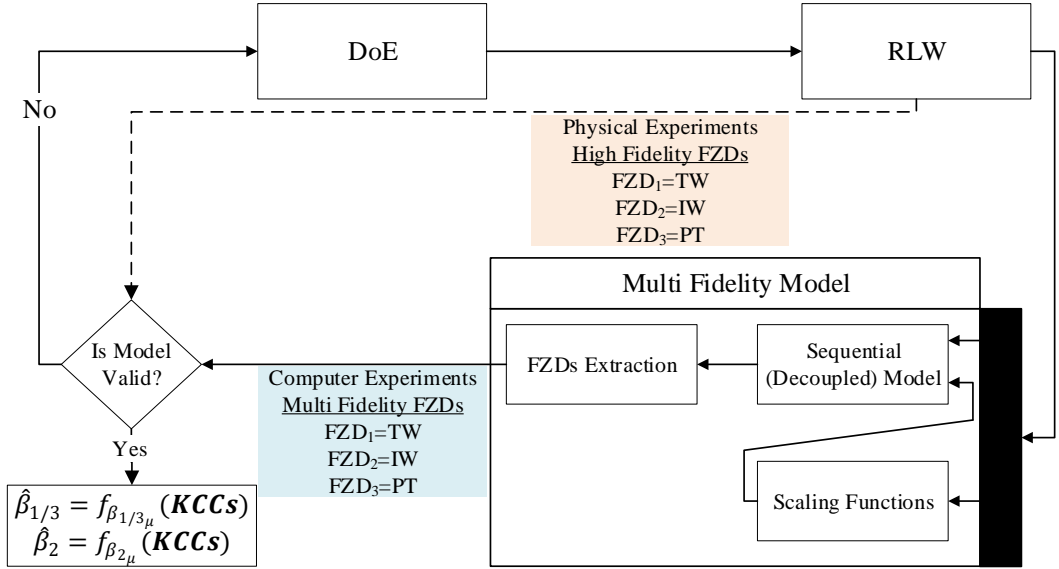
It is noteworthy that the validation experiments are conducted on the unseen experimental configurations. These configurations are not used for the developing scaling factors and scaling functions. Thus, another design of experiment (i.e. validation DoE) table is created for the validation experiments. The experiments were conducted according to the defined experimental procedure (See Table 5.3).

It is obvious that physical experiments are subject to process variation. Thus, different results are obtained when the same experiment is repeated. Therefore, the mean and standard deviation are important values to explain physical experiment results. However, computer experiments yield a single result which cannot be express either the mean value or standard deviation. To compare physical experiments and computer results, some statistical metrics are presented. The maximum absolute error (MAE), which is one of these statistical metrics, is utilized to assess the prediction accuracy of the MF model and scaling functions. The MAE value is found for each experimental configuration defined by the validation DoE table. Thus, the

local accuracy of the MF model is found. The formulation of the MAE is as follows:

$$MAE_j^{(k)} = \max \left( \left\{ \left| {}^{HF}FZD_j^{(k,l)} - {}^{MF}FZD_j^{(k)} \right| \forall l = 1, \dots, N_l \right\} \right) \quad (5.32)$$

where  $k$  is the index of the experimental configuration,  $j$  is the index of FZD,  $l$  is the index of replication,  $N_l$  is the total number of replications,  ${}^{HF}FZD_j^{(k,l)}$  is the HF model result (i.e. physical experimental result), and  ${}^{MF}FZD_j^{(k)}$  is the MF model result (i.e. computer experimental result). The process flow diagram describing how to conduct validation experiments to verify the MF model and scaling functions is illustrated in Fig. 5.10.



**Fig. 5.10.** The process flow of the validation experiments to verify the MF model and scaling functions utilized in the MF model

## 5.4 Results & Discussion

### 5.4.1 The Results of the High-Fidelity, Multi-Fidelity, & Low-Fidelity Models

Graphical interpretation of the results is always useful because it shows the variability of the results within an experiment and the variability between experiments. Therefore, it is easier to compare the variation occurring in an experiment with the variation occurring in another experiment. A point that should be emphasized is that there is not an error in experiments, instead, there is a certain variation in each experiment.

The allowance limits of each FZD and the results of each FZDs according to the HF, the MF, and the LF models are plotted in Figs. 5.11 to 5.13, respectively. The results of the HF model (i.e. physical experiments) are presented in the form of the error bar graph over the KCC-space. It is customary to define the “*allowance limits*”, which may be set by standards or the designer, *etc.* However, the “*tolerance limits*” (*the whiskers of each error bar*) are determined by  $\mp 3$  standard deviations ( $\mp 3\sigma$ ) from the mean value (6-Sigma method). The 6-Sigma is a well-established method in the Statistical Process Control (SPC). A distribution defined by the 6-Sigma includes 99.73% of the results of the HF model.

According to the results of the HF model (See Fig. 5.11), the top width reduces with increasing welding speed and joining gap, but it increases with increasing incidence angle. This is mainly because of the increase of the laser beam spot area acting on the workpiece surface. However, the top width will gradually decrease if the incidence angle continues to increase since the laser intensity will reduce as the spot area gets larger.

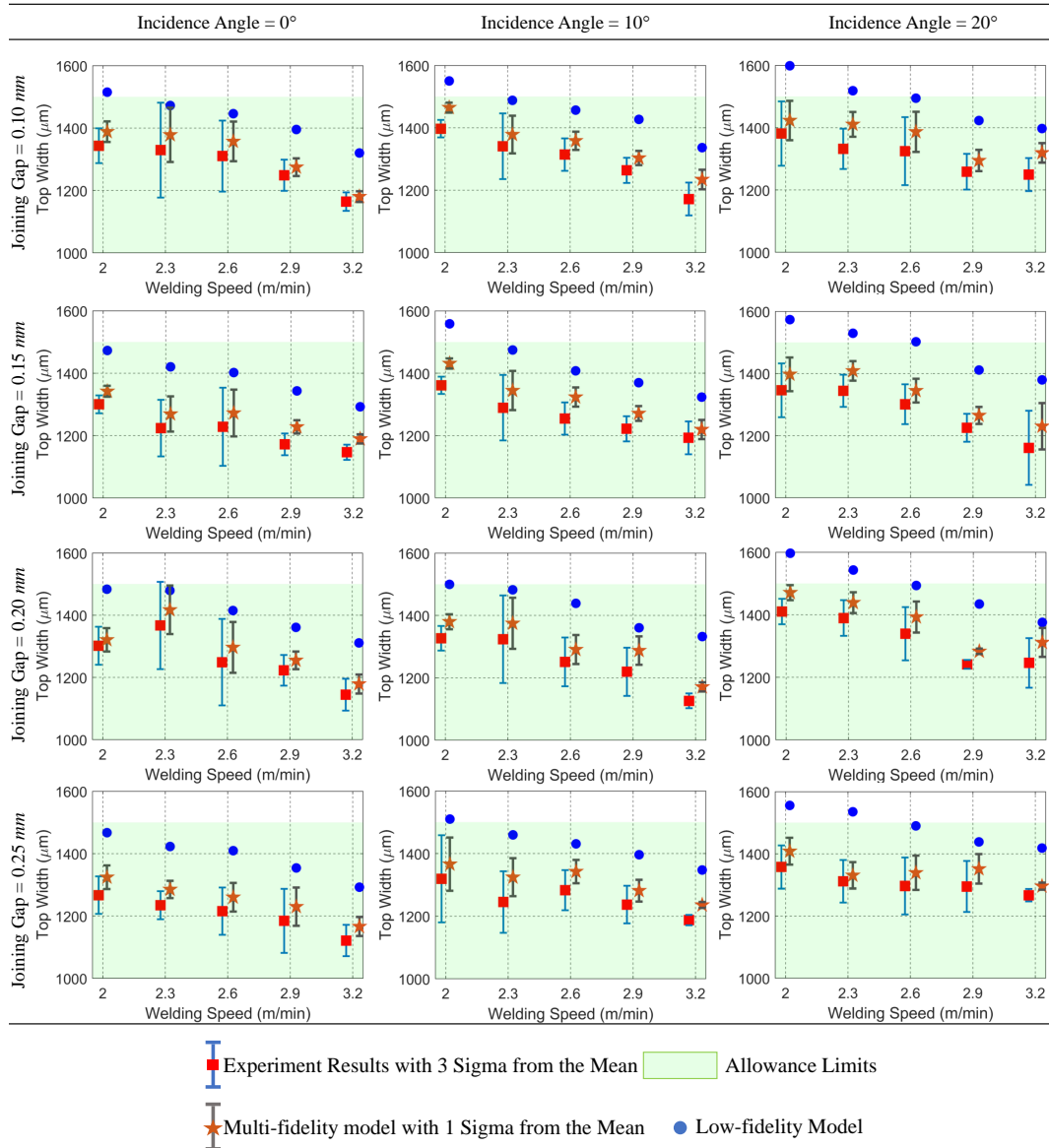
The MF model simultaneously calculates one value for each FZD for given process parameters. The MF model is basically the LF model by utilizing two different scaling factors, which are calculated using two different scaling functions. These functions are developed for three options, the mean value, one standard deviation above and below the mean value (See Section 5.3.3). For a given option, the MF model simultaneously calculates one value for each FZD. By running the MF model for three options at the same process parameters, three different values for each FZD are obtained. Therefore, a range for each FZD can be obtained to describe the process variation in the MF model.

It is noteworthy to mention that the results of the HF model (i.e. physical experiments) are also distribution which has a mean value and a standard deviation. This distribution is defined according to the 6-Sigma method.

If a result of the MF model, for example the calculated result of Top Width in a given experimental configuration, is within the  $\mp 3\sigma$  tolerance limits of the HF model, the result of the MF model can be considered as a sample obtained from the 6-Sigma distribution. This is because the 6-Sigma distribution includes 99.73% of the possible results of the HF model, and one of the replicates can be the result of the MF model. Therefore, the range to be obtained by using the MF model should be within the range defined by the HF model to utilize the MF model for the in-process monitoring of FZDs.

According to Fig. 5.11, the results of the LF model decreases as the welding speed increases. This can be attributed to the decrease in the interaction time, and

there is not a certain correlation between the results of the LF and the HF model. However, the results of the LF model follow the same pattern as the results of the HF model. The reason for this is the scaling factors used in the MF model are developed based on the variation in the HF model (See Eqs. (5.16) to (5.30)).



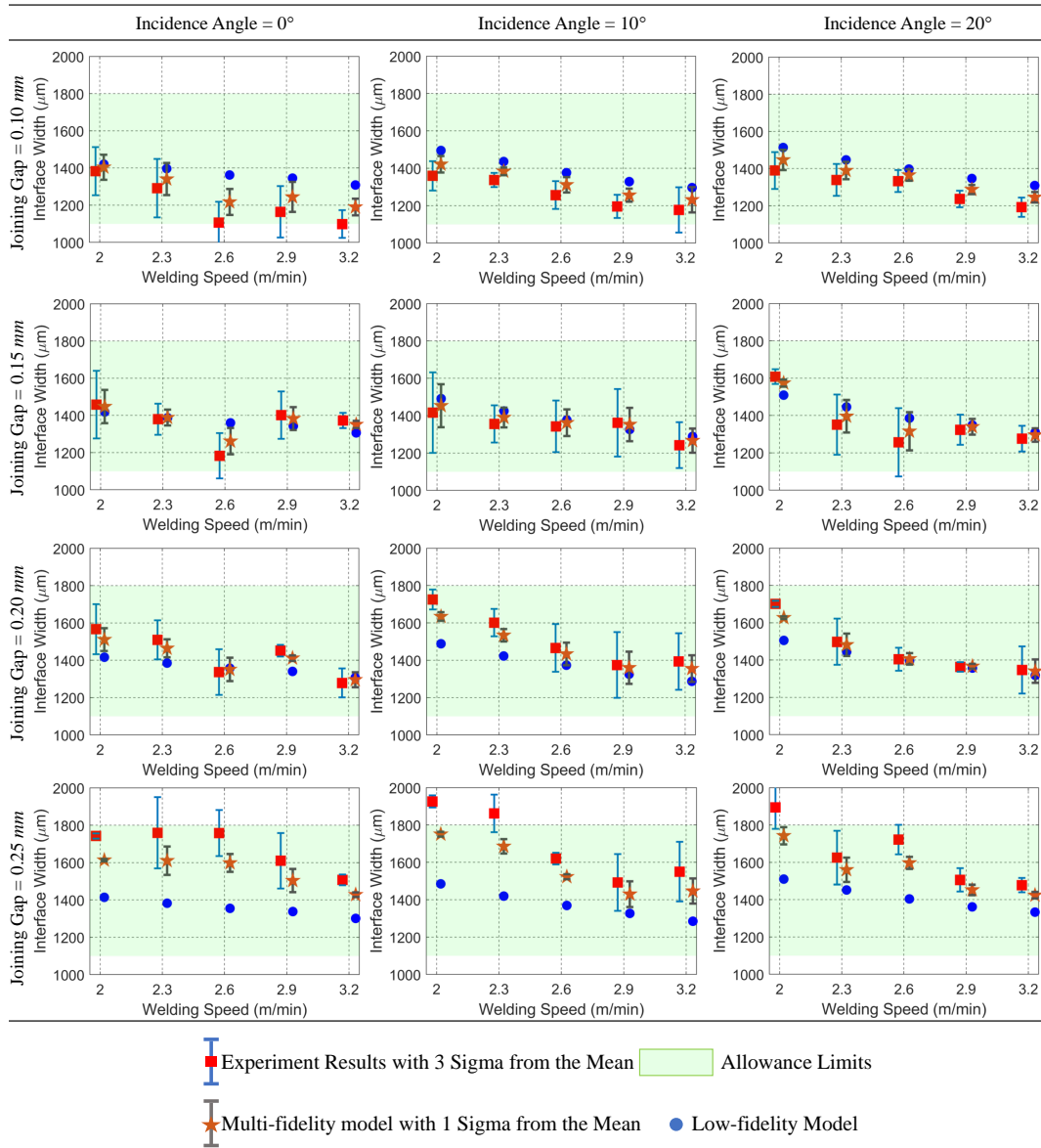
**Fig. 5.11.** The results of the HF, the LF and the MF models are presented to the characterization of Top Width (TW) over the KCC-space. TW reduces with increasing welding speed and joining gap, but it increases with increasing incidence angle. The results of the MF model follow the same pattern as the results of the HF model, and they are within the tolerance limits.

According to the results of the HF model presented in Fig. 5.12, the interface

width decreases with the increasing welding speed. An increase in welding speed leads to a decrease in heat input. As a result, the less volume of the base metal is melted. Moreover, the increasing of joining gap leads to an increase in the interface width. A larger joint gap means that the more molten material is needed to fill the volume between the two sheet metals in order to accomplish the weld. Thus, the top width shrinks; whereas, the interface width increases. On the other hand, the effect of the incidence angle is not significant for the interface width. However, a tilted laser beam means a wide on-surface spot size of the laser beam results in spreading the laser intensity onto a wide area. Therefore, melting occurs in a larger area on the surface of the metal leading to an increase in the top width.

As the gap increases, the results of the LF model will become lower than the results of the HF model (i.e. experimental results). This is because mass transfer due to the sagging effect is not considered in the LF model. Furthermore, the results of the LF model are monotonically decreasing with increasing welding speed, and there is not any correlation with the results of the HF model. However, the use of the scaling factor in the MF model improves the calculated interface width. The scaling factor is not a fixed value over the KCC-space, but it is obtained using scaling functions for given KCCs. Based on the formulation three different functions are developed for a scaling factor. Therefore, a range for each FZD can be obtained to describe the process variation in the MF model.

The calculated range for interface width is within the allowance limits even though some results of the HF model (i.e. physical experiments) violets the allowance limits. This violation can be seen for a larger joining gap. Moreover, the calculated range follows the same pattern as the results of the HF model, but it is not within the tolerance limits in some experimental configuration. This is because the results calculated without scaling factor (i.e. the LF model) are far from the experimental results.

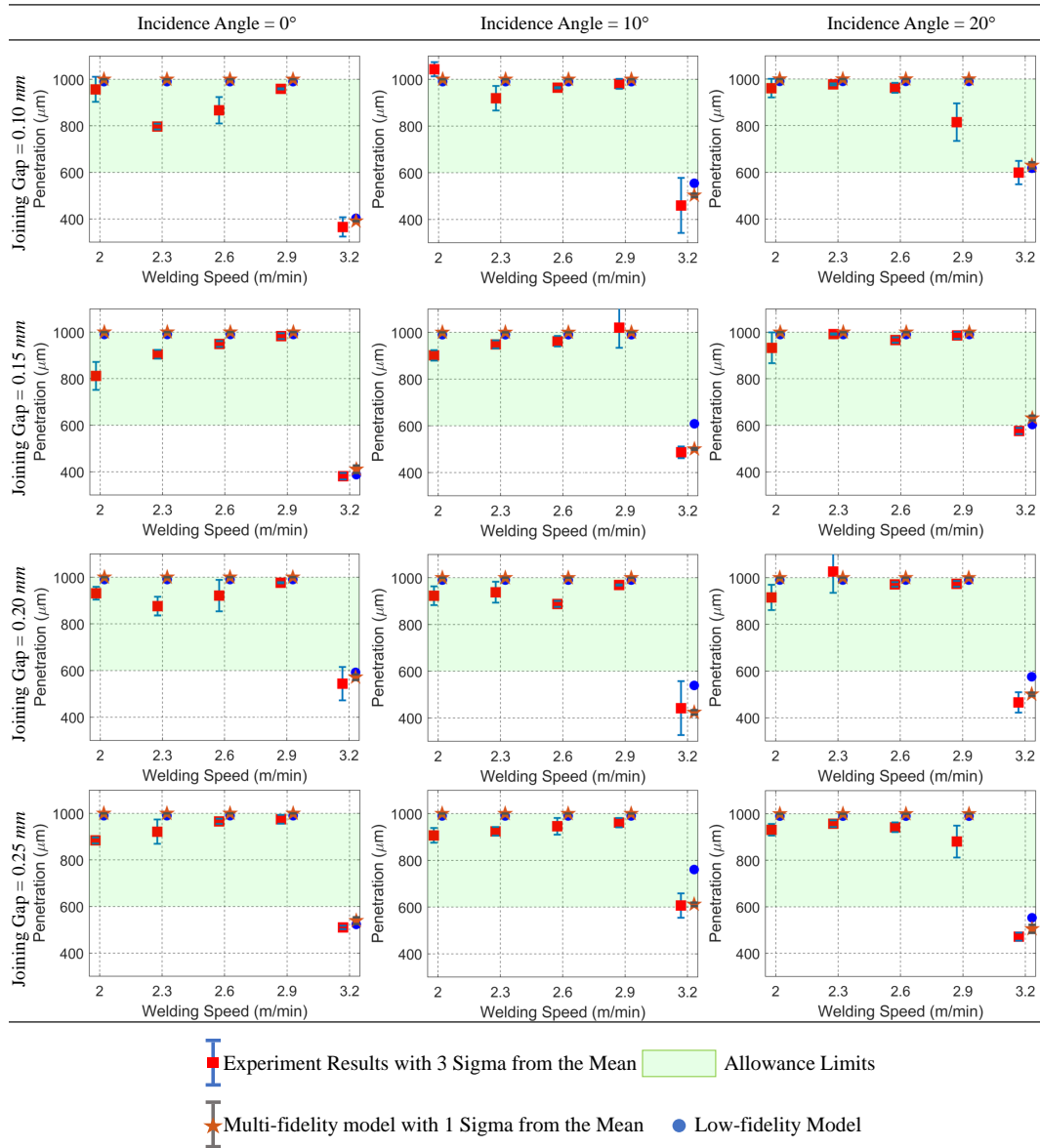


**Fig. 5.12.** The results of the HF, the LF and the MF models are presented to the characterization of Interface Width (IW) over the KCC-space. IW reduces with increasing welding speed, but it increases with joining gap and increasing incidence angle. At the larger joining gap, the HF model results (i.e. physical experiments) violate the allowance limits. At these points, the results of the LF model will become lower than the results of the HF model because the mass transfer is not considered in the LF model. The results of the MF model follow the same pattern as the results of the HF model, and they are within the tolerance limits.

Generally, all the fusion zone dimensions, including penetration decrease with the increasing welding speed. The results of the HF model clearly show this fact

and the results are given in Fig. 5.13. This fact can be explained in the decreased heat input per unit length. Thus, the lower amount of materials is molten, the weld becomes shallow and narrow. Moreover, if the joining gap is too large, more molten metal fills the gap and thus prevents the laser intensity reaching the lower metal. A large part of the laser is absorbed in the gap, resulting in a lower penetration. In addition, bottom concavities are seen in the weld. These have occurred during welding due to the backflow of the molten pool which is driven by the “*Marangoni effect*”. Since the penetration is defined as the extension of the weld only in the lower sheet. In most of the experiments, penetration is less than the thickness of the lower sheet metal.

According to the penetration results of the HF model (i.e. physical experiments), two different conditions can be seen. In the first case, the keyhole is more than the thickness of the metal (i.e. the open keyhole mode). In the second case, the keyhole is less than the thickness of the metal (i.e. the blind keyhole mode). In the open keyhole mode, the backflow and thus bottom concavities are seen. Thus, the results are less than the thickness of the metal (i.e. 1 mm). However, the results of both LF and MF models give a constant value of 1 mm because the backflow is not considered in these models and the scaling factor is not applied. In blind keyhole mode, the calculated results of the LF model over the KCC-space are within the tolerance limits of penetration defined separately for each experiment. The penetration is mainly driven by the absorption mechanisms inside the keyhole. If the penetration results of the HF and the LF models are close to each other, this approves the considered laser absorption mechanism through the path of the laser beam inside the keyhole. The results of the MF model in the blind keyhole mode follow the same pattern as the results of the HF model, and they are within the tolerance limits. However, the results of the HF model in the blind keyhole mode are out of the allowance limits.



**Fig. 5.13.** The results of the HF, the LF and the MF models are presented to the characterization of Penetration (PT) over the KCC-space. PT reduces with increasing welding speed. Two modes are seen, the open keyhole mode, and the blind keyhole mode. The results of the HF model in the blind keyhole mode are out of the allowance limits. The results of both LF and MF models are constant values (1 mm) due to fluid flow is not considered in these models. The results of the MF model are within the tolerance limits.

The comparison of the macro-section images obtained by the HF model (i.e. experiments) against the computed by the MF model is given for the open and the blind keyhole modes in Figs. 5.14 and 5.15, respectively. In both modes, the extreme (the low and the high) process parameters are selected to demonstrate the



effects of process parameters on the macro-section image and FZDs. The presented cross-sectional images are selected among the actual macro-section images, which are obtained from the experiments. This selection is made considering the best image representing the mean values of each FZD.

As aforementioned, the MF model utilizes the scaling factors, which are calculated using the scaling functions. These functions are developed for three options, the mean value, one standard deviation above and below the mean value. For a given option, the MF model calculates one value for each FZD. By running the MF model for three options, three different values for each FZD are obtained. Therefore, a range for each FZD can be determined to describe the process variation in the MF model.

Let us consider two options. In the first option, the obtained FZDs using the scaling functions based on the mean value scenario represent the mean values. In the second option, the obtained FZDs using the scaling functions based on one standard deviation above/below the mean value scenario represent the extreme values. The difference between the result of an FZD obtained according to the first option and the result of the same FZD obtained according to the second option is considered as the standard deviation of the FZD in the MF model.

In the open keyhole mode (See Fig. 5.14), bottom concavities are seen in the HF model (i.e. experimental results). These bottom concavities reduce the measured penetration. Since the fluid flow is not considered in the LF model, the penetration values obtained in the MF model always equal to the thickness of the material in this mode. Therefore, there is not a good correlation between the results of the HF and MF models.

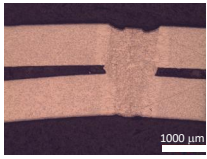
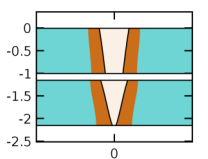
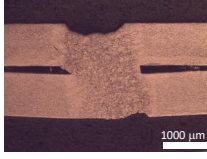
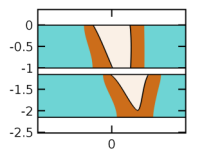
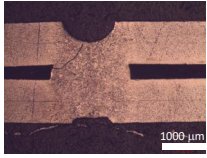
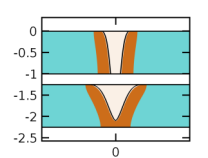
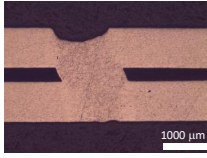
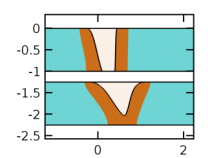



The error between the measured and the computed FZDs are given in terms of the MAE value. The MAE value is found for each experimental configuration, and it describes the local accuracy of the MF model. If the computed FZD is close to the measured FZD, the MF model is considered as accurate. The formulation of the MAE value is given in Eq. (5.32). The MAE values for top width, interface width, and penetration are around  $80 \mu m$ ,  $100 \mu m$ , and  $100 \mu m$ , respectively. Overall, it can be concluded that when the variation in the HF model (i.e. physical experiments), the MAE value is less for each FZD. It is better to analyse the results for penetration in the blind keyhole mode due to the appearance of the bottom concavity.

In the literature, the cross-sectional image of the laser welded joint in the keyhole mode is characterized as a Y (goblet) shape. This characteristic shape is obtained in the lower sheet metal for the blind keyhole mode (See Fig. 5.15). As the incidence angle increases, the FZ profile lies in the direction of the laser. This

effect of the incidence angle is also seen in the computed FZ profiles.

The MF employs two scaling factors. The first scaling factor considers the joint behaviour of TW and PT, and the second scaling factor takes into account the behaviour of IW. The laser intensity that enters the keyhole in the upper sheet metal is scaled with the first scaling factor, and the laser intensity that enters the upper sheet metal is scaled with the second scaling factor.

The measured and computed values of penetration have a good correlation as the MAE value for all presented configuration is around  $50 \mu m$ . This means that both scaling factors have a good agreement with the experiments. Furthermore, the MAE values for top width is around  $50 \mu m$ . This also indicates that the scaling factor is in good agreement with the experiments. The MAE is maximum ( $140 \mu m$ ) when the angle is  $20^\circ$  and the gap is  $0.15 mm$ . This is because the variation in the physical experiment is high. However, the results in this experiment are within the allowance limits.

Incidence Angle Joining Gap	0 (°)						20 (°)					
	Experiment			MF Model			Experiment			MF Model		
0.15 (mm)												
	<i>FZD</i>	$\mu$ ( $\mu\text{m}$ )	$\sigma$ ( $\mu\text{m}$ )	$\mu$ ( $\mu\text{m}$ )	$\sigma$ ( $\mu\text{m}$ )	<i>MAE</i>	<i>FZD</i>	$\mu$ ( $\mu\text{m}$ )	$\sigma$ ( $\mu\text{m}$ )	$\mu$ ( $\mu\text{m}$ )	$\sigma$ ( $\mu\text{m}$ )	<i>MAE</i>
	<i>TW</i>	1300.42	14.35	1342.13	18.48	58.26	<i>TW</i>	1345.95	43.25	1397.51	57.21	96.16
	<i>IW</i>	1457.99	95.86	1447.62	94.48	100.28	<i>IW</i>	1608.19	20.93	1573.72	19.84	57.08
	<i>PT</i>	868.80	60.27	1000	-	131.19	<i>PT</i>	933.04	65.97	1000	-	66.95
0.25 (mm)												
	<i>FZD</i>	$\mu$ ( $\mu\text{m}$ )	$\sigma$ ( $\mu\text{m}$ )	$\mu$ ( $\mu\text{m}$ )	$\sigma$ ( $\mu\text{m}$ )	<i>MAE</i>	<i>FZD</i>	$\mu$ ( $\mu\text{m}$ )	$\sigma$ ( $\mu\text{m}$ )	$\mu$ ( $\mu\text{m}$ )	$\sigma$ ( $\mu\text{m}$ )	<i>MAE</i>
	<i>TW</i>	1266.97	30.05	1324.30	39.70	91.89	<i>TW</i>	1357.91	34.71	1408.34	45.49	88.99
	<i>IW</i>	1742.09	7.51	1613.07	6.16	129.02	<i>IW</i>	1894.15	60.11	1742.60	48.44	125.37
	<i>PT</i>	895.90	12.52	1000	-	104.09	<i>PT</i>	931.38	24.93	1000	-	91.24
												

**Fig. 5.14.** The comparison of (i) the macro-section images obtained by the HF model (i.e. experiment) against the computed by the MF model, and (ii) the measured FZDs against the computed FZDs using the MF model. The process parameters not specified in the graph are welding speed ( $W_S$ ): 2.0 m/min, focal offset ( $F_O$ ): 0 mm, and laser power ( $P_L$ ): 3 kW

Incidence Angle Joining Gap	0 (°)						20 (°)					
	Experiment			MF Model			Experiment			MF Model		
0.15 (mm)												
	<i>FZD</i>	$\mu$ ( $\mu\text{m}$ )	$\sigma$ ( $\mu\text{m}$ )	$\mu$ ( $\mu\text{m}$ )	$\sigma$ ( $\mu\text{m}$ )	<i>MAE</i>	<i>FZD</i>	$\mu$ ( $\mu\text{m}$ )	$\sigma$ ( $\mu\text{m}$ )	$\mu$ ( $\mu\text{m}$ )	$\sigma$ ( $\mu\text{m}$ )	<i>MAE</i>
	<i>TW</i>	1146.77	12.27	1189.46	15.43	50.80	<i>TW</i>	1160.85	59.61	1230.32	78.69	137.79
	<i>IW</i>	1372.98	21.65	1350.85	20.80	47.13	<i>IW</i>	1276.00	36.39	1295.64	37.77	55.32
	<i>PT</i>	380.84	14.15	410.97	17.23	46.34	<i>PT</i>	575.84	13.17	631.19	10.89	70.23
0.25 (mm)												
	<i>FZD</i>	$\mu$ ( $\mu\text{m}$ )	$\sigma$ ( $\mu\text{m}$ )	$\mu$ ( $\mu\text{m}$ )	$\sigma$ ( $\mu\text{m}$ )	<i>MAE</i>	<i>FZD</i>	$\mu$ ( $\mu\text{m}$ )	$\sigma$ ( $\mu\text{m}$ )	$\mu$ ( $\mu\text{m}$ )	$\sigma$ ( $\mu\text{m}$ )	<i>MAE</i>
	<i>TW</i>	1121.47	25.04	1166.34	32.22	66.45	<i>TW</i>	1266.96	10.01	1295.96	12.09	39.22
	<i>IW</i>	1507.34	15.02	1427.94	13.10	93.58	<i>IW</i>	1477.67	20.18	1423.73	18.39	71.36
	<i>PT</i>	510.23	7.52	539.16	14.86	37.56	<i>PT</i>	471.44	17.51	505.20	18.16	49.05

Base Metal	Keyhole	Fusion Zone

**Fig. 5.15.** The comparison of (i) the macro-section images obtained by the HF model (i.e. experiment) against the computed by the MF model, and (ii) the measured FZDs against the computed FZDs using the MF model. The process parameters not specified in the graph are welding speed ( $W_S$ ): 3.2 m/min, focal offset ( $F_O$ ): 0 mm, and laser power ( $P_L$ ): 3 kW

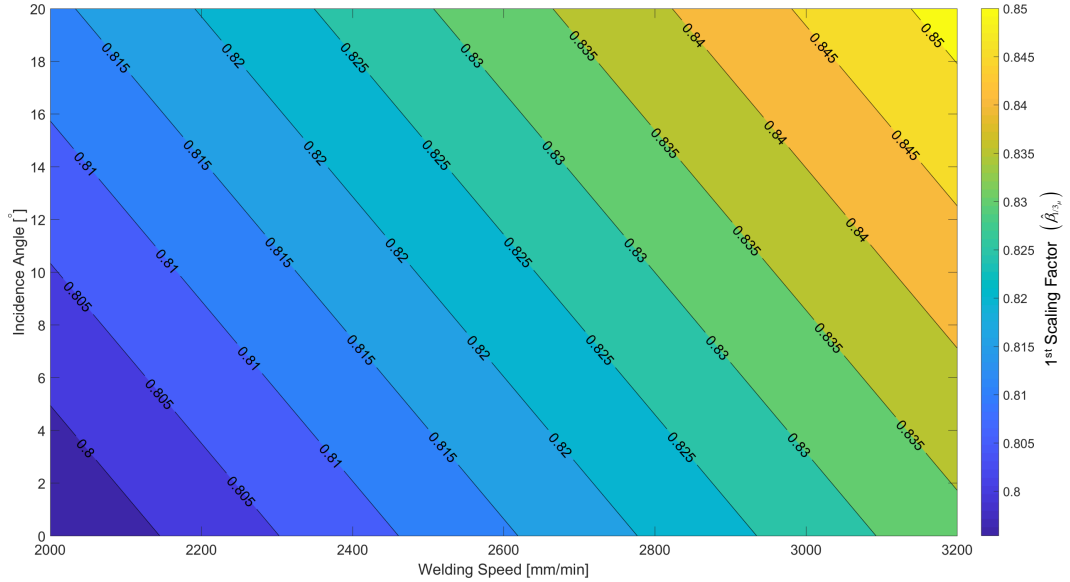
#### 5.4.2 Scaling Functions

The scaling factors are estimated over the KCC-scape by using the scaling functions. The estimated scaling factors are utilized in the MF model to calculate the defined FZDs (Top Width, Interface Width, and Penetration) for given process parameters.

The top width is directly correlated to the keyhole opening radius ( $r_{KH_0}$ ). The radius is computed by initially calculating the spot size of the laser on the surface and then solving the pressure balance acting on the keyhole. The spot size is related to the geometry of the laser beam. It is evident that the on-surface spot dimensions increase with the tilting of the laser beam. The pressure acting on the

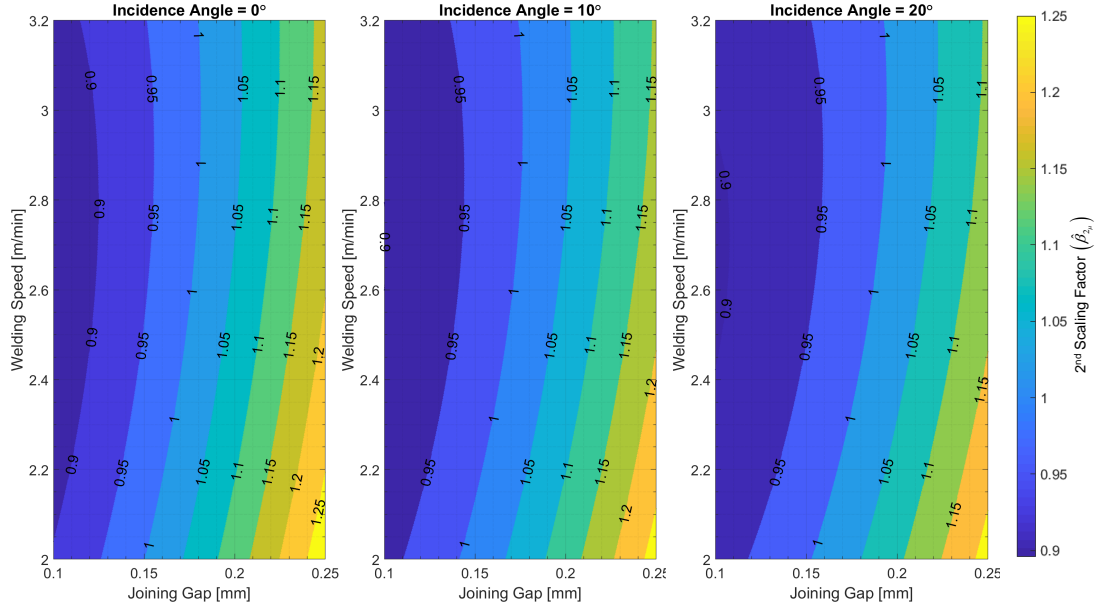
keyhole is related to the process parameters, such as the ablation pressure reduces with increasing welding speed; whereas, it increases with increasing laser intensity. The surface tension pressure, which tries to close the keyhole, is more dominant slightly away from the on-surface spot of the laser beam. On the other hand, the ablation pressure, which tries to close the keyhole, is more dominant under the laser. Therefore, the keyhole opening radius is slightly larger than the laser beam radius.

In addition, the absorption mechanism inside the keyhole becomes more dominant as the keyhole gets deeper resulting in a shorter keyhole than the computed keyhole by the LF model since only the Fresnel absorption is considered in the LF model. Furthermore, the plasma plume is also formed above the keyhole and the laser intensity is attenuated while it passes through. When the interaction time is long, more particles will be generated, and much denser plasma plume is formed. Thus, more laser intensity is lost at low welding speed and high laser power. On the contrary, the attenuation of the laser intensity is less at high welding speed and incidence angle because the absorption of the laser intensity inside and outside of the keyhole is less. As a result, the measured penetration and top width are close to the simulated results by using the LF model at high welding speed and incidence angle. The scaling factor ( $\hat{\beta}_{1/3\mu}$ ), which is the ratio between the results of the HF and the LF models, gets higher values. The first scaling factor over the KCC-space is given in Fig. 5.16.



**Fig. 5.16.** The estimated first scaling factor ( $\hat{\beta}_{1/3\mu}$ ) over the KCC-space using the first scaling function ( $f_{\beta_{1/3\mu}}$ ) developed based on the mean-only analysis (See Eq. (5.24))

The second scaling factor ( $\hat{\beta}_{2\mu}$ ), which is shown in Fig. 5.17, is introduced to understand the occurring physical phenomena inside the gap. According to the physical experimental results, the joining gap works as an obstacle for delivering the laser beam energy into the lower sheet metal. Moreover, decreasing the interaction time, which also means increasing the welding speed, reduces the heat input per unit time resulting in very shallow welding in the lower sheet metal. Furthermore, when the joining gap is larger, more molten material is required to bridge the joining gap to accomplish a weld between two sheet metals. This results in a larger interface width than the top width. Therefore, the second scaling factor takes into account the discrepancy between the measured interface width, and the value computed using the LF model. In summary, the first scaling factor controls the joint behaviour of the top width and the penetration, and the second scaling factor considers the interface width.



**Fig. 5.17.** The estimated second scaling factor ( $\hat{\beta}_{2\mu}$ ) over the KCC-space using the second scaling function ( $f_{\beta_{2\mu}}$ ) developed based on the mean-only analysis (See Eq. (5.24))

### 5.4.3 Validation Results

In the literature, there are well-established analytical solutions that calculate the temperature distribution on the surface of the metal. These solutions are (i) point source solution, (ii) line source solution, known as “Rosenthal’s solution”, and (iii) disc source solution (Dowden, 2001). They are developed according to the

bead-on-plate welding, and they do not consider the fluid flow and the sagging effect in the overlap welding.

The proposed MF is the LF model using scaling factors. The LF model consists of three sub-models which are the laser intensity model, the keyhole profile model, and the temperature distribution model. The laser intensity and the keyhole profile model are solved analytically, and the temperature distribution model utilizes the FEM. Since the top width is subject to the fluid flow and the sagging effect, the keyhole opening radius ( $r_{KH_0}$ ) is calculated in order to have an unbiased comparison among the LF model and these analytical solutions. The calculation procedure of the keyhole opening radius is given in Sections 5.2.1 and 5.2.2.

These solutions calculate the temperature distribution on the surface of a material. By selecting the evaporation temperature ( $T_v$ ) as a reference temperature, an isotherm is obtained. This isotherm corresponds a spot on the surface of the metal, and the keyhole opening radius can be measured from this spot. The computed keyhole opening radius ( $r_{KH_0}$ ) according to each solution and the result of the LF model are given in Table 5.5.

**Table 5.5:** The comparison of the keyhole opening radius ( $r_{KH_0}$ ) for different models at various welding speeds

Welding Speed ( $m/min$ )	Keyhole Opening Radius ( $r_{KH_0}$ )			
	Point Heat Source ( $mm$ )	Line Heat Source ( $mm$ )	Disc Source ( $mm$ )	LF Model ( $mm$ )
2	0.5	0.6	0.54	0.493
2.3	0.46	0.52	0.52	0.483
2.6	0.43	0.46	0.5	0.474
2.9	0.4	0.42	0.485	0.466
3.2	0.38	0.39	0.465	0.458

The validation experimental results for overlap welding are given in Table 5.6. The formulation of the MAE value is given in Eq. (5.32). The higher value of MAE is around  $150 \mu m$  and the lower value is around  $40 \mu m$ . In general, the MAE values for each FZD decrease with increasing welding speed. This validates the welding mode changes from the open keyhole to the blind keyhole. The MAE values for top and interface widths increase with increasing joining gap. This can be explained that the LF model considers only heat transfer and neglects the fluid flow during welding. Therefore, the molten metal can easily bridge the joining gap to form the weld for low levels of process parameters. However, when the joining gap gets

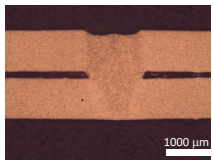
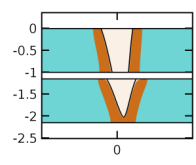
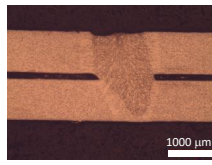
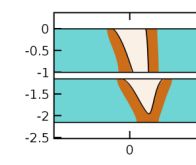
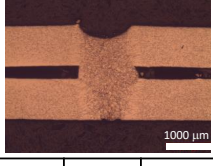
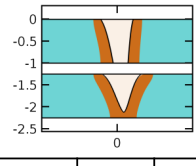
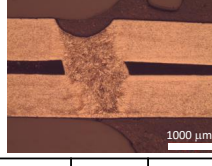
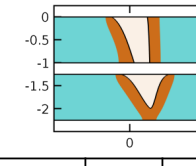
larger, more molten metal flows into the joining gap to form the weld. This results in higher values than computed values using the MF model and the higher MAE values are obtained in these conditions. Likewise, the increase in the welding speed stimulates turbulence in the fluid flow inside the molten pool. Therefore, the MAE value is larger for larger joining gap sizes and higher welding speeds. Some of the macro-section images are shown to compare the validation experiments results with the computed results using the MF model in Figs. 5.18 and 5.19.

Incidence Angle Joining Gap	0 (°)						15 (°)					
	Experiment			MF Model			Experiment			MF Model		
0.15 (mm)												
	<i>FZD</i>	$\mu$ ( $\mu\text{m}$ )	$\sigma$ ( $\mu\text{m}$ )	$\mu$ ( $\mu\text{m}$ )	$\sigma$ ( $\mu\text{m}$ )	<i>MAE</i>	<i>FZD</i>	$\mu$ ( $\mu\text{m}$ )	$\sigma$ ( $\mu\text{m}$ )	$\mu$ ( $\mu\text{m}$ )	$\sigma$ ( $\mu\text{m}$ )	<i>MAE</i>
	<i>TW</i>	1224.10	45.37	1269.32	59.30	94.84	<i>TW</i>	1344.41	26.00	1408.66	33.00	93.73
	<i>IW</i>	1379.45	44.14	1388.45	44.87	43.05	<i>IW</i>	1351.01	85.00	1395.98	92.14	43.04
	<i>PT</i>	904.72	18.70	1000.00	0.10	116.83	<i>PT</i>	992.09	2.73	1000.00	0.10	10.53
0.25 (mm)												
	<i>FZD</i>	$\mu$ ( $\mu\text{m}$ )	$\sigma$ ( $\mu\text{m}$ )	$\mu$ ( $\mu\text{m}$ )	$\sigma$ ( $\mu\text{m}$ )	<i>MAE</i>	<i>FZD</i>	$\mu$ ( $\mu\text{m}$ )	$\sigma$ ( $\mu\text{m}$ )	$\mu$ ( $\mu\text{m}$ )	$\sigma$ ( $\mu\text{m}$ )	<i>MAE</i>
	<i>TW</i>	1234.70	22.52	1285.37	29.16	70.91	<i>TW</i>	1311.66	34.21	1330.93	44.51	57.70
	<i>IW</i>	1759.41	100.24	1610.14	79.72	43.67	<i>IW</i>	1625.75	75.68	1560.28	68.37	102.86
	<i>PT</i>	921.43	52.21	1000.00	0.10	103.94	<i>PT</i>	957.75	14.44	1000.00	0.10	58.26

	Base Metal		Keyhole		Fusion Zone
--	------------	--	---------	--	-------------

**Fig. 5.18.** The comparison of (i) the macro-section images obtained by the validation experiments against the computed by the MF model, and (ii) the measured FZDs against the computed FZDs using the MF model. The process parameters not specified in the graph are welding speed ( $W_S$ ): 2.45 m/min, focal offset ( $F_O$ ): 0 mm, and laser power ( $P_L$ ): 3 kW



Incidence Angle Joining Gap	0 (°)						15 (°)					
	Experiment			MF Model			Experiment			MF Model		
0.15 (mm)												
	<i>FZD</i>	$\mu$ ( $\mu\text{m}$ )	$\sigma$ ( $\mu\text{m}$ )	$\mu$ ( $\mu\text{m}$ )	$\sigma$ ( $\mu\text{m}$ )	<i>MAE</i>	<i>FZD</i>	$\mu$ ( $\mu\text{m}$ )	$\sigma$ ( $\mu\text{m}$ )	$\mu$ ( $\mu\text{m}$ )	$\sigma$ ( $\mu\text{m}$ )	<i>MAE</i>
	<i>TW</i>	1172.05	17.50	1228.06	22.17	69.51	<i>TW</i>	1225.19	22.54	1265.11	29.05	65.87
	<i>IW</i>	1401.33	67.14	1382.82	65.08	92.34	<i>IW</i>	1323.73	42.57	1339.69	43.85	55.79
	<i>PT</i>	982.83	12.65	1000.00	0.10	30.51	<i>PT</i>	986.54	15.03	1000.00	0.10	30.39
0.25 (mm)												
	<i>FZD</i>	$\mu$ ( $\mu\text{m}$ )	$\sigma$ ( $\mu\text{m}$ )	$\mu$ ( $\mu\text{m}$ )	$\sigma$ ( $\mu\text{m}$ )	<i>MAE</i>	<i>FZD</i>	$\mu$ ( $\mu\text{m}$ )	$\sigma$ ( $\mu\text{m}$ )	$\mu$ ( $\mu\text{m}$ )	$\sigma$ ( $\mu\text{m}$ )	<i>MAE</i>
	<i>TW</i>	1184.42	51.35	1229.97	64.47	104.85	<i>TW</i>	1295.13	40.96	1351.53	49.97	100.96
	<i>IW</i>	1609.57	78.06	1503.37	65.63	95.79	<i>IW</i>	1506.07	33.14	1452.22	30.27	84.58
	<i>PT</i>	974.73	18.75	1000.00	0.10	44.47	<i>PT</i>	880.62	68.50	1000.00	0.10	95.50

Base Metal	Keyhole	Fusion Zone

**Fig. 5.19.** The comparison of (i) the macro-section images obtained by the validation experiments against the computed by the MF model, and (ii) the measured FZDs against the computed FZDs using the MF model. The process parameters not specified in the graph are welding speed ( $W_S$ ): 3.0 m/min, focal offset ( $F_O$ ): 0 mm, and laser power ( $P_L$ ): 3 kW

**Table 5.6:** The results of the validation experiments to determine the accuracy of the MF model. The accuracy is computed based on the MAE values.

Welding Speed ( $m/min$ )	Incidence Angle ( $^{\circ}$ )	Joining Gap ( $mm$ )	MAE Top Width ( $\mu m$ )	MAE Interface Width ( $\mu m$ )	MAE Penetration ( $\mu m$ )
2.45	0	0.10	121.47	129.99	114.11
3.00	0	0.10	45.99	102.02	43.88
2.45	5	0.10	98.30	69.70	129.28
3.00	5	0.10	62.76	85.79	43.74
2.45	15	0.10	109.24	102.19	25.32
3.00	15	0.10	52.76	75.54	147.29
2.45	0	0.15	94.84	43.05	116.83
3.00	0	0.15	69.51	92.34	30.51
2.45	5	0.15	113.64	94.84	66.24
3.00	5	0.15	61.72	113.91	113.44
2.45	15	0.15	93.73	43.04	10.53
3.00	15	0.15	65.87	55.79	30.39

**Table 5.6 Continued:** The results of the validation experiments to determine the accuracy of the MF model. The accuracy is computed based on the MAE values.

Welding Speed ( $m/min$ )	Incidence Angle ( $^{\circ}$ )	Joining Gap ( $mm$ )	MAE Top Width ( $\mu m$ )	MAE Interface Width ( $\mu m$ )	MAE Penetration ( $\mu m$ )
2.45	0	0.20	126.59	103.86	63.06
3.00	0	0.20	58.60	54.63	25.21
2.45	5	0.20	97.70	109.27	100.95
3.00	5	0.20	109.64	95.42	32.98
2.45	15	0.20	73.65	81.16	111.60
3.00	15	0.20	46.64	14.92	39.54
2.45	0	0.25	70.91	43.67	103.94
3.00	0	0.25	104.85	95.79	44.47
2.45	5	0.25	132.21	137.27	96.62
3.00	5	0.25	66.67	139.15	61.64
2.45	15	0.25	57.70	102.86	58.26
3.00	15	0.25	100.96	84.58	95.50

## 5.5 Summary of the Chapter

A computationally cost-effective novel model is presented to estimate penetration, top and interface widths for the RLW process. The proposed model has the capability to be used for direct in-process monitoring of multi FZDs and it is a necessary enabler for the development of the closed loop quality control framework. This is because the proposed model can estimate FZDs within a few seconds in a common desktop computer with acceptable accuracy. It has been successfully verified conducting the bead-on-plate and the overlap welding experiments on DX54D+Z stainless steel. The following conclusions can be drawn:

1. The main effects of process parameters on FZDs reveal that *(i)* welding speed has the most significant negative contribution to all FZDs (PT, TW, IW), *(ii)* joining gap shows a positive contribution to IW; whereas, TW and PT decreases with increasing joining gap, and *(iii)* incidence angle has a positive correlation with TW, but it has not a significant contribution to the IW and PT.
2. The proposed model makes full use of the information from the numeric simulation and physical experiments. Furthermore, the model consists of two steps: *(i)* calculating the keyhole profile in overlap joint using an analytic method with surrogate driven scaling function; and then, *(ii)* numerically solving the generalized heat equation to obtain FZDs from the FZ profile. It is determined by selecting a reference isotherm, which is the melting isotherms. The computational time for the proposed model is around 30 seconds with a maximum element size of 0.3 mm.
3. The accuracy of the proposed modelling approach is calculated with the MAE value which is the error term between the experimental and the simulated results. In general, the proposed modelling approach is accurate the obtain maximum error is around 150  $\mu m$  and the minimum error is around 40  $\mu m$ .

Overall, the proposed model provides a promising way to estimate FZDs. The scaling factors are obtained by the experiment-based statistical model off-line. Once scaling factors are obtained for a given process parameter, they are embedded into the closed loop quality control framework. Together with in-process data such as process parameter (i.e. laser power, laser welding speed, joining gap, incidence angle), beam properties (i.e. wavelength, Rayleigh length), scaling factors are used in the decoupled multi-physics, multi-fidelity model to estimate FZDs.

## **Acknowledgements**

This study was partially supported by the EU research project EU-FP7 FoF-ICT-2011.7.4: RLW Navigator, by the UK EPSRC project EP/K019368/1: Self-Resilient Reconfigurable Assembly Systems with In-process Quality Improvement and by the Republic of Turkey Ministry of National Education Post-Graduate Scholarship. Furthermore, the partial results of this chapter were submitted to the “Journal of Laser Application” on the 16th October 2016 and accepted for publication on the 28th March 2017 with a DOI number of <http://dx.doi.org/10.2351/1.4983234>.

# Chapter 6

## Conclusions and Future Works

This chapter summarizes the methodologies developed in this thesis and discusses the conclusions and overall findings derived from the research presented in the previous chapters. Moreover, a critical review of the proposed methods in terms of advantages and limitations is presented. The broader impact of the research in terms of engineering relevance and applications is also discussed. Furthermore, future work based on the current research is discussed.

### 6.1 Conclusions

Remote Laser Welding (RLW) is a non-contact joining process characterised by its high focussed laser intensity, which can produce deep penetration with narrow width (i.e. high aspect ratio) welds in many metallic materials. It can be performed in relatively low heat input at atmospheric pressure compared to other welding processes. The current generation of solid-state laser sources (Nd:YAG, Yb: Fibre, and Yb:YAG disc lasers) emits a laser beam with a wavelength of  $1 \mu m$ , which can be delivered through optical fibres. The Beam Product Parameter (BPP) is used to determine the quality of the laser beam. The BPP should be small to create a long focal length with a high-quality laser beam (See Fig. 2.6). Consequently, RLW employs a laser beam with a long focal length with a small BPP. RLW is also easily automated using robotic manipulators, providing extensive flexibility in terms of part size and shape. Table 6.1 details the characteristics of RLW, and the industrial advantage of the process.

**Table 6.1:** Characteristics of the remote laser welding process

Characteristic	Industrial advantage
High processing speed	<ul style="list-style-type: none"><li>▶ high productivity, potential for material savings</li><li>▶ possibility for longer weld seams increasing component stiffness</li></ul>
Better weld quality	<ul style="list-style-type: none"><li>▶ high aspect ratio</li><li>▶ narrow HAZ</li><li>▶ minimal thermal distortion</li><li>▶ possibility for simpler clamping</li></ul>
Flexible process	<ul style="list-style-type: none"><li>▶ complex welding geometries possible</li><li>▶ variety of joint configurations</li><li>▶ accurate reliable welding process</li><li>▶ autogenous process without filler material</li></ul>

Although RLW is increasingly being adopted by the automotive industry, the most important challenge to be addressed is achieving a high-quality weld in the presence of process variation. The weld quality examines the integrity of the weld and its requirements are expressed in terms of Key Performance Indicators (KPIs) defined by industrial standards (EN ISO 13919-1, 1997; EN ISO 13919-2, 2001). The weld quality is unknown until the results of the inspection tests and statistical analysis become available. The traditional off-line monitoring methods involve in selecting random samples from a batch of finished welds and checking critical KPIs against the quality standard. The result of the quality test is taken as representative of the whole batch. However, the drawback is that only samples can be measured and not the whole parts. Instead, the weld quality of each part can be determined during the process by in-process quality monitoring methods. The purpose of these methods is to obtain data about the process state using sensors. The obtained data is converted to quality-related information, but the major challenge is to capture the required data to assess the weld quality in a very small amount of time. Furthermore, the limitations of current in-process monitoring methods were (i) sensor signals are multi-dimensional and multi-modal, and (ii) sensor signals can detect external KPIs (e.g. spatter, undercut, humping, *etc.*), but this is insufficient to assess the weld quality based on internal KPIs. To this end, the major achievements of this thesis are summarized as follows:

(i) to control minimum joining gap requirement:

According to the revised literature in Section 3.1, the joining gap could be between 0.1 mm and 0.4 mm for laser welding of zinc coated steels. Further-

more, the laser dimpling process was found out that it was the most promising manufacturing process to control the minimum joining gap. This is because it did not require any additional equipment and was not restricted by the shape and curvature of the workpiece and weld location. However, the leading challenge is the lack of comprehensive characterization of the laser dimpling process considering inherent changes in variability of process parameters. To overcome this challenge, a novel methodology was developed which includes:

1. identification of relevant KCCs and KPIs:

Process parameters were evaluated by Key Control Characteristics (KCCs), and the dimple quality was assessed by Key Performance Indicators (KPIs). The defined KCCs were scanning speed ( $S_S$ ), focal offset ( $F_0$ ), incidence angle ( $\alpha$ ), and laser track ( $L_T$ ). These KCCs were selected due to process cycle time, the visibility and the accessibility of the laser beam. According to the revised literature, the only KPI studied was dimple height ( $D_H$ ). However, it was important but not sufficient for the comprehensive characterization of the process. Thus, two new KPIs were offered namely; dimple upper surface area ( $D_U$ ) and dimple lower surface area ( $D_L$ ) to assess the durability and aesthetic quality of the dimple.

2. estimation of process fallout rate:

The success rate (SR), a new term, was offered to measure the process fallout rate. It was the area under the probability density function (PDF). The SR (i.e. probability value) was determined by the integral of the PDF over the given allowance limits of the KPIs. The PDF is a function of the mean and the standard deviation of the conducted experiments.

3. developing surrogate models:

A critical element of the methodology was the surrogate model mapping KCCs with KPIs and SRs. The first objective of this work was to compute surrogate models between KCCs and KPIs, and between KCCs and SRs. A full factorial design approach was employed for this purpose with 3-levels 4-factors with 5 replications.

4. calculating process capability space:

The second objective of this work was to calculate the deterministic and the stochastic process capability spaces based on the developed surrogate models. The deterministic process capability space was used to determine if all KPIs satisfy the given allowance limits; whereas, the stochastic process capability space was used to estimate the probability of satisfying the given allowance limits of all KPIs.



5. computing optimum KCCs which are less sensitive process variation:

The last objective of this work was to determine the robust KCCs based on the deterministic and the stochastic process capability spaces. The proposed optimization strategy was to maximize the stochastic process capability space subject to deterministic process capability space and bounded KCCs. The optimization strategy was given in Table 4.5.

The major impact of the developed methodology was to select the robust KCCs which were less sensitive to process variation so that the minimum gap requirement was guaranteed. The robust KCCs were verified by validation experiments. According to experiments, the dimple lower surface area was eliminated and there was not any visible dark spot. Furthermore, the minimum gap was achieved throughout the whole part assembly so that there were not any spatters around the weld seam. Based on these experimental results and discussions, some general conclusions were drawn as follows:

- ▶ Dimples were formed in the opposite direction of the scanning direction for a lower focal offset; whereas, they were generated in the same direction for a larger defocus
- ▶ The reduction in dimple lower surface area was achieved either by a larger focal offset or by a longer laser track
- ▶ Dimple height and dimple upper surface area increased while decreasing scanning speed and increasing laser track
- ▶ Increasing incidence angle affected dimple height and dimple upper surface area but it was not significant for dimple lower surface area

*(ii) to an effective prediction of FZDs to assess the weld quality:*

The weld quality has been a critical issue for effective implementation of laser welding. Several methods have been proposed for in-process monitoring. These methods are (i) capturing in-process process emissions, and (ii) analysing/training/mapping gathered signal with the defined KPIs/FZDs. However, sensor-driven monitoring methods are an indirect monitoring of FZDs, and they are limited to external FZDs. An alternative method is the physics-driven monitoring method which understands the occurring physics and links in-process monitoring weld signals with multi FZDs (i.e. internal FZDs) and welding process parameters. As highlighted in Section 3.3, the challenge is the long computational time of the physics-based numeric simulation of laser welding. To overcome this challenge, a novel methodology was developed based on:

1. identification of relevant KCCs and KPIs:

KCCs were identified as follows: incidence angle ( $\alpha$ ), welding speed ( $W_S$ ), and joining gap ( $g$ ). As highlighted, there was always a joining gap in laser welding of zinc coated steels for mitigation of zinc vapour. The only KPI considered in the relevant studies was penetration ( $PT$ ). However, the mechanical quality of the weld was generally measured with the tensile test. It was theoretically a function of applied force per unit area. Thus, top width ( $TW$ ), and interface width ( $IW$ ) was considered as two new KPIs.

2. decoupling multi-physics phenomena according to objectives:

The numerical simulation of laser welding was primarily accomplished through the Finite Element Method (FEM). Currently, the numerical simulation of laser welding involved a high level of physical complexity, such as the keyhole surface generation, heat transfer, and fluid flow. The calculation time of some studies related to the numerical simulation of the welding process (computational welding mechanism) was presented in Table 3.5. Depending on the simulation objectives, the multi-physics phenomenon was decoupled by initially calculating the keyhole profile considering the incidence angle and the joining gap. Then, the general heat transfer via heat conduction in solid was solved numerically using the Finite Element Method.

3. calculation of scaling function:

The scaling function was adapted to consider the influence of the process parameters on the actual keyhole profile. It was expressed as the ratio between the experimental value (i.e. high fidelity) and the simulated value (i.e. low fidelity). The most significant deviations were found at low welding speed and high laser power values.

The major impact of the developed methodology was to implement a computationally cost effective physical model to predict multi FZDs (i.e. penetration, top and interface widths). With the presented approach, the FZDs was estimated within a few minutes on a common desktop computer with acceptable accuracy.

## 6.2 Engineering Contribution

The main engineering contributions of this research are (i) to develop a novel methodology for selecting the robust KCCs for the laser dimpling process, and (ii) to develop a novel simulation approach of the RLW process for in-process

monitoring of multi-FZDs. The zinc-coated (galvanized) steel is used extensively by the automotive industry. The successful implementation of the proposed model on selection of the robust KCCs for the laser dimpling process parameters can provide a solution to obtain and guarantee the minimum joining gap requirement for the RLW process. The weld quality is traditionally monitored by off-line monitoring methods. These are time-consuming and costly. The current practice is to monitor weld quality by the sensor-driven in-process monitoring methods. This research offers the capability for in-process monitoring of multi FZDs and linking them to welding process parameters. The results of the research can be exploited on a broader spectrum and integrated as a closed-loop quality control strategy which helps to eliminate, reduce and correct defects before they occur which will lead to increased productivity and product quality.

### 6.3 Limitations & Future Works

The disadvantages of the methodology presented in Chapter 4 can be summarized as follows: *(i)* the required number of replications to calculate a smooth PDF function to compute the success rate, and *(ii)* the deterministic and the stochastic surrogate models are developed based on KCCs which can be easily controllable, without neglecting the noise and their interaction with KCCs.

There are several research articles dealing with the temperature fields and shape of the fusion zone, considering different process parameters by using *(i)* experiment-based modelling, *(ii)* numeric simulation-based modelling. In general, the level of accuracy of the experiment-based modelling increases with the number of the sampling point, while the experimental cost will also increase. Furthermore, variation is observed in the measurements resulting from the process and measurement error. The level of accuracy of the numeric simulation-based modelling models depends on whether all the occurring physics have been considered or the number of assumptions which is needed to simplify the physics. The future scope analyses can be listed as follows: *(i)* to improve the prediction of the keyhole shape in the low fidelity model, *(ii)* to reduce the sampling points in the high fidelity model; whereas, to increase the sampling points in the low fidelity model, and *(iii)* to calculate scaling factors based on the new sampling points according to the defined methodology in Chapter 5. If the accuracy is improved, the sampling point is reduced in the high fidelity. Thus, the time devoted to the experiments may be reduced. As an extension of the considered physics, one may include a ray-tracing to model the intensity distribution in the keyhole or improve the modelling of heat transport by considering fluid dynamics.

# Bibliography

Abt, F., Heider, A., Weber, R., Graf, T., Blug, A., Carl, D., Höfler, H., Nicolosi, L., and Tetzlaff, R. (2011). Camera Based Closed Loop Control for Partial Penetration Welding of Overlap Joints. *Physics Procedia*, 12(PART 1):730–738.

Abt, F., Hess, A., and Dausinger, F. (2007). Focusing of High-Power Single Mode Laser Beams. In *ICALEO 2007 - International Congress on Applications of Laser and Electro-Optics*, page 202.

Ai, Y., Shao, X., Jiang, P., Li, P., Liu, Y., and Liu, W. (2016). Welded Joints Integrity Analysis and Optimization for Fibre Laser Welding of Dissimilar Materials. *Optics and Lasers in Engineering*, 86:62–74.

Akhter, R. (1990). *Laser Welding of Zinc-Coated Steels*. Phd thesis, Imperial College London (University of London).

Akhter, R., Steen, W. M., and Watkins, K. G. (1991). Welding Zinc-Coated Steel with a Laser and the Properties of the Weldment. *Journal of Laser Applications*, 3(2):9.

Alexander, N. J. and Izquierdo, E. (2010). *Robust Fixture Design for Remote Laser Welding*. Master thesis, University of Warwick.

Anawa, E. M. and Olabi, A. G. (2008). Using Taguchi Method to Optimize Welding Pool of Dissimilar Laser-Welded Components. *Optics and Laser Technology*, 40(2):379–388.

Ancona, A. and Sibillano, T. (2008). Monitoring Laser Welding. In Zhang, Y., editor, *Real-Time Weld Process Monitoring*, chapter 21 Monitor, pages 260–287. Woodhead Publishing, Cambridge, England.

ANSI/AWS D1.1 (2000). American National Standards Institute: Structural Welding Code - Steel.

- Assuncao, E. and Williams, S. (2013). Comparison of Continuous Wave and Pulsed Wave Laser Welding Effects. *Optics and Lasers in Engineering*, 51(6):674–680.
- Authier, N., Baptiste, A., Bruyere, V., Namy, P., and Touvrey, C. (2016). Implementation of an Interferometric Sensor for Measuring the Depth of a Capillary Laser Welding. In *ICALEO 2016 - International Congress on Applications of Laser and Electro-Optics*, number October, page 904.
- Bachmann, M., Avilov, V., Gumenyuk, A., and Rethmeier, M. (2014). Experimental and Numerical Investigation of An Electromagnetic Weld Pool Support System for High Power Laser Beam Welding of Austenitic Stainless Steel. *Journal of Materials Processing Technology*, 214(3):578–591.
- Baik, S. H., Kim, M. S., Park, S. K., Chung, C. M., Kim, C. J., and Kim, K. J. (2000). Process Monitoring of Laser Welding Using Chromatic Filtering of Thermal Radiation. *Measurement Science and Technology*, 11(12):1772–1777.
- Bailey, N. S., Tan, W., and Shin, Y. C. (2015). A Parametric Study on Laser Welding of Magnesium Alloy AZ31 by a Fiber Laser. *Journal of Manufacturing Science and Engineering*, 137(4):041003.
- Bardin, F., Cobo, A., Lopez-Higuera, J. M., Collin, O., Aubry, P., Dubois, T., Högström, M., Nylén, P., Jonsson, P., Jones, J. D. C., and Hand, D. P. (2005). Optical Techniques for Real-Time Penetration Monitoring for Laser Welding. *Applied optics*, 44(19):3869–3876.
- Bea, M., Brockmann, R., and Havrilla, D. (2011). Remote Laser Welding in Automotive Production. *Industrial Laser Solutions*, 10(October):8–12.
- Blondeau, R. (2013). *Metallurgy and Mechanics of Welding*, volume 91. Wiley & Sons.
- Breck, H. C. (1986). Lasers Transverse and Longitudinal Modes Affect the Output Beam. *Laser and Applications*, November.
- Cao, X., Jahazi, M., Immarigeon, J. P., and Wallace, W. (2006). A Review of Laser Welding Techniques for Magnesium Alloys. *Journal of Materials Processing Technology*, 171(2):188–204.
- Carlson, B., Kovacevic, R., and Yang, S. (2011). Laser Welding of High-Strength Galvanized Steels in a Gap-Free Lap Joint Configuration Under Different Shielding Conditions. *Welding Journal*, 90(January):8–18.

- Ceglarek, D., Colledani, M., Váncza, J., Kim, D. Y., Marine, C., Kogel-Hollacher, M., Mistry, A., and Bolognese, L. (2015). Rapid Deployment of Remote Laser Welding Processes in Automotive Assembly Systems. *CIRP Annals - Manufacturing Technology*, 64(1):389–394.
- Chen, G., Mei, L., Zhang, M., Zhang, Y., and Wang, Z. (2013). Research on Key Influence Factors of Laser Overlap Welding of Automobile Body Galvanized Steel. *Optics and Laser Technology*, 45(1):726–733.
- Chen, J., Wang, T., Gao, X., and Wei, L. (2018). Real-time monitoring of high-power disk laser welding based on support vector machine. *Computers in Industry*, 94:75–81.
- Chen, W., Ackerson, P., and Molian, P. (2009). CO2 Laser Welding of Galvanized Steel Sheets Using Vent Holes. *Materials and Design*, 30(2):245–251.
- Chen, Z. and Gao, X. (2014). Detection of Weld Pool Width Using Infrared Imaging During High-Power Fiber Laser Welding of Type 304 Austenitic Stainless Steel. *International Journal of Advanced Manufacturing Technology*, 74(9-12):1247–1254.
- Chen, Z., Yang, S., Wang, C., Hu, X., Shao, X., and Wang, J. (2014). A Study of Fiber Laser Welding of Galvanized Steel Using a Suction Method. *Journal of Materials Processing Technology*, 214(7):1456–1465.
- Cho, W. I., Na, S. J., Thomy, C., and Vollertsen, F. (2012). Numerical Simulation of Molten Pool Dynamics in High-Power Disk Laser Welding. *Journal of Materials Processing Technology*, 212(1):262–275.
- Colombo, D. and Previtali, B. (2014). Laser Dimpling and Remote Welding of Zinc-Coated Steels for Automotive Applications. *International Journal of Advanced Manufacturing Technology*, 72(5-8):653–663.
- Courtois, M., Carin, M., Le Masson, P., Gaied, S., and Balabane, M. (2016). Guidelines in the Experimental Validation of a 3D Heat and Fluid Flow Model of Keyhole Laser Welding. *Journal of Physics D: Applied Physics*, 49(15):155503.
- Courtois, M., Carin, M., Masson, P. L., Gaied, S., and Balabane, M. (2013). A New Approach to Compute Multi-Reflections of Laser Beam in a Keyhole for Heat Transfer and Fluid Flow Modelling in Laser Welding. *Journal of Physics D: Applied Physics*, 46(50).
- Cunat, P.-J. (2000). Stainless Steel Properties for Structural Automotive Applications. In *International Automotive Materials Conference*, pages 1–10, Cologne.

- Das, A., Franciosa, P., and Ceglarek, D. (2015). Fixture Design Optimisation Considering Production Batch of Compliant Non-Ideal Sheet Metal Parts. *Procedia Manufacturing*, 1(May):157–168.
- Dasgupta, A. K. and Mazumder, J. (2008). Laser Welding of Zinc-Coated Steel: An Alternative to Resistance Spot Welding. *Science and Technology of Welding and Joining*, 13(3):289–293.
- Dasgupta, A. K., Mazumder, J., and Li, P. (2007). Physics of Zinc Vaporization and Plasma Absorption During CO<sub>2</sub> Laser Welding. *Journal of Applied Physics*, 102(5):053108.
- Davies, G. (2012). *Materials for Automobile Bodies*. Butterworth-Heinemann, second edition.
- De Wit, F. M. and Poulis, J. A. (2012). Joining Technologies for Automotive Components. *Advanced Materials in Automotive Engineering*, pages 315–329.
- Dean, R. B. and Dixon, W. J. (1951). Simplified Statistics for Small Numbers of Observations. *Analytical Chemistry*, 23(4):636–638.
- Dowden, J. M. (2001). *The Mathematics of Thermal: An Introduction to the Theory of Laser Material Processing*. Chapman and Hall/CRC, London.
- Duprat, J.-J. and Kelly, M. (2009). Dedicated Processes for Electroplating on Fasteners. In *National Association for Surface Finishing Annual Technical Conference*, pages 481–493.
- Earl, C., Hilton, P., and O’Neill, B. (2012). Parameter Influence on Surf-Sculpt Processing Efficiency. *Physics Procedia*, 39:327–335.
- EN ISO 10327 (2004). International Organization for Standardization: Continuously Hot-Dip Coated Strip and Sheet of Low Carbon Steels – Technical Delivery Conditions.
- EN ISO 13919-1 (1997). International Organization for Standardization: Welding - Electron and Laser Beam Welded Joints - Guidance on Quality Levels for Imperfections - Part 1: Steels.
- EN ISO 13919-2 (2001). International Organization for Standardization: Welding - Electron and Laser Beam Welded Joints - Guidance on Quality Levels for Imperfections - Part 2: Aluminium.

- EN ISO 5817 (2014). International Organization for Standardization: Welding. Fusion-Welded Joints in Steel, Nickel, Titanium and Their Alloys (Beam Welding Excluded). Quality Levels for Imperfections.
- Enz, J., Kumar, M., Riekehr, S., Ventzke, V., Huber, N., and Kashaev, N. (2017). Mechanical Properties of Laser Beam Welded Similar and Dissimilar Aluminium Alloys. *Journal of Manufacturing Processes*, 29:272–280.
- Eriksson, I., Powell, J., and Kaplan, A. F. (2010). Signal Overlap in the Monitoring of Laser Welding. *Measurement Science and Technology*, 21(10):105705.
- Fernández-Godino, M. G., Park, C., Nam-Ho, K., and Haftka, R. T. (2016). Review of Multi-Fidelity Models. Technical report, Cornell University arXiv preprint arXiv:1609.07196.
- Fetzer, F., Stritt, P., Berger, P., Weber, R., and Graf, T. (2017). Fast Numerical Method to Predict the Depth of Laser Welding. *Journal of Laser Applications*, 29(2):022012.
- Franciosa, P., Das, A., Ceglarek, D., Bolognese, L., Marine, C., and Mistry, A. (2014). Design Synthesis Methodology for Dimensional Management of Assembly Process with Compliant Non-Ideal Parts. In *Proceedings of Joint Conference on Mechanical, Design Engineering & Advanced Manufacturing*, volume 1, pages 1–7.
- Franciosa, P., Gerbino, S., and Ceglarek, D. (2016). Fixture Capability Optimisation for Early-Stage Design of Assembly System with Compliant Parts Using Nested Polynomial Chaos Expansion. *Procedia CIRP*, 41:87–92.
- Frewin, M. and Scott, D. (1999). Finite Element Model of Pulsed Laser Welding. *Welding Journal-New York-*, 78(1):15–s.
- Friedman, J. H. (1991). Multivariate Adaptive Regression Splines. *The Annals of Statistics*, 19(1):1–67.
- Gao, Z., Shao, X., Jiang, P., Cao, L., Zhou, Q., Yue, C., Liu, Y., and Wang, C. (2016). Parameters Optimization of Hybrid Fiber Laser-Arc Butt Welding on 316L Stainless Steel Using Kriging Model and GA. *Optics and Laser Technology*, 83:153–162.
- Geiger, M., Leitz, K. H., Koch, H., and Otto, A. (2009). A 3D Transient Model of Keyhole and Melt Pool Dynamics in Laser Beam Welding Applied to the Joining of Zinc-Coated Sheets. *Production Engineering*, 3(2):127–136.



- Ghassemieh, E. (2011). Materials in Automotive Application: State-of-the-Art and Prospects. *New Trends and Developments in Automotive Industry*, pages 365–394.
- Goldak, J., Chakravarti, A., and Bibby, M. (1984). A New Finite Element Model for Welding Heat Sources. *Metallurgical Transactions B*, 15(2):299–305.
- Graham, M. P., Hirak, D. M., Kerr, H. W., and Weckman, D. C. (1994). Nd:YAG Laser Welding of Coated Sheet Steel. *Journal of Laser Applications*, 6(4):212.
- Gu, H. (2010). Laser Lap Welding of Zinc Coated Steel Sheet with Laser Dimple Technology. *Journal of Laser Applications*, 22(3):87.
- Gu, H. and Shulkin, B. (2011). A Practical Use of Humping Effect in Laser Beam Welding. *Journal of Laser Applications*, 23(1):012001.
- Haider, M., Hubert, P., and Lessard, L. (2007). An Experimental Investigation of Class-A Surface Finish of Composites Made by the Resin Transfer Molding Process. *Composites Science and Technology*, 67(15-16):3176–3186.
- He, X., Fuerschbach, P., and DebRoy, T. (2003). Heat Transfer and Fluid Flow During Laser Spot Welding of 304 Stainless Steel. *Journal of Physics D: Applied Physics*, 36(12):1388–1398.
- Holliday, R., Parker, J., and Williams, N. (1996). Relative Contribution of Electrode Tip Growth Mechanisms in Spot Welding Zinc-Coated Steels. *Welding in the World, Le Soudage Dans Le Monde*, 37(4):186–193.
- Hong, K. M. and Shin, Y. C. (2017). Prospects of Laser Welding Technology in the Automotive Industry: A Review. *Journal of Materials Processing Technology*, 245:46–69.
- Hosking, N. C., Ström, M. A., Shipway, P. H., and Rudd, C. D. (2007). Corrosion Resistance of Zinc-Magnesium-Coated Steel. *Corrosion Science*, 49(9):3669–3695.
- Hu, B. and Richardson, I. M. (2006). Mechanism and Possible Solution for Transverse Solidification Cracking in Laser Welding of High Strength Aluminium Alloys. *Materials Science and Engineering: A*, 429(1-2):287–294.
- Huang, C., Kou, S., and Purins, J. R. (2001). Liquation, Solidification, Segregation and Hot Cracking in the Partially Melted Zone of Al-4.5 Cu Welds. In *In Proceedings of Merton C. Flemings Symposium on Solidification Processing*, pages 229–234.

- Iqbal, S., Gualini, M. M. S., and Rehman, A. (2010). Dual Beam Method for Laser Welding of Galvanized Steel: Experimentation and Prospects. *Optics and Laser Technology*, 42(1):93–98.
- Jacob, G. C., Fellers, J. F., Simunovic, S., and Starbuck, J. M. (2002). Energy absorption in polymer composites for automotive crashworthiness. *Journal of Composite Materials*, 36(7):813–850.
- Jekabsons, G. (2016). ARES-Lab: Adaptive Regression Splines Toolbox for Mat-Lab/Octave.
- Jiang, P., Cao, L., Zhou, Q., Gao, Z., Rong, Y., and Shao, X. (2016). Optimization of Welding Process Parameters by Combining Kriging Surrogate with Particle Swarm Optimization Algorithm. *International Journal of Advanced Manufacturing Technology*, 86(9-12):2473–2483.
- Jin, X., Cheng, Y., Zeng, L., Zou, Y., and Zhang, H. (2012). Multiple Reflections and Fresnel Absorption of Gaussian Laser Beam in an Actual 3D Keyhole During Deep-Penetration Laser Welding. *International Journal of Optics*, 2012.
- Jou, M. (2003). Real Time Monitoring Weld Quality of Resistance Spot Welding for the Fabrication of Sheet Metal Assemblies. *Journal of Materials Processing Technology*, 132(1-3):102–113.
- Kägeler, C. and Schmidt, M. (2010). Frequency-Based Analysis of Weld Pool Dynamics and Keyhole Oscillations at Laser Beam Welding of Galvanized Steel Sheets. *Physics Procedia*, 5:447–453.
- Kaplan, A. F. (1994). A Model of Deep Penetration Laser Welding Based on Calculation of the Keyhole Profile. *Journal of Physics D: Applied Physics*, 27:1805–1814.
- Kaplan, A. F. (2012). Fresnel Absorption of 1  $\mu\text{m}$  and 10  $\mu\text{m}$  Laser Beams at the Keyhole Wall During Laser Beam Welding: Comparison Between Smooth and Wavy Surfaces. *Applied Surface Science*, 258(8):3354–3363.
- Kaplan, A. F. and Powell, J. (2011). Spatter in Laser Welding. *Journal of Laser Applications*, 23(3).
- Kawahito, Y., Mizutani, M., Katayama, S., and Steel, S. (2007). Investigation of High-Power Fiber Laser Welding Phenomena of Stainless Steel. *Transactions of JWRI*, 36(2):11–16.

- Kawahito, Y., Ohnishi, T., and Katayama, S. (2009). In-Process Monitoring and Feedback Control for Stable Production of Full-Penetration Weld in Continuous Wave Fibre Laser Welding. *Journal of Physics D: Applied Physics*, 42(8):085501.
- Khan, M. M., Romoli, L., Dini, G., and Fiaschi, M. (2011). A Simplified Energy-Based Model for Laser Welding of Ferritic Stainless Steels in Overlap Configurations. *CIRP Annals - Manufacturing Technology*, 60(1):215–218.
- Kim, J., Oh, S., and Ki, H. (2015). A Study of Keyhole Geometry in Laser Welding of Zinc-Coated and Uncoated Steels Using A Coaxial Observation Method. *Journal of Materials Processing Technology*, 225:451–462.
- Kogel-Hollacher, M., Schoenleber, M., Schulze, J., and Pichot, J. F. (2017). Inline Measurement for Quality Control from Macro to Micro Laser Applications. *Proc. of SPIE Vol*, 10091:100910H.
- Kou, S. (2003). *Welding Metallurgy*. Wiley & Sons.
- Krauss, G., Matlock, D. K., and TMS Ferrous Metallurgy Committee. (1990). *Zinc-Based Steel Coating Systems: Metallurgy and Performance*. Minerals, Metals & Materials Society.
- Layus, P., Kah, P., Khlusova, E., and Orlov, V. (2018). Study of the Sensitivity of High-Strength Cold-Resistant Shipbuilding Steels to Thermal Cycle of Arc Welding. *International Journal of Mechanical and Materials Engineering*, 13(1):1–9.
- Lee, T., Chiu, C., Chou, Y., and Lu, C. (2006). Mining the Customer Credit Using Classification and Regression Tree and Multivariate Adaptive Regression Splines. *Computational Statistics & Data Analysis*, 50(4):1113–1130.
- Li, B., Shiu, B. W., and Lau, K. J. (2003). Robust Fixture Configuration Design for Sheet Metal Assembly with Laser Welding. *Journal of Manufacturing Science and Engineering*, 124(1):120–127.
- Li, X., Lawson, S., Zhou, Y., and Goodwin, F. (2007). Novel Technique for Laser Lap Welding of Zinc Coated Sheet Steels. *Journal of Laser Applications*, 19(4):259.
- Li, Y., Hu, S., Shen, J., and Liu, L. (2015). Microstructures and Mechanical Properties of H62 Brass-316L Stainless Steel in Overlap Welded Joints by Continuous-Wave Laser. *International Journal of Advanced Manufacturing Technology*, 79(1-4):627–634.

- Liao, Y. C. and Yu, M. H. (2007). Effects of Laser Beam Energy and Incident Angle on the Pulse Laser Welding of Stainless-Steel Thin Sheet. *Journal of Materials Processing Technology*, 190(1-3):102–108.
- Lienert, T., Siewert, T., Babu, S., and Acoff, V. (2011). Fundamentals of Weld Solidification. *ASM Handbook, Welding, Brazing and Soldering*, 6:96 –114.
- Liu, S., Mi, G., Yan, F., Wang, C., and Jiang, P. (2017). Correlation of High-Power Laser Welding Parameters with Real Weld Geometry and Microstructure. *Optics and Laser Technology*, 94:59–67.
- Longuet, A., Robert, Y., Aeby-Gautier, E., Appolaire, B., Mariage, J. F., Colin, C., and Cailletaud, G. (2009). A Multiphase Mechanical Model for Ti-6Al-4V: Application to the Modelling of Laser Assisted Processing. *Computational Materials Science*, 46(3):761–766.
- Luo, M. and Shin, Y. C. (2015). Vision-Based Weld Pool Boundary Extraction and Width Measurement During Keyhole Fibre Laser Welding. *Optics and Lasers in Engineering*, 64:59–70.
- Ma, J., Kong, F., Carlson, B., and Kovacevic, R. (2012). Mitigating Zinc Vapor Induced Weld Defects in Laser Welding of Galvanized High-Strength Steel by Using Different Supplementary Means. *Welding Processes*, pages 117–138.
- Ma, J., Kong, F., Carlson, B., and Kovacevic, R. (2013). Two-Pass Laser Welding of Galvanized High-Strength Dual-Phase Steel for a Zero-Gap Lap Joint Configuration. *Journal of Materials Processing Technology*, 213(3):495–507.
- Magnusson, C. and Anderson, R. (2001). Stainless Steel as a Lightweight Automotive Material. In *Forming and Materials, Swedish Tool & Die Technology*, pages 36–46.
- Maiman, T. H. (1960). Stimulated Optical Radiation in Ruby. *Nature*, 4736(187):493–494.
- Marsh, M. B. (2000). Development of Autobody Sheet Materials for Crash Performance. In *Materials and Structures for Energy Absorption*, pages 55–64.
- Marya, M. and Gayden, X. Q. (2005). Development of Requirements for Resistance Spot Welding Dual-Phase (DP600) Steels: Part 1 - The Cause of Interfacial Fracture. *Welding Journal*, 84(11):172–182.

- Midawi, A. R. H., Santos, E. B. F., Gerlich, A. P., Pistor, R., and Haghshenas, M. (2014). Comparison of Hardness and Microstructures Produced Using GMAW and Hot-Wire TIG Mechanized Welding of High Strength Steels. *ASME 2014 International Mechanical Engineering Congress and Exposition IMECE 2014*, (14):10–17.
- Milberg, J. and Trautmann, A. (2009). Defect-Free Joining of Zinc-Coated Steels by Bifocal Hybrid Laser Welding. *Production Engineering*, 3(1):9–15.
- Mirapeix, J., Vila, E., Valdiande, J. J., Riquelme, A., Garcia, M., and Cobo, A. (2016). Real-Time Detection of the Aluminium Contribution During Laser Welding of Usibor1500 Tailor-Welded Blanks. *Journal of Materials Processing Technology*, 235:106–113.
- Mishra, S. and Debroy, T. (1995). Grain Growth in the Heat-Affected Zone of Fusion Welds. *Reviews of Modern Physics*, 67(85):1–48.
- Miyazaki, Y. and Furusako, S. (2007). Tensile Shear Strength of Laser Welded Lap Joints. *Nippon Steel Technical Report*, (95):28–34.
- Montalvo-Urquizo, J., Akbay, Z., and Schmidt, A. (2009). Adaptive Finite Element Models Applied to the Laser Welding Problem. *Computational Materials Science*, 46(1):245–254.
- Moradi, M. and Ghoreishi, M. (2011). Influences of Laser Welding Parameters on the Geometric Profile of Ni-Base Superalloy Rene 80 Weld-Bead. *International Journal of Advanced Manufacturing Technology*, 55(1-4):205–215.
- Nagel, F., Brömme, L., and Bergmann, J. P. (2018). Description of the Influence of Two Laser Intensities on the Spatter Formation on Laser Welding of Steel. *Procedia CIRP*, 74(September):475–480.
- Nicolosi, L., Abt, F., Blug, A., Heider, A., Tetzlaff, R., and Höfler, H. (2012). A Novel Spatter Detection Algorithm Based on Typical Cellular Neural Network Operations for Laser Beam Welding Processes. *Measurement Science and Technology*, 23(1).
- Norman, P., Karlsson, J., and Kaplan, A. F. H. (2009). Monitoring Undercut, Blowouts and Root Sagging During Laser Beam Welding. *5th International WLT-Conference on Lasers in Manufacturing*, (June):355.
- Olabi, A. G., Alsinani, F. O., Alabdulkarim, A. A., Ruggiero, A., Tricarico, L., and Benyounis, K. Y. (2013). Optimizing the CO<sub>2</sub> Laser Welding Process for Dissimilar Materials. *Optics and Lasers in Engineering*, 51(7):832–839.

- Olsson, R., Eriksson, I., Powell, J., Langtry, a. V., and Kaplan, a. F. H. (2011). Challenges to the Interpretation of the Electromagnetic Feedback from Laser Welding. *Optics and Lasers in Engineering*, 49(2):188–194.
- Otto, A., Koch, H., Leitz, K.-H., and Schmidt, M. (2011). Numerical Simulations - A Versatile Approach for Better Understanding Dynamics in Laser Material Processing. *Physics Procedia*, 12:11–20.
- Pang, S., Chen, X., Li, W., Shao, X., and Gong, S. (2016). Efficient Multiple Time Scale Method for Modelling Compressible Vapor Plume Dynamics Inside Transient Keyhole During Fibre Laser Welding. *Optics and Laser Technology*, 77:203–214.
- Pang, S., Chen, X., Zhou, J., Shao, X., and Wang, C. (2015). 3D Transient Multi-phase Model for Keyhole, Vapor Plume, And Weld Pool Dynamics in Laser Welding Including the Ambient Pressure Effect. *Optics and Lasers in Engineering*, 74:47–58.
- Papkala, H. (1992). Technological Problems in Spot Welding of Galvanized Car Body Sheet. *Welding International*, 6(5):341–346.
- Porter, F. (1991). *Zinc Handbook: Properties, Processing, and Use in Design*. Marcel Dekker, New York, USA.
- Rai, R., Roy, G. G., and DebRoy, T. (2007). A Computationally Efficient Model of Convective Heat Transfer and Solidification Characteristics During Keyhole Mode Laser Welding. *Journal of Applied Physics*, 101(5):054909.
- Ribolla, A., Damoulis, G. L., and Batalha, G. F. (2005). The Use of Nd:YAG Laser Weld for Large Scale Volume Assembly of Automotive Body in White. *Journal of Materials Processing Technology*, 164-165:1120–1127.
- Rizzi, D., Sibillano, T., Pietro Calabrese, P., Ancona, A., and Mario Lugarà, P. (2011). Spectroscopic, Energetic and Metallographic Investigations of the Laser Lap Welding of AISI 304 Using the Response Surface Methodology. *Optics and Lasers in Engineering*, 49(7):892–898.
- Rong, Y., Zhang, Z., Zhang, G., Yue, C., Gu, Y., Huang, Y., Wang, C., and Shao, X. (2015). Parameters Optimization of Laser Brazing in Crimping Butt Using Taguchi and BPNN-GA. *Optics and Lasers in Engineering*, 67:94–104.
- Saldi, Z. S., Kidess, A., Kenjereš, S., Zhao, C., Richardson, I. M., and Kleijn, C. R. (2013). Effect of Enhanced Heat and Mass Transport and Flow Reversal During Cool Down on Weld Pool Shapes in Laser Spot Welding of Steel. *International Journal of Heat and Mass Transfer*, 66:879–888.

- Salonitis, K., Drougas, D., and Chryssolouris, G. (2010). Finite Element Modelling of Penetration Laser Welding of Sandwich Materials. *Physics Procedia*, 5(PART 2):327–335.
- Saucedo, F. V., Chann, B., Samson, B., and Tayebati, P. (2016). Direct Diode vs Other Laser Systems Used in Laser Cutting. *Industrial Laser Solutions*.
- Schmidt, M., Otto, A., and Kägeler, C. (2008). Analysis of YAG Laser Lap Welding of Zinc Coated Steel Sheets. *CIRP Annals - Manufacturing Technology*, 57(1):213–216.
- Shaibu, V. B., Sahoo, S. K., and Kumar, A. (2015). Computational Modelling of Dissimilar Metal CO2 Laser Welding: Applied to Copper and 304 Stainless Steel. *Procedia Engineering*, 127:208–214.
- Sinha, A. K., Kim, D. Y., and Ceglarek, D. (2013). Correlation Analysis of The Variation of Weld Seam and Tensile Strength in Laser Welding of Galvanized Steel. *Optics and Lasers in Engineering*, 51(10):1143–1152.
- Sokolov, M., Salminen, A., Kuznetsov, M., and Tsibulskiy, I. (2011). Laser Welding and Weld Hardness Analysis of Thick Section S355 Structural Steel. *Materials and Design*, 32(10):5127–5131.
- Song, L., Huang, W., Han, X., and Mazumder, J. (2017). Real-Time Composition Monitoring Using Support Vector Regression of Laser-Induced Plasma for Laser Additive Manufacturing. *IEEE Transactions on Industrial Electronics*, 64(1):633–642.
- Speka, M., Mattei, S., Pilloz, M., and Ilie, M. (2008). The Infrared Thermography Control of The Laser Welding of Amorphous Polymers. *NDT and E International*, 41(3):178–183.
- Stavridis, J., Papacharalampopoulos, A., and Stavropoulos, P. (2017). Quality Assessment in Laser Welding: A Critical Review. *The International Journal of Advanced Manufacturing Technology*.
- Sturgeon, T. J., Memedovic, O., Biesebroeck, J. V., and Gereffi, G. (2009). Globalisation of The Automotive Industry: Main Features and Trends. *International Journal of Technological Learning, Innovation and Development*, 2:7–24.
- Suder, W. J., Ganguly, S., Williams, S. W., Paradowska, A. M., and Colegrove, P. (2011). Comparison of Joining Efficiency and Residual Stresses in Laser and Laser Hybrid Welding. *Science and Technology of Welding and Joining*, 16(3):244–248.

- Suder, W. J. and Williams, S. W. (2012). Investigation of the Effects of Basic Laser Material Interaction Parameters in Laser Welding. *Journal of Laser Applications*, 24(3):032009.
- Tenner, F., Brock, C., Klämpfl, F., and Schmidt, M. (2015). Analysis of the Correlation Between Plasma Plume and Keyhole Behaviour in Laser Metal Welding for the Modelling of The Keyhole Geometry. *Optics and Lasers in Engineering*, 64(2015):32–41.
- Thiery, L. and Frédéric, R. (2007). Advances in Trivalent Passivates on Zinc and Zinc Alloys. *Galvanotechnik*, 98(4):862–870.
- Thode, H. (2002). *Testing for Normality*. Marcel Dekker, New York, USA.
- Tsirkas, S. A., Papanikos, P., and Kermanidis, T. (2003). Numerical Simulation of the Laser Welding Process in Butt-Joint Specimens. *Journal of Materials Processing Technology*, 134(1):59–69.
- Tzeng, Y. F. and Yih-Fong, T. (2006). Gap-Free Lap Welding of Zinc-Coated Steel Using Pulsed CO<sub>2</sub> Laser. *International Journal of Advanced Manufacturing Technology*, 29(3-4):287–295.
- Volpp, J. and Vollertsen, F. (2016). Keyhole Stability During Laser Welding—Part I: Modelling and Evaluation. *Production Engineering*, 10(4-5):443–457.
- Williams, N. and Parker, J. (2004). Review of Resistance Spot Welding of Steel Sheets: Part-1 Modelling and Control of Weld Nugget Formation. *International Materials Reviews*, 49(2):45–75.
- Winkler, C., Amberg, G., Inoue, H., and Koseki, T. (1997). A Numerical and Experimental Investigation of Qualitatively Different Weld Pool Shapes. *Numerical Analysis of Weldability*, pages 37–69.
- Wu, C., Wang, H. G., and Zhang, Y. M. (2006). A New Heat Source Model for Keyhole Plasma Arc Welding in FEM Analysis of the Temperature Profile. *Welding Journal*, 85(12):284–291.
- Wu, C. S., Hu, Q. X., and Gao, J. Q. (2009). An Adaptive Heat Source Model for Finite-Element Analysis of Keyhole Plasma Arc Welding. *Computational Materials Science*, 46(1):167–172.
- Yang, S. L. and Kovacevic, R. (2009). Welding of Galvanized Dual-Phase 980 Steel in a Gap-Free Lap Joint Configuration. *Welding Journal*, 88(August):168s–178s.



- Yang, Y. S. and Lee, S. H. (1999). Study on the Joining Strength of Laser Spot Welding for Automotive Applications. *Journal of Materials Processing Technology*, 94(2):151–156.
- Ye, X.-H. and Chen, X. (2002). Three-Dimensional Modelling of Heat Transfer and Fluid Flow in Laser Full-Penetration Welding. 35:1049–1056.
- You, D. Y., Gao, X. D., and Katayama, S. (2014). Review of Laser Welding Monitoring. *Science and Technology of Welding and Joining*, 19(3):181–201.
- Zhang, L., Li, X., Nie, Z., Huang, H., and Niu, L. (2016). Comparison of Microstructure and Mechanical Properties of TIG and Laser Welding Joints of a New Al-Zn-Mg-Cu Alloy. *Materials and Design*, 92:880–887.
- Zhang, L.-J., Zhang, G.-F., Bai, X.-Y., Ning, J., and Zhang, X.-J. (2015). Effect of the Process Parameters on the Three-Dimensional Shape of Molten Pool During Full-Penetration Laser Welding Process. *The International Journal of Advanced Manufacturing Technology*, 86(5-8):1273–1286.
- Zhao, Y., Zhang, Y., Hu, W., and Lai, X. (2012). Optimization of Laser Welding Thin-Gage Galvanized Steel Via Response Surface Methodology. *Optics and Lasers in Engineering*, 50(9):1267–1273.
- Zhao, Y. Y., Zhang, Y. S., and Hu, W. (2013). Effect of Welding Speed on Microstructure, Hardness and Tensile Properties in Laser Welding of Advanced High Strength Steel. *Science and Technology of Welding and Joining*, 18(7):581–590.
- Zhou, J. and Tsai, H. L. (2007). Effects of Electromagnetic Force on Melt Flow and Porosity Prevention in Pulsed Laser Keyhole Welding. *International Journal of Heat and Mass Transfer*, 50(11-12):2217–2235.
- Zhou, J., Tsai, H. L., and Lehnhoff, T. F. (2006). Investigation of Transport Phenomena and Defect Formation in Pulsed Laser Keyhole Welding of Zinc-Coated Steels. *Journal of Physics D: Applied Physics*, 39(24):5338–5355.

# Appendix A

## Experimental Results for Laser Dimpling

Table A.1: DoE Table and Experimental Results for Laser Dimpling

Exp. ID	Rep.	Scanning Speed ( <i>m/min</i> )	Incidence Angle ( $^{\circ}$ )	Laser Track ( <i>mm</i> )	Focal Offset ( <i>mm</i> )	Dimple Height ( <i>mm</i> )	Dimple Upper Surface Area ( <i>mm</i> <sup>2</sup> )	Dimple Lower Surface Area ( <i>mm</i> <sup>2</sup> )
1	1	2	0	2	25	0.07694	1.13106	2.90893
1	2	2	0	2	25	0.04622	0.18471	2.24879
1	3	2	0	2	25	0.09062	0.47648	1.28272
1	4	2	0	2	25	0.05679	0.59959	2.45810
1	5	2	0	2	25	0.08686	0.80505	1.92677
2	1	3	0	2	25	0.05148	0.06740	0.92313
2	2	3	0	2	25	0.08657	0.42793	0.51524
2	3	3	0	2	25	0.03907	0.02811	1.18075
2	4	3	0	2	25	0.06699	0.28010	0.00000
2	5	3	0	2	25	0.05067	0.22039	0.77822
3	1	4	0	2	25	0.06692	0.23506	0.00000
3	2	4	0	2	25	0.08896	0.43299	0.00000
3	3	4	0	2	25	0.07227	0.27956	0.00000
3	4	4	0	2	25	0.08808	0.41128	0.00000
3	5	4	0	2	25	0.07927	0.24562	0.00000
4	1	2	10	2	25	0.14367	1.68121	2.78339
4	2	2	10	2	25	0.14439	1.69226	2.78339
4	3	2	10	2	25	0.08363	0.56320	2.19713
4	4	2	10	2	25	0.10646	1.27649	2.19713
4	5	2	10	2	25	0.11127	1.23206	2.51931
5	1	3	10	2	25	0.06239	0.51375	1.11441
5	2	3	10	2	25	0.07114	0.54373	1.05631
5	3	3	10	2	25	0.07490	0.49985	0.65491
5	4	3	10	2	25	0.05910	0.65903	0.71829
5	5	3	10	2	25	0.10644	0.51305	0.62851
6	1	4	10	2	25	0.11608	0.53979	0.00000
6	2	4	10	2	25	0.10079	0.45276	0.00000
6	3	4	10	2	25	0.11519	0.53510	0.00000
6	4	4	10	2	25	0.12670	0.43839	0.00000
6	5	4	10	2	25	0.09719	0.46601	0.00000

**Table A.1 Continued:** DoE Table and Experimental Results for Laser Dimpling

Exp. ID	Rep.	Scanning Speed ( <i>m/min</i> )	Incidence Angle ( $^{\circ}$ )	Laser Track ( <i>mm</i> )	Focal Offset ( <i>mm</i> )	Dimple Height ( <i>mm</i> )	Dimple Upper Surface Area ( <i>mm</i> <sup>2</sup> )	Dimple Lower Surface Area ( <i>mm</i> <sup>2</sup> )
7	1	2	20	2	25	0.07517	1.22602	4.71807
7	2	2	20	2	25	0.06947	0.66596	3.09844
7	3	2	20	2	25	0.08225	0.82648	2.31880
7	4	2	20	2	25	0.07945	1.26020	1.65485
7	5	2	20	2	25	0.06533	1.08179	1.65988
8	1	3	20	2	25	0.08726	0.43128	0.00000
8	2	3	20	2	25	0.07487	0.43898	0.00000
8	3	3	20	2	25	0.07570	0.39036	0.00000
8	4	3	20	2	25	0.06193	0.24934	0.00000
8	5	3	20	2	25	0.05935	0.34474	0.00000
9	1	4	20	2	25	0.08985	0.39435	0.00000
9	2	4	20	2	25	0.10968	0.53263	0.00000
9	3	4	20	2	25	0.10521	0.63012	0.00000
9	4	4	20	2	25	0.07201	0.29302	0.00000
9	5	4	20	2	25	0.06573	0.33521	0.00000
10	1	2	0	3	25	0.07214	0.83361	4.61615
10	2	2	0	3	25	0.07770	0.89053	4.75365
10	3	2	0	3	25	0.12184	1.41051	4.26748
10	4	2	0	3	25	0.09777	1.02100	4.01212
10	5	2	0	3	25	0.14769	1.56735	4.02194
11	1	3	0	3	25	0.08474	0.84679	2.39156
11	2	3	0	3	25	0.04932	0.24400	2.43576
11	3	3	0	3	25	0.06477	0.29407	0.00000
11	4	3	0	3	25	0.05528	0.24004	0.00000
11	5	3	0	3	25	0.05639	0.27633	0.89377
12	1	4	0	3	25	0.05109	0.24140	1.21297
12	2	4	0	3	25	0.08014	0.45050	0.00000
12	3	4	0	3	25	0.09107	0.37808	0.00000
12	4	4	0	3	25	0.09806	0.45168	0.00000
12	5	4	0	3	25	0.07126	0.44975	0.00000
13	1	2	10	3	25	0.11809	1.60663	5.53563
13	2	2	10	3	25	0.15510	1.39239	6.26645
13	3	2	10	3	25	0.14793	2.14058	4.89810
13	4	2	10	3	25	0.14967	1.35384	4.64412
13	5	2	10	3	25	0.12175	0.99000	4.39015
14	1	3	10	3	25	0.07764	0.55492	1.94887
14	2	3	10	3	25	0.06768	0.41723	1.96960
14	3	3	10	3	25	0.07459	0.46930	1.23878
14	4	3	10	3	25	0.10222	1.35050	2.30651
14	5	3	10	3	25	0.10662	1.08055	2.23395

**Table A.1 Continued:** DoE Table and Experimental Results for Laser Dimpling

Exp. ID	Rep.	Scanning Speed ( <i>m/min</i> )	Incidence Angle ( $^{\circ}$ )	Laser Track ( <i>mm</i> )	Focal Offset ( <i>mm</i> )	Dimple Height ( <i>mm</i> )	Dimple Upper Surface Area ( <i>mm</i> <sup>2</sup> )	Dimple Lower Surface Area ( <i>mm</i> <sup>2</sup> )
15	1	4	10	3	25	0.08599	0.32119	0.00000
15	2	4	10	3	25	0.10683	0.56715	0.00000
15	3	4	10	3	25	0.12488	0.66927	0.00000
15	4	4	10	3	25	0.12088	0.62469	0.00000
15	5	4	10	3	25	0.10293	0.50755	0.00000
16	1	2	20	3	25	0.12211	1.21916	5.23195
16	2	2	20	3	25	0.18262	1.59221	4.81419
16	3	2	20	3	25	0.10879	1.48952	4.79429
16	4	2	20	3	25	0.10536	1.66829	3.70513
16	5	2	20	3	25	0.10588	0.59854	4.40637
17	1	3	20	3	25	0.11569	0.69193	3.19288
17	2	3	20	3	25	0.10397	0.59716	1.75061
17	3	3	20	3	25	0.09086	0.53166	1.65115
17	4	3	20	3	25	0.09776	0.50894	0.00000
17	5	3	20	3	25	0.09307	0.70182	1.43729
18	1	4	20	3	25	0.16091	0.81244	0.00000
18	2	4	20	3	25	0.14140	0.72841	0.00000
18	3	4	20	3	25	0.14661	0.68006	0.00000
18	4	4	20	3	25	0.11505	0.57632	0.00000
18	5	4	20	3	25	0.10359	0.60913	0.00000
19	1	2	0	4	25	0.15921	2.14320	6.51060
19	2	2	0	4	25	0.13522	2.17169	5.02878
19	3	2	0	4	25	0.12114	2.16936	4.57718
19	4	2	0	4	25	0.13528	2.08542	4.86413
19	5	2	0	4	25	0.12147	2.18739	5.08993
20	1	3	0	4	25	0.06568	0.88268	2.45559
20	2	3	0	4	25	0.06650	0.86483	2.37562
20	3	3	0	4	25	0.07036	1.04642	2.66728
20	4	3	0	4	25	0.06630	0.36932	3.38702
20	5	3	0	4	25	0.06647	0.71710	3.27882
21	1	4	0	4	25	0.05705	0.19109	0.00000
21	2	4	0	4	25	0.08700	0.48669	0.00000
21	3	4	0	4	25	0.06632	0.41150	0.00000
21	4	4	0	4	25	0.07804	0.35796	0.00000
21	5	4	0	4	25	0.06788	0.27187	0.00000
22	1	2	10	4	25	0.11809	1.89760	9.13117
22	2	2	10	4	25	0.17188	2.18928	7.98322
22	3	2	10	4	25	0.15543	1.91650	6.51477
22	4	2	10	4	25	0.13257	1.38176	6.42736
22	5	2	10	4	25	0.12602	1.67277	6.81196

**Table A.1 Continued:** DoE Table and Experimental Results for Laser Dimpling

Exp. ID	Rep.	Scanning Speed ( <i>m/min</i> )	Incidence Angle ( $^{\circ}$ )	Laser Track ( <i>mm</i> )	Focal Offset ( <i>mm</i> )	Dimple Height ( <i>mm</i> )	Dimple Upper Surface Area ( <i>mm</i> <sup>2</sup> )	Dimple Lower Surface Area ( <i>mm</i> <sup>2</sup> )
23	1	3	10	4	25	0.14899	1.70787	5.61739
23	2	3	10	4	25	0.12387	1.35524	4.67339
23	3	3	10	4	25	0.11277	1.57799	4.60346
23	4	3	10	4	25	0.11269	1.09029	2.85531
23	5	3	10	4	25	0.16315	1.56062	4.60346
24	1	4	10	4	25	0.11493	1.24686	2.79121
24	2	4	10	4	25	0.09935	0.53578	0.00000
24	3	4	10	4	25	0.12303	0.64786	0.00000
24	4	4	10	4	25	0.09297	0.31415	0.68761
24	5	4	10	4	25	0.08996	0.37467	0.00000
25	1	2	20	4	25	0.08244	0.83575	7.58856
25	2	2	20	4	25	0.11565	0.72767	7.79119
25	3	2	20	4	25	0.13576	0.93600	6.83375
25	4	2	20	4	25	0.13448	1.25245	6.63112
25	5	2	20	4	25	0.10015	0.89909	5.68888
26	1	3	20	4	25	0.09541	0.63838	3.82974
26	2	3	20	4	25	0.08628	0.34384	3.72842
26	3	3	20	4	25	0.08604	0.51507	4.00198
26	4	3	20	4	25	0.08307	0.70686	2.57342
26	5	3	20	4	25	0.09502	0.88887	3.44474
27	1	4	20	4	25	0.07842	0.37160	0.00000
27	2	4	20	4	25	0.12425	0.74135	1.10434
27	3	4	20	4	25	0.12813	0.80827	0.00000
27	4	4	20	4	25	0.11580	0.66953	0.00000
27	5	4	20	4	25	0.05855	0.26914	1.40322
28	1	2	0	2	35	0.11479	1.10260	1.27700
28	2	2	0	2	35	0.11245	1.06880	1.80900
28	3	2	0	2	35	0.09276	0.88104	1.84600
28	4	2	0	2	35	0.11326	1.02953	1.09500
28	5	2	0	2	35	0.06858	0.91020	1.69600
29	1	3	0	2	35	0.11073	0.74241	0.00000
29	2	3	0	2	35	0.12367	0.90334	0.00000
29	3	3	0	2	35	0.14956	0.91996	0.00000
29	4	3	0	2	35	0.10789	0.69606	0.00000
29	5	3	0	2	35	0.11100	0.63113	0.00000
30	1	4	0	2	35	0.08818	0.48855	0.00000
30	2	4	0	2	35	0.07373	0.21417	0.00000
30	3	4	0	2	35	0.13121	0.61579	0.00000
30	4	4	0	2	35	0.08826	0.38524	0.00000
30	5	4	0	2	35	0.10021	0.50783	0.00000

**Table A.1 Continued:** DoE Table and Experimental Results for Laser Dimpling

Exp. ID	Rep.	Scanning Speed ( <i>m/min</i> )	Incidence Angle ( $^{\circ}$ )	Laser Track ( <i>mm</i> )	Focal Offset ( <i>mm</i> )	Dimple Height ( <i>mm</i> )	Dimple Upper Surface Area ( <i>mm</i> <sup>2</sup> )	Dimple Lower Surface Area ( <i>mm</i> <sup>2</sup> )
31	1	2	10	2	35	0.11972	1.05333	2.63550
31	2	2	10	2	35	0.18426	1.19247	0.00000
31	3	2	10	2	35	0.16969	1.32049	0.00000
31	4	2	10	2	35	0.13740	1.31531	1.61616
31	5	2	10	2	35	0.18067	1.81401	0.86090
32	1	3	10	2	35	0.13780	1.02821	0.00000
32	2	3	10	2	35	0.15431	1.14148	0.00000
32	3	3	10	2	35	0.19314	1.27245	0.00000
32	4	3	10	2	35	0.15829	1.06814	0.00000
32	5	3	10	2	35	0.16244	1.06668	0.00000
33	1	4	10	2	35	0.14071	0.58578	0.00000
33	2	4	10	2	35	0.16323	0.58392	0.00000
33	3	4	10	2	35	0.15098	0.87339	0.00000
33	4	4	10	2	35	0.14381	0.77692	0.00000
33	5	4	10	2	35	0.13997	0.69312	0.00000
34	1	2	20	2	35	0.10516	1.16287	1.10658
34	2	2	20	2	35	0.12813	1.27278	0.41748
34	3	2	20	2	35	0.10374	1.14345	1.32790
34	4	2	20	2	35	0.10743	1.33206	1.18203
34	5	2	20	2	35	0.10180	1.09171	1.36311
35	1	3	20	2	35	0.15006	1.12890	0.00000
35	2	3	20	2	35	0.10996	0.86240	0.00000
35	3	3	20	2	35	0.15318	1.06409	0.00000
35	4	3	20	2	35	0.16467	1.19343	0.00000
35	5	3	20	2	35	0.16949	1.28601	0.00000
36	1	4	20	2	35	0.11586	0.57088	0.00000
36	2	4	20	2	35	0.08387	0.51511	0.00000
36	3	4	20	2	35	0.10430	0.56006	0.00000
36	4	4	20	2	35	0.11150	0.56955	0.00000
36	5	4	20	2	35	0.08621	0.39456	0.00000
37	1	2	0	3	35	0.10627	1.17697	4.00721
37	2	2	0	3	35	0.05512	0.25181	3.90900
37	3	2	0	3	35	0.08354	1.17502	3.04961
37	4	2	0	3	35	0.11277	1.40969	1.77771
37	5	2	0	3	35	0.11827	1.51155	1.98887
38	1	3	0	3	35	0.09854	1.00735	1.79735
38	2	3	0	3	35	0.10018	1.11501	1.14422
38	3	3	0	3	35	0.15531	1.43771	0.00000
38	4	3	0	3	35	0.13807	1.07047	0.00000
38	5	3	0	3	35	0.17563	1.21071	0.39286

**Table A.1 Continued:** DoE Table and Experimental Results for Laser Dimpling

Exp. ID	Rep.	Scanning Speed ( <i>m/min</i> )	Incidence Angle ( $^{\circ}$ )	Laser Track ( <i>mm</i> )	Focal Offset ( <i>mm</i> )	Dimple Height ( <i>mm</i> )	Dimple Upper Surface Area ( <i>mm</i> <sup>2</sup> )	Dimple Lower Surface Area ( <i>mm</i> <sup>2</sup> )
39	1	4	0	3	35	0.15456	1.09647	0.00000
39	2	4	0	3	35	0.15424	1.02906	0.00000
39	3	4	0	3	35	0.16484	1.98964	0.00000
39	4	4	0	3	35	0.18301	1.07095	0.00000
39	5	4	0	3	35	0.17490	0.83376	0.00000
40	1	2	10	3	35	0.12882	1.38316	4.54600
40	2	2	10	3	35	0.17801	1.86802	2.82000
40	3	2	10	3	35	0.16015	1.60870	3.62300
40	4	2	10	3	35	0.16522	2.33253	3.18200
40	5	2	10	3	35	0.10728	1.33049	3.54500
41	1	3	10	3	35	0.14521	1.34251	2.42572
41	2	3	10	3	35	0.15329	1.17337	1.44092
41	3	3	10	3	35	0.18171	1.31248	1.35799
41	4	3	10	3	35	0.18875	1.44876	0.96925
41	5	3	10	3	35	0.12445	1.29950	1.39427
42	1	4	10	3	35	0.16244	1.21542	0.00000
42	2	4	10	3	35	0.18173	1.13676	0.00000
42	3	4	10	3	35	0.18326	0.99583	0.00000
42	4	4	10	3	35	0.19301	1.13661	0.00000
42	5	4	10	3	35	0.17158	1.14453	0.00000
43	1	2	20	3	35	0.12832	1.23996	3.83941
43	2	2	20	3	35	0.11030	1.55527	3.68524
43	3	2	20	3	35	0.16294	1.92119	2.85967
43	4	2	20	3	35	0.16973	2.29596	3.02379
43	5	2	20	3	35	0.16000	2.02479	3.47139
44	1	3	20	3	35	0.16905	1.64730	1.59147
44	2	3	20	3	35	0.11256	1.70095	1.68596
44	3	3	20	3	35	0.16886	1.48580	0.90017
44	4	3	20	3	35	0.16808	1.65988	0.00000
44	5	3	20	3	35	0.16705	1.80049	0.44263
45	1	4	20	3	35	0.14935	1.25024	0.00000
45	2	4	20	3	35	0.19471	1.26190	0.00000
45	3	4	20	3	35	0.19717	1.18414	0.00000
45	4	4	20	3	35	0.19592	1.34556	0.00000
45	5	4	20	3	35	0.17586	1.21665	0.00000
46	1	2	0	4	35	0.10580	1.12076	6.30362
46	2	2	0	4	35	0.10701	1.20089	5.10405
46	3	2	0	4	35	0.12459	1.55806	3.81039
46	4	2	0	4	35	0.11225	1.41035	4.76535
46	5	2	0	4	35	0.10783	1.71838	3.81980

**Table A.1 Continued:** DoE Table and Experimental Results for Laser Dimpling

Exp. ID	Rep.	Scanning Speed ( <i>m/min</i> )	Incidence Angle ( $^{\circ}$ )	Laser Track ( <i>mm</i> )	Focal Offset ( <i>mm</i> )	Dimple Height ( <i>mm</i> )	Dimple Upper Surface Area ( <i>mm</i> <sup>2</sup> )	Dimple Lower Surface Area ( <i>mm</i> <sup>2</sup> )
47	1	3	0	4	35	0.11528	1.32957	2.34269
47	2	3	0	4	35	0.09373	1.08248	2.37091
47	3	3	0	4	35	0.11413	1.41946	1.72173
47	4	3	0	4	35	0.11785	0.99931	1.35481
47	5	3	0	4	35	0.14836	1.40314	1.08667
48	1	4	0	4	35	0.12713	1.39566	0.00000
48	2	4	0	4	35	0.13626	1.20657	0.00000
48	3	4	0	4	35	0.10095	1.14796	0.00000
48	4	4	0	4	35	0.13105	1.19558	0.00000
48	5	4	0	4	35	0.11755	1.13900	0.00000
49	1	2	10	4	35	0.12296	2.18697	7.62200
49	2	2	10	4	35	0.11784	1.27654	6.59100
49	3	2	10	4	35	0.12799	1.61454	5.40800
49	4	2	10	4	35	0.14046	1.67865	5.49500
49	5	2	10	4	35	0.10113	1.72663	5.63500
50	1	3	10	4	35	0.19869	1.86442	3.64781
50	2	3	10	4	35	0.14649	1.62212	2.63388
50	3	3	10	4	35	0.15245	1.47766	1.80642
50	4	3	10	4	35	0.19365	1.63212	0.61768
50	5	3	10	4	35	0.19242	1.40018	1.82390
51	1	4	10	4	35	0.16862	1.51557	0.00000
51	2	4	10	4	35	0.20310	1.32595	0.00000
51	3	4	10	4	35	0.16662	1.17060	0.00000
51	4	4	10	4	35	0.12348	1.00601	0.00000
51	5	4	10	4	35	0.13866	1.01781	0.00000
52	1	2	20	4	35	0.14322	1.37627	6.93000
52	2	2	20	4	35	0.14893	1.94062	5.46599
52	3	2	20	4	35	0.17157	1.98623	5.91685
52	4	2	20	4	35	0.18980	2.16420	5.12658
52	5	2	20	4	35	0.19548	2.26064	5.00500
53	1	3	20	4	35	0.16359	1.94290	3.06987
53	2	3	20	4	35	0.20402	1.74348	0.84599
53	3	3	20	4	35	0.17080	1.87127	2.80645
53	4	3	20	4	35	0.16134	2.12626	2.07697
53	5	3	20	4	35	0.19102	1.65221	0.76493
54	1	4	20	4	35	0.18599	1.48834	0.00000
54	2	4	20	4	35	0.17890	1.74219	0.00000
54	3	4	20	4	35	0.18850	1.62005	0.00000
54	4	4	20	4	35	0.16611	1.53743	0.00000
54	5	4	20	4	35	0.20727	1.48648	0.00000



**Table A.1 Continued:** DoE Table and Experimental Results for Laser Dimpling

Exp. ID	Rep.	Scanning Speed ( <i>m/min</i> )	Incidence Angle ( $^{\circ}$ )	Laser Track ( <i>mm</i> )	Focal Offset ( <i>mm</i> )	Dimple Height ( <i>mm</i> )	Dimple Upper Surface Area ( <i>mm</i> <sup>2</sup> )	Dimple Lower Surface Area ( <i>mm</i> <sup>2</sup> )
55	1	2	0	2	55	0.07282	0.40677	1.42763
55	2	2	0	2	55	0.10961	0.82535	0.00000
55	3	2	0	2	55	0.09149	1.18304	0.00000
55	4	2	0	2	55	0.09039	0.63571	0.00000
55	5	2	0	2	55	0.08226	0.52262	0.00000
56	1	3	0	2	55	0.06813	0.33210	0.00000
56	2	3	0	2	55	0.10818	0.68439	0.00000
56	3	3	0	2	55	0.05150	0.20308	0.00000
56	4	3	0	2	55	0.04196	0.03298	0.00000
56	5	3	0	2	55	0.09245	0.24901	0.00000
57	1	4	0	2	55	0.00878	0.00000	0.00000
57	2	4	0	2	55	0.01395	0.00000	0.00000
57	3	4	0	2	55	0.00000	0.00000	0.00000
57	4	4	0	2	55	0.00000	0.00000	0.00000
57	5	4	0	2	55	0.00000	0.00000	0.00000
58	1	2	10	2	55	0.13344	1.08762	0.00000
58	2	2	10	2	55	0.11864	1.04594	0.00000
58	3	2	10	2	55	0.16641	1.57434	0.83449
58	4	2	10	2	55	0.15697	1.24907	0.53872
58	5	2	10	2	55	0.14124	1.14966	0.00000
59	1	3	10	2	55	0.07984	0.73994	0.00000
59	2	3	10	2	55	0.07175	0.19927	0.00000
59	3	3	10	2	55	0.10686	0.73775	0.00000
59	4	3	10	2	55	0.07331	0.56484	0.00000
59	5	3	10	2	55	0.10533	0.61883	0.00000
60	1	4	10	2	55	0.01813	0.00000	0.00000
60	2	4	10	2	55	0.04528	0.12994	0.00000
60	3	4	10	2	55	0.01031	0.00000	1.00000
60	4	4	10	2	55	0.00000	0.00000	0.00000
60	5	4	10	2	55	0.00000	0.00000	0.00000
61	1	2	20	2	55	0.10246	1.20210	0.00000
61	2	2	20	2	55	0.08053	0.65875	0.00000
61	3	2	20	2	55	0.09475	0.83141	0.00000
61	4	2	20	2	55	0.18051	1.17634	0.00000
61	5	2	20	2	55	0.09103	0.60982	0.00000
62	1	3	20	2	55	0.01440	0.00000	0.00000
62	2	3	20	2	55	0.07225	0.11108	0.00000
62	3	3	20	2	55	0.01868	0.00000	0.00000
62	4	3	20	2	55	0.08743	0.68022	0.00000
62	5	3	20	2	55	0.00647	0.00000	0.00000

**Table A.1 Continued:** DoE Table and Experimental Results for Laser Dimpling

Exp. ID	Rep.	Scanning Speed ( <i>m/min</i> )	Incidence Angle ( $^{\circ}$ )	Laser Track ( <i>mm</i> )	Focal Offset ( <i>mm</i> )	Dimple Height ( <i>mm</i> )	Dimple Upper Surface Area ( <i>mm</i> <sup>2</sup> )	Dimple Lower Surface Area ( <i>mm</i> <sup>2</sup> )
63	1	4	20	2	55	0.00557	0.00000	0.00000
63	2	4	20	2	55	0.01721	0.00000	0.00000
63	3	4	20	2	55	0.00832	0.00000	0.00000
63	4	4	20	2	55	0.00367	0.00000	0.00000
63	5	4	20	2	55	0.00220	0.00000	0.00000
64	1	2	0	3	55	0.16079	1.86492	2.25897
64	2	2	0	3	55	0.17766	1.53713	2.26879
64	3	2	0	3	55	0.17536	2.21129	2.90719
64	4	2	0	3	55	0.15110	2.03347	0.51563
64	5	2	0	3	55	0.11622	1.44062	1.13931
65	1	3	0	3	55	0.08399	0.80229	0.00000
65	2	3	0	3	55	0.07979	0.70720	0.00000
65	3	3	0	3	55	0.08104	0.72204	0.00000
65	4	3	0	3	55	0.08703	0.86345	0.00000
65	5	3	0	3	55	0.10253	0.96409	0.00000
66	1	4	0	3	55	0.01901	0.00000	0.00000
66	2	4	0	3	55	0.04278	0.03997	0.00000
66	3	4	0	3	55	0.06294	0.31635	0.00000
66	4	4	0	3	55	0.06692	0.11254	0.00000
66	5	4	0	3	55	0.02493	0.00000	0.00000
67	1	2	10	3	55	0.18589	2.14196	3.53492
67	2	2	10	3	55	0.19543	1.91017	1.92296
67	3	2	10	3	55	0.17738	1.91434	1.70526
67	4	2	10	3	55	0.19149	1.88332	1.86594
67	5	2	10	3	55	0.20714	1.69477	1.92296
68	1	3	10	3	55	0.12860	1.19921	0.00000
68	2	3	10	3	55	0.14813	1.33616	0.00000
68	3	3	10	3	55	0.14739	1.22838	0.00000
68	4	3	10	3	55	0.16189	1.06330	0.00000
68	5	3	10	3	55	0.15295	1.35120	0.00000
69	1	4	10	3	55	0.11544	0.78409	0.00000
69	2	4	10	3	55	0.10211	0.42603	0.00000
69	3	4	10	3	55	0.09037	0.36681	0.00000
69	4	4	10	3	55	0.00000	0.00000	0.00000
69	5	4	10	3	55	0.12438	0.83512	0.00000
70	1	2	20	3	55	0.17914	1.95028	3.06357
70	2	2	20	3	55	0.17547	2.34638	3.29732
70	3	2	20	3	55	0.12984	2.14843	2.42699
70	4	2	20	3	55	0.16327	2.22938	2.12859
70	5	2	20	3	55	0.18313	2.30194	2.89945

**Table A.1 Continued:** DoE Table and Experimental Results for Laser Dimpling

Exp. ID	Rep.	Scanning Speed ( <i>m/min</i> )	Incidence Angle ( $^{\circ}$ )	Laser Track ( <i>mm</i> )	Focal Offset ( <i>mm</i> )	Dimple Height ( <i>mm</i> )	Dimple Upper Surface Area ( <i>mm</i> <sup>2</sup> )	Dimple Lower Surface Area ( <i>mm</i> <sup>2</sup> )
71	1	3	20	3	55	0.14289	1.38704	0.00000
71	2	3	20	3	55	0.12812	1.43045	0.00000
71	3	3	20	3	55	0.12697	1.51371	0.00000
71	4	3	20	3	55	0.12764	1.50362	0.00000
71	5	3	20	3	55	0.14785	1.35140	0.00000
72	1	4	20	3	55	0.10718	0.91393	0.00000
72	2	4	20	3	55	0.09658	0.77650	0.00000
72	3	4	20	3	55	0.09557	0.47922	0.00000
72	4	4	20	3	55	0.08891	0.20239	0.00000
72	5	4	20	3	55	0.05388	0.12053	0.00000
73	1	2	0	4	55	0.12218	2.67782	4.68067
73	2	2	0	4	55	0.13527	2.54187	4.99585
73	3	2	0	4	55	0.11449	2.28847	4.41724
73	4	2	0	4	55	0.13837	2.23038	3.60341
73	5	2	0	4	55	0.14821	2.33504	4.07853
74	1	3	0	4	55	0.11593	1.46313	1.74996
74	2	3	0	4	55	0.14902	2.44612	1.89579
74	3	3	0	4	55	0.10683	1.53005	0.00000
74	4	3	0	4	55	0.07100	1.35272	0.00000
74	5	3	0	4	55	0.08580	1.18747	0.00000
75	1	4	0	4	55	0.10495	1.10132	0.00000
75	2	4	0	4	55	0.04815	0.18118	0.00000
75	3	4	0	4	55	0.07234	0.86226	0.00000
75	4	4	0	4	55	0.05716	0.26917	0.00000
75	5	4	0	4	55	0.06415	0.52242	0.00000
76	1	2	10	4	55	0.13989	2.10520	6.93433
76	2	2	10	4	55	0.18616	2.85066	5.38430
76	3	2	10	4	55	0.20112	2.75091	3.84010
76	4	2	10	4	55	0.21798	2.74150	3.68860
76	5	2	10	4	55	0.22892	2.62801	4.02074
77	1	3	10	4	55	0.14823	1.57570	0.00000
77	2	3	10	4	55	0.13432	0.94000	0.00000
77	3	3	10	4	55	0.15269	1.45249	0.00000
77	4	3	10	4	55	0.16667	1.42693	0.00000
77	5	3	10	4	55	0.18965	1.72926	1.70153
78	1	4	10	4	55	0.09435	0.79795	0.00000
78	2	4	10	4	55	0.10112	0.28311	0.00000
78	3	4	10	4	55	0.00000	0.00000	0.00000
78	4	4	10	4	55	0.00000	0.00000	0.00000
78	5	4	10	4	55	0.03339	0.00000	0.00000

**Table A.1 Continued:** DoE Table and Experimental Results for Laser Dimpling

Exp. ID	Rep.	Scanning Speed ( <i>m/min</i> )	Incidence Angle ( $^{\circ}$ )	Laser Track ( <i>mm</i> )	Focal Offset ( <i>mm</i> )	Dimple Height ( <i>mm</i> )	Dimple Upper Surface Area ( <i>mm</i> <sup>2</sup> )	Dimple Lower Surface Area ( <i>mm</i> <sup>2</sup> )
79	1	2	20	4	55	0.19542	2.92423	5.06579
79	2	2	20	4	55	0.22175	3.41902	6.11948
79	3	2	20	4	55	0.20864	2.87722	6.25119
79	4	2	20	4	55	0.17944	2.95947	5.18737
79	5	2	20	4	55	0.18567	2.73094	4.85809
80	1	3	20	4	55	0.13115	1.60579	0.00000
80	2	3	20	4	55	0.13958	1.61547	1.61092
80	3	3	20	4	55	0.16342	1.88776	0.00000
80	4	3	20	4	55	0.13533	1.93716	0.00000
80	5	3	20	4	55	0.14796	1.34051	0.00000
81	1	4	20	4	55	0.05073	0.43226	0.00000
81	2	4	20	4	55	0.11833	1.31035	0.00000
81	3	4	20	4	55	0.14172	1.57679	0.00000
81	4	4	20	4	55	0.13979	1.43018	0.00000
81	5	4	20	4	55	0.06987	0.91363	0.00000

# Appendix B

## Laser Beam - Plane Intersection

A point  $\mathbf{X} = [x, y, z]$  on a hyperboloid in canonical form is defined in Eq. (B.1).

$$[x, y, z]^T \cdot M \cdot [x, y, z] = 1$$

$$M = \begin{bmatrix} \frac{1}{W_0^2} & 0 & 0 \\ 0 & \frac{1}{W_0^2} & 0 \\ 0 & 0 & -\frac{1}{Z_r^2} \end{bmatrix} \quad (\text{B.1})$$

Furthermore, a plane spanned by vectors  $\mathbf{r} = [r_1, r_2, r_3]$  and  $\mathbf{s} = [s_1, s_2, s_3]$ ; and, containing an interior or boundary point  $\mathbf{p} = [p_1, p_2, p_3]$  of hyperboloid is described in parametric form by;

$$X = \mathbf{p} + x \cdot \mathbf{r} + y \cdot \mathbf{s} \quad (\text{B.2})$$

The intersection between hyperboloid and plane can be found by combining Eq. (B.1) and Eq. (B.2) resulting a conic section which is the sets of points whose coordinates satisfy a second-degree polynomial equation defined in Eq. (B.3).

$$Q(x, y) = Ax^2 + Bxy + CAy^2 + Dx + Ey + F = 0 \quad (\text{B.3})$$

The Eq. (B.3) can be written in matrix notation as;

$$[x, y, 1]^T \cdot A_q \cdot [x, y, 1] = 0$$

$$A_q = \begin{bmatrix} A & B/2 & D/2 \\ B/2 & C & E/2 \\ D/2 & E/2 & F \end{bmatrix} \quad (\text{B.4})$$

where  $A_q$  is symmetric matrix of the quadratic equation. The type of the conic section is computing the determinant of the minor matrix ( $M_{3,3}$ ) of  $A_q$  matrix. If  $\det M_{3,3} \geq 0$ , the intersection is an ellipse. Thus, if  $\lambda_1$  and  $\lambda_2$  are the eigenvectors of the minor matrix ( $M_{3,3}$ ), the centred ellipse equation can be written in the intersection plane as;

$$\lambda_1 \frac{x^2}{W_{x_0}^2} + \lambda_2 \frac{y^2}{W_{y_0}^2} = -\frac{\det A_q}{\det M_{3,3}} \quad (\text{B.5})$$

where  $W_x$  and  $W_y$  are semi-major and semi-minor axes, respectively. If the Eq. (B.5) is rearranged the dimensions of axes on-surface can be found as;

$$\begin{aligned} W_{x_0} &= \sqrt{-\lambda_1 \frac{\det M_{33}}{\det A_q}} \\ W_{y_0} &= \sqrt{-\lambda_2 \frac{\det M_{33}}{\det A_q}} \end{aligned} \tag{B.6}$$

The semi-major and semi-minor axes along the beam axis can be formulated as;

$$\begin{aligned} W_x(z) &= W_{x_0} \sqrt{1 + \left(\frac{z - F_O}{Z_r}\right)^2} \\ W_y(z) &= W_{y_0} \sqrt{1 + \left(\frac{z - F_O}{Z_r}\right)^2} \end{aligned} \tag{B.7}$$

# Appendix C

## Experimental Results for Bead-on-plate Welding

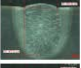
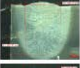
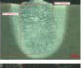
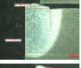
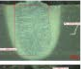
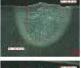
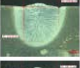
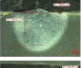
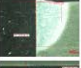
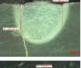
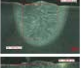
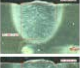
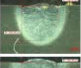
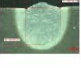
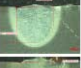
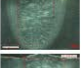
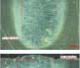
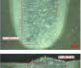

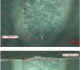

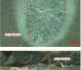
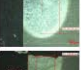
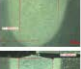
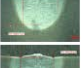

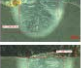
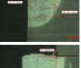
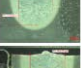
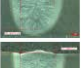
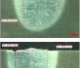
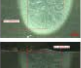
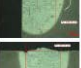
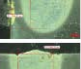

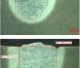

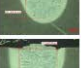

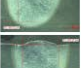
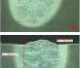
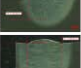
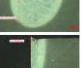
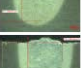
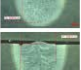
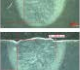
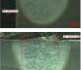
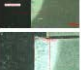
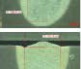
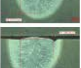
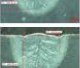
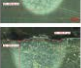

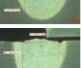
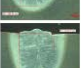
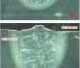
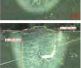
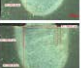
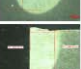
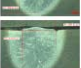
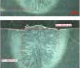
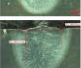
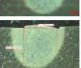

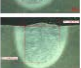
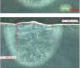
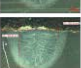
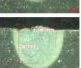
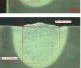
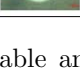


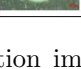

**Table C.1:** DoE Table and Experimental Results for Penetration ( $PT$ ) in Bead-on-plate Welding

Exp. ID	Welding Speed ( $mm/min$ )	Incidence Angle ( $^{\circ}$ )	Rep. 1 ( $\mu m$ )	Rep. 2 ( $\mu m$ )	Rep. 3 ( $\mu m$ )	Rep. 4 ( $\mu m$ )	Rep. 5 ( $\mu m$ )
1	2000	0	1975.22	2037.87	2025.84	2043.76	1969.51
2	3200	20	1404.35	1413.3	1365.53	1410.33	1497.07
3	3200	0	1452.26	1461.11	1449.16	1482.03	1428.4
4	2000	10	1912.29	2005.19	1996.01	2001.95	1978.11
5	2000	20	1969.06	1966.19	1894.48	1915.47	1963.23
6	3200	10	1389.41	1461.11	1398.36	1437.22	1383.42
7	2600	10	1616.71	1613.52	1565.69	1631.43	1586.63
8	2900	0	1494.05	1473.11	1419.39	1422.47	1362.72
9	2300	20	1697.25	1721.16	1712.23	1682.29	1739.2
10	2300	10	1828.64	1834.63	1762.9	1834.62	1715.15
11	2600	0	1571.71	1538.82	1604.54	1499.96	1580.65
12	2900	20	1386.44	1440.2	1365.51	1362.52	1404.66
13	2300	0	1885.44	1840.67	1870.46	1858.51	1744.98
14	2600	20	1613.5	1667.45	1661.31	1703.26	1679.45
15	2900	10	1488.03	1544.82	1508.93	1532.85	1538.8

**Table C.2:** DoE Table and Experimental Results for Top Width ( $TW$ ) in Bead-on-plate Welding

Exp. ID	Welding Speed ( $mm/min$ )	Incidence Angle ( $^{\circ}$ )	Rep. 1 ( $\mu m$ )	Rep. 2 ( $\mu m$ )	Rep. 3 ( $\mu m$ )	Rep. 4 ( $\mu m$ )	Rep. 5 ( $\mu m$ )
1	2000	0	1401.43	1452.15	1344.63	1437.41	1494.12
2	3200	20	1491.07	1419.29	1389.41	1517.96	1598.63
3	3200	0	1404.6	1461.11	1496.97	1583.64	1386.42
4	2000	10	1496.97	1410.47	1437.36	1407.48	1470.08
5	2000	20	1619.47	1560.2	1547.77	1502.95	1553.74
6	3200	10	1419.31	1464.1	1601.61	1520.92	1356.56
7	2600	10	1419.29	1446.2	1461.11	1455.15	1526.99
8	2900	0	1488.01	1320.71	1419.33	1446.17	1494.03
9	2300	20	1410.33	1550.85	1583.66	1583.62	1601.57
10	2300	10	1491.07	1395.58	1416.3	1541.8	1464.25
11	2600	0	1449.47	1583.64	1514.91	1434.22	1577.69
12	2900	20	1362.54	1485.2	1670.31	1499.97	1598.57
13	2300	0	1419.31	1523.96	1467.52	1527.03	1571.77
14	2600	20	1401.43	1506	1446.18	1488.3	1622.53
15	2900	10	1428.29	1500.14	1622.49	1488.01	1467.09



ID	Process Para.		Replication 1			Replication 2			Replication 3			Replication 4			Replication 5		
	Speed	Angle	Penetration	Width	Picture	Penetration	Width	Picture	Penetration	Width	Picture	Penetration	Width	Picture	Penetration	Width	Picture
1	2000	0	1975.22	1401.43		2037.87	1452.15		2025.84	1344.63		1774.85	1320.8		2064.04	1410.32	
2	3200	20	1404.35	1491.07		1413.3	1419.29		1365.53	1389.41		1816.69	2085.62		1407.33	1694.3	
3	3200	0	1452.26	1404.6		1461.11	1461.11		1449.16	1496.97		1502.95	1407.36		1422.28	1499.96	
4	2000	10	1912.29	1496.97		2005.19	1410.47		1996.01	1437.36		-	-	NaN	1930.37	1550.82	
5	2000	20	1969.06	1619.47		1966.19	1560.2		1894.48	1547.77		1571.67	1416.3		1963.09	1568.68	
6	3200	10	1389.41	1419.31		1461.11	1464.1		1398.36	1601.61		1201.16	1542.36		1410.32	1380.83	
7	2600	10	1616.71	1419.29		1613.52	1446.2		1565.69	1461.11		1655.43	1553.74		1646.37	1425.28	
8	2900	0	1494.05	1488.01		1473.11	1320.71		1419.39	1419.33		1407.33	1437.21		1595.64	1464.13	
9	2300	20	1697.25	1410.33		1721.16	1550.85		1712.23	1583.66		1721.07	1547.76		1784.01	1598.56	
10	2300	10	1828.64	1491.07		1834.63	1395.58		1762.9	1416.3		1625.55	269.95		1888.41	1422.3	
11	2600	0	1571.71	1449.47		1538.82	1583.64		1604.54	1514.91		1876.46	1254.96		1476.1	1470.15	
12	2900	20	1386.44	1362.54		1440.2	1485.2		1365.51	1670.31		1467.16	1401.36		1422.28	1479.11	
13	2300	0	1885.44	1419.31		1840.67	1523.96		1870.46	1467.52		2031.85	1556.74		1885.59	2049.74	
14	2600	20	1613.5	1401.43		1667.45	1506		1661.31	1446.18		1425.26	1374.54		1664.36	1664.32	
15	2900	10	1488.03	1428.29		1544.82	1500.14		1508.93	1622.49		1440.45	1524.1		1511.98	1521.01	

**Fig. C.1.** DoE table and experimental results showing cross-section images in bead-on-plate welding

# Appendix D

## Experimental Results for Overlap Welding

**Table D.1:** DoE Table and Experimental Results for Penetration ( $PT$ ) in Overlap Welding

Exp. ID	Welding Speed ( $mm/min$ )	Incidence Angle ( $^\circ$ )	Joining Gap ( $mm$ )	Rep. 1 ( $\mu m$ )	Rep. 2 ( $\mu m$ )	Rep. 3 ( $\mu m$ )	Rep. 4 ( $\mu m$ )	Rep. 5 ( $\mu m$ )	Rep. 6 ( $\mu m$ )	Rep. 7 ( $\mu m$ )
1	2000	0	0.1	748.99	795.47	986.15	917.16	985.48	891.1	828.83
2	3200	20	0.1	808.71	395.51	499.83	638.66	310.49	675.07	685.81
3	3200	0	0.1	305.42	489.89	324.24	323.83	337.49	270.03	333.34
4	2000	10	0.15	987.34	642.67	869.08	926.51	931.48	958.61	1039.51
5	2000	20	0.15	940.785	831.44	945.62	1000	863.98	702.08	1080.37
6	3200	10	0.15	NaN	849.4	688.96	1052.44	431.99	594.07	433.43
7	2600	10	0.2	797.99	880.87	986.14	892.86	904.48	864.1	NaN
8	2900	0	0.2	972.92	1020.18	968.13	963.44	958.48	701.51	876.45
9	2300	20	0.2	433.74	1000	896.08	918.42	863.98	971.32	986.5
10	2300	10	0.25	927.43	755.04	882.59	882.4	986.48	957.83	NaN
11	2600	0	0.25	963.45	880.91	905.09	978.78	972.96	NaN	933.83
12	2900	20	0.25	306.18	952.77	824.05	980.7	851.34	795.94	1009.02
13	2000	20	0.1	1044.49	1000.22	891.59	899.73	999.99	930.85	1000
14	3200	10	0.1	841.9	385.76	742.98	981.07	472.97	607.08	374.75
15	2000	10	0.1	985.96	1027.13	999.65	980.7	1000	998.3	800
16	2900	0	0.15	1012.98	977.79	977.14	998.69	1000	984.81	862.93
17	2300	20	0.15	819.39	959.86	927.62	971.74	986.48	903.87	905.41
18	2600	10	0.15	895.93	892.58	941.11	629.87	972.96	998.3	NaN
19	2900	20	0.2	972.45	1067.51	875.367	971.7	NaN	984.81	513.53
20	2300	10	0.2	909.43	847.73	697.96	NaN	986.48	890.38	993.87
21	2600	0	0.2	995.61	870.14	810.54	NaN	959.45	836.41	884.5
22	2300	0	0.25	837.16	977.79	903.76	972.78	837.83	863.4	834.05
23	2600	20	0.25	999.46	950.88	980.18	NaN	959.45	944.34	856.48
24	2900	10	0.25	922.93	1013.68	1016.16	945.76	918.91	418.21	976.93
25	2300	20	0.1	969.72	937.43	975.69	836.38	972.45	930.85	975.12
26	2600	10	0.1	951.76	923.97	750.89	890.35	891.89	971.32	777.4
27	2900	0	0.1	951.76	932.94	948.71	557.59	648.64	998.39	975.22
28	2600	0	0.15	915.84	944.64	1000	963.02	959.45	971.32	911.93
29	2900	20	0.15	1010.13	949.14	NaN	954.02	986.48	971.32	882.53
30	2300	10	0.15	978.71	953.64	1038.64	909.02	959.45	863.5	1004.15
31	2600	20	0.2	983.23	971.63	966.7	972.02	972.96	NaN	895.91
32	2900	10	0.2	960.74	908.67	968.65	945.02	999.99	984.81	973.14
33	2300	0	0.2	813.64	805.25	901.07	850.52	892.05	971.32	890.92
34	2000	0	0.25	759.69	886.18	905.56	849.36	932.6	849.91	890.91
35	3200	20	0.25	530.43	NaN	459.56	404.46	473.06	756.75	422.73

**Table D.1 Continued:** DoE Table and Experimental Results for Penetration ( $PT$ ) in Overlap Welding

Exp. ID	Welding Speed ( $mm/min$ )	Incidence Angle ( $^{\circ}$ )	Joining Gap ( $mm$ )	Rep. 1 ( $\mu m$ )	Rep. 2 ( $\mu m$ )	Rep. 3 ( $\mu m$ )	Rep. 4 ( $\mu m$ )	Rep. 5 ( $\mu m$ )	Rep. 6 ( $\mu m$ )	Rep. 7 ( $\mu m$ )
36	3200	0	0.25	485.5	NaN	522.61	NaN	540.64	486.48	504.57
37	2300	10	0.1	714.74	972	756.94	984.18	1013.7	959.45	909.1
38	2600	0	0.1	629.34	616.46	1000.17	889.8	1055.65	743.24	995.46
39	2900	20	0.1	818.13	873.03	351.41	687.85	404.48	486.48	913.73
40	2900	10	0.15	1000	967.49	991.16	984.18	1011.19	716.21	877.91
41	2300	0	0.15	705.75	891	991.16	971.88	755.02	959.45	832.9
42	2600	20	0.15	979.95	1003.48	973.14	809.99	984.22	472.97	783.38
43	3200	20	0.2	NaN	NaN	468.55	540.16	525.82	729.72	328.65
44	3200	0	0.2	NaN	521.99	702.82	566.99	512.34	621.62	337.66
45	2000	0	0.2	NaN	1034.99	1000.17	904.48	997.71	959.45	882.41
46	2000	20	0.25	1002.43	927	970.12	755.98	984.22	891.88	823.88
47	3200	10	0.25	NaN	758.11	NaN	NaN	660.64	NaN	400.69
48	2000	10	0.25	952.99	845.98	955.12	904.48	903.33	NaN	850.9
49	2300	0	0.1	921.52	729	856	755.98	970.74	864.86	967.66
50	2600	20	0.1	930.51	931.5	955.12	823.48	633.68	972.96	580.77
51	2900	10	0.1	804.64	940.49	874.02	742.48	687.61	999.99	675.33
52	3200	0	0.15	710.26	486.01	351.34	391.49	350.55	378.38	279.17
53	2000	0	0.15	876.56	805.43	873.6	688.49	970.74	918.91	NaN
54	3200	20	0.15	746.22	1021.49	585.57	418.49	620.2	NaN	508.74
55	3200	10	0.2	773.17	1012.48	396.39	391.49	364.03	783.78	373.67
56	2000	10	0.2	939.4	917.88	882.86	863.98	808.95	891.88	NaN
57	2000	20	0.2	890.06	841.68	900.88	850.48	NaN	864.86	1012.98
58	2300	20	0.25	966.48	NaN	882.86	931.48	903.33	891.88	877.91
59	2600	10	0.25	970.96	886.5	855.88	971.98	889.85	918.91	918.43
60	2900	0	0.25	885.56	923.11	936.91	850.48	930.29	999.99	1044.49

**Table D.2:** DoE Table and Experimental Results for Top Width ( $TW$ ) in Overlap Welding

Exp. ID	Welding Speed ( $mm/min$ )	Incidence Angle ( $^{\circ}$ )	Joining Gap ( $mm$ )	Rep. 1 ( $\mu m$ )	Rep. 2 ( $\mu m$ )	Rep. 3 ( $\mu m$ )	Rep. 4 ( $\mu m$ )	Rep. 5 ( $\mu m$ )	Rep. 6 ( $\mu m$ )	Rep. 7 ( $\mu m$ )
1	2000	0	0.1	1632.84	1249.39	1449.95	1222.88	1498.47	1309.65	1436.95
2	3200	20	0.1	1288.08	1119.06	1125.74	1277.32	1241.98	1201.63	1171.96
3	3200	0	0.1	1323.28	1141.56	1139.24	1187.37	1160.98	1147.63	1058.95
4	2000	10	0.15	1412.46	1271.87	1256.32	1439.23	1241.98	1350.15	1379.28
5	2000	20	0.15	1444.84	1483.09	1440.94	1448.23	1430.97	1215.13	1155.76
6	3200	10	0.15	NaN	1096.58	1139.28	1421.24	1187.98	1188.13	1240.19
7	2600	10	0.2	1271.39	1253.88	1238.31	1164.65	1295.98	1269.21	NaN
8	2900	0	0.2	1266.79	1204.45	1224.8	1233.56	1390.47	1214.15	1303.42
9	2300	20	0.2	1469.11	1393.23	1251.82	1458.66	1484.97	1389.53	1322.09
10	2300	10	0.25	1218.61	1235.9	1170.76	1179.54	1283.77	1308.58	NaN
11	2600	0	0.25	1166.04	1235.9	1134.74	1176.33	1243.23	NaN	1256.49
12	2900	20	0.25	1296.61	1280.85	1377.9	1331.59	1324.31	1254.62	1252.28
13	2000	20	0.1	1382.26	1296.24	1440.94	1385.57	1527.01	1564.91	1392.32
14	3200	10	0.1	1094.24	1206.51	1148.28	1187.64	1121.61	1227.64	1130.93
15	2000	10	0.1	1616.26	1246.91	1576.06	1385.57	1405.39	1551.41	1338.21
16	2900	0	0.15	1112.05	1134.77	1170.76	1250.62	1162.15	1200.66	1235.99
17	2300	20	0.15	1260.59	1264.86	1512.99	1376.58	1432.42	1308.58	1423.42
18	2600	10	0.15	1215.57	1273.82	1224.8	1232.62	1270.26	1254.62	NaN
19	2900	20	0.2	1139.03	1260.36	1301.35	1214.63	NaN	1241.13	1325.08
20	2300	10	0.2	1125.52	1314.19	1319.36	NaN	1486.47	1430	1262.65
21	2600	0	0.2	1238.08	1220	1323.86	NaN	1189.18	1349.06	1488.73
22	2300	0	0.25	1152.54	1202.05	1137.55	1197.96	1135.13	1160.19	1233.14
23	2600	20	0.25	1359.63	1269.33	1367.05	NaN	1310.8	1335.57	1470.8
24	2900	10	0.25	1134.53	1273.82	1124.07	1270.02	1216.21	1227.64	1233.53
25	2300	20	0.1	1391.72	1278.3	1443.3	1358	1337.83	1322.08	1348.94
26	2600	10	0.1	1234.67	1287.28	1438.87	1268.07	1256.75	1335.57	1379.55
27	2900	0	0.1	1131.34	1229.04	1339.89	1483.91	1202.69	1308.58	1235.76
28	2600	0	0.15	1221.13	1255.03	1164.53	1233.03	1135.13	1362.55	1226.58
29	2900	20	0.15	1203.18	1250.53	NaN	1161.02	1162.15	1349.06	1301.29
30	2300	10	0.15	1131.35	1223.55	1366.86	1323.03	1405.39	1281.6	1251.76
31	2600	20	0.2	1203.17	1309.01	1335.39	1386.03	1270.26	NaN	1301.09
32	2900	10	0.2	1252.58	1196.55	1265.99	1233.03	1189.18	1241.13	1171.37
33	2300	0	0.2	1375.53	1309.01	1450.7	1377.03	1392.14	1430	1381.82
34	2000	0	0.25	1267.68	1219.04	1175.96	1402.12	1175.89	1227.64	1222.73
35	3200	20	0.25	1384.52	NaN	1351.58	1402.12	1311.05	1324.31	1313.64
36	3200	0	0.25	1069.86	NaN	1387.66	NaN	1121.82	972.96	1172.73
37	2300	10	0.1	1330.58	1237.48	1360.59	1267.3	1581.36	1472.96	1377.27
38	2600	0	0.1	1339.57	1228.48	1342.57	1199.89	1401.17	1351.34	1350.12
39	2900	20	0.1	1393.51	1205.98	1252.47	1105.52	1496.56	1351.34	1295.85
40	2900	10	0.15	1258.66	1187.98	1207.42	1213.37	1159.5	1256.75	1211.06
41	2300	0	0.15	1015.92	1156.49	1243.46	1485.22	1253.875	1486.47	1242.58
42	2600	20	0.15	1299.11	1268.99	1306.53	1295.98	1348.25	1540.53	1287.6
43	3200	20	0.2	NaN	NaN	1297.52	1309.48	1280.84	1229.72	1283.22
44	3200	0	0.2	NaN	1102.48	1162.36	1079.98	1172.98	1135.13	1116.53
45	2000	0	0.2	NaN	1169.99	1261.48	1228.48	1226.91	1405.39	1386.65
46	2000	20	0.25	1308.1	1390.48	1369.61	1363.47	1375.22	1554.04	1346.16
47	3200	10	0.25	NaN	1142.99	NaN	NaN	1105.57	NaN	1116.52

**Table D.2 Continued:** DoE Table and Experimental Results for Top Width ( $TW$ ) in Overlap Welding

Exp. ID	Welding Speed ( $mm/min$ )	Incidence Angle ( $^{\circ}$ )	Joining Gap ( $mm$ )	Rep. 1 ( $\mu m$ )	Rep. 2 ( $\mu m$ )	Rep. 3 ( $\mu m$ )	Rep. 4 ( $\mu m$ )	Rep. 5 ( $\mu m$ )	Rep. 6 ( $\mu m$ )	Rep. 7 ( $\mu m$ )
48	2000	10	0.25	1101.32	1273.48	1423.67	1214.98	1388.7	NaN	1296.6
49	2300	0	0.1	1326.08	1192.48	1297.52	1241.98	1429.15	1405.39	1413.66
50	2600	20	0.1	1281.13	1210.48	1378.62	1309.48	1415.66	1310.8	1440.67
51	2900	10	0.1	1276.64	1138.48	1252.47	1255.48	1240.39	1297.29	1260.59
52	3200	0	0.15	1123.8	1124.99	1153.35	1160.98	1199.94	1094.59	1107.51
53	2000	0	0.15	1249.67	1160.99	1315.28	1349.97	1334.77	1391.88	NaN
54	3200	20	0.15	1200.22	1273.55	1234.2	1268.98	1267.36	NaN	1188.63
55	3200	10	0.2	1114.89	1291.48	1126.09	1133.98	1146.01	1094.59	1098.51
56	2000	10	0.2	1249.67	1282.48	1216.18	1349.97	1456.11	1405.39	NaN
57	2000	20	0.2	1393.51	1426.48	1432.39	1390.47	NaN	1391.88	1427.19
58	2300	20	0.25	1290.12	NaN	1324.41	1363.47	1307.8	1310.8	1323.61
59	2600	10	0.25	1263.15	1367.99	1621.58	1268.98	1240.39	1270.26	1166.04
60	2900	0	0.25	1141.86	1184.27	1261.23	1282.48	1213.43	1189.18	1116.53

**Table D.3:** DoE Table and Experimental Results for Interface Width (*IW*) in Overlap Welding

Exp. ID	Welding Speed ( <i>mm/min</i> )	Incidence Angle ( $^{\circ}$ )	Joining Gap ( <i>mm</i> )	Rep. 1 ( $\mu\text{m}$ )	Rep. 2 ( $\mu\text{m}$ )	Rep. 3 ( $\mu\text{m}$ )	Rep. 4 ( $\mu\text{m}$ )	Rep. 5 ( $\mu\text{m}$ )	Rep. 6 ( $\mu\text{m}$ )	Rep. 7 ( $\mu\text{m}$ )
1	2000	0	0.1	1485.95	1307.82	1404.92	1474.65	1363.54	1485.16	1468.47
2	3200	20	0.1	1410.06	1164.01	1220.37	1250.33	1079.98	1228.64	1126.16
3	3200	0	0.1	1300.95	1276.35	1364.4	1106.41	1012.48	972.11	1231.32
4	2000	10	0.15	1704.45	1460.62	1359.89	1718.08	1457.97	1471.66	1435.92
5	2000	20	0.15	1783.31	1815.66	1567.03	2149.85	1700.97	1242.14	1498.87
6	3200	10	0.15	NaN	1343.77	1454.45	1502.63	1309.48	1485.16	1273.13
7	2600	10	0.2	1616.27	1770.71	1675.09	1385.53	1093.48	1309.65	NaN
8	2900	0	0.2	1565.47	1478.59	1607.55	1485.68	1093.48	1187.17	1051.69
9	2300	20	0.2	1040.49	1977.45	1522	1467.69	1349.97	1268.11	1427.93
10	2300	10	0.25	2047.12	2022.39	1999.31	1926.88	1783.77	1848.21	NaN
11	2600	0	0.25	1823.35	1883.07	1922.76	1840.83	1662.15	NaN	1673.69
12	2900	20	0.25	1319.12	1559.49	1594.05	1547.52	1445.93	1443.49	1391.92
13	2000	20	0.1	1278.59	1551.91	1643.57	1637.58	1432.42	1430	1342.53
14	3200	10	0.1	1238.08	1000.23	1143.75	1295.6	1337.83	1254.62	1309.26
15	2000	10	0.1	1332.63	1556.8	1517.49	1340.59	1391.88	1362.55	1306.31
16	2900	0	0.15	1413.84	1296.25	1436.44	1466.65	1175.67	1146.7	1141.71
17	2300	20	0.15	1481.36	1538.45	1571.52	1286.64	1148.64	1403.02	1247.95
18	2600	10	0.15	1278.59	1202.06	1319.37	1286.61	1148.64	1295.09	NaN
19	2900	20	0.2	1472.29	1511.54	1562.53	1358.58	NaN	1376.04	1278.06
20	2300	10	0.2	1841.49	2040.8	1499.48	NaN	1391.88	1416.51	1316.77
21	2600	0	0.2	1755.82	1856.9	1103.22	NaN	1256.75	1227.64	1008.93
22	2300	0	0.25	2080.09	1910.73	2077.27	1810.46	1189.18	1821.23	1444.06
23	2600	20	0.25	1850.37	1825.6	1812	NaN	1499.99	1524.43	1242.11
24	2900	10	0.25	1710.8	1699.93	1740.05	1594.28	1405.39	1254.62	1427.18
25	2300	20	0.1	1216.71	1291.77	1398.37	1340.01	1283.77	1416.51	1271.7
26	2600	10	0.1	1346.84	1318.74	1295.2	1196.12	1310.8	1268.11	1262.72
27	2900	0	0.1	1261.56	1071.98	1142.05	1034.28	1337.83	1200.66	1073.99
28	2600	0	0.15	1530.92	1767.84	1321.9	1161.02	1202.69	1146.7	1267.01
29	2900	20	0.15	1333.63	1380.98	NaN	1224.03	1229.72	1295.09	1121.19
30	2300	10	0.15	1512.94	1551.92	1240.98	1161.02	1256.75	1349.06	1278.77
31	2600	20	0.2	1400.71	1488.95	1443.31	1422.03	1418.91	NaN	1152.52
32	2900	10	0.2	1557.83	1371.99	1473.23	1395.06	1391.88	1308.58	1256.97
33	2300	0	0.2	1326.08	1354	1211.93	1323.03	1311.05	1187.17	1236.37
34	2000	0	0.25	1496.91	1862.31	2284.18	1927.91	1811.14	1659.34	1822.73
35	3200	20	0.25	1550.84	NaN	1549.82	1685.24	1432.69	1608.09	1490.92
36	3200	0	0.25	1537.36	NaN	1549.82	NaN	1567.85	1635.12	1495.46
37	2300	10	0.1	1335.07	1318.49	1225.44	1172.93	1378.63	1351.34	1136.51
38	2600	0	0.1	1321.59	1322.99	1054.27	1105.52	1334.08	1256.75	1009.09
39	2900	20	0.1	1141.86	1304.98	1162.39	1226.85	1388.7	1297.29	1286.44
40	2900	10	0.15	1474.43	1232.98	1639.92	1294.26	1226.91	1202.69	1328.24
41	2300	0	0.15	1240.67	1444.51	1522.78	1282.48	1280.84	1310.8	1323.62
42	2600	20	0.15	1541.88	1327.48	1153.35	1295.98	1253.95	1459.45	1295.61
43	3200	20	0.2	NaN	NaN	1333.56	1444.47	1307.8	1175.67	1301.1
44	3200	0	0.2	NaN	1512.04	1459.71	1444.47	1415.66	1405.39	1400.22
45	2000	0	0.2	NaN	2105.97	1621.9	1727.97	1671.83	1364.85	1656.77
46	2000	20	0.25	1991.37	1988.97	2180.56	1862.96	2157.2	1567.55	1733.31

**Table D.3 Continued:** DoE Table and Experimental Results for Interface Width (*IW*) in Overlap Welding

Exp. ID	Welding Speed ( <i>mm/min</i> )	Incidence Angle (°)	Joining Gap ( <i>mm</i> )	Rep. 1 ( $\mu\text{m}$ )	Rep. 2 ( $\mu\text{m}$ )	Rep. 3 ( $\mu\text{m}$ )	Rep. 4 ( $\mu\text{m}$ )	Rep. 5 ( $\mu\text{m}$ )	Rep. 6 ( $\mu\text{m}$ )	Rep. 7 ( $\mu\text{m}$ )
47	3200	10	0.25	NaN	1673.97	NaN	NaN	1577.45	NaN	1557.73
48	2000	10	0.25	2220.63	1781.97	1982.32	1903.46	1496.56	NaN	1841.36
49	2300	0	0.1	1330.59	1439.98	1297.52	1160.98	1253.87	1337.83	13305.61
50	2600	20	0.1	1308.11	1390.49	1315.54	1336.47	1388.7	1378.37	12566.21
51	2900	10	0.1	1155.27	1205.99	1099.29	1174.48	1307.8	1229.72	1170.76
52	3200	0	0.15	1393.01	1268.99	1406.65	1363.47	1307.8	1405.39	1292.1
53	2000	0	0.15	1487.91	1486.5	1675.63	1430.97	1523.52	1378.37	NaN
54	3200	20	0.15	1294.65	1318.49	1243.24	1295.98	1186.46	NaN	1359.7
55	3200	10	0.2	1546.67	1547.98	1585.54	1525.47	1429.15	1297.29	1323.62
56	2000	10	0.2	1762.12	1943.98	1828.78	1687.47	1685.31	1445.53	NaN
57	2000	20	0.2	1838.54	1889.97	1549.51	1660.47	NaN	1594.58	1674.78
58	2300	20	0.25	1132.83	NaN	1720.67	1700.97	1914.52	1310.8	1463.19
59	2600	10	0.25	1766.61	1993.47	1378.34	1637.97	1550.49	1567.58	1782.85
60	2900	0	0.25	1384.53	1760.65	1639.59	1430.97	1510.04	1567.55	1639.26

Number	Speed	Angle	Gap	Rep 1	Rep 2	Rep 3	Rep 4	Rep 5	Rep 6	Rep 7	Rep 8
1	2	0	0.1								
2	3.2	20	0.1								
3	3.2	0	0.1								
4	2	10	0.15							No Weld	
5	2	20	0.15								
6	3.2	10	0.15								
7	2.6	10	0.2								
8	2.9	0	0.2								
9	2.3	20	0.2								
10	2.3	10	0.25								
11	2.6	0	0.25						No Weld		
12	2.9	20	0.25								
13	2	20	0.1								
14	3.2	10	0.1								
15	2	10	0.1								
16	2.9	0	0.15								
17	2.3	20	0.15								
18	2.6	10	0.15								
19	2.9	20	0.2								
20	2.3	10	0.2				No Weld				

**Fig. D.1.** DoE table and experimental results showing cross-section images in overlap welding



Number	Speed	Angle	Gap	Rep 1	Rep 2	Rep 3	Rep 4	Rep 5	Rep 6	Rep 7	Rep 8
21	2.6	0	0.2				No Weld				
22	2.3	0	0.25								
23	2.6	20	0.25								
24	2.9	10	0.25								
25	2.3	20	0.1								
26	2.6	10	0.1								
27	2.9	0	0.1								
28	2.6	0	0.15								
29	2.9	20	0.15								
30	2.3	10	0.15								
31	2.6	20	0.2								
32	2.9	10	0.2								
33	2.3	0	0.2								
34	2	0	0.25								
35	3.2	20	0.25								
36	3.2	0	0.25				No Weld				
37	2.3	10	0.1								
38	2.6	0	0.1								
39	2.9	20	0.1								
40	2.9	10	0.15								

**Fig. D.1 Continued:** DoE table and experimental results showing cross-section images in overlap welding

Number	Speed	Angle	Gap	Rep 1	Rep 2	Rep 3	Rep 4	Rep 5	Rep 6	Rep 7	Rep 8
41	2.3	0	0.15								
42	2.6	20	0.15								
43	3.2	20	0.2								
44	3.2	0	0.2	No Weld							
45	2	0	0.2	No Weld							
46	2	20	0.25								
47	3.2	10	0.25								
48	2	10	0.25								
49	2.3	0	0.1							No Weld	
50	2.6	20	0.1								
51	2.9	10	0.1								
52	3.2	0	0.15								
53	2	0	0.15								
54	3.2	20	0.15						No Weld		
55	3.2	10	0.2								
56	2	10	0.2								
57	2	20	0.2								
58	2.3	20	0.25								
59	2.6	10	0.25								
60	2.9	0	0.25								

**Fig. D.1 Continued:** DoE table and experimental results showing cross-section images in overlap welding

## Appendix E

Published Journal 1: Laser dimpling process parameters selection and optimization using surrogate-driven process capability space



Full length article

## Laser dimpling process parameters selection and optimization using surrogate-driven process capability space



Erkan Caner Ozkat\*, Pasquale Franciosa, Dariusz Ceglarek

Warwick Manufacturing Group, University of Warwick, Gibbet Hill Rd., Coventry CV4 7AL, UK

### ARTICLE INFO

*Article history:*  
Received 1 September 2016  
Received in revised form 2 January 2017  
Accepted 14 February 2017

*Keywords:*  
Laser dimpling  
Zinc coated steel  
Surrogate modelling  
Design of experiment  
Multivariate adaptive regression splines  
Process capability space

### ABSTRACT

Remote laser welding technology offers opportunities for high production throughput at a competitive cost. However, the remote laser welding process of zinc-coated sheet metal parts in lap joint configuration poses a challenge due to the difference between the melting temperature of the steel (~1500 °C) and the vapourizing temperature of the zinc (~907 °C). In fact, the zinc layer at the faying surface is vapourized and the vapour might be trapped within the melting pool leading to weld defects. Various solutions have been proposed to overcome this problem over the years. Among them, laser dimpling has been adopted by manufacturers because of its flexibility and effectiveness along with its cost advantages. In essence, the dimple works as a spacer between the two sheets in lap joint and allows the zinc vapour escape during welding process, thereby preventing weld defects. However, there is a lack of comprehensive characterization of dimpling process for effective implementation in real manufacturing system taking into consideration inherent changes in variability of process parameters. This paper introduces a methodology to develop (i) surrogate model for dimpling process characterization considering multiple-inputs (i.e. key control characteristics) and multiple-outputs (i.e. key performance indicators) system by conducting physical experimentation and using multivariate adaptive regression splines; (ii) process capability space ( $C_p$ -Space) based on the developed surrogate model that allows the estimation of a desired process fallout rate in the case of violation of process requirements in the presence of stochastic variation; and, (iii) selection and optimization of the process parameters based on the process capability space. The proposed methodology provides a unique capability to: (i) simulate the effect of process variation as generated by manufacturing process; (ii) model quality requirements with multiple and coupled quality requirements; and (iii) optimize process parameters under competing quality requirements such as maximizing the dimple height while minimizing the dimple lower surface area.

© 2017 Elsevier Ltd. All rights reserved.

### 1. Introduction

Thin zinc coated steel sheets are widely used in the automotive industry due to its high corrosion resistance, especially in body-in-white and closure panels [1,2]. With the advancement of the laser technology, laser welding has been gradually replacing traditional welding methods since it offers cheaper and faster manufacturing process as well as better mechanical and aesthetic joint quality [3–5]. Despite such benefits, it is nonetheless challenging to achieve high quality joint in lap joint configuration of zinc coated steel since the boiling point of zinc (~907 °C) is significantly lower than the melting point of steel (~1500 °C), resulting in highly

pressurized zinc vapour on the faying surfaces during the welding process. Left unaddressed, such zinc vapour can easily be trapped inside the molten pool which can lead to welding defects such as porosity, spatter, burn-through, and severe undercuts [6,7].

Over the past few years, significant amount of researches have been conducted to prevent the molten pool from being destroyed by the zinc vapour and several solutions have been proposed which can be classified as:

- *Ventilation* – This method is based on degasification of zinc vapour from the medium without causing any weld defects either by enlarging molten pool [8,9]; stabilizing the keyhole by employing shielding gas [10,11]; creating pre-drilled ventilation channels [12]; applying appropriate spacers at the faying surfaces [13–15]; or adopting a suction method to remove the vapour [16];

\* Corresponding author.  
E-mail addresses: [E.C.Ozkat@warwick.ac.uk](mailto:E.C.Ozkat@warwick.ac.uk) (E.C. Ozkat), [P.Franciosa@warwick.ac.uk](mailto:P.Franciosa@warwick.ac.uk) (P. Franciosa), [D.J.Ceglarek@warwick.ac.uk](mailto:D.J.Ceglarek@warwick.ac.uk) (D. Ceglarek).

Nomenclature			
$D_H$	dimple height	$\hat{\mu}_{KPI_j}$	estimated mean value of the $j^{th}$ KPI
$D_U$	dimple upper surface area	$\zeta_{KPI_j^{(k)}}$	success rate of the $j^{th}$ KPI in the $k^{th}$ experimental configuration
$D_L$	dimple lower surface area	$\zeta_{KPI_1^{(k)} \dots KPI_d^{(k)}}$	success rate of the dependent KPIs in the $k^{th}$ experimental configuration
$S_s$	scanning speed	$\zeta_{KPI_j}$	estimated success rate of the $j^{th}$ KPI
$\alpha$	incidence angle	$\zeta_{KPI_1 \dots KPI_d}$	estimated success rate of dependent KPIs
$F_O$	focal offset	$F_{KPI_j}^{\mu}$	deterministic surrogate model of the $j^{th}$ KPI
$L_T$	laser track	$F_{KPI_j}^{\zeta}$	stochastic surrogate model of the $j^{th}$ KPI
KCCs	key control characteristics	$F_{KPI_1 \dots KPI_d}^{\zeta}$	stochastic surrogate model of dependent KPIs
KPIs	key performance indicators	PDF	probability density function
$N_j$	number of KCCs	SR	success rate
$N_j$	number of KPIs	$\beta$	minimal desirable success rate
$N_k$	number of experimental configurations	LL	lower limit
$N_k$	number of experiment replications	UL	upper limit
$d$	number of dependent KPIs	KCC – space	process parameter space
$N_s^{(k)}$	number of KPIs in the $k^{th}$ experimental configuration	<b>C<sub>p</sub></b> – space	process capability space
$KCC_i^{(k)}$	$i^{th}$ KCC value in the $k^{th}$ experimental configuration	<b>DC<sub>p</sub></b> – Space	deterministic process capability space of $j^{th}$ KPI
$KPI_j^{(k,l)}$	$j^{th}$ KPI value in the $k^{th}$ experimental configuration at the $l^{th}$ replication	<b>SC<sub>p</sub></b> – Space	stochastic process capability space of $j^{th}$ KPI
$\mu_{KPI_j^{(k)}}$	mean value of the $j^{th}$ KPI in the $k^{th}$ experimental configuration	<b>DC<sub>p</sub></b> – Space	deterministic process capability space
$\sigma_{KPI_j^{(k)}}$	standard deviation of the $j^{th}$ KPI in the $k^{th}$ experimental configuration	<b>SC<sub>p</sub></b> – Space	stochastic process capability space

- *Inserting a thin metal foil* – This involves adding another material (e.g. Al & Cu) into the faying surface which absorbs zinc vapour or reacts with zinc vapour in such a way that a liquid alloy with a high boiling point is formed [17,18];
- *Tandem beams* – This approach employs a dual laser beam or a secondary heat source. The first beam applies pre-heating which vapourizes zinc coating and second beam performs actual welding [19–21];
- *Controlling keyhole oscillation* – The molten pool shape can be controlled based on the pulsed wave mode of laser beam so that more stable keyhole oscillation can be achieved, allowing the zinc vapour to escape during the keyhole closure [22,23]
- *Surf-sculpt* – This method creates surface features from the base metal by repeated movement of the low power on-focus laser beam in a short distance. These features increase surface area of the material and can be utilized as a spacer between the faying surface in lap joint [24,25].

All of the above solutions have been shown to produce satisfactory welds in lap joint configuration. However, they do have number of disadvantages due to: (i) challenges in development of system automation for robotic joining process (see *inserting a thin metal foil* solution); (ii) increased system complexity (see *ventilation* and *tandem beam* solutions) due to the need for installation of additional equipment which increases processing cost as well; and, (iii) increased cycle time (see *tandem beam*, *controlling keyhole oscillation* and *surf-sculpt* solutions) due to lower processing speed.

A promising technique for mitigation of zinc vapour is “*laser dimpling*” which makes a dimple on the faying surface of the upper sheet metal by rapid and single movement of the laser beam. Hence, the zinc vapour is vented out through the generated gap between the faying surfaces which is illustrated in Fig. 1. The laser dimpling process has been used by the automotive industry as it does not require any additional equipment and can be performed using the same laser source and fixture adopted for welding [26,27]. Furthermore, it is not restricted by the shape and curvature of the workpiece and weld location.

The physical principle behind laser dimpling process can be explained by the “*humping effect*” which is influenced by the heat

and mass transfer in the molten pool. In general, humps occur periodically along the weld bead which deteriorate the homogeneity of molten pool. In laser welding process, when the beam hits the workpiece, it creates a deep narrow cavity, known as keyhole. While laser beam is moving, the liquid material at the bottom of the keyhole flows upwards to the rear of the molten pool and generates a backward trail of a thin jet due to the surface tension on the keyhole walls. The solidification of this jet on the surface forms the hump at the rear and leading to a valley of cavity at the front which is given in Fig. 2. There has been significant research which look at the humping effect as a negative phenomenon during joining process, explained causes of humping effect and described ways to suppress the occurrence of the hump [28–32]. However, the “*humping effect*” can be beneficially utilized by laser dimpling process to create the required gap in lap welding of zinc coated steels.

According to Gu [26,27], humping effect was used to generate dimple for laser welding process first, by studying the influence of a single parameter, focal offset, on the dimple height. Then, they used this information to generate dimples at different scanning speed and incidence angle, while other parameters such as focal offset were kept constant. Results indicated that dimple height monotonically decreased with increasing both scanning speed and incidence angle; whereas, the dimple height firstly, increased and then decreased whilst increasing the focal offset. In a more recent study conducted by Colombo and Previtali [33] applied univariate linear regression model to determine influence of scanning speed on the dimple height keeping constant laser power, focal offset, and laser track. They found that linear energy, which is the amount of the energy supplied per unit time, was the primary factor affecting the dimple height. However, this study has limitation as authors considered only the influence of a single process parameter without exploring other important process parameters and their interactions.

The existing literature has focussed mainly on single-input (i.e. scanning speed) and single-output (i.e. dimple height) scenario which is necessary but not sufficient to give a complete characterisation of the dimpling process. Furthermore, the laser material processes are characterized as multiple-inputs and

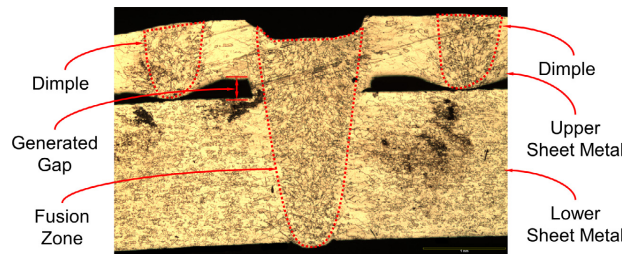


Fig. 1. Micro-section of laser welded joint with laser dimpling technique.

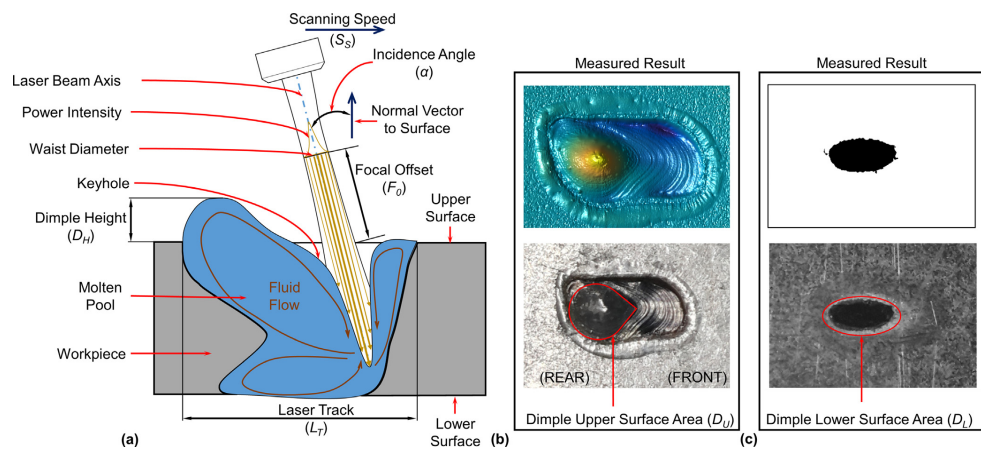


Fig. 2. (a) Illustration of humping effect during a dimpling process, (b) dimple upper surface, (c) dimple lower surface.

multiple-outputs (MIMO) system with non-linear functional relationship [34–36].

Thus, it is important to take into consideration MIMO-based scenario for dimpling process. It was observed in this paper that it is important to include the following multiple-inputs parameters for a dimpling process: scanning speed ( $S_s$ ), focal offset ( $F_o$ ), incidence angle ( $\alpha$ ); and, laser track ( $L_T$ ) as well as the following three key performance indicators (KPIs) to be addressed as multiple-outputs parameters: dimple height ( $D_H$ ), dimple upper surface area ( $D_U$ ); and, dimple lower surface area ( $D_L$ ).

Another limitation associated with the current literature is the lack of modelling variation in the dimpling process. The current models are developed under the assumption of ideal process performance neglecting process variation. As a result of lack of understanding process variation, the measurement of selected KPI (e.g. dimple height) for given process parameters might violate the given allowance limits and it will lead to erroneous process parameters selection. However, no comprehensive research work has been reported in the laser dimpling process that considers MIMO-based scenario with process variation.

This study is, therefore, focused on development of: (i) surrogate model for dimpling process characterization considering multiple-inputs and multiple-outputs (MIMO) system by conducting physical experimentation and using multivariate adaptive

regression splines; (ii) process capability space ( $C_p$ -space) for deterministic and stochastic cases based on the developed surrogate models; and (iii) optimization of the process parameters based on the process capability space.

The methodology is developed by introducing the concepts of deterministic and stochastic process capability spaces. The deterministic  $C_p$ -space is a measure of the dimpling process capability to satisfy simultaneously all the KPIs allowance limits requirements. Whereas, the stochastic  $C_p$ -space is the estimation of process fallout rate which is the probability of making a dimple which satisfies simultaneously all the KPIs limits requirements. The stochastic  $C_p$ -space is then used to develop robust dimpling process by identifying process parameters which are less sensitive to the variation in process.

## 2. Problem formulation

### 2.1. Definition of key control characteristics (KCCs) and key performance indicators (KPIs)

The quality performance of a dimple is evaluated by multiple-outputs called in this paper as Key Performance Indicators (KPIs), which are delivered by process parameters (multiple-inputs),

named in this paper as Key Control Characteristics (KCCs). As shown in Fig. 2, the KCCs considered in this study are:

- *Scanning speed* ( $S_s$ ) – The travelling speed of the laser beam along the upper surface of the workpiece;
- *Focal offset* ( $F_o$ ) – The distance along the beam axis between the focal point and the interaction of beam and upper surface of the workpiece;
- *Incidence angle* ( $\alpha$ ) – The angle along the beam movement between the beam axis and the normal vector to the upper surface of the workpiece;
- *Laser track* ( $L_T$ ) – The linear distance of the beam movement to make a dimple which is parallel to the upper surface of the workpiece.

We observe that the aforementioned KCCs affect not only the selected dimpling process KPIs, but also KPIs of other downstream processes. For example, scanning speed and laser track can affect process cycle time and fixture clamp layout design [37]. Moreover, focal offset and incidence angle can be related to not only dimple height or dimple upper surface area but also they can affect detailed 3D fixture design includes the beam visibility, accessibility and offline programming of the robotic scanner head. This is caused by the fact that the robotic system used to make dimples needs to gain access to the workpiece with no collision between the workpiece/fixture and the laser beam. These examples illustrate the importance analysing dimpling process as MIMO-based system and also to develop methodology which can be expanded to include additional KPIs as required by downstream processes.

Let us define that four KCCs ( $S_s, F_o, \alpha, L_T$ ) are gathered as in Eq. (1), where  $i$  and  $k$  represent index of KCC and experimental configuration ( $KCC_i^{(k)}$ ); whereas,  $N_i$  and  $N_k$  are the total number of KCCs and experimental configurations, respectively.

$$KCCs = \begin{bmatrix} KCC_1^{(1)} & \dots & KCC_{N_i}^{(1)} \\ \vdots & KCC_i^{(k)} & \vdots \\ KCC_1^{(N_k)} & \dots & KCC_{N_i}^{(N_k)} \end{bmatrix} \quad (1)$$

The following KPIs are proposed to measure the functionality, strength and aesthetic quality requirements of the dimple which are illustrated in Fig. 2.

- *Dimple Height* ( $D_H$ ) – This KPI is needed to evaluate the required and predetermined gap between over lapped sheet metal parts which is the main functional objective of a dimple. It is reported in the literature that to make joints with satisfactory quality in laser lap welding dimple height needs to be in the range of [0.1, 0.3] mm [13,33].
- *Dimple upper surface area* ( $D_U$ ) – This KPI assesses (i) strength of the dimple to prevent excessive deformation of the dimple height under compression of clamping force applied during welding process; and, (ii) uncertainty as measured by difference between dimple height and the required gap between the faying surfaces during consecutive welding process and caused by geometric surface defects such as roughness, scratches, lines and etc. In essence, the larger dimple upper surface area generates stronger and higher dimples but it creates unwanted surface feature such as dark spots in the lower surface of the workpiece. According to initial screening experiments, we propose dimple upper surface area should be in the range of [1.0, 5.0] mm<sup>2</sup> in order to generate sufficient gap between faying surfaces to achieve satisfactory joint in laser lap welding.
- *Dimple lower surface area* ( $D_L$ ) – The dark spot appeared in the dimple lower surface is an aesthetic quality requirement which is an unwanted feature in Class-A surfaces in the automotive

industry [38]. Thus, the objective is to determine dimple lower surface area which minimizes dimple height variation under compression clamping force in lap joint. According to initial screening experiments, we propose dimple lower surface area should be in the range of [0, 1.5] mm<sup>2</sup>.

Let us define three KPIs ( $D_H, D_U$  and  $D_L$ ), as shown in Eq. (2), where  $j, k$  and  $l$  represent index of KPI, experimental configuration number and its replication ( $KPI_j^{(k,l)}$ ); whereas,  $N_j, N_k$  and  $N_l$  are the total number of KPIs, experimental configurations and replicates, respectively.

$$KPIs = \{KPI_j | \forall j = 1, \dots, N_j\}$$

$$KPI_j = \begin{bmatrix} KPI_j^{(1,1)} & \dots & KPI_j^{(1,N_l)} \\ \vdots & KPI_j^{(k,l)} & \vdots \\ KPI_j^{(N_k,1)} & \dots & KPI_j^{(N_k,N_l)} \end{bmatrix} \quad (2)$$

The aforementioned three KPIs are selected as the primary indicators used in this paper to evaluated dimpling process. Additionally, the paper defines lower limits ( $LL$ ) and upper limits ( $UL$ ) for each KCC and KPI, which are given in Tables 1 and 2, respectively.

The lower and upper limits of all KCCs have been defined by taking into account technological constraints such as maximum scanning speed of the laser beam, minimum laser power intensity on the upper surface of the workpiece to create a dimple. These limits were determined by conducting initial dimpling and welding experiments, results of which are not reported in the paper. The set of all possible KCCs within the allowance limits defines the process parameters space (KCC-space). On the other hand, the lower and upper allowance limits of all KPIs are determined based on aforementioned quality requirements.

### 2.2. Formulation of surrogate modelling for the dimpling process characterization

The proposed modelling approach addresses two key limitations of the currently available models for dimpling process characterization as discussed in the introduction section by taking into consideration; (i) approximation of a comprehensive multi-variate relations between multiple-inputs (KCCs) and multiple-outputs (KPIs) of the dimpling process, and (ii) process variation over the KCC-space which can be either homoscedasticity (all KPIs across the KCC-space have the same variance) or heteroscedasticity (variability of a KPI is unequal across the KCC-space). The process capability space ( $C_p$ -space) is presented to address both limitations by defining a set of KPIs comprehensively evaluate

**Table 1**  
KCCs and their corresponding allowance limits.

KCC	Unit	KCC <sup>LL</sup>	KCC <sup>UL</sup>
Scanning speed	m/min	2	4
Incidence angle	°	0	20
Laser track	mm	2	4
Focal offset	mm	25	55

**Table 2**  
KPIs and their corresponding allowance limits.

KPI	Unit	KPI <sup>LL</sup>	KPI <sup>UL</sup>
Dimple height	mm	0.1	0.3
Dimple upper surface area	mm <sup>2</sup>	1.0	5.0
Dimple lower surface area	mm <sup>2</sup>	0.0	1.5

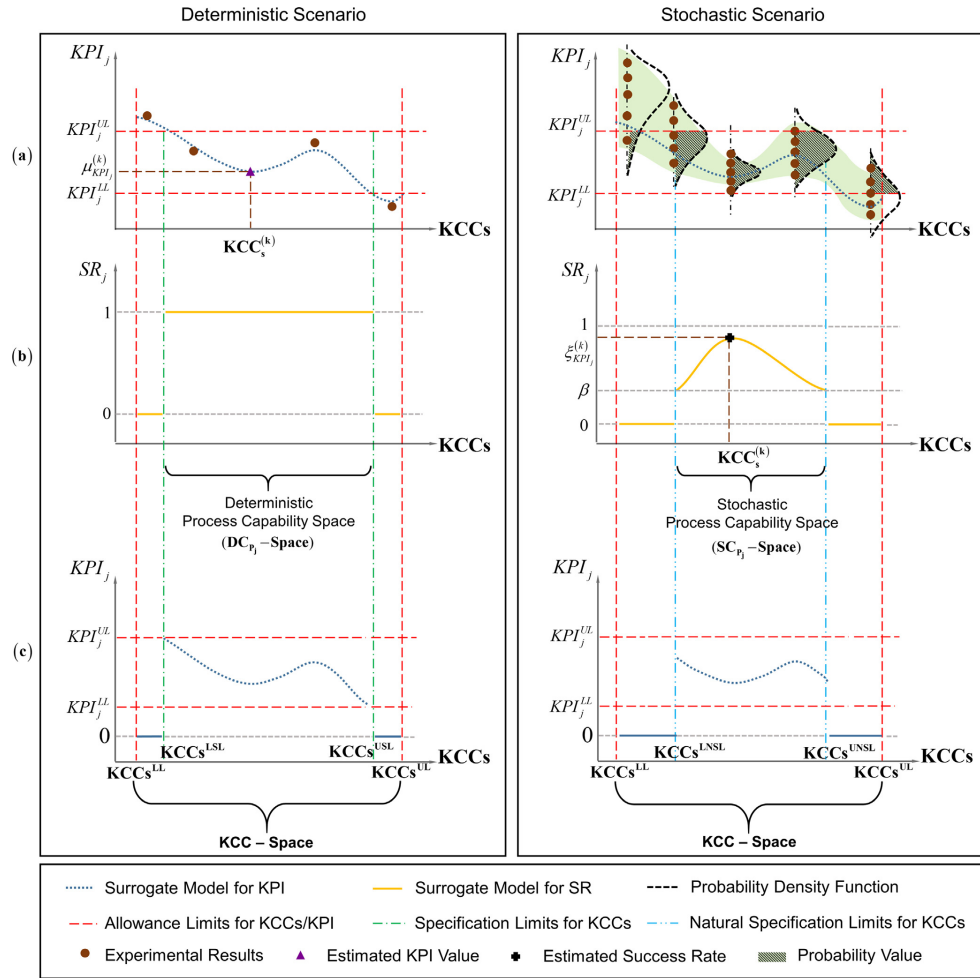


Fig. 3. Conceptual representation deterministic and stochastic scenarios; (a) Experimental results. (b) Success rate models. (c) Tolerance limits.

dimpling process and identifying process parameters inside the KCC-space that satisfy the given quality requirements.

Two different scenarios are considered: deterministic and stochastic. In the deterministic scenario, one or many measurements of the KPIs are conducted. Then, the mean values are calculated to compute deterministic surrogate model which estimates the KPI values over the KCC-space. A success rate (binary function) is therefore calculated which determines whether the estimated value is within its lower and upper allowance limits for a given KPI. In case of success, the given process parameters (KCCs) are said to be feasible. However, this modelling approach has its own limitations. Indeed, due the stochastic nature of the KPI measurements, some individual measurements might violate the limits contrary to its estimated value which does not and vice-versa as highlighted in Fig. 3a.

Thus, stochastic scenario is proposed to take into account the mean and variance to calculate the SR which is directly computed from the measured KPI values. Therefore, the effect of variation can be represented as in the form of the success rate function. Initially, the probability density function is developed either normal or non-normal distribution, using the measured KPI values. Afterwards, the SR value is calculated which is the probability value of satisfying the allowance limits as illustrated shaded regions in Fig. 3a. Finally, stochastic surrogate model (non-binary function) is developed to calculate the SR values over the KCC-space to determine the feasible KCCs for achieving given success rate ( $\beta$ ) as highlighted in Fig. 3b

Furthermore, the success rate is also referred as (1 – process fallout rate) in the manufacturing terminology and note is made that the higher success rate is the lower the process fallout rate.



Moreover, the allowance limits for KCCs are determined by the equipment capability; whereas, the specification limits for KCCs are determined to satisfy the allowance limits for KPIs and the natural specification limits are determined to satisfy desirable success rate, which are illustrated in Fig. 3c.

The observed KPIs might not be independent each other and their joint relationship becomes important to define the PDF function. Therefore, the Pearson correlation coefficient test has been initially conducted to measure dependence among all KPIs, which is defined in Eq. (3).

$$\rho_{mn} = \frac{\text{cov}(\mathbf{KPI}_m, \mathbf{KPI}_n)}{\sigma_{\mathbf{KPI}_m} \sigma_{\mathbf{KPI}_n}} \quad \forall m, n = \{1, \dots, N_j\} \quad (3)$$

The correlation result ( $\rho_{ij}$ ) indicates the linear relationship among KPIs which takes a value between  $-1$  and  $+1$ . Even though correlation and dependency are statistically different terms, if KPIs are linearly correlated, it can be deduced that they are dependent each other. As a result, the dependence among KPIs changes the form of the PDF function. The mean value of the  $k^{\text{th}}$  experimental configuration of the  $j^{\text{th}}$  KPI is defined in Eq. (4), where  $N_s^{(k)}$  is the sample size in the  $k^{\text{th}}$  experimental configuration.

$$\mu_{\mathbf{KPI}_j^{(k)}} = \frac{1}{N_s^{(k)}} \sum_{l=1}^{N_s^{(k)}} \mathbf{KPI}_j^{(k,l)} \quad (4)$$

$$\mathbf{\mu}_{\mathbf{KPI}_j} = \left[ \mu_{\mathbf{KPI}_j^{(1)}}, \dots, \mu_{\mathbf{KPI}_j^{(k)}}, \dots, \mu_{\mathbf{KPI}_j^{(N_k)}} \right]^T$$

The PDF function that describes the simultaneous behaviour of the dependent KPIs is defined as “joint probability density function” is given in Eq. (5).

$$\begin{aligned} PDF_{\mathbf{KPI}_1^{(k)} \dots \mathbf{KPI}_d^{(k)}} &\sim \mathcal{N}(\mathbf{\mu}_{\mathbf{KPI}_j^{(k)}}, \mathbf{\Sigma}^{(k)}) \\ \mathbf{\mu}_{\mathbf{KPI}_j^{(k)}} &= \left[ \mu_{\mathbf{KPI}_1^{(k)}}, \dots, \mu_{\mathbf{KPI}_d^{(k)}} \right]^T \quad \forall k = \{1, \dots, N_k\} \end{aligned} \quad (5)$$

where  $d$  is the number of the dependent KPIs and it will equal to the number of KPIs ( $N_j$ ), if all KPIs are dependent to each other. The symmetric covariance matrix in the  $k^{\text{th}}$  experimental configuration is given as  $\mathbf{\Sigma}^{(k)}$ . On the other hand, The PDF function is represented as function of mean value ( $\mu_{\mathbf{KPI}_j^{(k)}}$ ) and standard deviation ( $\sigma_{\mathbf{KPI}_j^{(k)}}$ ) for univariate independent KPI, which is given in Eq. (6).

$$PDF_{\mathbf{KPI}_j^{(k)}} \sim \mathcal{N} \left( \mu_{\mathbf{KPI}_j^{(k)}}, \sigma_{\mathbf{KPI}_j^{(k)}} \right) \quad \forall j = \{d+1, \dots, N_j\} \quad \forall k = \{1, \dots, N_k\} \quad (6)$$

The Shapiro–Wilk normality test, which provides better results than other normality tests for small sample size [39], is applied to assess the normality assumption for each experimental configuration; and hence, the PDF function is given as a normal distribution. Furthermore, the number of replication is quite small to directly calculate the standard deviation. Therefore, it is formulated using the range statistics and corrective coefficient ( $d_2$ ) constant.

The success rate is calculated as a probabilistic approach that is the area under the PDF function. The probability is determined by the integral of the PDF over the given allowance limits, and it is formulated in Eq. (7) for dependent KPIs; whereas, in Eq. (8) for each independent KPI.

$$\xi_{\mathbf{KPI}_1^{(k)} \dots \mathbf{KPI}_d^{(k)}} = \int_{KPI_1^{(k)l}}^{KPI_1^{(k)u}} \dots \int_{KPI_d^{(k)l}}^{KPI_d^{(k)u}} PDF_{\mathbf{KPI}_1^{(k)} \dots \mathbf{KPI}_d^{(k)}} dKPI_1^{(k)} \dots dKPI_d^{(k)} \quad \forall k = \{1, \dots, N_k\} \quad (7)$$

$$\xi_{\mathbf{KPI}_j^{(k)}} = \int_{KPI_j^{(k)l}}^{KPI_j^{(k)u}} PDF_{\mathbf{KPI}_j^{(k)}} dKPI_j^{(k)} \quad \forall j = \{d+1, \dots, N_j\} \quad \forall k = \{1, \dots, N_k\} \quad (8)$$

The general forms of deterministic and stochastic surrogate models for estimating KPI value and the success rate for dependent and independent KPIs are given in Eqs. (9)–(11), respectively.

$$\hat{\mu}_{\mathbf{KPI}_j} = \mathbf{F}_{\mu_{\mathbf{KPI}_j}}(KCC_1, \dots, KCC_{N_i}) \quad \forall j = \{1, \dots, N_j\} \quad (9)$$

$$\hat{\xi}_{\mathbf{KPI}_1 \dots \mathbf{KPI}_d} = \mathbf{F}_{\xi_{\mathbf{KPI}_1 \dots \mathbf{KPI}_d}}(KCC_1, \dots, KCC_{N_i}) \quad (10)$$

$$\hat{\xi}_{\mathbf{KPI}_j} = \mathbf{F}_{\xi_{\mathbf{KPI}_j}}(KCC_1, \dots, KCC_{N_i}) \quad \forall j = \{d+1, \dots, N_j\} \quad (11)$$

### 2.3. Formulation of deterministic and stochastic process capability space

A sub-set of KCC-space is the process capability space ( $\mathbf{C}_p$ -space), which envelops all the feasible KCCs satisfying the KPIs allowance limits. For the  $j^{\text{th}}$  KPI, deterministic process capability space ( $\mathbf{DC}_{p_j}$ -Space) is expressed in Eq. (12).

$$\begin{aligned} \mathbf{DC}_{p_j}\text{-Space}(KCC_1, \dots, KCC_{N_i}) \\ = \begin{cases} \hat{\mu}_{\mathbf{KPI}_j} & \text{if } \beta \leq \hat{\mu}_{\mathbf{KPI}_j} \leq 1 \\ 0 & \text{otherwise} \end{cases} \quad \forall j = \{d+1, \dots, N_j\} \end{aligned} \quad (12)$$

The stochastic process capability spaces are defined in Eqs. (13) and (14) for dependent and independent KPIs, respectively.

$$\begin{aligned} \mathbf{SC}_{p_{\mathbf{KPI}_1 \dots \mathbf{KPI}_d}}\text{-Space}(KCC_1, \dots, KCC_{N_i}) \\ = \begin{cases} \hat{\xi}_{\mathbf{KPI}_1 \dots \mathbf{KPI}_d} & \text{if } \beta \leq \hat{\xi}_{\mathbf{KPI}_1 \dots \mathbf{KPI}_d} \leq 1 \\ 0 & \text{otherwise} \end{cases} \end{aligned} \quad (13)$$

$$\begin{aligned} \mathbf{SC}_{p_j}\text{-Space}(KCC_1, \dots, KCC_{N_i}) \\ = \begin{cases} \hat{\xi}_{\mathbf{KPI}_j} & \text{if } \beta \leq \hat{\xi}_{\mathbf{KPI}_j} \leq 1 \\ 0 & \text{otherwise} \end{cases} \quad \forall j = \{d+1, \dots, N_j\} \end{aligned} \quad (14)$$

is the minimal desirable success rate. The identification of the final deterministic and stochastic process capability spaces is done by aggregation individual deterministic and stochastic process capability spaces and obtained from Eq. (15) and Eq. (16), respectively.

$$\begin{aligned} \mathbf{DC}_p\text{-Space}(KCC_1, \dots, KCC_{N_i}) \\ = \bigcap_{j=1}^{N_i} \mathbf{DC}_{p_j}\text{-Space}(KCC_1, \dots, KCC_{N_i}) \end{aligned} \quad (15)$$

$$\begin{aligned} \mathbf{SC}_p\text{-Space}(KCC_1, \dots, KCC_{N_i}) \\ = \mathbf{SC}_{p_{\mathbf{KPI}_1 \dots \mathbf{KPI}_d}}\text{-Space}(KCC_1, \dots, KCC_{N_i}) \\ \times \prod_{j=1}^{N_i} \mathbf{SC}_{p_j}\text{-Space}(KCC_1, \dots, KCC_{N_i}) \end{aligned} \quad (16)$$

It is noteworthy that  $d$  is the number of the dependent KPIs which is determined according to the Pearson correlation coefficient test. The final stochastic process capability space is obtained by the probability theory which is a product of the independent and dependent stochastic process capability spaces. If the all KPIs are dependent, final stochastic process capability is only computed from the dependent stochastic process capability space.

### 2.4. Process parameter optimization using calculated surrogate models

The aim of this study is to identify optimum KCCs which maximize KPI (evaluated by deterministic surrogate model) and the probability of satisfying the allowance limits of that KPI (evaluated by stochastic surrogate model) at the same time. Therefore, the multi-objective optimization problem can be formally stated in Eq. (17).

$$\begin{aligned}
 & \text{maximize} && \mathbf{F}_{\mu_{KPI_j}}(KCC_1, \dots, KCC_{N_i}) \\
 & && \mathbf{F}_{\sigma_{KPI_1-KPI_{N_i}}}(KCC_1, \dots, KCC_{N_i}) \\
 & && \mathbf{F}_{\sigma_{KPI_j}}(KCC_1, \dots, KCC_{N_i}) \\
 & \text{subject to} && KCC_i^{LL} \leq KCC_i \leq KCC_i^{UL} \\
 & && KPI_j^{LL} \leq KPI_j \leq KPI_j^{UL} \\
 & && \forall i = \{1, \dots, N_i\}, \forall j = \{1, \dots, N_j\}
 \end{aligned} \tag{17}$$

**Table 5**  
Laser focusing and repositioning module (SmartLaser).

Characteristic feature	Unit	Specification
Collimating length	mm	50
Max focal length	mm	~1200
Measured spot size	µm	900
Working area	mm	700 × 450 × 400
Working distance	mm	min 894 max 1216

**3. Generation of the deterministic and the stochastic surrogate models**

**3.1. Materials**

The material used in this study was DX54D hot dip galvanized (GI) steels with nominal zinc coating thicknesses of 20 µm. The chemical composition and mechanical properties of this steel are given in Tables 3 and 4, respectively.

Two series of experiments were carried out. The first series served to characterise the dimpling process and develop the deterministic and stochastic process capability spaces; dimples were generated on the top surface of zinc coated sheet metal with a thickness of 0.75 mm. The second series was used to validate the calculated optimum KCCs based on the process capability spaces by confirmation experiments which were carried out on coupon experiments.

**3.2. Experimental setup**

Dimpling experiments were carried out using IPG Photonics YLR-4000 laser source with a nominal power of 3 kW at a wave-

length of 1064 nm. The laser beam was delivered using an optical fiber of core diameter of 50 µm, projecting the laser beam to a spot of 900 µm diameter. The laser source generates a multi-mode beam with an M<sup>2</sup> of 31.4 (measured by Primes Focus meter) at a central wavelength of 1064 nm. Neither shielding nor backing gases were used during the experiments.

Fig. 4 shows the experimental setup for beam quality measurement, laser dimpling and remote welding systems. The laser beam is delivered by COMAU SmartLaser robotic system which is a dedicated system for remote laser welding/dimpling and consists of 4 axes with dynamics and kinematics of a standard industrial robot with an optical system able to deflect the focused beam with high dynamics. The system specifications are given in Table 5.

3D optical surface profilometer (Bruker, Contour GT) was used to measure dimple height ( $D_H$ ) and dimple upper spot area ( $D_U$ ). The top surface of the zinc coated steel was scanned at speed 5 µm/s with a vertical resolution of ~10 nm on a rectangle region 4.5 × 6.5 mm. Thus, there are some gaps in the obtained data. The raw data obtained from the optical profilometer was filtered and then reconstructed in 3D which was meshing of the scanned surface area using “Laplacian smoothing filter”. The experimental setup for profilometer and an example of scanning result with corresponding process parameters are shown in Fig. 5.

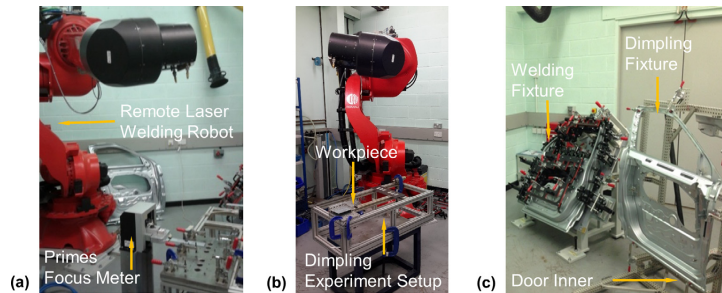
On the other hand, dimple lower surface area ( $D_L$ ) was computed by image segmentation method using MatLab®. Each image is captured with high resolution camera (3264 × 2448 pixels), with focal axis perpendicular to the surface of the workpiece to avoid image distortion. Initially, the number of pixel is calculated in 10 mm straight line to obtain scale from pixel length to millimetre; and then, the image was converted into 256 grey levels. After removing the background from the original image, it was binarized (black and white image). The number of black pixels inside the binarized image gives the area in pixel unit. This is converted into millimetre square using the obtain scale to get the corresponding lower surface area ( $D_L$ ). As an example, the reconstructed  $D_L$  measurement is illustrated in Fig. 6.

**Table 3**  
Chemical composition DX54D steel (wt%).

Material	Elements (wt%)					
	C	Si	Mn	P	S	Ti
DX54D	0.12	0.5	0.6	0.1	0.045	0.3

**Table 4**  
Mechanical properties of steel DX54D.

Material	Yield strength (MPa)	Tensile strength (MPa)	Total elongation (%)
DX54D	120–220	260–350	38



**Fig. 4.** Overview of the experimental setup (a) Beam quality measurement. (b) Laser Dimpling setup (first series of experiments). (c) Remote Laser Welding setup (second series of experiments).

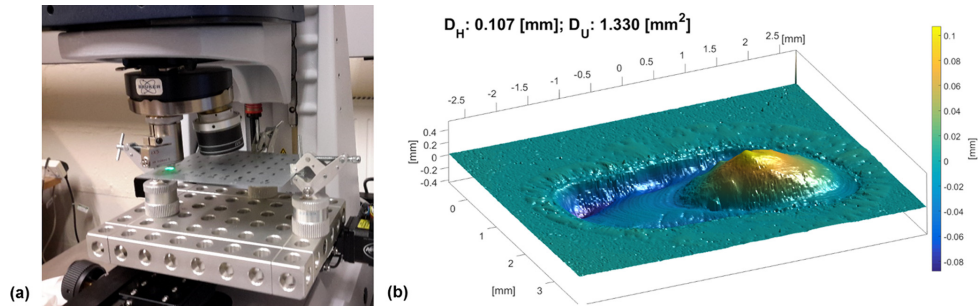


Fig. 5. (a) Experimental setup for profilometer. (b) An example of 3D reconstruction. Process parameters:  $S_s$ : 2 m/min,  $F_0$ : 35 mm,  $\alpha$ : 20°,  $L_r$ : 4 mm.

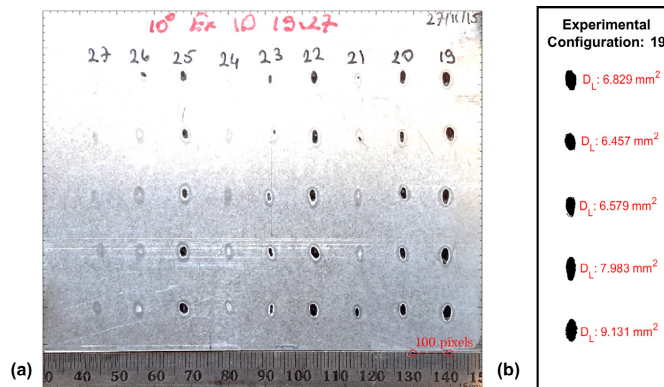


Fig. 6. Measurement of the dimple lower surface area (a) Grabbed image with scale bar. (b) Dimple lower surface area ( $D_L$ ) for experiment configuration 19 with 5 replications. Process parameters:  $S_s$ : 2 m/min,  $F_0$ : 25 mm,  $\alpha$ : 10°,  $L_r$ : 4 mm.

### 3.3. Design of experiments

Several methods are available for the design of experiments to establish the relationship between input and output variables, which include, among others, single-factor by single-factor approach, factorial or fractional factorial approaches, Box-Behnken, Doehlet or Taguchi experimental designs. Even though the full factorial design requires larger number of experimental configurations than others alternative techniques, it allows to spread out design point uniformly to obtain complete information on an unknown design function with a limited sample size for capturing both main factors and interactions. Therefore, we adopted a full factorial design approach with 4 – factor and 3 – level requires 81 experimental configurations ( $N_e$ ) with five replicates resulting 405 experimental runs. The design of experiment table was created in randomize order and it was distributed into 9 batches of sheet metal plates (130 × 110 mm). Thus, each plate had equal number of dimples and dimpling experiments were conducted according to the created DoE table. However, this equal division did not guarantee that each replicate was conducted in different metal plates. Due to the expected non-linear and stochastic nature of the dimpling process, we selected 3 levels for each KCC and the selected experimental levels were shown in Table 6.

Table 6

Key control characteristics and corresponding levels.

KCC	Unit	Level [1]	Level [2]	Level [3]
Scanning speed	m/min	2.0	3.0	4.0
Incidence angle	°	0.0	10.0	20.0
Focal offset	mm	25.0	35.0	55.0
Laser track	mm	2.0	3.0	4.0

Replication is conducted to detect the variation of system. Note is made that the more number of replications is the more accurate estimation of variation within the system. We selected 5 replications because they represent the right balance between expected model accuracy and time needed to perform experiments and collect data (one single dimple experiment, including laser processing, measurement and data collection, took about 2 h). The paper is intended to provide a general methodological approach, whose accuracy may be enhanced whenever more replications are made available.

### 3.4. Developing of surrogate models

The first objective of this work is to compute a surrogate model capable of analytically formulate relationships between multiple-

inputs (KCCs) and multiple-outputs (KPI values and success rates). This study applied multivariable adaptive regression spline (MARS) method developed by Friedman [40]. The MARS method is a non-linear and non-parametric regression that is able to model complex non-linear relationship among input variables by developing regression models locally rather than globally by the dividing the parameter space into several pieces and then performing piecewise fitting in each piece. Furthermore, it does not require larger number of training data sets and long training process compared to other methods such as neural networks, support vector machines [41].

The piecewise fitting is more appropriate for obtained data in dimpling experiments which are actual measurements and calculated success rates. The behaviour of the obtained data in one region inside the KCC-space cannot be easily correlated to its behaviour in other region caused by a sudden change which reduces the goodness of the regression. For instance, high success rate can be achieved in one experimental configuration but low success rate might be obtained in the next experimental configuration. This sudden change can be handle by using piecewise fitting methods.

The MARS models was developed using ARESLab© [42], a dedicated MatLab toolbox. The parameters used for developing the surrogate models were; (i) the maximum number of basis functions that included the intercept terms was set as 101. These functions were necessary to build the model in the forward building phase; (ii) the maximum degree of interactions between KCCs was set as 4; (iii) piecewise cubic type was chosen; (iv) the least important basis functions and high-order interactions were eliminated by feature selection and Generalized Cross-Validation (GCV) score in the backward elimination phase and set as 3; and, (v) k-fold cross validation (with 20 k-fold) was used for model validation.

**4. Development of the deterministic and the stochastic process capability spaces**

The second objective of this work is to develop deterministic and stochastic process capability spaces. A probabilistic approach was used to developed the stochastic capability space. In some problems, the measured KPIs might be dependent each other and their simultaneous behaviour defines the probability space. Therefore, the Pearson correlation coefficient test was initially conducted to determine the number of the dependent KPIs (*d*). As a consequence, a stochastic surrogate model and a stochastic process capability space were computed for the dependent KPIs; whereas, different stochastic surrogate models and stochastic process capability spaces were computed for each independent KPIs.

The Dixon's Q test was employed for identification of outliers for each experimental configuration and KPIs since it was designed for small sample size and assumed normal distribution [43]. When an outlier detected in one of the dependent KPI, the corresponding values in other KPIs were also considered as outlier even if the passed were not identified as outliers. The procedure flow for computing final deterministic and stochastic process capability spaces are summarized in Table 7.

**5. Process parameters optimization**

The last objective of this work is optimization of the process parameters based on the deterministic and stochastic process capability spaces. Both deterministic and stochastic  $C_p$ -spaces provide necessary models for selection KCCs to optimize the KPIs using various strategies reflecting the engineering needs of the dimpling process. In general, the optimisation entails two compet-

**Table 7**  
The procedure flow for computing process capability spaces.

Step	The methodology for computing final process capability spaces
1	Gather measurements for each KPI using Eq. (2)
2	Define number of dependent KPIs using Eq. (3)
3.1	Calculate outliers for each experimental configuration of each KPI using The Dixon's Q test
3.2	Update the number of sample size for each experimental configuration
4.1	Calculate mean for each experimental configuration for each KPI using Eq. (4)
4.2	Calculate standard deviation for each experimental configuration for each KPI
	$\sigma_{KPI^i} = \frac{\max(KPI^{(k)}) - \min(KPI^{(k)})}{d}$
	$\sigma_{KPI^i} = [\sigma_{KPI^i}, \dots, \sigma_{KPI^i}, \dots, \sigma_{KPI^i}]^T \quad \forall j = \{1, \dots, N_j\}$
5.1	Calculate PDF for each experimental configuration for dependent KPIs using Eq. (5)
5.2	Calculate PDF for each experimental configuration for each independent KPI using Eq. (6)
6.1	Calculate SR for each experimental configuration for dependent KPIs using Eq. (7)
6.2	Calculate SR for each experimental configuration for each independent KPI using Eq. (8)
7.1	Calculate deterministic surrogate model for each KPI using Eq. (9)
7.2	Calculate stochastic surrogate model for dependent KPIs using Eq. (10)
7.3	Calculate stochastic surrogate model for each independent KPI using Eq. (11)
8.1	Calculate deterministic process capability space for each KPI using Eq. (12)
8.2	Calculate stochastic process capability space for dependent KPIs using Eq. (13)
8.3	Calculate stochastic process capability space for each independent KPI using Eq. (14)
9.1	Calculate final deterministic process capability over KCC-space using Eq. (15)
9.2	Calculate final stochastic process capability over KCC-space using Eq. (16)

ing objectives; (i) to obtain maximum KPI value; and, (ii) to maximize the probability of satisfying the allowance limits of selected KPI. It is important to note that the requirements for dimpling process are determined by downstream processes such as assembly fixture design and optimization [37]. For example, assembly fixture design for welding which is a downstream process might require a specific KCCs/KPIs configuration which will impose the dimpling process to achieve the best success rate in satisfying the requirements of achieving lower allowance limits of KPIs. Therefore, the proposed optimization strategy is based on  $\epsilon$ -constraint method rather than solving Pareto Frontier. This involves optimization of success rate in achieving pre-selected KPIs configuration and using the other functions as constraints.

In this paper, three design options are defined to optimize all KPIs. The first design option maximizes success rate of the dependent KPIs which addresses the functional and strength requirement of a dimple (i.e.  $D_H, D_L$ ) to control simultaneously minimum gap requirement and strength of dimple. Similarly, the second design option evaluates the success rate of the independent KPI which focuses on aesthetic requirements of a dimple (i.e.  $D_L$ ) that is important for Class-A surfaces. The other design options are combination of these options and handled as multi-objective optimization. Table 8 describes the proposed optimization strategies for various pre-defined KCCs/KPIs configurations.

**6. Results and discussions**

**6.1. Statistical data analysis**

The total number of KCCs, KPIs, experimental configurations, replication and dependent KPIs are determined as  $N_i, N_j, N_k, N_l$  and *d*, respectively. The dependency among KPIs are evaluated

**Table 8**  
Proposed options for process parameters selection.

Design option	Objective function	Constraint functions		
		Deterministic constraint	Stochastic constraint	Bounded process parameters
1	$\max F_{\text{dipH}_1, \text{dipH}_2}$	$F_{\text{dipH}_1} \geq KPI_1^L$ $F_{\text{dipH}_2} \geq KPI_2^L$	-	$KCC_1^L \leq KCC_1 \leq KCC_1^H$ $\forall i = \{1, \dots, N_i\}$
2	$\max F_{\text{dipH}_3}$	$F_{\text{dipH}_3} = KPI_3^L$	-	
3	$\max F_{\text{dipH}_1, \text{dipH}_2}$	$F_{\text{dipH}_1} \geq KPI_1^L$ $F_{\text{dipH}_2} \geq KPI_2^L$ $F_{\text{dipH}_3} = KPI_3^L$	$F_{\text{dipH}_3} \geq \beta$	

**Table 9**  
 $R^2$  & RSME values for different surrogate models.

Surrogate model	MARS		2nd order polynomial		3rd order polynomial	
	$R^2$	RSME	$R^2$	RSME	$R^2$	RSME
$F_{\text{dipH}_1}$	0.9281	0.011	0.9527	0.0266	0.9624	0.0235
$F_{\text{dipH}_2}$	0.9634	0.1219	0.9293	0.3288	0.9358	0.3025
$F_{\text{dipH}_3}$	0.9874	0.2213	0.9506	0.5621	0.9534	0.5329
$F_{\text{dipH}_1, \text{dipH}_2}$	0.8872	0.1450	0.8068	0.2766	0.8114	0.1866
$F_{\text{dipH}_3}$	0.9754	0.0684	0.9187	0.2241	0.9039	0.1353

using the Pearson product-moment correlation coefficient test and its result ( $\rho$ ) takes a value between +1 and -1, where 1 is total positive linear correlation, 0 is no linear correlation, and -1 is total negative linear correlation. The result of the Pearson test is given in Eq. (18). According to results, dimple height ( $D_H$ ) and dimple upper surface area ( $D_U$ ) are chosen as dependent KPIs and dimple lower surface area ( $D_L$ ) is independent from other KPIs.

$$\rho_{mn} = \frac{\text{cov}(KPI_m, KPI_n)}{\sigma_{KPI_m} \sigma_{KPI_n}} \quad \forall m, n = \{1, \dots, 3\}$$

$$= \begin{bmatrix} 1 & 0.7852 & 0.2409 \\ 0.7852 & 1 & 0.5515 \\ 0.2409 & 0.5515 & 1 \end{bmatrix} \quad (18)$$

The goodness of surrogate models is assessed by computing the determination of coefficient ( $R^2$ ) and root mean square error (RMSE) and the MARS models are compared with second and third order polynomial regressions which are reported in Table 9. The success rate in the stochastic case is not a binary value and it gets any value between zero and one. However, its behaviour in one region inside the KCC-space cannot be easily correlated to its behaviour in other region. This change can be handle by using piecewise fitting methods and better  $R^2$  and RMSE are obtained in MARS model. The obtained MARS models and the measured KPIs are given in the in the Appendix.

6.2. Deterministic surrogate models

In the deterministic scenario, the mean values are calculated to compute surrogate model which estimates the KPI values over the KCC-space. The results of these deterministic surrogate models are illustrated in Figs. 7–9 for varying scanning speed ( $S_s$ ) and incidence angle ( $\alpha$ ) for constant laser track ( $L_T$ ) and focal offset ( $F_O$ ) values. These figures provide two types of information; (i) the effect of the process parameters on KPIs which can be directly used by the automotive industry; and, (ii) individual deterministic process capability spaces (**DC<sub>p</sub>-Space**) which lead to final deterministic process capability space (**DC<sub>p</sub>-Space**). It is interesting to note that dimple is formed in the same direction with laser track movement for higher defocus (~5 mm) whereas dimple is formed in the oppo-

site direction of the laser movement for lower focal offset (~25 mm). This behaviour is one of the findings of this study and is shown in Fig. 10. It can be explained by the fact that larger defocusing generates bigger laser beam spot size which leads to a drop in power intensity. In this case the molten material is moved forward by the movement of the laser beam. The dimples obtained in this condition are characterized by a cavity in the rear and higher dimple in front, which is highlighted in Fig. 2.

6.2.1. Characterization of dimple height ( $D_H$ )

According to the literature, dimple height decreases with scanning speed. However, as predicted in Fig. 7, this can only be obtained for high focal offset (~55 mm) and constant incidence angle. For low focal offset (~25 mm), the laser track clearly affects the dimple height, whilst a bipolarized pattern can be observed because of the mutual interaction between speed and incidence angle. At medium focal offset (~35), scanning speed slightly affects dimple height, whilst the interaction between laser track and incidence angle generates a unipolar pattern. The highest dimple height is observed around 5 – 10 degrees. The reason for this could be the amount of energy absorbed by the material and tilted key-hole that pushes the melting upwards. It can be deduced that the dimple height increases while increasing laser track as also indicated in the literature [27].

6.2.2. Characterization of dimple upper surface area ( $D_U$ )

Dimple upper surface area ( $D_U$ ) decreases with increasing scanning speed whilst other parameters are kept constant. However, it increases with increasing both scanning speed and laser track but decreases with increasing both scanning speed and focal offset. It is evident that increasing laser track results in higher and larger dimple since the longer displacement creates longer trailing jet on the surface as also indicated in the literature [24]. The correlation patterns exhibit a unipolar shape, which tends to be elongated moving toward higher laser track and focal offset.

6.2.3. Characterization of dimple lower surface area ( $D_L$ )

It is interesting to note that the main and interaction effects of incidence angle into dimple lower surface area ( $D_L$ ) can be negligi-

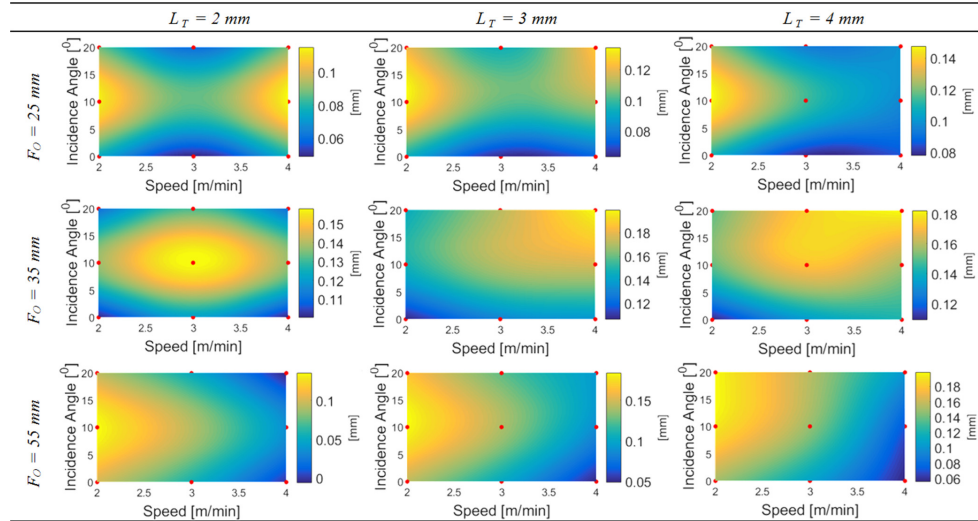


Fig. 7. The estimated dimple height value ( $D_n$ ) over KCC-space in the deterministic scenario.

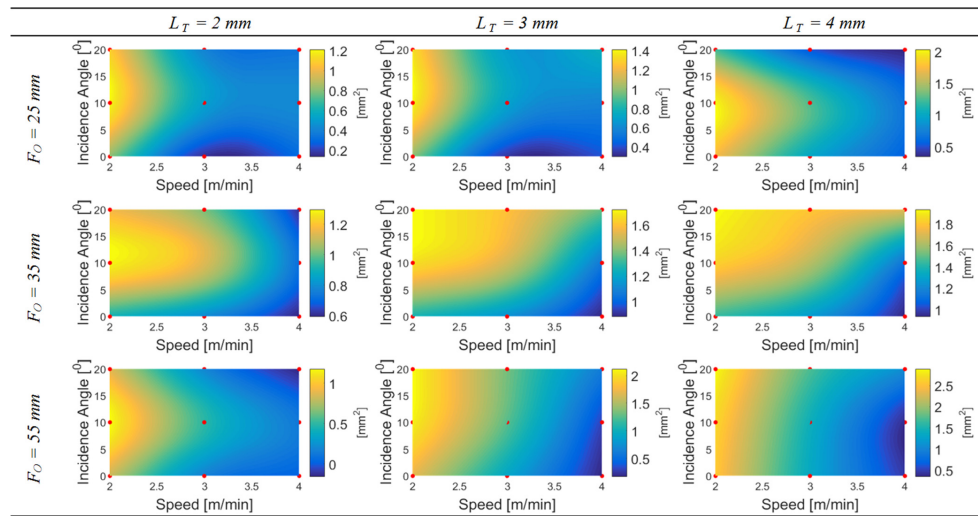


Fig. 8. The estimated dimple upper surface value ( $D_u$ ) over KCC-space in the deterministic scenario.

ble and it can be seen in Fig. 9 that the correlation pattern is almost identical. On the other hand,  $D_i$  is directly correlated with laser track and inversely correlated with focal offset and scanning speed. The minimum  $D_i$  is observable for medium (~35 mm) and high (~55 mm) focal offset and lower laser track (~2 mm).

6.3. Deterministic process capability space ( $DC_p - Space$ )

The deterministic process capability space ( $DC_p - Space$ ) is illustrated in Fig. 11. The shaded area represents the feasible region

and any value inside corresponds to feasible process parameters (KCCs) which simultaneously satisfy all quality requirements defined in Table 2. According to the  $DC_p - Space$  result, feasible process parameters cannot be achieved for lower focal offset (~25 mm) since dimple lower surface area ( $D_i$ ) is more likely to exceed its allowance limits that is highlighted in Fig. 9. The reason might be lower focal offset creates higher power intensity and thus more amount of material is molten which results in wider and deeper molten pool. The rate of change of the laser intensity determines the physical phenomena between material and laser beam. For

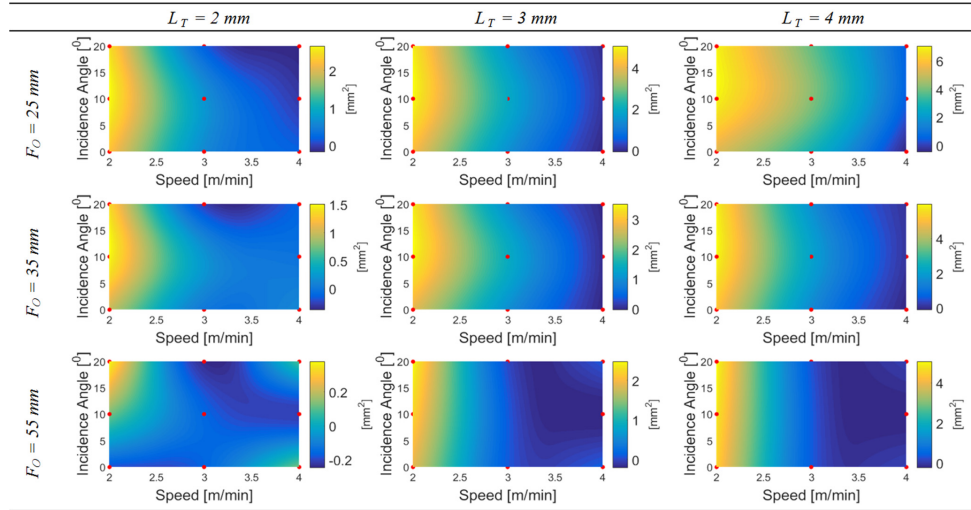


Fig. 9. The estimated dimple lower surface value ( $D_L$ ) over KCC-space in the deterministic scenario.

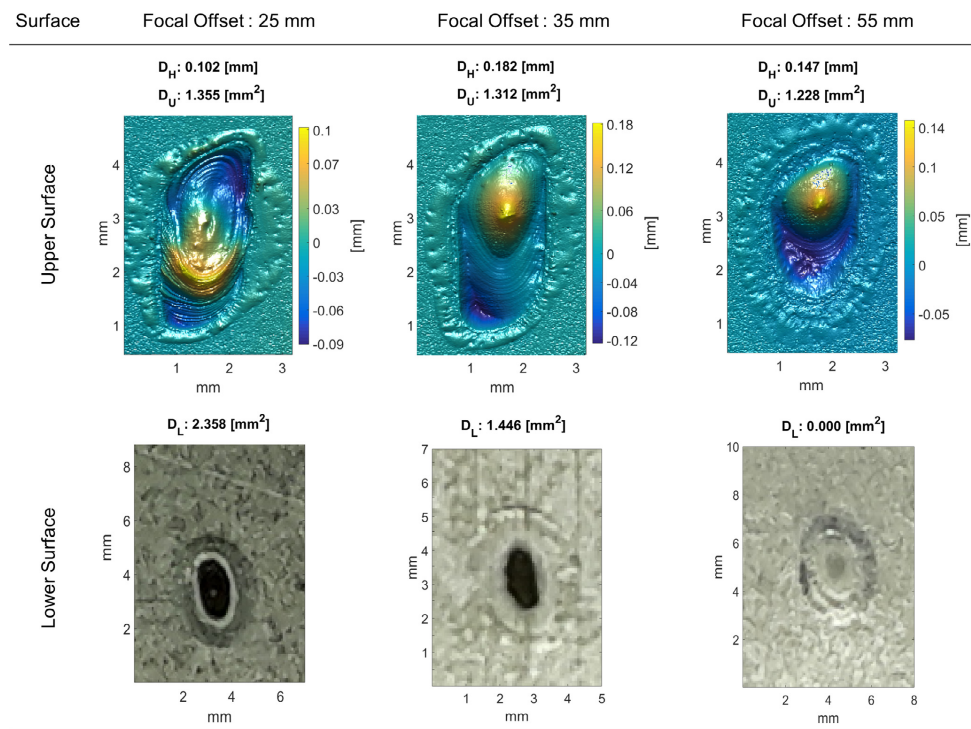


Fig. 10. Effect of focal offset on three KPIs when process parameters are constant at  $S_f$ : 3 m/min,  $\alpha$ : 10°,  $L_T$ : 3 mm. (Upper Surface) Surface profilometer results – (Lower Surface) Image processing results.

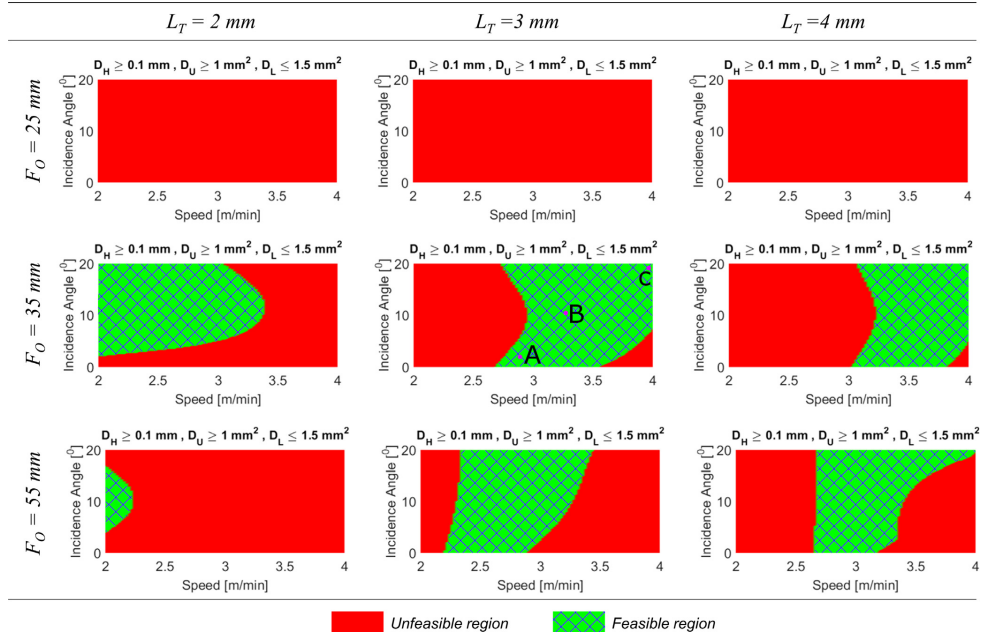


Fig. 11. Deterministic process capability space ( $DC_p$  – Space) for laser dimpling process.

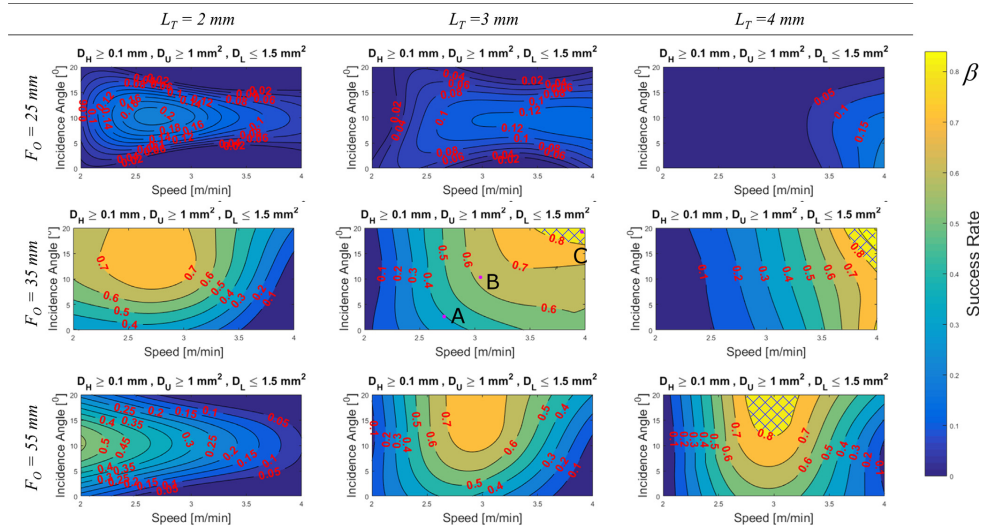


Fig. 12. Stochastic process capability space ( $SC_p$  – Space) for laser dimpling process.



instance, slow speed, short laser track and low focal offset result higher energy intensity rate and thus, higher dimple but larger dimple lower surface area is occurred. Therefore, feasible regions are gathered in the medium level of the process parameters.

6.4. Stochastic process capability space (SC<sub>p</sub> – Space)

The calculated stochastic process capability space (SC<sub>p</sub>–Space) is presented in Fig. 12. It represents the simultaneous product of the stochastic process capability spaces defined in Eq. (16). The achievable success rates of the dimpling process are displayed in contour plot by initially selecting minimal desirable success rate (β) at zero in Fig. 12. Therefore, it will provide more information to select a set of KCCs. For example, point A and B are inside the feasible region in Fig. 11 which define two different sets of KCCs that simultaneously satisfy KPIs allowance limits. On the contrary, these points represented in Fig. 12 are different success rates since the process variation is less at the point B. Therefore, point B provide more robust process parameters (KCCs) and SC<sub>p</sub>–Space can be utilized to select KCCs according to pre-defined success rate (β = 0.8). Furthermore, the deterministic process capability space and stochastic process capability space have to follow same pattern since probability value is a function of mean and variation.

According to results, higher success rate regions are concentrated at the medium focal offset (~35 mm). The success rate is nearly zero at lower focal offset (~25 mm) thus confirming the results obtained by the DC<sub>p</sub>–Space model. According to the results, the minimal desirable success rate (β) was set at 0.8 and it was highlighted in shaded region in Fig. 10.

6.5. Process parameters selection and optimisation

Despite the fact that evolutionary algorithms do not guarantee the global optimum, their convergence speeds to the optimal results (nearly global) are better than those of the traditional techniques. Thus, evolutionary algorithms have been used for optimization of real-world problems in many applications instead of traditional techniques [44–47]. Therefore, genetic algorithm was implemented to solve the process parameter selection and optimization problem. Population size, probability of crossover and mutation numbers were selected as 500, 0.60 and 0.12, respectively.

In this paper, we define three design options to optimize all KPIs which are described in Table 8 and the optimization results are given in Table 10. The results indicate that the optimum configurations are concentrated between medium (~35 mm) and high (~55 mm) focal offset and higher laser track (~4 mm) and medium scanning speed (~3 mm). This can be explained by the amount of time spent by the laser power intensity on the workpiece. It can be deduced that by decreasing interaction time less amount of materials was molten and molten pool becomes shallow because less amount of laser energy was absorbed. The design option three is approximately illustrated as Point C in Figs. 11 and 12.

In order to validate the optimization results obtained in Table 10 and estimated values from the surrogate models defined in Eqs. (9), confirmation experiments were carried out by coupon experiments. Five replications of each design option were performed on a 10 × 40 mm sheet metal with a thickness of 0.75 mm and the results are reported in Table 11. It shows measured 5 replications for each KPI and their mean and success rate. These values are computed according to the methodological flow from Step 1 to Step 6.2 which are presented in Table 7. These calculated values are compared against estimated values from the developed surrogate models.

These design options are offered to find robust process parameters to obtain maximum dimple height and upper surface; and, minimum dimple lower surface area. The first option studies maximizing mean and success rate of dimple height and upper surface area without considering the dimple lower surface. According to the results, the calculated and estimated mean and success rates are quite similar. However, this similarity is not achieved for the second design option. The second option considers only to obtain robust parameters for minimum dimple lower surface area. The variation of the D<sub>H</sub> and D<sub>U</sub> at this point are more than measured values and dimple upper surface might be also correlated with dimple lower surface area. These reasons might cause the different in the calculated and estimated values.

The laser dimpling process is currently utilized for the laser lap welding of zinc coated steels, especially automotive industry. The dimples generate a small gap between faying surfaces where the zinc vapour is vented out through. However, obtaining a constant gap without having a darker spot at the back side of the steel are the major challenges of the process. An optimum set of process parameter was validated by welding experiments and results are given in Fig. 13. The figure shows images of welded specimen

Table 10  
Optimization results.

Design option	S <sub>s</sub>	α	L <sub>T</sub>	F <sub>O</sub>	μ <sub>KPI1</sub>	μ <sub>KPI2</sub>	μ <sub>KPI3</sub>	ξ̂ <sub>KPI1, KPI2</sub>	ξ̂ <sub>KPI2</sub>
1	2.0020	15.0069	3.9692	54.9941	0.198	2.756	4.868	1.000	0.000
2	3.3709	0.2704	3.0229	52.8982	0.092	0.710	0.000	0.283	1.000
3	3.9967	19.9778	3.4845	37.2153	0.199	1.592	0.000	1.000	0.993

Table 11  
Validation of the optimization results for all design options.

Design option	KPI	Rep. 1	Rep. 2	Rep. 3	Rep. 4	Rep. 5	μ <sub>KPI</sub>	μ̂ <sub>KPI</sub>	ξ̂ <sub>KPI</sub>	ξ̂ <sub>KPI</sub>
1	D <sub>H</sub>	0.183	0.190	0.185	0.209	0.189	0.1912	0.198	1	1
	D <sub>U</sub>	2.184	2.055	2.080	2.192	2.154	2.133	2.756	1	1
	D <sub>L</sub>	4.467	4.318	4.415	5.028	3.417	4.329	4.868	0	0
2	D <sub>H</sub>	0.124	0.13	0.114	0.084	0.118	0.114	0.092	0.588	0.283
	D <sub>U</sub>	1.123	1.186	1.037	0.776	1.076	1.0396	0.710	0.588	0.283
	D <sub>L</sub>	0.000	0.000	0.000	0.000	0.000	0.000	0.000	1	1
3	D <sub>H</sub>	0.207	0.198	0.184	0.179	0.179	0.1894	0.199	0.996	1
	D <sub>U</sub>	1.741	1.707	1.647	1.261	1.438	1.513	1.592	0.996	1
	D <sub>L</sub>	0.000	0.000	0.000	0.000	0.000	0.000	0.000	1	0.993

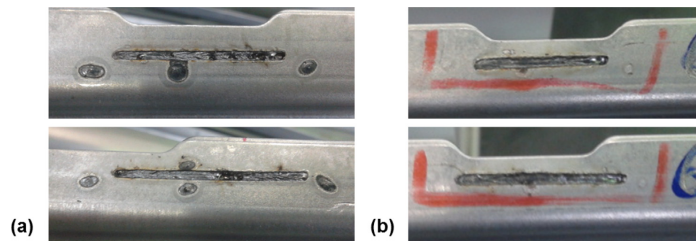


Fig. 13. Remote laser welded joint. (a) Trial and error approach before optimization. (b) Optimized configuration based on the proposed methodology.

before and after the optimization of laser dimpling process. The dark spots are not visible on the lower surface and there are no spatters around the stitch after implementing optimum laser dimpling process parameters. Likewise, the quality of weld seam is improved, no blow holes are detected in the weld seam.

## 7. Conclusions and final remarks

This paper presents a novel methodology to select process parameters for laser dimpling process. It is based on the process capability space which allows the estimation of a desired process fallout rate in the case of quality failures or violation of process requirements. The success rate is offered to measure the process fallout rate using probabilistic approach. First, two surrogate models are developed to estimate mean and success rate over the defined process parameters space; and then, the process capability space is computed using the developed surrogate models. Finally, the optimize the mean and success rate based on the minimal desirable success rate ( $\beta$ ) using multi-objective optimization methods to reduce variation in the process and to find the robust parameters. Furthermore, the process mean is illustrated in deterministic process capability space (**DC<sub>p</sub>-Space**); whereas, success rate, indirectly process variation, is in stochastic process capability space (**SC<sub>p</sub>-Space**). It is noteworthy that optimization the process variation does not guarantee maximizing the mean value. Thus optimization problem is considered as multi-objective optimization with two competing objectives.

The industrial needs are also addressed in the paper and two new key performance indicators ( $D_U$ ,  $D_L$ ) which are first time offered in this paper. The  $D_U$  is required to control the gap between faying surfaces whereas the  $D_L$  affects post weld operations. For example, a large  $D_L$  (a dark black spot) is unwanted for the downstream process such as it requires additional process to cover these dark spots. Furthermore, four process parameters ( $S_s$ ,  $\alpha$ ,  $L_r$ ,  $F_o$ ) are offered to have more comprehensive characterization of the process and to determine their effect on the proposed KPIs. These parameters are selected because scanning speed and laser track can affect process cycle time and focal offset and incidence angle can be related to the beam visibility, accessibility and offline programming of the robotic scanner head.

The following guidelines have been pointed out: for lower focal offset, dimples are formed in the opposite direction of the laser beam movement; whereas, they generate in the same direction for larger defocus ( $\sim 55$  mm). In addition to that, larger defocus will lead to reduction in the dimple lower surface area. Conversely, increasing laser track will result in reduction of the dimple lower surface area. It can be concluded that power intensity and the rate of change of the power intensity are the key factors affecting the formation of the laser dimple.

The current best practice for process parameters selection is based on costly and time consuming trial and error approaches

(up to 2–3 weeks to setup the proper combination of process parameter for door assembly systems). The proposed methodology offers the following opportunity and applicability: (i) selection and optimization of process parameters at early design stage; (ii) identification of risky areas and low reliable parameters settings which help to speed-up the process of detecting and correcting defects. This will lead to shorten the time for design and commissioning and reduce production scraps.

The disadvantages of this approach can be summarized as follow: (i) the required number of replication to calculate a smooth PDF function to compute success rate. This number can be determined by an initial screen experiments with high number of replication. (ii) deterministic and stochastic surrogate models are developed based on the process parameters which can be easily controllable without neglecting the noise variables and their interaction with process parameters. However, this can be handled by accurately designing experiment.

The proposed methodology offers a unique simulation tool which is generic and can be applied not only to laser dimpling process but can also be exploited in the context of selection and optimization of process parameters with heteroscedasticity. This research will be further expanded to integrate the developed surrogate models with task planning and sequencing algorithms in order to simultaneously optimize quality, cost and cycle time of robotic remote laser welding systems.

## Acknowledgements

This study was partially supported by the EU research project EU-FP7 FoF-ICT-2011.7.4: RLW Navigator, by the UK EPSRC project EP/K019368/1: Self-Resilient Reconfigurable Assembly Systems with In-process Quality Improvement and by the Republic of Turkey Ministry of National Education Post-Graduate Scholarship.

## Appendix A. Supplementary material

Supplementary data associated with this article can be found, in the online version, at <http://dx.doi.org/10.1016/j.optlastec.2017.02.012>.

## References

- [1] D. Ceglarek, M. Colledani, J. Vanca, D.Y. Kim, C. Marine, M. Kogel-Hollacher, A. Mistry, L. Bolognese, Rapid deployment of remote laser welding processes in automotive assembly systems, *CIRP Ann. – Manuf. Technol.* 64 (2015) 389–394, <http://dx.doi.org/10.1016/j.cirp.2015.04.119>.
- [2] S. Hörnström, J. Karlsson, W.J. Van Ooij, N. Tang, H. Klang, Paint adhesion and corrosion performance of chromium-free pretreatments of 55% Al-Zn-coated steel, *J. Adhes. Sci. Technol.* 10 (1996) 883–904, <http://dx.doi.org/10.1163/156856196X00913>.
- [3] A. Ribolla, G.L. Damoulis, G.F. Batalha, The use of Nd:YAG laser weld for large scale volume assembly of automotive body in white, *J. Mater. Process. Technol.*

- 164–165 (2005) 1120–1127, <http://dx.doi.org/10.1016/j.jmatprotec.2005.02.104>.
- [4] Y. Kawahito, M. Mizutani, S. Katayama, S. Steel, Investigation of high-power fiber laser welding phenomena of stainless steel, *Trans. JWRI* 36 (2007) 11–16.
- [5] A.K. Sinha, D.Y. Kim, D. Ceglarek, Correlation analysis of the variation of weld seam and tensile strength in laser welding of galvanized steel, *Opt. Lasers Eng.* 51 (2013) 1143–1152, <http://dx.doi.org/10.1016/j.optlaseng.2013.04.012>.
- [6] P. Norman, J. Karlsson, A.F.H. Kaplan, Monitoring undercut, blowouts and root sagging during laser beam welding, in: 5th Int. WLT-Conference Lasers Manuf., 2009, pp. 355.
- [7] G. Chen, L. Mei, M. Zhang, Y. Zhang, Z. Wang, Research on key influence factors of laser overlap welding of automobile body galvanized steel, *Opt. Laser Technol.* 45 (2013) 726–733, <http://dx.doi.org/10.1016/j.optlastec.2012.05.002>.
- [8] R. Fabbro, F. Coste, D. Goebels, M. Kielwasser, Study of CW Nd-Yag laser welding of Zn-coated steel sheets, *J. Appl. Phys. D* (2006) 401–409, <http://dx.doi.org/10.1088/0022-3727/39/2/024>.
- [9] Y. Pan, I.M. Richardson, Keyhole behaviour during laser welding of zinc-coated steel, *J. Phys. D Appl. Phys.* 44 (2011) 45502, <http://dx.doi.org/10.1088/0022-3727/44/4/045502>.
- [10] F. Briand, K. Chouf, P. Lefebvre, Method and installation for laser welding with a N<sub>2</sub>/He gas mixture, the N<sub>2</sub>/He content being controlled according to the laser power, 7385158B2, 2008.
- [11] S. Yang, B. Carlson, R. Kovacevic, Laser welding of high-strength galvanized steels in a gap-free lap joint configuration under different shielding conditions, *Weld. J.* 90 (2011) 8–18.
- [12] W. Chen, P. Ackerson, P. Molian, CO<sub>2</sub> laser welding of galvanized steel sheets using vent holes, *Mater. Des.* 30 (2009) 245–251, <http://dx.doi.org/10.1016/j.matdes.2008.05.009>.
- [13] R. Akhter, W.M. Steen, K.G. Watkins, Welding zinc-coated steel with a laser and the properties of the weldment, *J. Laser Appl.* 3 (1991) 9, <http://dx.doi.org/10.2351/1.4745277>.
- [14] D.C. Weckman, H.W. Kerr, D.M. Hirak, Nd : YAG laser beam welding of coated steels using a modified lap joint geometry, *Weld. J.* 162–170 (1996).
- [15] T.J. Jokinen, A.S. Hovikorp, V. Kujanpaa, Effect of an air gap on the properties of high power Nd: YAG laser welds, in: ICALEO'98–Int. Congr. Appl. Laser Electro-Optics, Orlando, US, 1998, pp. 103–112. RI.
- [16] Z. Chen, S. Yang, C. Wang, X. Hu, X. Shao, J. Wang, A study of fiber laser welding of galvanized steel using a suction method, *J. Mater. Process. Technol.* 214 (2014) 1456–1465, <http://dx.doi.org/10.1016/j.jmatprotec.2014.02.013>.
- [17] X. Li, S. Lawson, Y. Zhou, F. Goodwin, Novel technique for laser lap welding of zinc coated sheet steels, *J. Laser Appl.* 19 (2007) 259, <http://dx.doi.org/10.2351/1.2795755>.
- [18] A.K. Dasgupta, J. Mazumder, Laser welding of zinc coated steel: an alternative to resistance spot welding, *Sci. Technol. Weld. Join.* 13 (2008) 289–293.
- [19] S. Iqbal, M.M.S. Gualini, F. Grassi, Laser welding of zinc-coated steel with tandem beams: analysis and comparison, *J. Mater. Process. Technol.* 184 (2007) 12–18, <http://dx.doi.org/10.1016/j.jmatprotec.2006.10.043>.
- [20] M.R. Kronthaler, S. Braunreuther, M.F. Zaeh, Bifocal hybrid laser welding – more than a superposition of two processes, *Phys. Procedia* 12 (2011) 208–214, <http://dx.doi.org/10.1016/j.phpro.2011.03.027>.
- [21] J. Ma, F. Kong, B. Carlson, R. Kovacevic, Two-pass laser welding of galvanized high-strength dual-phase steel for a zero-gap lap joint configuration, *J. Mater. Process. Technol.* 213 (2013) 495–507, <http://dx.doi.org/10.1016/j.jmatprotec.2012.10.019>.
- [22] J. Zhou, H.L. Tsai, T.F. Lehnhoff, Investigation of transport phenomena and defect formation in pulsed laser keyhole welding of zinc-coated steels, *J. Phys. D Appl. Phys.* 39 (2006) 5338–5355, <http://dx.doi.org/10.1088/0022-3727/39/24/036>.
- [23] Y.F. Tzeng, T. Yih-Fong, Gap-free lap welding of zinc-coated steel using pulsed CO<sub>2</sub> laser, *Int. J. Adv. Manuf. Technol.* 29 (2006) 287–295, <http://dx.doi.org/10.1007/s00170-005-2522-3>.
- [24] J. Blackburn, P. Hilton, Producing surface features with a 200 W Yb-fibre laser and the Surf-Sculpt process, *Phys. Procedia* 12 (2011) 529–536, <http://dx.doi.org/10.1016/j.phpro.2011.03.065>.
- [25] C. Earl, P. Hilton, B. O'Neill, Parameter influence on surf-sculpt processing efficiency, *Phys. Procedia* 39 (2012) 327–335, <http://dx.doi.org/10.1016/j.phpro.2012.10.045>.
- [26] H. Gu, Laser lap welding of zinc coated steel sheet with laser-dimple technology, *J. Laser Appl.* 22 (2010) 87, <http://dx.doi.org/10.2351/1.3485596>.
- [27] H. Gu, B. Shulkin, A practical use of humping effect in laser beam welding, *J. Laser Appl.* 23 (2011) 12001, <http://dx.doi.org/10.2351/1.3538988>.
- [28] M.H. Cho, D.F. Farson, Understanding bead hump formation in gas metal arc welding using a numerical simulation, *Metall. Mater. Trans. B* 38 (2007) 305–319, <http://dx.doi.org/10.1007/s11663-007-9034-5>.
- [29] C.S. Wu, Z.K. Hu, Y.M. Zhang, Suppression of weld-bead defects and increase in the critical welding speed during high-speed arc welding, *Proc. Inst. Mech. Eng. Part B: J. Eng. Manuf.* 223 (2009) 751–757, <http://dx.doi.org/10.1243/09544054JEM13695C>.
- [30] P. Berger, H. Hügel, A. Hess, R. Weber, T. Graf, Understanding of humping based on conservation of volume flow, *Phys. Procedia* 12 (2011) 232–240, <http://dx.doi.org/10.1016/j.phpro.2011.03.030>.
- [31] T. Ilar, I. Eriksson, J. Powell, A. Kaplan, Root humping in laser welding – an investigation based on high speed imaging, *Phys. Procedia* 39 (2012) 27–32, <http://dx.doi.org/10.1016/j.phpro.2012.10.010>.
- [32] C. Thomy, T. Seefeld, F. Vollertsen, Humping effect in welding of steel with single-mode fibre laser, *Weld. World* 52 (2013) 9–18, <http://dx.doi.org/10.1007/BF03266636>.
- [33] D. Colombo, B. Previtali, Laser dimpling and remote welding of zinc-coated steels for automotive applications, *Int. J. Adv. Manuf. Technol.* 72 (2014) 653–663, <http://dx.doi.org/10.1007/s00170-014-5690-1>.
- [34] W. Huang, R. Kovacevic, A neural network and multiple regression method for the characterization of the depth of weld penetration in laser welding based on acoustic signatures, *J. Intell. Manuf.* 22 (2011) 131–143, <http://dx.doi.org/10.1007/s10845-009-0267-9>.
- [35] U. Reising, M. Schleser, O. Mokrov, E. Ahmed, Statistical modeling of laser welding of DP/TRIP steel sheets, *Opt. Laser Technol.* 44 (2012) 92–101, <http://dx.doi.org/10.1016/j.optlastec.2011.05.025>.
- [36] Q. Shi, D. Gu, M. Xia, S. Cao, T. Rong, Effects of laser processing parameters on thermal behavior and melting/solidification mechanism during selective laser melting of TiC/Inconel 718 composites, *Opt. Laser Technol.* 84 (2016) 9–22, <http://dx.doi.org/10.1016/j.optlastec.2016.04.009>.
- [37] P. Franciosa, S. Gerbino, D. Ceglarek, Fixture capability optimization for early-stage design of assembly system with compliant parts using nested polynomial chaos expansion, *Procedia CIRP* 41 (2016) 87–92, <http://dx.doi.org/10.1016/j.procir.2015.12.101>.
- [38] M. Haider, P. Hubert, L. Lessard, An experimental investigation of class A surface finish of composites made by the resin transfer molding process, *Compos. Sci. Technol.* 67 (2007) 3176–3186, <http://dx.doi.org/10.1016/j.compscitech.2007.04.010>.
- [39] H. Thode, Testing for Normality, Marcel Dekker, New York, USA, 2002.
- [40] J.H. Friedman, Multivariate adaptive regression splines, *Ann. Stat.* 19 (1991) 1–67, <http://dx.doi.org/10.1214/aos/1176347963>.
- [41] T.S. Lee, C.C. Chiu, Y.C. Chou, C.J. Lu, Mining the customer credit using classification and regression tree and multivariate adaptive regression splines, *Comput. Stat. Data Anal.* 50 (2006) 1113–1130.
- [42] G. Jekabsons, ARESLab Adaptive Regression Splines toolbox for Matlab/Octave ver. 1.13.0 User's manual, 2016. <<http://www.cs.rtu.lv/jekabsons/>> (accessed November 28, 2016).
- [43] R.B. Dean, W.J. Dixon, Simplified statistics for small numbers of observations, *Anal. Chem.* 23 (1951) 636–638. <http://pubs.acs.org/doi/abs/10.1021/ac60052a025>.
- [44] E.M. Anawa, A.G. Olabi, Using Taguchi method to optimize welding pool of dissimilar laser-welded components, *Opt. Laser Technol.* 40 (2008) 379–388, <http://dx.doi.org/10.1016/j.optlastec.2007.07.001>.
- [45] Y. Zhao, Y. Zhang, W. Hu, X. Lai, Optimization of laser welding thin-gage galvanized steel via response surface methodology, *Opt. Lasers Eng.* 50 (2012) 1267–1273, <http://dx.doi.org/10.1016/j.optlaseng.2012.03.010>.
- [46] Y. Rong, Z. Zhang, G. Zhang, C. Yue, Y. Gu, Y. Huang, C. Wang, X. Shao, Parameters optimization of laser brazing in crimping butt using Taguchi and BPNN-GA, *Opt. Lasers Eng.* 67 (2015) 94–104, <http://dx.doi.org/10.1016/j.optlaseng.2014.10.009>.
- [47] Z. Gao, X. Shao, P. Jiang, L. Cao, Q. Zhou, C. Yue, Y. Liu, C. Wang, Parameters optimization of hybrid fiber laser-arc butt welding on 316L stainless steel using Kriging model and GA, *Opt. Laser Technol.* 83 (2016) 153–162, <http://dx.doi.org/10.1016/j.optlastec.2016.04.001>.

# Appendix F

Development of decoupled multi-physics  
simulation for laser lap welding considering  
part-to-part gap

**Development of decoupled multi-physics simulation for laser lap welding considering part-to-part gap**

Erkan Caner Ozkat, Pasquale Franciosa, and Dariusz Ceglarek

Citation: *Journal of Laser Applications* **29**, 022423 (2017); doi: 10.2351/1.4983234

View online: <http://dx.doi.org/10.2351/1.4983234>

View Table of Contents: <http://lia.scitation.org/toc/jla/29/2>

Published by the [Laser Institute of America](#)

---

---

## Development of decoupled multi-physics simulation for laser lap welding considering part-to-part gap

Erkan Caner Ozkat, Pasquale Franciosa, and Dariusz Ceglarek

Warwick Manufacturing Group, Gibbet Hill Road, University of Warwick, Coventry CV4 7AL, United Kingdom

(Received 28 March 2017; accepted for publication 28 March 2017; published 19 June 2017)

Remote laser welding is increasingly being adopted within the automotive industry due to its high production throughput at lower cost and flexibility, making the welding process much faster and more accurate. However, a leading challenge preventing its systematic uptake in the industry is the lack of efficient in-process monitoring and assuring high weld quality in the presence of process variability. Weld quality is generally assessed by measuring the key geometrical features of the melt pool such as penetration depth, interface width; and, both upper and bottom concavity which are directly correlated to static and fatigue performance. Existing solutions extract patterns from real-time data such as: plasma charge, acoustic or optical emissions measurements, etc. and integrate multivariate statistics and machine learning algorithms to estimate only a single key geometrical feature of the weld. For example, acoustic or optical emissions provide molten pool oscillation frequency, leading to penetration depth; the dimension of the molten pool obtained by visual sensing with high speed camera is correlated to interface width. The lack of comprehensive multiphysics models linking monitoring data and multiple welding process parameters (i.e. laser power, welding speed, and focal offset) with multiple key geometrical features underscores the limitations of the current methods toward delivering automatic in-process closed-loop quality control system. The multiphysics model should have capabilities for monitoring multiple key geometrical features; and, capabilities for on-the-fly process adjustment to guarantee high quality weld. This paper presents a novel analytical physics-driven simulation approach to monitor multiple key geometrical features. The developed model has the capability to be used for in-process monitoring of key geometrical features and, furthermore is a necessary enabler for the development of in-process closed-loop process adjustment applicable for remote laser welding. The proposed method is applicable for in-process monitoring of zinc coated steel in overlap joint configuration considering part-to-part gap. © 2017 Laser Institute of America. [<http://dx.doi.org/10.2351/1.4983234>]

Key words: laser welding, part-to-part gap, keyhole modeling, decoupled multiphysics simulation, in-process monitoring

### I. INTRODUCTION

Remote laser welding (RLW) is an advanced joining process and is increasingly used in the automotive industry since it offers high production throughput at a very competitive cost.<sup>1</sup> In essence, RLW can be defined as laser beam welding with larger focal length (400–2000 mm) which takes the three main advantages of laser beam welding i.e., non-contact, single-sided access, and high power beam which is capable of achieving deep penetration weld and small heat effect zone within a fraction of a second.<sup>2</sup> However, a leading challenge preventing its systematic uptake is the lack of efficient in-process monitoring and control to achieve and guarantee high quality weld in the presence of process variability. This can be achieved either by choosing optimum welding process parameters or by detecting the welding defects during the process (*in-process monitoring*) or afterward (*off-process monitoring*). In-process monitoring is envisaged because it offers the capability to accelerate defects identification and develop corrective strategies for on-the-fly process adjustment.

Weld quality is defined by multiple key geometrical features, classified as *surface-related features* (surface spatter, blowout, melt pool width, upper and bottom concavity) and *inner-related features* (penetration depth, interface width, porosity). The state-of-the-art of in-process monitoring for (remote) laser welding mainly relies on *sensor-based methods*, comprising either photodiode<sup>3–5</sup> or high speed camera based systems.<sup>6–8</sup> In the case of photodiode-based monitoring, the reflected light is converted into electrical signals by photodiode along with an optical filter. Key features, such as keyhole temperature, reflected laser intensity, and plasma intensity, are predefined for a good quality weld and associated to a reference signal. The comparison of the measured signal against the reference signal provides capability for measuring the weld quality. On the other hand, 2D images of the melt pool are captured by utilizing high speed cameras (e.g. CMOS, CCD) which are generally mounted on the laser head for coaxial viewing. The recorded images are used to measure surface related features (e.g. spatters, melt pool width, etc.). However, the important geometrical features

(i.e. penetration, interface width) cannot be seen by the camera in coaxial viewing. Current solutions for sensor-based monitoring are mostly *data-driven*, implying that predictive models are trained on gathered data using secondary information (plasma intensity, 2D images, etc.) and cannot be fully exploited outside of the training data set. As a result, changes in welding process parameters (e.g. laser power, welding speed, focal offset) or material properties can be handled only by rebuilding the predictive models. Furthermore, these models provide the estimation of the geometrical features of the melt pool, not of the direct measurements. To overcome this limitation, Bautze *et al.*<sup>9</sup> proposed directly measuring keyhole depth by utilizing low coherence interferometry. The approach has been demonstrated on laser welding applications with short focal length; however, it is not fully applicable for remote welding with dynamic and longer focal length.

Alternative solutions to data-driven approaches have been developed over the last two decades and can be classified as *physics-driven* approaches which aim to predict multiple key geometrical features based on simulated physical principles and implemented by ordinary differential equations (ODEs) and partial differential equations (PDEs) models. The first models have been developed based on finite element modeling (FEM) formulation and addressed the beam-to-material interaction and heat transfer neglecting fluid flow around the melt pool to describe the temperature field<sup>10-12</sup> and thermal stress.

The fluid flow around the melt pool and pressure balance inside the keyhole were later taken into account resulting in prediction of the shape and size of both the keyhole and the melt pool. The interface between the liquid and metal vapor phase is represented either by applying level-set<sup>13</sup> or volume of fluid<sup>14</sup> methods. More recent models have considered fluid flow not only as part of the liquid phase but also for the metal vapor phase (plasma plume).<sup>15</sup> Thus, the effect of evaporation and interaction between the plume and the melt pool allows to reduce the keyhole fluctuation. However, comprehensive FEM simulation of laser welding process considering part-to-part gap in overlap joint is still missing. Furthermore, increasing complexity of the model involving thermodynamic, thermocapillary fluid flow among other phenomena will eventually hinder the calculation time.

For instance, Zhou *et al.*<sup>16</sup> modeled pulsed model Nd:YAG laser welding for stainless steel taking into account metal vapor inside the keyhole and inverse Bremsstrahlung and Fresnel absorption along with heat transfer and thermocapillary fluid flow. According to the authors, the calculation time took 6 h of CPU time to simulate 100 ms of welding. Similarly, Courtois *et al.*<sup>15</sup> proposed a model for continuous wave (CW) operation of Nd:YAG laser welding. This model took into account solid, liquid and the metal vapor phases by coupling the heat and Navier-Stokes equations. The calculation time for 10 ms of welding process took 16 h at fixed 10  $\mu$ s time step. Therefore, the long calculation time for a given set of process parameters and material settings is the primary limitation of the complex 2D and 3D multiphysics models, which are not viable for in-process monitoring and control.

A promising solution for in-process monitoring with integrated physics-driven simulation is offered by the analytical formulation, which have been proposed to estimate the melt pool geometry and keyhole profile under the assumption of state-state condition and 2D heat flow. The pioneering attempt was made by Kaplan<sup>17</sup> for CO<sub>2</sub> laser welding. In his work, the keyhole shape was estimated considering the energy balance equation with multiple reflections at the keyhole wall. The author proposed an asymmetrical keyhole shape due to different heat conduction rates at different regions of the keyhole and it was found that the front of the keyhole was inclined as the welding speed increased. Lampa *et al.*<sup>18</sup> computed the melt pool geometry for blind laser welding of steel by applying Kaplan's method. The authors proposed that the thermal conductivity on the top of the keyhole is 2.5 times bigger than the actual thermal conductivity, when neglecting the thermocapillary fluid flow. Likewise, Zhao and DebRoy<sup>19</sup> applied the same modeling approach to estimate macroporosity formation during laser welding of aluminum alloys. Fabbro and Chouf<sup>20</sup> developed a novel analytical model to explain the dynamic behavior of the keyhole. The researchers proposed that the displacement of the keyhole wall acts in the direction of the combination of welding velocity and drilling velocity which was perpendicular to the keyhole wall surface and proportional to the absorbed laser intensity. The major advantage of physics-driven analytical modeling, when compared to expensive 2D and 3D FEM simulations, is the possibility to directly estimate the shape of the melt pool in much shorter time.

In this paper, we aim to develop a physics-driven analytical model of the keyhole shape and the melt pool applicable for process monitoring of zinc coated steel in overlap joint configuration with consideration of part-to-part gap. The method is derived based on the works of Kaplan<sup>17</sup> and Lampa *et al.*,<sup>18</sup> and then expanded to take into account the part-to-part gap interaction between upper and lower metals, Fresnel absorption and energy balance between the absorbed energy flux delivered from the laser beam and the heat flux conducted into metal on the keyhole wall. The keyhole and the melt pool profiles are calculated solving energy balance equations point-by-point. The thermo-capillary fluid flow is not considered in this study. However, a scaling factor, called "*thermal conductivity coefficient*", is used in the upper sheet metal part to consider the effect of the fluid flow. Thus, the thermal conductivity used in the upper sheet metal part is higher than the actual value of the material. The coefficient is estimated experimentally as a function of welding process parameters and is shown in the result section. Furthermore, the part-to-part gap reduces the laser energy flow between welded part as its energy gradually dissipates in the gap before affecting the lower sheet metal part. This energy

TABLE I. Chemical composition DX54D steel (wt. %).

Material	Elements (wt. %)					
	C	Si	Mn	P	S	Ti
DX54D	0.12	0.5	0.6	0.1	0.045	0.3

TABLE II. Mechanical properties of steel DX54D.

Material	Yield strength (MPa)	Tensile strength (MPa)	Total elongation (%)
DX54D	120–220	260–350	38

dropped is termed in this paper as “*line source damping coefficient*”. It is estimated from the experiments by initially measuring the melt pool distance at the top surface of the lower sheet metal part ( $r_{ML}$ ) from the cross-section images and then computing the corresponding line source strength. The coefficient represents the difference between the computed line source strength at the bottom surface of the upper sheet metal part and the top surface of the lower sheet metal. The model predicts both penetration depth and interface width. Experimental trials with different levels of welding speed and part-to-part gap have been performed to validate the model predictions. The nomenclature used in the paper is presented in the Nomenclature section.

II. MATERIALS AND EQUIPMENT

The material used in this study was DX54D hot dip galvanized (GI) steel with nominal zinc coating thicknesses of 20  $\mu\text{m}$  with a thickness of 0.50 mm for upper sheet metal and 1.8 mm for lower sheet metal. The chemical composition and mechanical properties of this steel are given in Tables I and II, respectively.

Welding experiments were carried out using IPG Photonics YLR-4000 laser source with a nominal power of 2.2 kW. The laser beam was delivered using an optical fiber of core diameter of 50  $\mu\text{m}$ , projecting the laser beam to a spot of 900  $\mu\text{m}$  diameter. The laser source generates a multimode beam with an  $M^2$  of 31.4 (measured by Primes Focus meter) at a central wavelength of 1064 nm. Neither shielding nor backing gases were used during the experiments. For each experimental configuration, three replications were executed and overall dimension of the melt pool was measured for each weld using an Optical Microscope. The process parameters and material properties used in laser welding experiments are given in Table III.

TABLE III. Process parameters and material properties used in laser welding experiments.

Process parameter	Unit	Value(s)
$P_L$	W	2200
$\beta$	$^\circ$	0
$z_O$	mm	0
$L_T$	mm	25
$z_R$	mm	14.13
$r_{fO}$	mm	0.45
$\rho$	$\text{kg/m}^3$	7860
$C_p$	$\text{J/kg}\cdot\text{K}$	465
$T_a, T_m, T_v$	K	300, 1893, 3123
$v_w$	m/min	[1 3]
$g$	mm	[0.05 0.30]

TABLE IV. Laser focusing and repositioning module.

Characteristic feature	Unit	Specification
Collimating length	mm	50
Focal length	mm	~1200
Working area	mm	$700 \times 450 \times 400$
Working distance	mm	min 894.308 max 1216.352

The laser beam was delivered by COMAU SmartLaser robotic system. The SmartLaser system is a dedicated system for remote laser dimpling/welding and consists of four axes with dynamics and kinematics of a standard industrial robot with an optical system able to deflect the focused beam with high dynamics. The system specifications are given in Table IV.

III. PROPOSED MODELING APPROACH

A. Model definition for single material

The energy balance method proposed in Refs. 17 and 18 is applied to estimate penetration depth and interface width in overlap joint configuration. This model takes into account energy balance on the keyhole wall. The energy absorbed by the keyhole wall from the incoming laser beam is balanced with the heat flux conducted into the keyhole wall. The keyhole wall angle is determined locally point-by-point solving the energy balance equation. Figure 1 illustrates the model and experimental cross section.

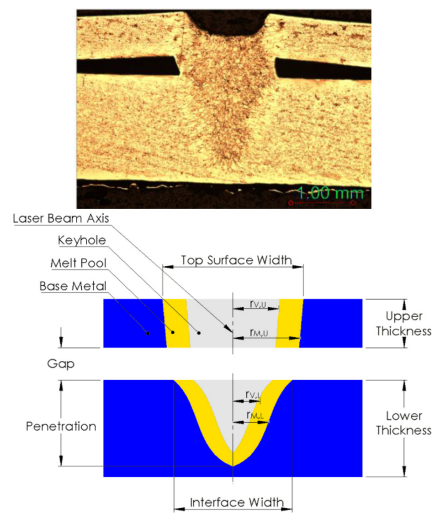


FIG. 1. (Top)—Weld cross section of overlap joint with gap. (Bottom)—Conceptual cross section showing overall shape of the melt pool and key parameters.



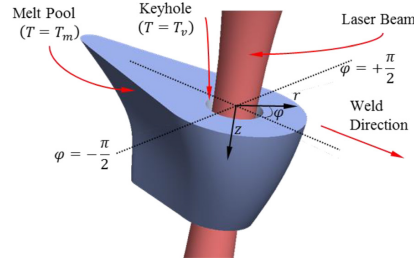


FIG. 2. Keyhole and the melt pool boundary in cylindrical coordinate.

The distance of keyhole wall ( $r_v$ ) and the melt pool boundary ( $r_m$ ) are measured from the laser beam axis in both upper and lower metal. Overall, the model predicts the shape of the melt pool as well as penetration and interface width in the time step when the keyhole is fully opened. The following assumptions have been made (refer also to Fig. 2):

- Line heat source is proposed to simulate keyhole mode laser welding which acts along the center of the keyhole;
- Gaussian distribution is assumed for the intensity of the laser beam;
- The temperature on the keyhole wall is assumed equal to the evaporation temperature, similarly, the temperature on the boundary layer between solid and liquid phases equals the melting temperature;
- The keyhole profile is asymmetrical in the plane parallel to the weld direction ( $\varphi = 0$ ). However, the model has been specifically developed for the plane perpendicular to the welding direction ( $\varphi = \pm \pi/2$ ), which corresponds to the same plane with cross section of the weldment. Nevertheless, the model can be generalized to any cross section;
- Heat flow is mainly transported in perpendicular to the laser beam axis;<sup>17</sup>
- The keyhole wall absorbs incoming laser beam directly by Fresnel absorption.
- The Fresnel absorption coefficient depends on the wall angle and material's optical properties.

The model is developed in cylindrical coordinate, where  $\varphi = 0$  and  $\varphi = \pi$  gives the front and rear keyhole wall profile, respectively. The plane of interest in this study is the cross section of the weldment at  $\varphi = \pm \pi/2$  (see Fig. 2).

The governing equation of temperature distribution for a moving line heat source was developed by Rosenthal<sup>21</sup> and it is given as

$$T(r) = T_a + \frac{P'}{2\pi\lambda} K_0(Pe' \cdot r), \quad (1)$$

with a modified Péclet number

$$Pe' = \frac{v_w}{2 \cdot \kappa}. \quad (2)$$

The heat flux at any point on inside the melt pool is defined as

$$q(r) = (T(r) - T_a) \lambda P e' \left( \frac{K_1(Pe' \cdot r)}{K_0(Pe' \cdot r)} \right), \quad (3)$$

where  $r$  is the radial distance from the line source axis. In the plane of interest, the laser beam axis and the line source axis are coincident each other and located in the center of the keyhole. Thus, the keyhole shape is symmetrical. When  $r$  equals the distance of the keyhole wall from the line source axis ( $r_v$ ) if the keyhole wall temperature is assumed to be at the evaporation temperature ( $T_v$ ), then equation

$$q_v = q(r_v) = (T_v - T_a) \lambda P e' \left( \frac{K_1(Pe' \cdot r_v)}{K_0(Pe' \cdot r_v)} \right). \quad (4)$$

Gaussian distribution is assumed for the intensity of the laser beam and is defined as

$$I(r, z) = I_0 \left( \frac{r_{fo}}{r_f} \right)^2 e^{-2(r/r_f)^2}, \quad (5)$$

where  $I_0$  is the peak laser beam intensity and  $r_f$  is the local laser beam radius in the laser beam propagation direction, defined as

$$r_f(z) = r_{fo} \left[ 1 + \left( \frac{z - z_0}{z_R} \right)^2 \right]^{1/2}. \quad (6)$$

In Kaplan's model,<sup>17</sup> the energy balance at the keyhole wall can be written considering only Fresnel absorption, as in Eq. (7), where  $\alpha_{FR}$  is the Fresnel absorption coefficient depending on the material optical properties and the wavelength of the emitted laser<sup>22</sup>

$$\tan(\theta) = \frac{q_v(r_v)}{\alpha_{FR}(\theta) \cdot I(r_v, z)}. \quad (7)$$

## B. Model calculation procedure for two material considering part-to-part gap

According to the literature, most of the laser energy is absorbed by the top surface of the material causing a thermocapillary fluid flow due to the temperature difference between the liquid metal and air. The flow pushes the liquid material outward from the keyhole and enlarges the top surface width. In the absence of the thermocapillary flow, Lampa *et al.*<sup>18</sup> proposed to use a constant artificial thermal conductivity at top surface which is greater than the actual (real) thermal conductivity. In this study, a similar approach was applied and following assumptions were made:

- The temperature at the melt pool boundary (between liquid and solid) was at the melting temperature ( $T_m$ ).
- The distance of the melt pool boundary in upper sheet metal ( $r_{M,U}$ ) on the top surface ( $z = 0$ ) was measured from the experimental cross sections. This corresponds to half of the top surface width.

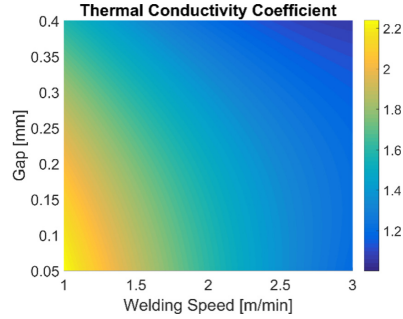


FIG. 3. Thermal conductivity coefficient used in the upper sheet metal.

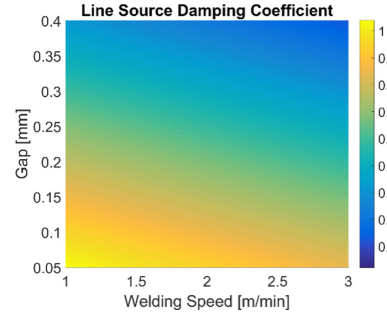


FIG. 4. Line source damping coefficient used in the lower sheet metal.

- Due to neglecting fluid flow around the keyhole, an artificial thermal conductivity is utilized which is a function of the welding speed and part-to-part gap.
- The initial melt boundary angle was assumed to be at  $5^\circ$ . This assumption was made after observing the cross-section images of weld in which the melt pool boundary in the upper sheet metal part appeared to be almost a straight line.
- The line heat source strength ( $P'$ ) was reduced while passing through part-to-part gap. The gap was considered as an obstacle.

The process for determining the melt pool profile is as follows:

- (1) Equations (3), (5), and (7) are solved together to find the artificial thermal conductivity ( $\lambda_{artificial}$ ) for  $T(r) = T_m$ ,  $\theta = 5^\circ$  on the top surface ( $z = 0$ ) in upper sheet metal.
- (2) Thermal conductivity coefficient ( $\alpha_{TC}$ ) can be found by dividing artificial thermal conductivity ( $\lambda_{artificial}$ ) to the actual thermal conductivity ( $\lambda_{actual}$ )

$$\lambda_{artificial} = \alpha_{TC} \cdot \lambda_{actual} \quad (8)$$

- (3) The distance of keyhole wall in upper sheet metal ( $r_{v,U}$ ) on the top surface ( $z = 0$ ) in upper sheet metal is computed rearranging Eq. (1) for  $T(r) = T_v$  using the artificial thermal conductivity.
- (4) By considering discrete values of  $z$ , the distance of keyhole wall ( $r = r_v$ ) and the melting boundary ( $r = r_m$ ) is

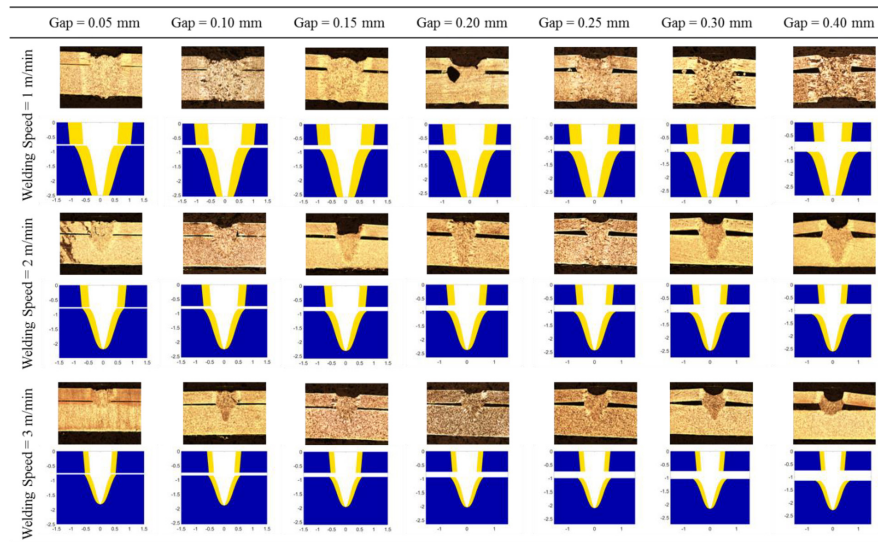


FIG. 5. Temperature distribution and the melt pool comparisons between model and experiment (■: Base metal ■: The melt pool □: Keyhole).

calculated point-by-point using Eqs. (7) and (9) from the top surface downward until the depth reaches the upper thickness using the artificial thermal conductivity.<sup>17</sup> ( $\Delta z = 1 \mu\text{m}$ )

$$\Delta r = \Delta z \tan \theta. \quad (9)$$

- (5) The line heat source strength at the bottom of the upper sheet metal part was calculated using Eq. (1) and applying artificial thermal conductivity.
- (6) The strength of the line source was calculated using Eq. (1) considering actual thermal conductivity and obtained interface width from the experiments.
- (7) Line source damping coefficient ( $\alpha_{TC}$ ) can be found by dividing lower strength value to upper strength value

$$P'_{Lower} = \alpha_{LD} \cdot P'_{Upper}. \quad (10)$$

- (8) According to the line heat source strength at the lower sheet metal the position of keyhole wall ( $r = r_{V,L}$ ) solving Eq. (1).
- (9) Step 7 was repeated until the keyhole radius reaches zero or when the depth of penetration equalled to the lower sheet metal thickness.

#### IV. CASE STUDY

The proposed analytical model simulates laser welding of overlap joint for given welding speed and part-to-part gap. Instead of using a constant correction factor of thermal conductivity, an experimental based factor was defined as a function of welding speed and gap in Fig. 3.

Lampa *et al.*<sup>18</sup> proposed to use a constant artificial thermal conductivity at top surface equal to 2.5, which corresponds to the minimum gap configuration ( $\sim 0.05 \text{ mm}$ ). However, this artificial thermal conductivity was almost equal to actual conductivity in maximum welding speed and gap configuration. This can be explained by the sagging effect of the melt pool. When the gap was too wide, liquid metal inside the melt pool started to fill the gap resulting in a narrow top surface width.

The laser welding of zinc-coated steels in overlap joint configuration posed a challenge due to the difference between the melting temperature of steel and the vaporizing temperature of zinc. Left unaddressed, highly pressurized zinc vapor can easily be trapped inside the molten pool which leads to welding defects.<sup>23-26</sup> Therefore, a gap is needed to evacuate the zinc vapor from the molten pool in lap welding of zinc coated steel. The formation of the keyhole in case of part-to-part gap is explained as follows: the keyhole is created in the upper sheet immediately when the laser beam hits the surface. Before the keyhole reaches the bottom of the upper sheet metal, the molten material fills the part-to-part gap and two sheet metals are in contact with each-other so the heat transfers to the lower sheet metal by conduction mechanism. Then, the keyhole opens inside the filled gap before reaching the lower sheet metal and some of the energy is absorbed here. Thus, a smaller keyhole in the lower sheet metal is formed. The amount of energy absorbed by the filled gap is

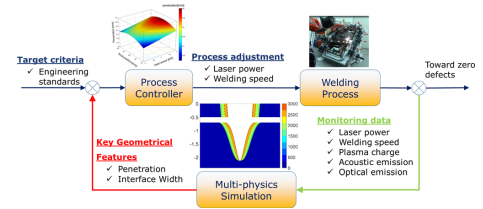


FIG. 6. An example of on-line in-process monitoring and adaptive quality improvement for remote laser welding assembly system.

associated to the damping coefficient of the line source energy in the keyhole. The coefficient is given in Fig. 4, which is estimated from the experiments by initially measuring melt pool distance from the cross-section images and then computing the strength of the line source in the top surface of the lower sheet metal.

The comparison between experimental and modelling results of melt pool shapes are illustrated in Fig. 5 for different welding speed and part-to-part gaps. The experimental results for penetration and interface width are given in Table V. In case of full penetration, the lower sheet-metal shrinks inward creating a concavity which reduces the penetration depth. This phenomenon is particularly true for low speeds (1 m/min) and triggers scenarios wherein the proposed model tends to overestimate the keyhole penetration, because it neglects the material shrinkage. However, in the case of higher welding speed (2 to 3 m/min), the keyhole is blind (i.e., it partially penetrates the lower metal) and the predicted

TABLE V. Comparison between the experimental and the simulation results.

Speed (m/min)	Gap (mm)	Measured		Simulated	
		Penetration (mm)	Interface Width (mm)	Penetration (mm)	Interface Width (mm)
1	0.05	1.75	1.78	1.75	1.82
1	0.10	1.61	2.01	1.75	2.02
1	0.15	1.62	1.96	1.75	2.02
1	0.20	1.58	2.32	1.75	2.13
1	0.25	1.53	1.97	1.75	1.99
1	0.30	1.51	2.09	1.75	1.97
1	0.40	1.4	1.8	1.75	2.07
2	0.05	1.16	1.3	1.45	1.35
2	0.10	1.31	1.29	1.49	1.40
2	0.15	1.56	1.37	1.52	1.42
2	0.20	1.69	1.49	1.64	1.44
2	0.25	1.7	1.19	1.59	1.39
2	0.30	1.72	1.58	1.56	1.53
2	0.40	1.47	1.86	1.57	1.82
3	0.05	0.52	1.01	0.87	1.13
3	0.10	1.05	1.13	0.94	1.12
3	0.15	0.81	1.17	0.95	1.18
3	0.20	0.78	1.16	1.30	1.27
3	0.25	0.92	1.33	1.26	1.34
3	0.30	0.89	1.29	1.26	1.39
3	0.40	0.46	1.23	0.82	1.38

values and experimental data show a good correlation. The maximum error is obtained for larger gap and higher welding speed. This could be imputed to the energy dissipated into the filled part-to-part interface, before the keyhole is fully developed in the lower metal.

## V. CONCLUSION AND FUTURE WORK

An analytical model based on energy balance was developed to estimate penetration and interface width in the overlap joint. The model was validated with the cross sectional images of the weldment. The overall dimension of the melt pool is correctly estimated for partial penetration, but it is overestimated for the full penetration due to the occurrence of the bottom surface concavity.

The proposed model has the capability to be used for direct in-process monitoring of key geometrical features and it is a necessary enabler for the development of the closed-loop quality control system. The conceptual framework of the closed-loop quality control system is shown in Fig. 6 which will be explored and implemented in future research. The main concept is based on the integration of the in-process monitoring data (e.g. laser power, welding speed, plasma charge, acoustic and optical emissions, etc.) with multiple key geometrical features such as weld penetration and interface width. This integration offers capabilities for on-the-fly process (in-process) adjustments to correct or prevent weld defects by changing welding process parameters such as laser power, welding speed, etc. The broad impact of this research is to use the developed framework to reduce and eliminate the weld defect before they occur.

## NOMENCLATURE

$C_p$	specific heat capacity (J/kg · K)
$g$	part-to-part gap (mm)
$I(r, \varphi, z)$	local laser beam intensity (W/m <sup>2</sup> )
$I_0$	peak laser beam intensity (W/m <sup>2</sup> )
$K_0()$	modified Bessel function second kind zero order,
$K_1()$	and first order (-)
$L_T$	laser track (mm)
$\dot{P}$	line source strength (W/m)
$Pe$	modified Péclet number (1/m)
$P_L$	laser power (W)
$q_v$	heat flux on the keyhole (W/m <sup>2</sup> )
$r_{M.U.}, r_{M.L.}$	distance of the melt pool boundary in upper metal, and lower metal (mm)
$r_{V.U.}, r_{V.L.}$	distance of keyhole wall in upper metal, and lower metal (mm)
$r_f(z)$	local laser beam radius (mm)
$r_{fo}$	on-focus laser beam radius (mm)
$T_a, T_m, T_v$	temperature of ambient, the melting and vaporization (K)
$v_w$	Welding speed (m/min)
$z_R$	Rayleigh length (mm)
$z_0$	focal offset (mm)
$\alpha_{FR}$	Fresnel absorption coefficient (-)
$\alpha_{LD}$	line source damping coefficient (-)

$\alpha_{TC}$	thermal conductivity coefficient (-)
$\beta$	incidence angle (deg)
$\theta$	Keyhole wall angle (deg)
$\lambda$	thermal conductivity (W/m · k)
$\rho$	density (kg/m <sup>3</sup> )
$\varkappa$	thermal diffusivity (m <sup>2</sup> /s)

## ACKNOWLEDGMENTS

This study was partially supported by the EU research project EU-FP7 FoF-ICT-2011.7.4: RLW Navigator and by the UK EPSRC project EP/K019368/1: Self-Resilient Reconfigurable Assembly Systems with In-process Quality Improvement.

- D. Ceglarek, M. Colledani, J. Vanca, D. Y. Kim, C. Marine, M. Kogel-Hollacher, A. Mistry, and L. Bolognese, "Rapid deployment of remote laser welding processes in automotive assembly systems," *CIRP Ann. - Manuf. Technol.* **64**, 389–394 (2015).
- A. K. Sinha, D. Y. Kim, and D. Ceglarek, "Correlation analysis of the variation of weld seam and tensile strength in laser welding of galvanized steel," *Opt. Lasers Eng.* **51**, 1143–1152 (2013).
- Y. W. Park, H. Park, S. Rhee, and M. Kang, "Real time estimation of CO<sub>2</sub> laser weld quality for automotive industry," *Opt. Laser Technol.* **34**, 135–142 (2002).
- I. Eriksson, J. Powell, and A. Kaplan, "Signal overlap in the monitoring of laser welding," *Meas. Sci. Technol.* **21**, 105705 (2010).
- A. R. Konuk, R. G. K. M. Aarts, A. J. H. Veld, T. Sibillano, D. Rizzi, and A. Ancona, "Process control of stainless steel laser welding using an optical spectroscopic sensor," *Phys. Procedia* **12**, 744–751 (2011).
- F. Abt, A. Blug, L. Nicolosi, F. Dausinger, H. Höfler, R. Tetzlaff, and R. Weber, "Real time closed loop control of full penetration keyhole welding with cellular neural network cameras," *J. Laser Micro Nanoeng.* **6**, 131–137 (2011).
- J. Beersiek, "New aspects of monitoring with a CMOS camera for laser materials processing," *21st International Congress on Application Lasers Electro-Optics*, Vol. 2(2002), pp. 1181–1190.
- D. Colombo, B. M. Colosimo, and B. Previtali, "Comparison of methods for data analysis in the remote monitoring of remote laser welding," *Opt. Lasers Eng.* **51**, 34–46 (2013).
- B. Thibault and M. Kogel-Hollacher, "Keyhole Depth is just a Distance," *Laser Technik Journal* **11**(4), 39–43 (2014).
- J. Ma, F. Kong, and R. Kovacevic, "Finite-element thermal analysis of laser welding of galvanized high-strength steel in a zero-gap lap joint configuration and its experimental verification," *Mater. Des.* **36**, 348–358 (2012).
- N. S. Shanmugam, G. Buvanashakaran, K. Sankaranarayanan, and S. Ramesh Kumar, "A transient finite element simulation of the temperature and bead profiles of T-joint laser welds," *Mater. Des.* **31**, 4528–4542 (2010).
- S. A. Tsirkas, P. Papanikos, and T. Kermanidis, "Numerical simulation of the laser welding process in butt-joint specimens," *J. Mater. Process. Technol.* **134**, 59–69 (2003).
- M. Courtois, M. Carin, P. L. Masson, S. Gaied, and M. Balabane, "A new approach to compute multi-reflections of laser beam in a keyhole for heat transfer and fluid flow modelling in laser welding," *J. Phys. D: Appl. Phys.* **46**, 505305 (2013).
- R. G. Vázquez, H. M. Koch, and A. Otto, "Multi-physical simulation of laser welding," *Phys. Procedia* **56**, 1334–1342 (2014).
- S. Pang, X. Chen, J. Zhou, X. Shao, and C. Wang, "3D transient multiphase model for keyhole, vapor plume, and weld pool dynamics in laser welding including the ambient pressure effect," *Opt. Lasers Eng.* **74**, 47–58 (2015).
- J. Zhou, H. Tsai, and P. Wang, "Transport phenomena and keyhole dynamics during pulsed laser welding," *J. Heat Transfer* **128**, 680–690 (2006).
- A. Kaplan, "A model of deep penetration laser welding based on calculation of the keyhole profile," *J. Phys. D: Appl. Phys.* **27**, 1805–1814 (1994).
- C. Lampa, A. Kaplan, J. Powell, and C. Magnusson, "An analytical thermodynamic model of laser welding," *J. Phys. D: Appl. Phys.* **30**, 1293–1299 (1997).
- H. Zhao and T. DebRoy, "Macroporosity free aluminum alloy weldments through numerical simulation of keyhole mode laser welding," *J. Appl. Phys.* **93**, 10089–10096 (2003).

- <sup>20</sup>R. Fabbro and K. Chouf, "Keyhole modeling during laser welding," *J. Appl. Phys.* **87**, 4075–4083 (2000).
- <sup>21</sup>D. Rosenthal, "The theory of moving sources of heat and its application to metal treatments," *Transactions of ASME* **68**, 849–866 (1946).
- <sup>22</sup>A. Kaplan, "Fresnel absorption of 1 mm- and 10  $\mu$ m - laser beams at the keyhole wall during laser beam welding: Comparison between smooth and wavy surfaces," *Appl. Surf. Sci.* **258**, 3354–3363 (2012).
- <sup>23</sup>Z. Chen, S. Yang, C. Wang, X. Hu, X. Shao, and J. Wang, "A study of fiber laser welding of galvanized steel using a suction method," *J. Mater. Process. Technol.* **214**, 1456–1465 (2014).
- <sup>24</sup>O. E. Caner, P. Franciosa, and D. Ceglarek, "Laser dimpling process parameters selection and optimization using surrogate-driven process capability space," *Optics & Laser Technology* **93**, 149–164 (2017).
- <sup>25</sup>J. Ma, F. Kong, B. Carlson, and R. Kovacevic, "Two-pass laser welding of galvanized high-strength dual-phase steel for a zero-gap lap joint configuration," *J. Mater. Process. Technol.* **213**, 495–507 (2013).
- <sup>26</sup>R. Oh, D. Y. Kim, and D. Ceglarek, "The Effects of Laser Welding Direction on Joint Quality for Non-Uniform Part-to-Part Gaps," *Metals* **6**(8), 1–13 (2016).

### Meet the Authors

Mr. Erkan Caner Özkat is a Ph.D. student at WMG department of the University of Warwick. He received his M.Sc. in Automotive Engineering from the University of Bath, UK in 2007. His major research interests are CAD and FEA modeling, and multiphysics simulation for product/process performance improvement.

Dr. Pasquale Franciosa is a Senior Research Fellow at WMG department of the University of Warwick, UK. His research interests are manufacturing assembly process simulation, process monitoring/control, machine learning and multi-disciplinary/multiobjective optimization. Ph.D. in Mechanical Engineering System at the University of Naples Federico II, Italy in 2009. Visiting Fellow at MIT (Boston - USA) working on robotics and motion/constraint analysis. He has been

contributing on several academic and industrial projects involving: dimensional management control and innovative tools development to predict stack-up of variations propagating in multistage assembly systems, multiphysics simulation for product/process performance improvement, and remote laser welding design and control.

Professor Darek Ceglarek is EPSRC Star Research Chair at WMG, University of Warwick and a CIRP Fellow. Previously, he was Professor in Industrial and Systems Engineering at University of Wisconsin, Madison. He received his Ph.D. in Mechanical Engineering from University of Michigan-Ann Arbor in 1994. His research focusses on digital manufacturing, in-process quality control and root cause analysis across design, manufacturing and service. His research has been funded by: US (NSF, NIST), United Kingdom (EPSRC, InnovateUK and HVM Catapult and) and EU (FP7, Marie Curie) and industry. He has published over 150 papers and received several Best Paper Awards. He has received numerous awards including 2007 UK EPSRC STAR Award, US NSF 2003 CAREER Award; 1999 Outstanding Research Scientist Award from University of Michigan; the 1998 Dell K. Allen Outstanding Young Manufacturing Engineer of the Year Award from the SME. He has served on numerous Editorial Boards and is an Associate Editor (Europe) of the *ASTM Smart and Sustainable Manufacturing Systems Journal*. Prof. Ceglarek served as Chair of the Quality, Statistics and Reliability Section of INFORMS; Program Chair for the ASME Design-for-Manufacturing Life Cycle Conferences, Assoc Editor of the *IEEE Trans.*, and of the *ASME Trans., J. Manuf Sys & Eng.*